Early Characterization and Performance of Flexible Pavements Utilizing Asphalt Additives

by

Megan Marie Foshee

A thesis submitted to the Graduate Faculty of
Auburn University
in partial fulfillment of the
requirements for the Degree of
Master of Science

Auburn, Alabama
May 7, 2022

Keywords: Asphalt additives, Flexible pavement
instrumentation, Structural characterization

Approved by

Dr. David Timm, Chair, Brasfield & Gorrie Professor Civil and Environmental Engineering
Dr. Nam Tran, Assistant Director and Research Professor National Center for Asphalt Technology
Dr. Brian Anderson, Associate Professor Civil and Environmental Engineering

Abstract

Asphalt additives have been utilized for years to modify the performance of flexible pavements. They have the potential to lead to long-lasting and sustainable asphalt pavements. In recent years, several new categories of asphalt additives, such as recycled tire rubber, post-consumer recycled plastic, and synthetic fiber, have been introduced to the flexible pavement industry. These new additives are being marketed toward agencies and contractors increasingly with the potential of increased pavement performance or maintaining performance at reduced cost. Field testing, which can confirm or deny the claimed benefits, is costly and time consuming. With the rapidly advancing asphalt additive industry, there is a need to efficiently evaluate and deploy the new asphalt additive technologies. To address this need, the National Center for Asphalt Technology developed the Additive Group Experiment for the 2021 NCAT Test Track research cycle to evaluate a range of new asphalt additive technologies.

Full-scale pavement sections, each using a different asphalt additive, were constructed and instrumented at the Test Track. A primary objective of this thesis was to document the construction of these sections. Accelerated trafficking and monitoring of the sections then commenced. The data collected from the monitoring and testing of the sections was then used to achieve the secondary objective: preliminary surface performance evaluations and structural behavior characterizations. The performance and behavior of the additive modified sections were then compared to those of the control section. It was determined that the data analyzed for the relatively short timeframe did not allow for recommendations to be made in this thesis on the viability of the additives for use in real-world paving applications. It was recommended, however, to continue trafficking and field testing of the sections to more comprehensively characterize their performance and behavior.

Acknowledgments

I would like to thank my advisor Dr. David Timm and my advisory committee, Dr. Nam Tran and Dr. Brian Anderson, for all their support and guidance throughout the writing of this thesis and during my educational career. The knowledge that I gained from them has helped shape me into the engineer that I am today. Also, I would like to thank Matthew Sasser, Rachel Cousins, Juliana Wood, Hayden Harding, Amir Rahimzadeh, and Matthew Kmetz for all their hard work during construction, data collection, and data processing. They all worked diligently to ensure that our common goal of developing and studying quality asphalt pavements was achieved. Finally, I would like to thank my fiancé James Ratliff and my family for their continuous love and support throughout my time in this graduate program. They all played larger roles than they realize in helping me reach my true potential.

Table of Contents

List of Tables

List of Figures

List of Abbreviations

AASHO	American Association of State Highway Officials
AASHTO	American Association of State Highway and Transportation Officials
AC	Asphalt Concrete
AG	Additive Group
AMPT	Asphalt Mixture Performance Tester
ANOVA	Analysis of Variance
ASG	Asphalt Strain Gauge
ASTM	American Society for Testing and Materials
BMD	Balanced Mixture Design
BWP	Between Wheelpath
COGA	Center of Gauge Array
COV	Coefficient of Variation
CT_{Index}	Cracking Tolerance Index
DATAQ	Data Acquisition System
DOT	Department of Transportation
EICM	Enhanced Integrated Climatic Model
EPA	Environmental Protection Agency
EPC	Earth Pressure Cell
ESAL	Equivalent Single Axle Load
FHWA	Federal Highway Administration
FI	Flexibility Index
FWD	Falling Weight Deflectometer

GB	Granular Base
GTR	Ground Tire Rubber
HDPE	High-Density Polyethylene
HMA	Hot Mix Asphalt
HWTT	Hamburg Wheel Tracking Test
I	Interstate
IDEAL-CT	Indirect Tensile Asphalt Cracking Test
I-FIT	Illinois Flexibility Index Test
IRI	International Roughness Index
ITS	Indirect Tensile Strength
IWP	Inside Wheelpath
JMF	Job Mixture Formula
LCA	Life Cycle Analysis
LDPE	Low-Density Polyethylene
LLDPE	Linear Low-Density Polyethylene
MRP	Micronized Rubber Powder
NAPA	National Asphalt Pavement Association
NCAT	National Center for Asphalt Technology
NDAs	Non-Disclosure Agreements
NMAS	Nominal Maximum Aggregate Size
OBC	Optimum Binder Content
OT	Overlay Test
OWP	Outside Wheelpath

PASER	Pavement Service Evaluation and Rating
PCR	Post-Consumer Recycled
PEM	Porous European Mixture
PG	Performance Grade
QC	Quality Control
RAP	Reclaimed Asphalt Pavement
RET	Reactive Elastomeric Terpolymer
RMSE	Root Mean Square Error
rPE	Recycled Polyethylene
RTR	Recycled Tire Rubber
SBS	Styrene-Butadiene-Styrene
SCB	Semi-Circular Bend
SMA	Stone Matrix Asphalt
SN	Structural Number
SPM	Smart Pavement Monitoring
S-VECD	Simplified Viscoelastic Continuum Damage
TB	Terminal Blended
VMA	Voids in the Mineral Aggregate
WMA	Warm Mix Additive

CHAPTER 1

Introduction

1.1 Background

Asphalt additives have been used for decades to improve the performance and sustainability of flexible pavements. Additives modify the asphalt binder or the asphalt mixture to enhance the rutting and/or cracking resistance of an asphalt pavement. Some additives also increase the sustainability of an asphalt pavement by reducing the need for virgin materials, incorporating recycled waste products, and/or lowering the cost of the mixture. For example, if an asphalt additive enhances the fatigue cracking resistance of a mixture enough, the asphalt layer of the pavement structure could be designed thinner. This would enable agencies and contractors to use less virgin aggregate and asphalt binder per lane mile and to better utilize their budgets. This scenario is improved further if the additive is derived from recycled waste products, since they are most likely cheaper and address environmental concerns. Asphalt additives have the potential to lead to long-lasting and sustainable asphalt pavements.

In recent years, several new categories of asphalt additives, such as recycled tire rubber (RTR), post-consumer recycled (PCR) plastic, and synthetic fiber, have been introduced to the flexible pavement industry. Asphalt additives like these are being developed and marketed towards agencies and contractors increasingly with claims to enhance asphalt pavements in some form or fashion. For some new asphalt additives, laboratory testing and research already exist to verify the claimed benefits. However, field testing and evaluation, which is objectively the more reliable method for the determination of benefits, is not available for newer asphalt additives since it is time-consuming to produce such data. Theoretically, asphalt additive-modified mixtures could show promising results in a laboratory setting but unfavorable results in the field. In this case, if only laboratory tests are run on the additive-modified mixtures, potentially counterproductive asphalt additives could be utilized on projects. On the other hand, asphalt additive-modified mixtures could show promising results in both laboratory and field settings. In this case, the extra time that it takes to validate laboratory findings with field performance could be equated to lost revenue on the agency’s or contractor’s part due to not being able to use the asphalt additives on projects during this time. Either way, with the rapidly advancing asphalt additive industry, there is a need to efficiently evaluate and deploy new asphalt additive technologies. To address this need, the National Center for Asphalt Technology (NCAT) developed the Additive Group (AG) experiment for the 2021 NCAT Test Track research cycle to evaluate a range of new asphalt additive technologies.

The AG experiment is composed of three phases of work; I, II, and III. Phase I involved preliminary efforts, such as limited laboratory characterization and predictive structural analyses for several experimental and control mixtures. This phase was crucial, as it allowed sponsors to make informed decisions about which asphalt additive-modified test sections to construct at the NCAT Test Track. The importance of gathering full-scale data on mixtures with a range of predicted performance was stressed to the sponsors, since it could aid in the development and calibration of a framework that enables rapid evaluation and deployment of new asphalt additive technologies (Timm et al., 2022).

With this goal in mind, the sponsors chose five additives across the new asphalt additive categories to compare against a Styrene-Butadiene-Styrene (SBS) polymer-modified control test section. Phase II included the construction and instrumentation of the full-scale test sections. Phase III involves structural and performance evaluation. This phase can be further categorized by early and long-term evaluation, which will be referred to from this point on as Phases IIIa and IIIb, respectively. Phase IIIa was comprised of applying accelerated traffic, monitoring, and evaluating the performance of the test sections over the first few months after construction. Phase IIIb consists of applying accelerated traffic, monitoring, evaluating the performance, and conducting more comprehensive laboratory testing on the test sections over the remainder of the research cycle. From the information gathered in all three phases, various new asphalt additive-modified sections can be directly compared to a well-known and studied control section, and agencies and contractors may be able to efficiently and confidently decide what types of asphalt additives are viable for projects.

At the writing of this thesis, Phases I, II, and IIIa were complete. Due to non-disclosure agreements (NDAs) within Phase I, which was funded directly by material suppliers, it is not presented in depth in this thesis. However, Phase I will be discussed in the literature review using publicly available information.

1.2 Objectives

The main objectives of this thesis, within the framework of the 2021 NCAT Test Track AG experiment, were:

- Construct and document full-scale test sections using the selected asphalt additives.
- Evaluate the early field performances of the test sections.
- Compare the early field performance of the additive-modified test sections to that of the control test section.

1.3 Scope of Work

Several steps were taken to accomplish the research objectives. After five of the many asphalt additives were chosen for implementation by sponsors, full-scale test sections were constructed and instrumented at the NCAT Test Track. Accelerated traffic was then applied to the test sections by utilizing multiple heavy triple-trailer trucks. For the 2021 research cycle, traffic began on November 10, 2021. This thesis includes data from the start of traffic until March 15, 2022, accumulating approximately 956,884.2 equivalent single axle loads (ESALs). Over this timeframe, the sections were routinely monitored with subsurface instrumentation in addition to falling weight deflectometer (FWD) testing and backcalculation for structural characterization. The sections were also monitored and evaluated for early surface field performance (i.e., rutting, cracking, ride quality) over the same timeframe. Comparisons were made between each experimental section and the control.

1.4 Organization of Thesis

This thesis continues in Chapter 2 with a literature review that introduces the new asphalt additive technologies that are relevant to the AG Experiment, describes potential benefits and concerns of the new asphalt additive technologies, details previous testing and studies involving the new asphalt additive technologies, and presents the methods and publicly available results of the AG Experiment: Phase I. Chapter 3 describes the construction process and instrumentation implementation for the test sections. Chapter 4 discusses the early surface performance of the sections under accelerated traffic. Chapter 5 analyzes the early structural performance of the sections under accelerated traffic. Finally, Chapter 6 summarizes the findings and recommendations derived from this experiment as well as the plans for future research involving the AG experiment.

CHAPTER 2

Literature Review

This literature review first introduces the new asphalt additive technologies that are relevant to the AG Experiment. The additives, as well as the respective incorporation processes, are defined and described. Also, the state of practice for utilizing these new asphalt additives is revealed. Next, the potential benefits and concerns of each of the new asphalt additive technologies are listed and discussed. Previous testing and studies involving the new asphalt additive technologies are then presented. Finally, the methods and publicly available results from Phase I of the AG Experiment are stated and discussed.

2.1 Introduction of New Asphalt Additive Technologies

The types of new asphalt additives included in this study are recycled tire rubber (RTR), post-consumer recycled (PCR) plastic, and synthetic fiber. RTR is rubber that is made from PCR tires. It is available in many forms, including "whole tires, stamped items, chunks, shreds, chips, crumb, and ground" (Baumgardner et al., 2020). Ground tire rubber (GTR), which is also referred to as crumb rubber, is the more commonly used form of RTR in flexible asphalt pavement production. For this reason, GTR is focused on in this literature review. There are currently two ways of incorporating GTR into the asphalt binder and mixture, which are known as wet and dry processes, respectively (Baumgardner et al., 2020). The wet process involves modifying the asphalt binder with GTR particles and then using the modified binder to produce an asphalt mixture (Rath et al., 2021). This process is usually completed at the asphalt binder supply terminal or on site "with a prescribed reaction time prior to mixing the GTR-modified asphalt binder with aggregate" (Baumgardner et al., 2020). The dry process entails adding GTR particles directly into the asphalt mixture during production. According to Baumgardner et al. (2020), this process is usually performed on-site at the asphalt mixture plant, where it is added "to the aggregate in the asphalt plant mixing drum prior to introducing the asphalt binder". Rath et al. (2021) expand on this concept by explaining that it is typically added near the reclaimed asphalt pavement (RAP) collar, which is located toward the discharge end of a drum mix plant, "without any change in aggregate gradation". Figure 2.1 provides a flow chart for these GTR incorporation processes. Figures 2.2 and 2.3 show what typical GTR additives look like, when included via the wet and dry processes, respectively.

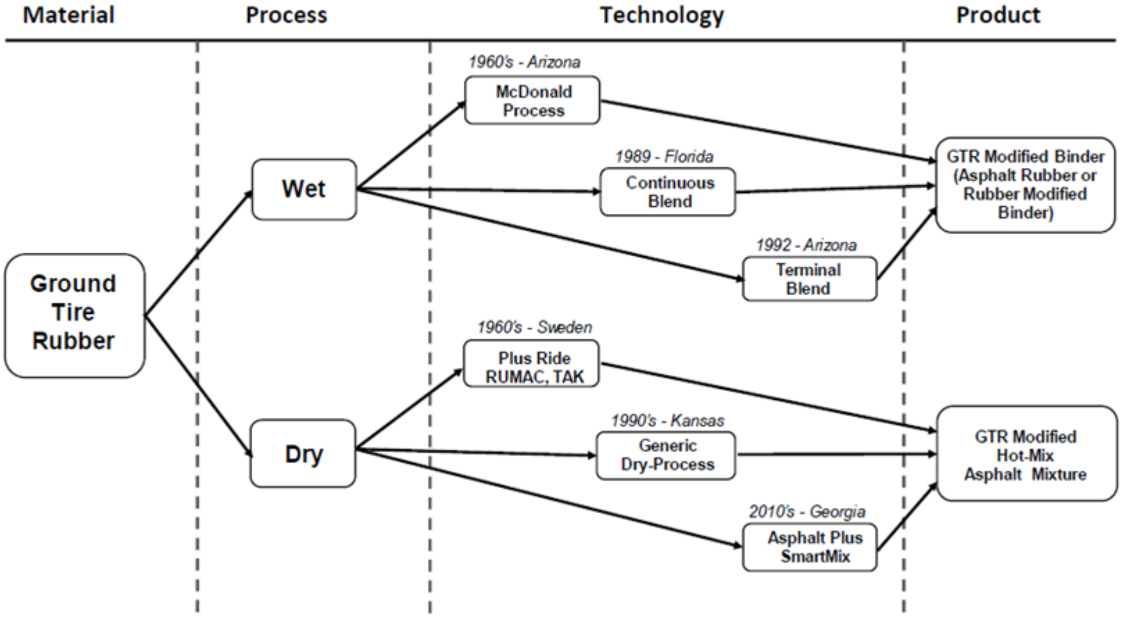

Figure 2.1: Primary Methods of Incorporating GTR into Asphalt Binders and Mixtures (Baumgardner et al., 2020)

Figure 2.2: Typical Wet Process GTR Additive ("Scrap Tires in Asphalt," 2021)

Figure 2.3: Typical Dry Process GTR Additive (“SmartMix,” 2021)

According to Baumgardner et al. (2020), state department of transportation (DOT) published specifications showed that only twelve states have published specifications that allow for the use of GTR-modified asphalt binders in the construction of asphalt pavements. The states are Oregon, Nevada, California, Arizona, Texas, Louisiana, Missouri, Tennessee, Florida, Georgia, South Carolina, and Ohio (Baumgardner et al., 2020). Also, the National Asphalt Pavement Association (NAPA) recently reported that twenty-one producers from eleven states indicated “using GTR in some asphalt mixtures” (Williams et al., 2019). Table 2.1 presents the reported tons of GTR used in 2018 by various states.

Table 2.1: Distribution Among States of Reported Tons of GTR Used in 2018 (Baumgardner et al., 2020)

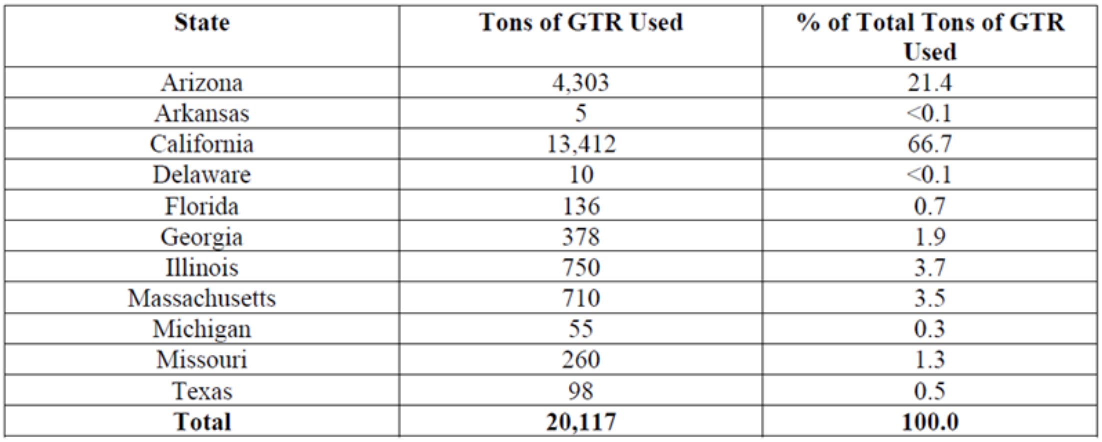

State	Tons of GTR Used	% of Total Tons of GTR Used
Arizona	4,303	21.4
Arkansas	5	<0.1
California	13,412	66.7
Delaware	10	<0.1
Florida	136	0.7
Georgia	378	1.9
Illinois	750	3.7
Massachusetts	710	3.5
Michigan	55	0.3
Missouri	260	1.3
Texas	98	0.5
Total	**20,117**	**100.0**

From the table, it is evident that California used the most GTR-modified asphalt binder (Baumgardner et al., 2020). However, several states have placed evaluation projects using GTR via wet and dry processes. Dry process projects, which are often referred to by the suppliers as "chemically engineered rubber" technology, have been constructed in Georgia, Illinois, Indiana, Louisiana, Maryland, Missouri, Oklahoma, Texas, Virginia, and Wisconsin since 2007 (Baumgardner et al., 2020). These projects account for approximately 5 million total tons of dry process GTR since 2007 ("Asphalt Plus," 2015). Also, Liberty Tire and Lehigh Industries have placed dry process projects, referring to them as "dry-mix" technology, in Michigan and Ohio ("Liberty Tire Recycling", 2021; "Micronized Rubber Powder (MRP)", 2022).

PCR plastic is another type of new asphalt additive that is included in this study. Out of all PCR plastics, linear low-density polyethylene (LLDPE), low-density polyethylene (LDPE), and high-density polyethylene (HDPE) together account for the largest portion at over 35% (Yin et al., 2021). For this reason, recycled polyethylene (rPE) is focused on in this literature review. There are currently two ways of incorporating rPE into the asphalt binder and mixture, which are known as wet and dry processes, respectively (Yin et al., 2021). For the wet process, the recycled plastics are "added to the asphalt binder as polymer modifiers, where mechanical mixing is required to achieve a homogenous plastic modified binder" (Yin et al., 2021). For the dry process, the recycled plastics are "added directly to the mixture as aggregate replacement or mixture modifiers" (Yin et al., 2021). These methods are essentially the same as the methods for GTR incorporation, so the paragraph detailing the processes for GTR incorporation can be read for further explanation. Figures 2.4 and 2.5 show what typical rPE additives look like, when included via the wet and dry processes, respectively.

Figure 2.4: Typical Wet Process rPE Additives ("Research Needed on Using Recycled Plastics in Asphalt," 2021)

Figure 2.5: Typical Dry Process rPE Additive (Yin, 2022)

According to Willis et al. (2020), approximately “200 field projects using recycled plastics in asphalt pavements were identified in literature”. Most of these field projects, which were completed in many countries between the late 1980s and the early 2000s, were constructed using Novophalt® (Willis et al., 2020). These projects included city streets, county roads, minor and principal arterials, interstates, and airports (Willis et al., 2020). Although limited, field performance data suggested that the pavement sections performed well; however, one study reported more cracking in these projects “compared to pavement sections using unmodified and SBS modified binders” (Willis et al., 2020). Willis et al. (2020) also claimed that many of the projects in the US are relatively new, so “the long-term durability of the pavements has yet to be determined”.

Synthetic fiber is the final type of new asphalt additive that is included in this study. Kadolph (2002) defines fibers that are used to reinforce asphalt mixtures as a natural or synthetic material that has greater length than width or has a high length to width ratio. Many types of fibers, like fiberglass, basalt, carbon, aramid, polyolefin, polypropylene, nylon, brucite, etc., have been evaluated for their potential to enhance the performance of hot mix asphalt (HMA) mixtures over the years (Alfalah et al., 2020). In reviewing literature, it was determined that aramid, polyolefin, and polypropylene fibers are among the most studied and tested. For this reason, these fiber types are focused on in this literature review.

Although some sources (Musa et al., 2019) have documented utilizing wet and dry processes for synthetic fiber dispersion, the dry process is most commonly used in the US. In fact, Musa et al. (2019) claim that the dry process is usually “preferred over the wet process” in field work “because of the production problems” associated with the wet process. The dry process for the inclusion of synthetic fibers is focused on in this literature review for this reason. This process is similar to the dry process for GTR and rPE asphalt additive inclusion, so the paragraph detailing dry process GTR incorporation can be read for further explanation. Essentially, they are all introduced directly into the asphalt mixture near the RAP collar during production. However, synthetic fibers must be blown into the asphalt mixture due to their small mass, elongated shape, and tendency to adhere to one another. Figure 2.6 shows what typical synthetic fiber asphalt additives look like.

Figure 2.6: Typical Synthetic Fiber Additives - Polyolefin and Aramid Fibers (Muftah et al., 2017)

According to McDaniel (2015), most states have used fibers in open-graded mixtures, but only a few states have utilized fibers in dense-graded asphalt mixtures. It was determined that the states used fiber types such as “mineral, glass, cellulose, and synthetic polymer” in these mixtures (McDaniel, 2015). The design procedure for the fiber mixtures was found to be the same as for conventional mixtures, but the purposes for the fibers varied (McDaniel, 2015). For stone matrix asphalt (SMA), open-graded, and porous friction course mixtures, fibers were primarily used to control the draindown of the asphalt binder in the mixture (McDaniel, 2015). For dense-graded mixtures, the fibers were used in only a few states to enhance rutting and cracking performance (McDaniel, 2015). Georgia, Oklahoma, Tennessee, Virginia, and Idaho were found to use fibers for the purpose of enhancing performance in both ways (McDaniel, 2015). However, New Hampshire was found to use fibers for improving only cracking performance, while Ohio was found to use fibers for improving only rutting performance (McDaniel, 2015).

2.2 Potential Benefits and Concerns of New Asphalt Additive Technologies

As mentioned in Chapter 1, the new categories of asphalt additives are introduced to the market with the goal of enhancing a flexible pavement’s performance, economy, and/or sustainability. It is generally accepted that “pavements with longer service lives should involve less maintenance and are environmentally friendly from the perspective that they involve less greenhouse gas” and that pavements with longer service lives are more economical and more efficiently serve public needs since there is less congestion due to recurring maintenance and construction (Baumgardner et al., 2020). So, if potential performance-enhancing benefits can be proven, arguments can logically be made for the environmental and economic benefits of an asphalt additive. In the literature, a number of potential benefits such as these, as well as possible concerns, are documented and discussed for the various asphalt additives. Since the expected mode of failure for the AG experiment is bottom-up fatigue cracking, benefits and concerns related to cracking and the additives themselves were the focus.

A noted potential benefit of adding GTR to asphalt binder is that it improves its elasticity and introduces various mechanisms that aid in mixture performance (Rath et al., 2021). Rath et al. (2021) goes on to write that this could solve two issues at once, which are the need to “construct more durable, distress resistant roads” and “find a suitable use for the billions of scrap tires that overwhelmed the landfills and were the source of various kinds of pollution including uncontrolled fires”. GTR is evidently an abundantly available waste material that can be tapped into for use in enhanced asphalt pavement applications. Also, a life cycle analysis (LCA) of rubber-modified asphalt has shown that net energy savings of 28.651 kWh/m^3 could be seen over the lifetime of a GTR-modified asphalt pavement relative to that of a conventional HMA pavement, as well as cost effectiveness from better pavement performance (Wang et al., 2018; Souliman et al., 2020). Greenhouse gas emissions derived from electricity consumption could be reduced by about 1×10^4 kg CO_2 when compared to conventional technologies, and budgets could be better utilized (Wang et al., 2018; Souliman et al., 2020).

The different methods for GTR incorporation also have benefits and concerns associated with them. An advantage of the dry process is that it is “logistically easier, as it does not require storage, and can be achieved with minimum modification to existing plant equipment” as opposed to the wet process (Rath et al., 2021). Contractors would not necessarily have to purchase all new equipment to pave with dry process GTR. Also, the dry process allows for a higher percentage of GTR to be added to the asphalt mixture (Bressi et al., 2019). This would enable more PCR tires to be repurposed, as well as potentially better pavement performance to be experienced. A concern of the wet process is that there is the potential for “settlement of rubber particles in the modified binder during storage and transport” (Presti, 2013). The time spent in storage in preparation for production might cause the asphalt binder to become non-homogeneous and perform differently than intended. Another concern of the wet process is that “depending on GTR content and asphalt binder compatibility,” it “may lead to binders having much higher viscosities than typical polymer modified binders” (Baumgardner et al., 2020). This increased viscosity may cause pumping issues at asphalt mixture production plants.

Similar to GTR, a documented potential benefit of adding rPE to asphalt mixtures is that it can reduce the amount of plastic that would “otherwise be landfilled, burned, or discarded in the natural environment as trash or litter” (Federal Highway Administration (FHWA), 2015). According to the U.S. Environmental Protection Agency (EPA), more than 35 million tons of plastics were disposed of in 2017, with only 2.9 million tons being recycled and the remaining being incinerated or sent to landfills (2018). To add to the sense of urgency, a report published NAPA stated that in 2018, China closed its borders to the import of waste plastics from other countries (Willis et al., 2020). Until 2018, China imported about 45% of the world’s plastic waste (Willis et al., 2020). So, the amount of incinerated or landfilled plastic in the US must have increased more in the last few years than previously. Clearly there is a pressing need to develop a better alternative for waste plastics after their initial service life. PCR plastic asphalt additives might be the solution. However, it has also been stated that due to “increased embrittlement and reduced relaxation properties, adding recycled plastics may have a detrimental impact on the fatigue and cracking resistance of asphalt binders and mixtures” (Yin et al., 2021). A balance between stiffness and softness must be achieved for an asphalt mixture to resist most forms of distress, but PCR plastics might make mixtures too stiff to resist cracking. Also, NAPA has reported that using certain recycled plastics in asphalt mixtures has health and safety concerns associated with it (Willis et al., 2020). If certain plastics get into stormwater runoff or otherwise come into contact with people, animals, and/or the environment, harm could be done. This could potentially be a reason to put a filtering process in place for PCR plastics before use in asphalt pavements. It might be able to ensure that these types of plastic additives are not utilized.

As with GTR, the different methods for rPE incorporation also have benefits and concerns associated with them. For the dry process, the main reported concern is the “lack of consistency in the quality of final produced asphalt mixtures” (Yin et al., 2021). This is possibly due to the variability of PCR plastic shapes, sizes, and makeups. This variability needs to be improved for asphalt pavement designs utilizing PCR plastic additives to be more reliable. For the wet process, there are concerns about the poor storage stability of the plastic modified binders, “where the plastic polymers have a tendency to separate from the asphalt binder as a result of the differences in density and viscosity, as well as the incompatibility between the two components” (Yin et al., 2021). Just like with wet process GTR, the time spent in storage in preparation for production might cause the asphalt binder to become non-homogeneous and perform differently than intended.

A possible benefit of adding synthetic fibers to asphalt mixtures is that it can strengthen the mixture and enhance its performance. This is because “the addition of fibers into HMA mixtures serves as a three-dimensional secondary reinforcement because of the fibers’ adhesion with asphalt binders and ability to interlock with aggregates” (Tapkin, 2008). Mahrez et al. (2005) expands on this concept by explaining that the use of fiber as reinforcing materials is mainly for the purpose of providing extra tensile strength to the asphalt mixture that may increase the amount of strain energy that can be absorbed throughout cracking of the mixture. Tapkin (2008) attributes the additional tensile strength to fibers like polypropylene fibers sometimes having tensile strengths greater than 276 MPa by themselves, which is evidently the minimum value accepted for polypropylene fibers by the Ohio Department of Transportation. It is believed that stresses can be transmitted to the fibers, which are strong in tension, thus reducing the stresses on the relatively weak asphalt mixture (McDaniel, 2015). This has the potential to improve a mixture’s cracking resistance as described later in this literature review.

However, good adhesion between the fibers and asphalt binder are necessary to efficiently transfer the stresses; larger surface area on the fibers can promote this adhesion (McDaniel, 2015). It has also been stated that there is a lack of understanding in this regard and that reinforcing mechanisms and ways of optimizing fiber properties need to be improved (Jahromi, 2015). Jahromi claims that fibers that are “too long” can create a “balling” problem where fibers may lump together, preventing a homogeneous mixture, and that fibers that are “too short” cannot provide enough reinforcing effect in the mixture (2015). Blowing the fibers into the mixture at the production plant can help alleviate homogeneity issues. Regardless, if the fibers do not possess the appropriate qualities like the examples listed and do not perform as intended, there could be negative consequences on mixture performance.

A major concern of using synthetic fibers in asphalt mixtures is the uncertainty associated with dosage rates, or fiber contents. It has been shown that fibers can improve the fatigue or structural performance of asphalt mixtures when high dosage rates (0.3% and greater) are used (Mahrez and Karim, 2010). Although, it has also been found that higher fiber dosage rates can cause issues in the mixture design, requiring major increases in binder content or alterations to the gradation to meet manufacturers’ mixture design specifications (Mahrez and Karim, 2010). Fiber manufacturers, therefore, recommend the use of fibers in asphalt mixtures at lower dosage rates (between 0.05% and 0.16%) and claim not to affect the original mixture design (FORTA, 2017). However, Alfalah et al. (2020) state that there is a lack of research on the impact of fibers on asphalt mixture performance “at these lower dosage rates”. To add to the dosage rate discussion, Alidadi and Khabiri (2016) propose that too low of a fiber dosage may increase the probability of constructing a weak cross-section, while too high of a fiber dosage may “reduce the cohesion between aggregates” and encourage fibers to lump together. Evidently, it is imperative that an appropriate amount of fiber is selected for a given asphalt mixture. Manufacturer dosage rates may be suitable, but laboratory tests like the ones discussed in the following section of this literature review could be conducted to optimize the fiber content to perform as desired.

2.3 Previous Testing and Studies Involving New Asphalt Additive Technologies

Possible benefits and concerns of the new additive technologies can be discussed and debated at length, but laboratory and field tests are necessary to determine whether or not the claims are true. Laboratory testing, depending on the type of test being run, can be a quick and easy way of predicting mixture performance, determining whether a mixture is adequate for production, and/or giving greater insight into the characteristics of a mixture. Field testing, on the other hand, is often a slower process since it can necessitate full-scale projects and longer timeframes. However, field testing is an extremely reliable method for evaluating mixture performance. Both laboratory and field testing are recommended to fully characterize and evaluate an asphalt mixture, though. To this end, laboratory test data and field study information was gathered and discussed for projects involving GTR, rPE, and synthetic fiber. Since the expected mode of failure for the AG experiment is bottom-up fatigue cracking, mixture laboratory tests and field studies related to general cracking and fatigue cracking were the focus.

In reviewing literature, it was found that several laboratory cracking tests have been conducted on GTR, rPE, and synthetic fiber modified asphalt mixtures. The various tests include the Illinois Flexibility Index Test (I-FIT) which can be completed according to American Association of State Highway and Transportation Officials (AASHTO) TP 124-16, the Indirect Tensile Asphalt Cracking Test (IDEAL-CT) which can be conducted per American Society for Testing and Materials (ASTM) D 8225-19, the Semi-Circular Bend (SCB) test which can be completed per ASTM D 8044-16, the Dynamic Complex Modulus (E*) test which can be performed in accordance with AASHTO T 342, and the Texas Overlay Test (OT) which can be conducted according to Tex-248-F. It was also found that some field experiments have been conducted using GTR and synthetic fiber modified asphalt mixtures. The various field experiments were conducted at different times and in different locations all over the US. However, field testing utilizing rPE modified asphalt mixtures was not found in the literature. Willis et al. (2020) state that several field projects using recycled plastic have been completed and perform well, but limited data exist to confirm or deny this assertion.

For the I-FIT, the Flexibility Index (FI) parameter is calculated from test data and used to evaluate the cracking propagation resistance of an asphalt mixture at an intermediate temperature (Abdalfattah et al., 2022). Figure 2.7 shows the test setup, where the test specimen is semi-circular with a precut notch and undergoes three-point bending (Rivera-Pérez et al., 2021). The FI is determined by dividing the fracture energy of the specimen by the load-displacement curve postpeak inflection point slope (Rivera-Pérez et al., 2021). The greater the FI value, the better the cracking resistance of the mixture.

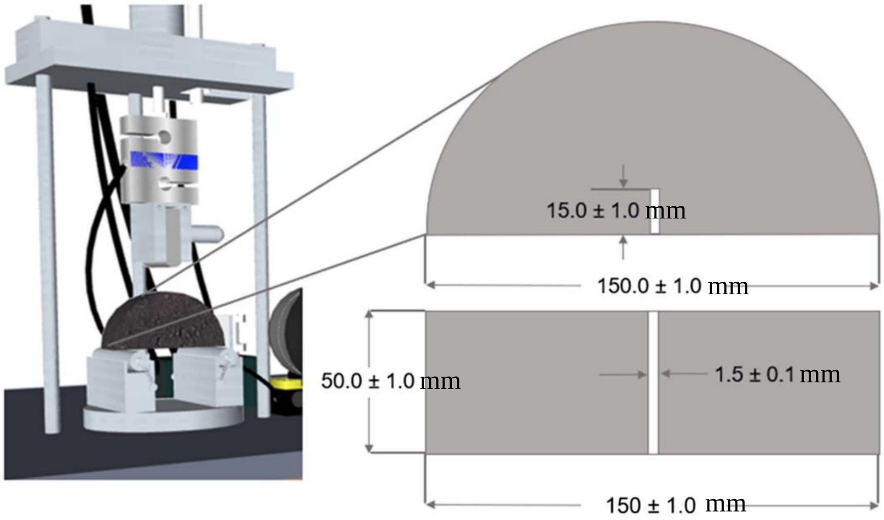

Figure 2.7: I-FIT Setup (Rivera-Pérez et al., 2021)

Using dry process GTR incorporation, Rath et al. conducted an I-FIT experiment involving 12 asphalt mixtures (2021). The FI values, which can be found in Figure 2.8, revealed that the "addition of rubber to the mixture decreases the cracking resistance" (Rath et al., 2021). Rath et al. (2021) conclude, however, that these FI results are inconsistent with field performance. This field performance study is discussed later in this literature review.

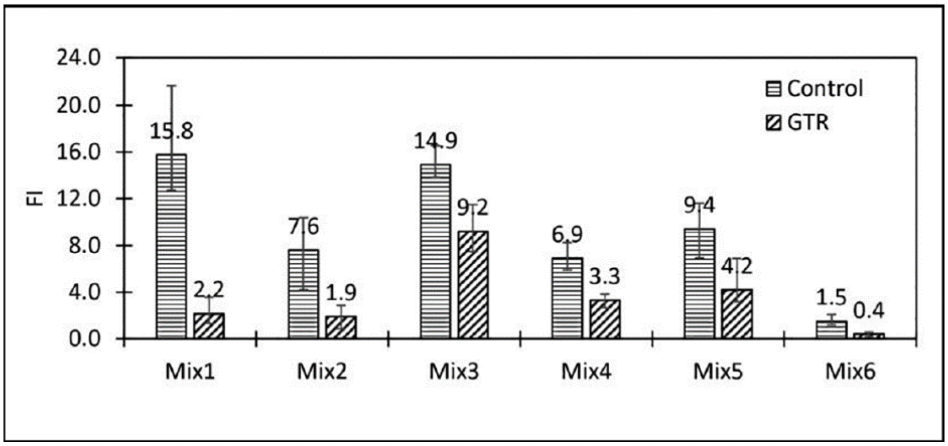

Figure 2.8: FI Results by Percentage of GTR Added (Rath et al., 2021)

Using rPE, Abdalfattah et al. (2022) completed an I-FIT experiment involving 12 wet process mixtures and 10 dry process mixtures. For the wet process part of the experiment, FI values show that "rPE modified asphalt mixtures are more susceptible to cracking at intermediate temperatures" than the control mixture as seen in Figure 2.9 (Abdalfattah et al., 2022). Two different asphalt binders were also utilized in this wet process experiment. The I-FIT results show that mixtures produced with one binder "exhibited slightly better cracking performance than" mixtures produced with the other binder, which can also be seen in Figure 2.9 (Abdalfattah et al., 2022). The researchers go on to say that this "confirms that the performance of rPE modified asphalt mixtures could be highly affected by the virgin binder source" (Abdalfattah et al., 2022). For the dry process part of the experiment, different dosages were utilized. The 2.5% and 5% rPE modified mixtures produced greater FI values than the control mixture, meaning that those amounts of rPE increased the cracking resistance of the mixture; however, as "the rPE dosage was increased incrementally, the FI values kept dropping" (Abdalfattah et al., 2022). As the dosage of rPE increased, the cracking resistance decreased. An optimum amount of rPE may exist in this case. It was also noted that "mixtures produced using the dry process yielded a better cracking propagation resistance compared with their counterparts fabricated using the wet process" (Abdalfattah et al., 2022). From the wet and dry process experiments, it is evident that virgin binder source as well as incorporation process have an impact on the performance of rPE modified mixtures.

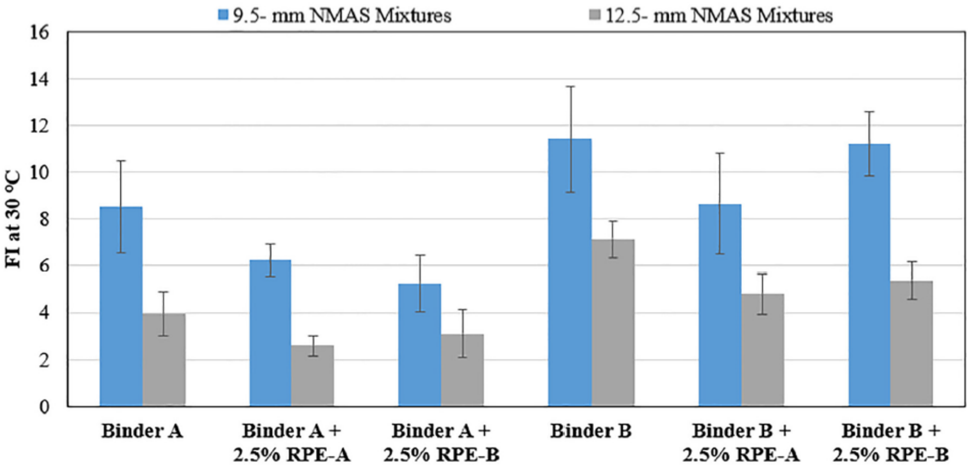

Figure 2.9: FI Results of Control and rPE Modified Mixtures via the Wet Process (Abdalfattah et al., 2022)

For the IDEAL-CT, the Cracking Tolerance Index (CT_{Index}) parameter is calculated from test data and used to determine the intermediate temperature cracking resistance of asphalt mixtures (Yin et al., 2021). Figure 2.10 shows the test setup ("Ideal-Ct - Simple, Reliable, Efficient, Repeatable, Cost Effective," 2022). The test specimen is uncut and undergoes indirect tension to determine the CT_{Index} of the mixture. The greater the CT_{Index} value, the better the cracking resistance of a mixture.

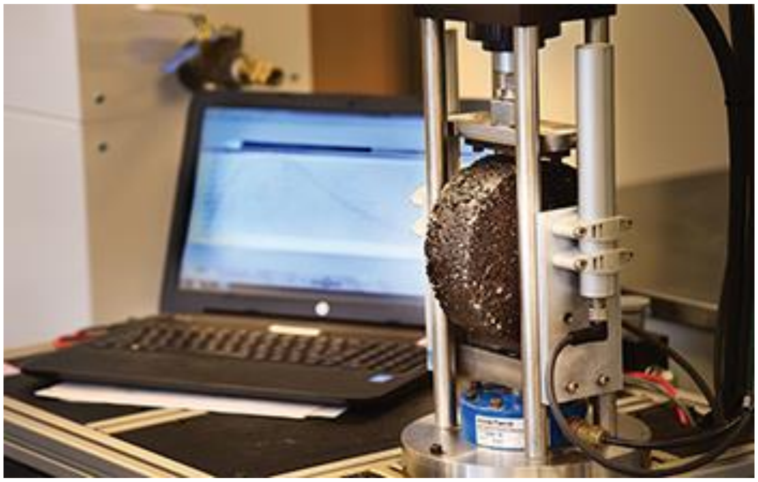

Figure 2.10: IDEAL-CT Setup ("Ideal-Ct - Simple, Reliable, Efficient, Repeatable, Cost Effective," 2022)

Using the same dry process GTR incorporation as in the I-FIT experiment, Rath et al. (2021) conducted an IDEAL-CT experiment with 12 mixtures. The researchers found that, similar to their I-FIT results, CT_{Index} values "penalize the mixtures for the addition of rubber," which can be seen in Figure 2.11 (Rath et al., 2021). Once again, Rath et al. (2021) conclude that these results are inconsistent with field performance. The field performance study is discussed in the following paragraphs. They go on to explain the issues that the results of their tests highlight. Rath et al. (2021) claim that the results "might inhibit the use of sustainable recycled materials such as GTR when Balanced Mixture Design (BMD) principles are used, depending on the selection of the mixture cracking test in the BMD specification". For example, if agencies and/or contractors are using I-FIT or IDEAL-CT parameters as their cracking test thresholds, GTR modified mixtures could possibly be deemed inadequate for production, even though they may perform well in the field. Thus, the benefits of GTR would not be realized. So, new additive modified mixtures may need to go through laboratory test and field calibration procedures before BMD based decisions are made, or cracking tests need to be chosen with the desired new additive in mind.

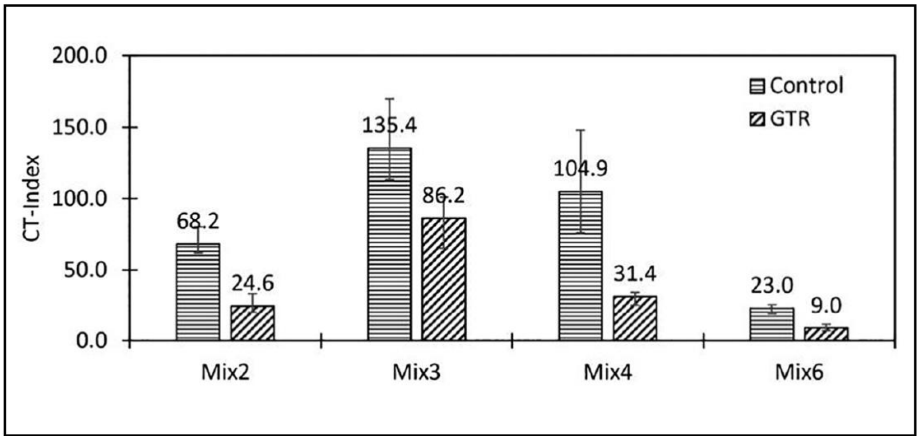

Figure 2.11: CT_{Index} Results by Percentage of GTR Added (Rath et al., 2021)

Rath et al. (2021) documented three field projects that utilized dry process GTR because they found the “discrepancies observed in cracking results in laboratory testing” were cause enough to “conduct a deeper examination of field cracking performance data”. The researchers visually inspected the projects, analyzed the limited field core data, and applied a complex smart pavement monitoring (SPM) software to measure the Pavement Service Evaluation and Rating (PASER) (Rath et al., 2021). The PASER system can be used to rate the condition of road sections on a scale of 1-10, with 1 being the worst condition and 10 being the best condition (Walker, 2002).

The first project that Rath et al. (2021) evaluated was a section of Interstate (I)-88 in Dekalb county, Chicago, Illinois. In 2016, a dry process GTR modified SMA mixture was placed in the left lane, which was next to an SBS modified SMA mixture that had been placed in the right lane in 2015 (Rath et al., 2021). Figure 2.12 shows the sections. In 2019, the researchers concluded via visual inspection that the sections were in “excellent condition” (Rath et al., 2021). Field cores were also collected from the sections and tested using the I-FIT (Rath et al., 2021). The results indicated that the SBS modified section had a higher FI value than the dry process GTR modified section, meaning that the SBS modified section had greater cracking resistance, “despite the additional field aging time” (Rath et al., 2021).

These I-FIT results are consistent with I-FIT and IDEAL-CT tests discussed earlier. However, the researchers emphasized that the dry process GTR modified section "did not exhibit any form of cracking," even though it produced a lower FI value and contained more RAP, while the SBS modified section "showed the onset of thermal cracking" (Rath et al., 2021). Also, the SPM software calculated the PASER rating to be 9.7 for the two sections combined, meaning that the sections are in excellent condition "with very few cracks, as confirmed by visual inspection" (Rath et al., 2021). Since it is evident that the section modified with dry process GTR performed well, the need to calibrate BMD cracking tests like the I-FIT and IDEAL-CT to correlate more accurately to field performance is apparent.

Figure 2.12: Picture of Dry Process GTR and SBS Modified Sections (Rath et al., 2021)

The second project that Rath et al. (2021) evaluated was a section of I-75 in Perry, Georgia. In 2007, a chemically modified dry process GTR mixture was placed next to an

SBS modified porous European mixture (PEM) (Rath et al., 2021). The GTR section was apparently expected to last only five to seven years, but “recent field visits have shown that the pavement lanes are still in good condition” (Rath et al., 2021). Also, the SPM software calculated the PASER rating to be 8.5 in 2019, which is a high rating for pavement that is over ten years old (Rath et al., 2021). Figure 2.13 shows a picture of the sections as well as pictures from the SPM software (Rath et al., 2021).

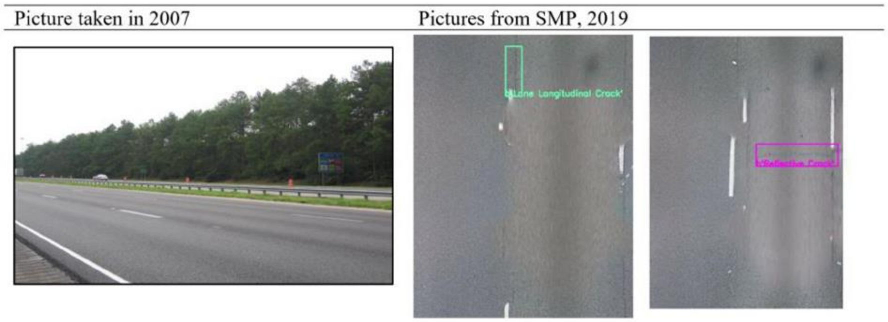

Figure 2.13: Chemically Modified Dry Process GTR and SBS Modified PEM Sections and SMP Software Pictures (Rath et al., 2021)

The third and final project that Rath et al. (2021) evaluated was a section of residential street in Davison, Michigan. The street “functions as an outlet for all the city’s school buses twice a day during the school year,” meaning that it consistently supports heavier traffic (Rath et al., 2021). In 2016, a dry process GTR modified mixture was placed. Recent visual inspections revealed that the section is “still in good condition with no cracking” (Rath et al., 2021). Also, the SPM software calculated the PASER rating to be 8.1 in 2019.

Using wet process rPE incorporation, Yin et al. (2021) conducted an IDEAL-CT experiment involving several different asphalt mixtures. One control mixture was unmodified, another was modified with rPE, another with rPE and Reactive Elastomeric Terpolymer (RET), and one more with SBS (Yin et al., 2021). The mixtures were also either short-term or long-term aged. Figure 2.14 shows the CT_{Index} results (Yin et al., 2021). For the short-term aged portion of the experiment, “the control mixture showed the highest average CT_{Index} value and thus was expected to have the best intermediate temperature cracking resistance, followed by the rPE-plus-RET modified, SBS modified, and rPE modified mixtures, respectively" (Yin et al., 2021). For the long-term aged portion of the experiment, "the control mixture still had the highest average CT_{Index} value while the rPE-plus-RET modified mixture had the lowest CT_{Index} value" (Yin et al., 2021). For both parts of the experiment, the control mixture has the best cracking resistance. This suggests that aging polymer and plastic modified mixtures increases their stiffnesses and reduces their ability to resist cracking, which is to be expected. This concept is supported by the observation that "long-term aged samples had significantly lower CT_{Index} values than the short-term aged samples" (Yin et al., 2021). However, it was also noted that "the differences among the four mixtures were less pronounced for long-term aged samples than short-term aged samples" (Yin et al., 2021). Regardless, IDEAL-CT results showed that using rPE and rPE+RET in short-term and long-term aged asphalt mixtures had a negative impact on intermediate temperature cracking resistance (Yin et al., 2021).

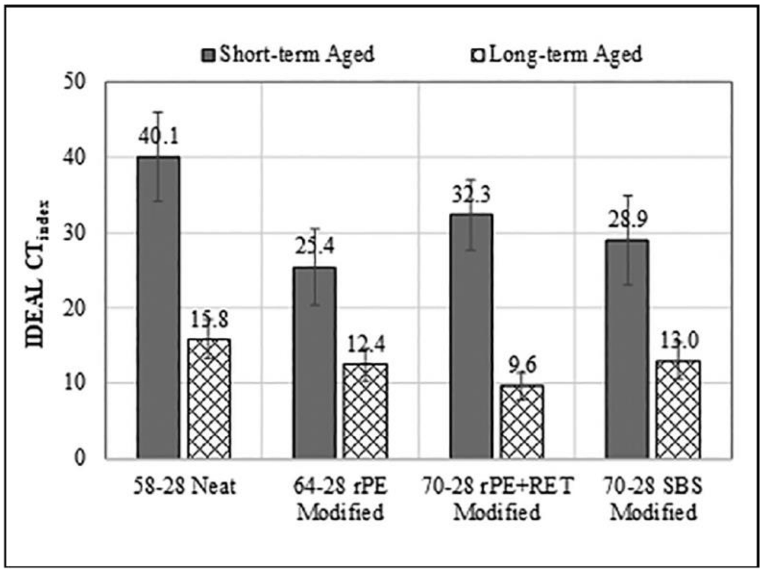

Figure 2.14: CT_{Index} Results of Short-Term and Long-Term Aged Asphalt Mixtures (Yin et al., 2021)

Using the same rPE as in the I-FIT experiment, Abdalfattah et al. (2022) also conducted an IDEAL-CT experiment with 12 wet process mixtures and 10 dry process mixtures. Only long-term aged mixtures were tested in this experiment. For the wet process part of the experiment, "rPE modified asphalt mixtures exhibited lower average CT_{Index} than the corresponding control mixture," meaning that the rPE modified mixtures may have worse cracking resistance than the control mixture (Abdalfattah et al., 2022). This trend can be visualized in Figure 2.15 (Abdalfattah et al., 2022). It was also observed that rPE modified mixtures using one virgin binder produced higher CT_{Index} values than when using another virgin binder, which can also be seen in Figure 2.15 (Abdalfattah et al., 2022). Thus, virgin binder source does have an impact on mixture cracking performance. For the dry process part of the experiment, different dosages were again utilized. It was discovered that “increasing the rPE percentage slightly decreased the average CT_{Index}” (Abdalfattah et al., 2022). This trend is consistent with the results of the I-FIT test that was conducted by the same researchers (Abdalfattah et al., 2022). It was also consistent in that the dry process yielded higher CT_{Index} values, and therefore better cracking resistance, than the wet process, which further confirms that the method of rPE incorporation affects performance (Abdalfattah et al., 2022).

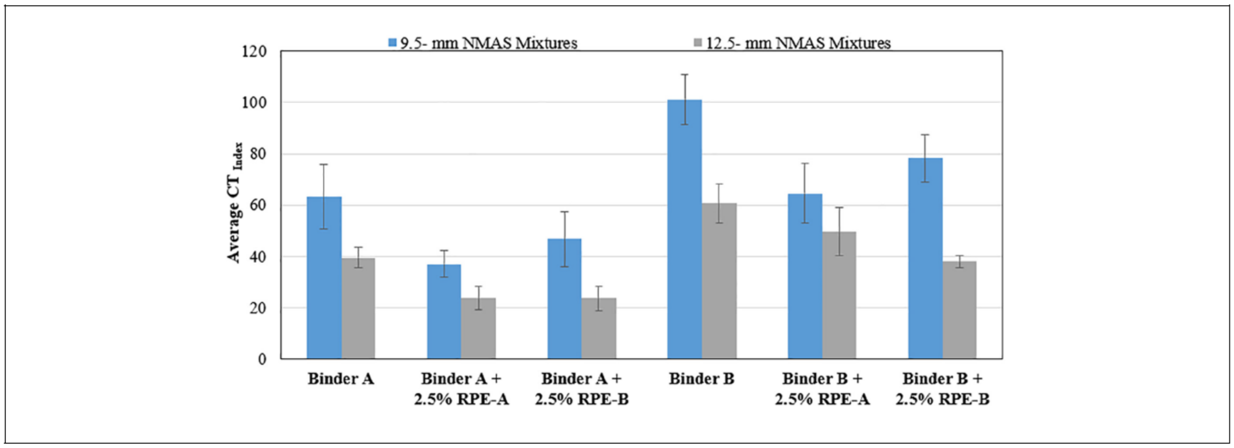

Figure 2.15: CT_{Index} Results of Control and rPE Modified Mixtures via the Wet Process (Abdalfattah et al., 2022)

Using a blend of polyolefin and aramid synthetic fibers, Alfalah et al. (2020) conducted an IDEAL-CT experiment on asphalt mixtures. It was determined that CT_{Index} values increased slightly when the fibers were used, as seen in Figure 2.16, but an Analysis of Variance (ANOVA) test showed that the CT_{Index} values were not significantly different for the control and fiber reinforced asphalt mixtures (Alfalah et al., 2020). So, it was concluded that use of the fibers does not improve the cracking resistance of asphalt mixtures (Alfalah et al., 2020).

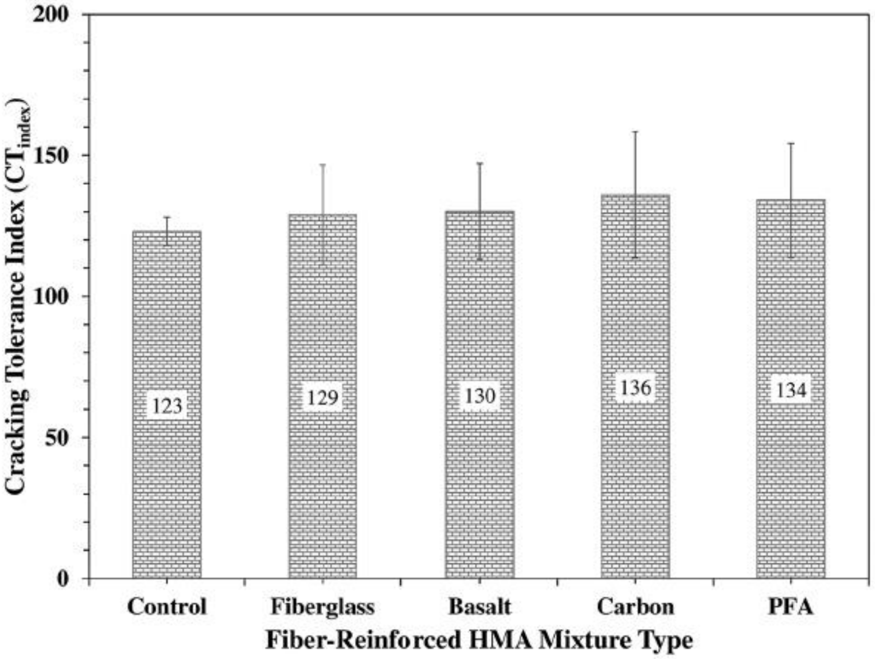

Figure 2.16: CT_{Index} Results of Control and Fiber Modified Mixtures (Alfalah et al., 2020)

For the SCB test, test data are used to determine the bottom-up fatigue cracking resistance of asphalt mixtures (Muftah et al., 2017). Figure 2.17 shows the geometry of a SCB test specimen (Mull et al., 2005). The test specimen is semi-circular with a precut notch and undergoes three-point bending, as with the I-FIT test. However, in the SCB test, FI is not determined. Several other parameters measured within the test, such as fracture energy, cycles to failure, and crack speed, are used instead to evaluate the cracking resistance of a mixture. The greater the fracture energy, which is the area under the load versus deformation curve, the more cycles it takes to fail a mixture specimen, and the lower the crack speed, the better cracking resistance a mixture has.

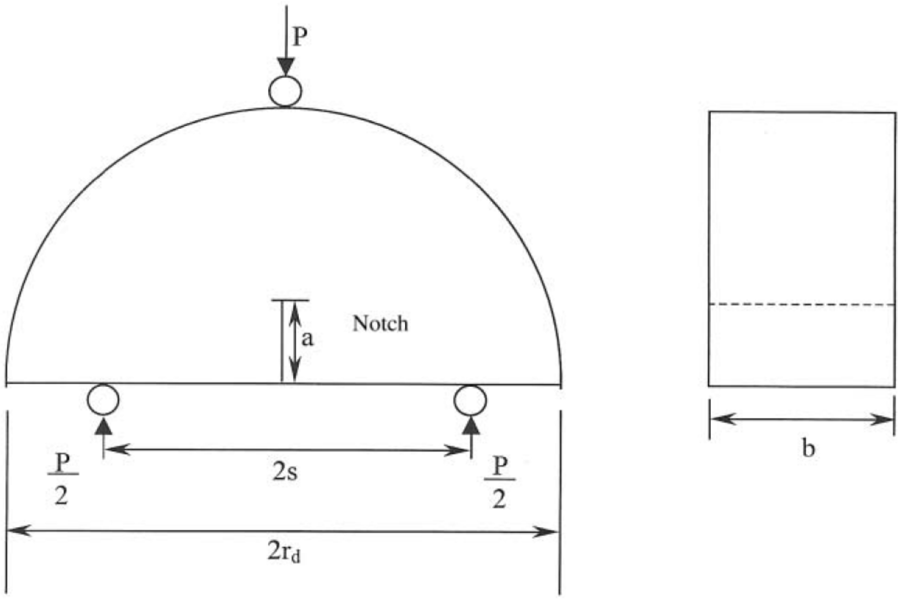

Figure 2.17: SCB Test Specimen Geometry (Mull et al., 2005)

Using dry process GTR incorporation, Mull et al. (2005) conducted a SCB experiment involving several asphalt mixtures. A control mixture, GTR modified mixture, and a chemically modified GTR mixture were tested. The resulting cycles to failure revealed that the chemically modified GTR mixture had the best fatigue cracking resistance, as seen in Figure 2.18 (Mull et al., 2005). This mixture achieved more cycles to failure and its crack propagated more slowly than the GTR modified and control mixtures, which can be seen in Figure 2.19, giving it about 2.2 times the fatigue life of the GTR modified mixture and about 5.6 times the fatigue life of the control mixture (Mull et al., 2005). Mull et al. (2005) attributed this increased fatigue crack resistance to enhanced asphalt binder performance. The researchers claim that this is “through an increase in both the interfacial adhesion between the asphalt binder and aggregate, and the cohesiveness properties of the binder itself” (Mull et al., 2005).

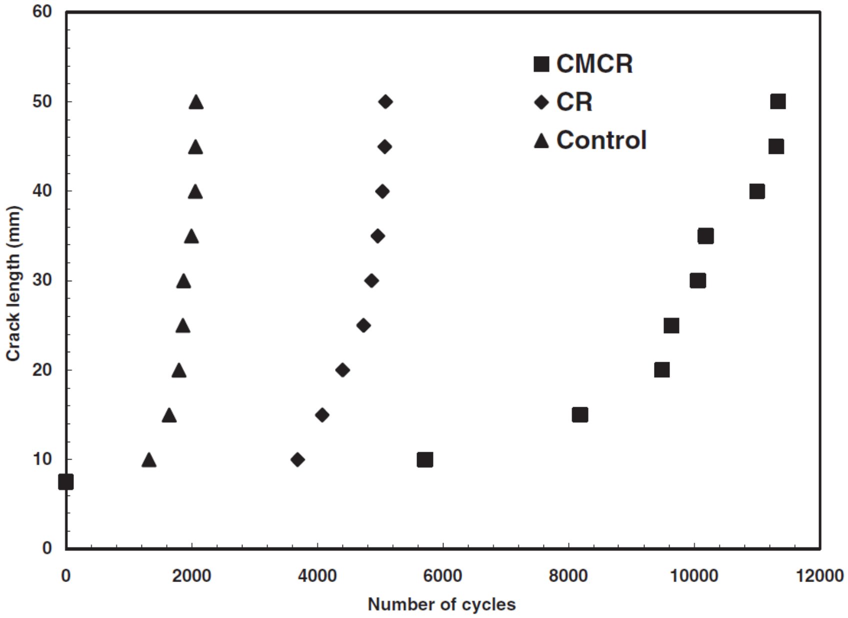

Figure 2.18: Crack Length as a Function of Number of Cycles (Mull et al., 2005)

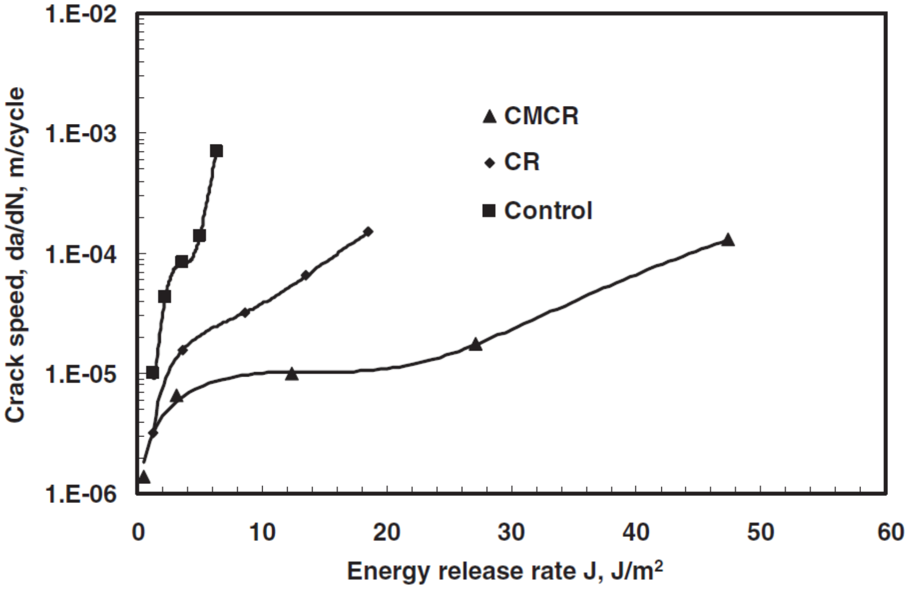

Figure 2.19: Crack Speed as a Function of Energy Release Rate (Mull et al., 2005)

Using a blend of polyolefin and aramid synthetic fibers as well as wax-treated aramid fibers, Muftah et al. (2017) conducted an SCB experiment on asphalt mixtures that were placed in the field for a project as well as field cores. For the experiment, both low and high fiber dosages were used, with the low dosage rates being manufacturer recommended. Figure 2.20 presents the resulting load versus deformation curves, which help visualize fracture energy (Muftah et al., 2017). From an ANOVA analysis of the low dosage results, it was determined that “no significant difference was found in the field mixes with respect to fracture energy” (Muftah et al., 2017). Muftah et al. (2017) claim that this finding may suggest that “fibers do not provide significant improvements to the cracking resistance of field mixes because of their low fiber content”. The fracture energies of the high dosage tests, however, showed different behavior. The researchers found that the fibers “might not have improved the performance of the mix before the peak load was reached,” but after the peak load was reached and the cracking was initiated, “fibers were found to reduce crack propagation significantly” (Muftah et al., 2017). They also suggest that this may have been the result of “the bridging effect of fibers,” which essentially means that the fibers likely prohibited further cracking by keeping the materials intact (Muftah et al., 2017). It was further stated that they observed this phenomenon during the test. It was determined that “the bonding of the fibers to the mixture’s constituents, as well as the content of the fibers, were key factors that contributed to the improved performance” (Muftah et al., 2017). The researchers conclude that at low strain levels the fibers simply acted as filler material and did not improve mixture performance, but at higher strain levels the fibers may have enhanced performance (Muftah et al., 2017). Since the mixtures utilizing fibers at the manufacturer recommended dosage rates were shown not to significantly affect mixture performance but higher fiber dosage was shown to improve performance, it was recommended that “the optimum amount of different fibers be checked before the production of fiber-modified asphalt mixtures” (Muftah et al., 2017).

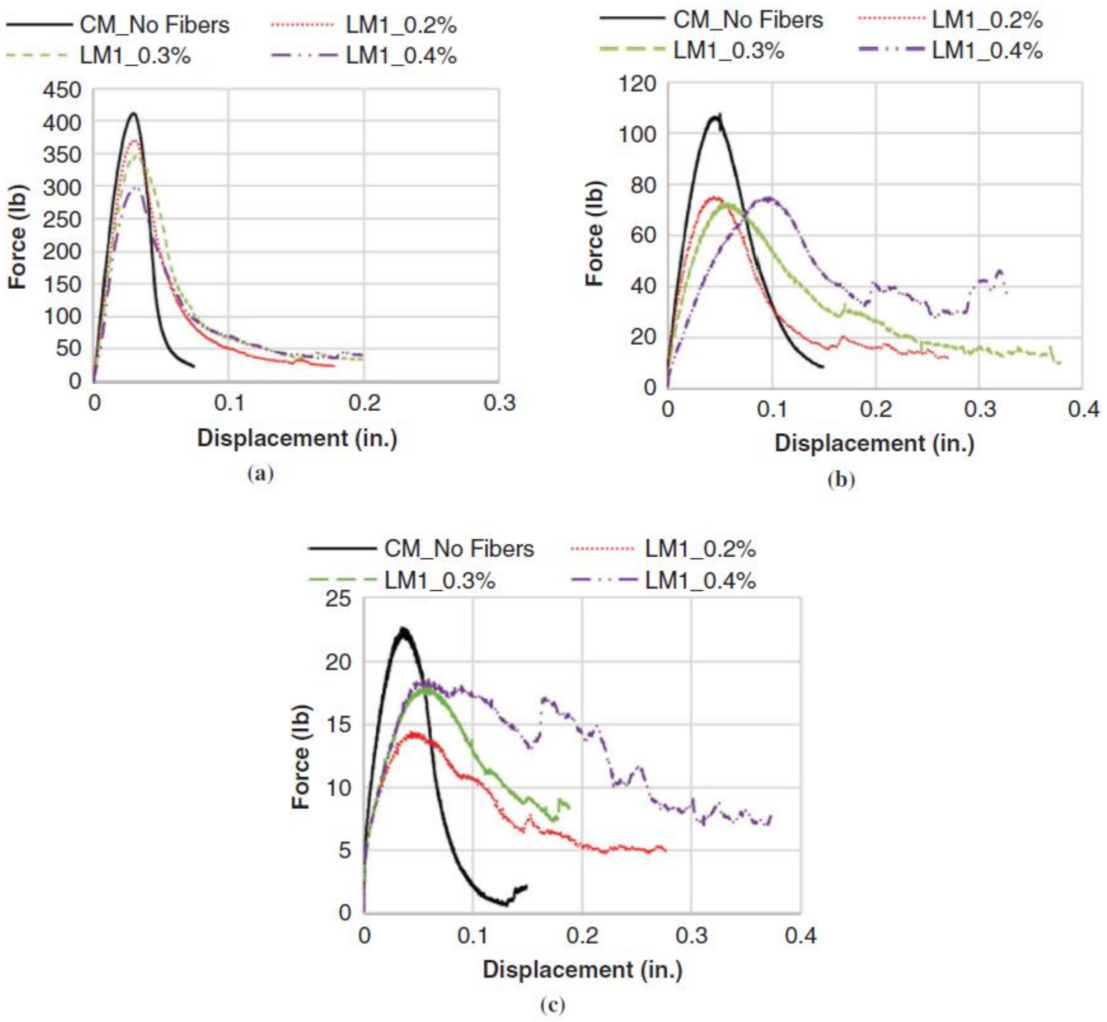

Figure 2.20: Load versus Deformation Curves at (a) 40˚F, (b) 70˚F, and (c) 100˚F (Muftah et al., 2017)

For the E* test, test data are used to create a master curve, allowing researchers to determine the modulus of asphalt mixtures over a wide range of testing temperatures and loading frequencies. Figure 2.21 shows the test setup. The test can be run in unconfined or confined modes using small or large specimens. Since it is a repeated load test, the modulus values can be used to evaluate the bottom-up fatigue cracking resistance of the mixtures when it is run at high frequencies. At a given test temperature and frequency, lower modulus values translate to a less stiff mixture, usually meaning that the mixture has better cracking resistance.

Figure 2.21: E* Test Setup

Willis (2013) documented a field project that utilized wet process GTR. The project was a section of US 231-S near Dothan, Alabama. In 2010, the wet process GTR modified mixture was placed in the outside lane of traffic, along with an SBS modified mixture (Willis, 2013). The mixtures were sampled during production and transported to the NCAT laboratory for testing (Willis, 2013). The results of confined and unconfined E* testing, which can be seen on a logarithmic scale in Figure 2.22 and on an arithmetic scale in Figure 2.23, show that the SBS modified mixture had only slightly better cracking resistance than the wet process GTR modified mixture (Willis, 2013). The performance of the field sections was then evaluated a year after placement in 2011. Willis (2013) explains that three subsections 100 feet long were randomly chosen to assess the cracking in both the wet process GTR and SBS modified test sections. Cracking was monitored visually, and it was determined that both sections were free of cracks (Willis, 2013). Longer duration field testing may be necessary, however, to truly evaluate the field performance of the wet process GTR modified mixture relative to the SBS modified mixture.

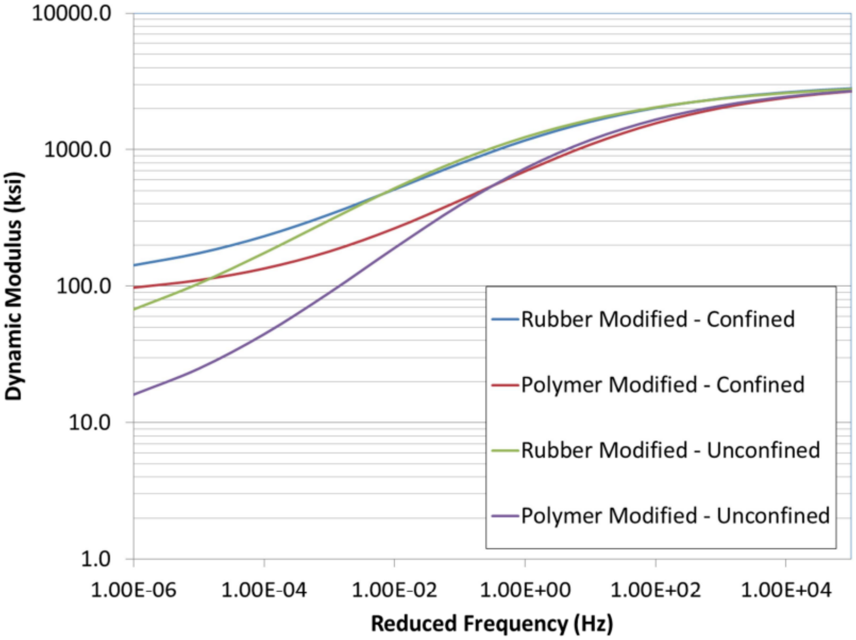

Figure 2.22: E* Master Curves on Logarithmic Scale (Willis, 2013)

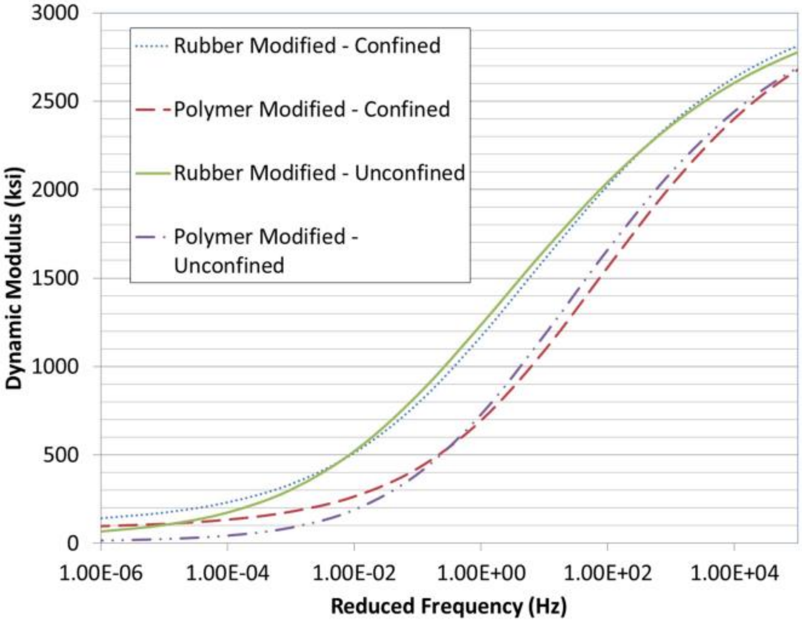

Figure 2.23: E* Master Curves on Arithmetic Scale (Willis, 2013)

Using the same blend of polyolefin and aramid synthetic fibers as in the IDEAL-CT experiment, Alfalah et al. (2020) conducted an E* experiment on asphalt mixtures. It was determined that the modulus values for all the fiber reinforced asphalt mixtures, which can be found in Figure 2.24, “are similar to or slightly lower than the control mixture at higher frequencies” (Alfalah et al., 2020). Since the differences were noted to be small or nonexistent, the findings indicate that the fibers used have “little impact on the cracking performance” of the mixtures (Alfalah et al., 2020). This conclusion is consistent with the results of the IDEAL-CT test that was conducted by the same researchers (Alfalah et al., 2020).

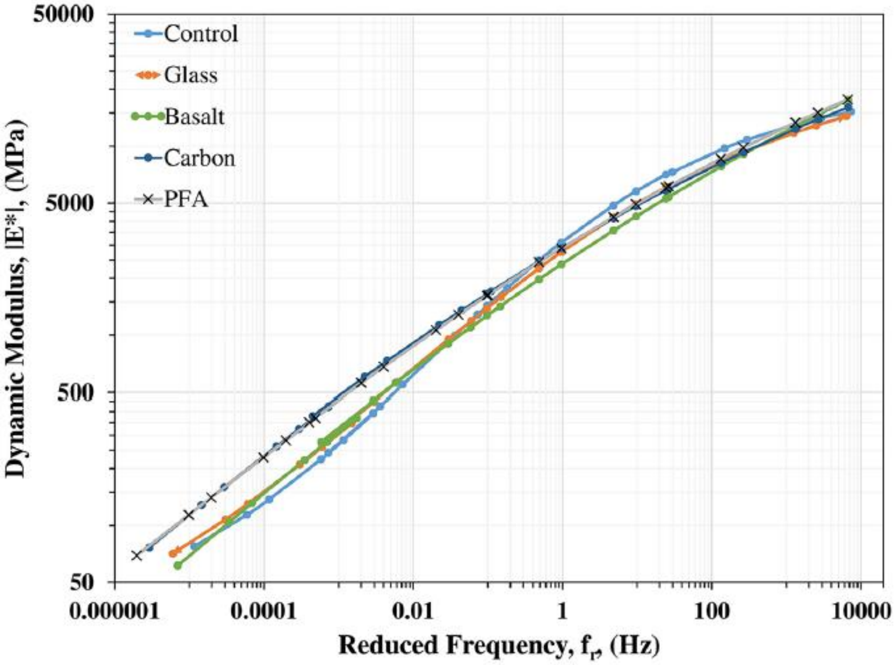

Figure 2.24: E* Master Curves on Logarithmic Scale (Alfalah et al., 2020)

Using the same blend of polyolefin and aramid synthetic fibers and wax-treated aramid fibers as in the SCB experiment, Muftah et al. (2017) conducted an E* experiment on asphalt mixtures that were placed in the field for a project as well as field cores. The results did not show any notable differences between the fiber reinforced mixtures and control mixture at low and high temperatures (Muftah et al., 2017). It was documented, however, that an ANOVA analysis revealed there was a significant difference between the control mixture and the polyolefin and aramid fiber reinforced mixtures at “an intermediate temperature of 70°F and at a frequency of 1 Hz” (Muftah et al., 2017). This may suggest that the fibers impacted the modulus of the mixture for those specific conditions, but since it was the only significant difference discovered it may be due to inherent variability of the samples or testing. Other than the one variation, the ANOVA analysis indicated that “no significant difference in the dynamic modulus values existed,” so the researchers concluded that the fibers used did not affect the performance of the mixtures (Muftah et al., 2017). This conclusion concurs with the results of the SCB test that was conducted by the same researchers (Muftah et al., 2017).

For the OT, the crack progression rate (β) parameter is calculated from test data and used to determine the reflective cracking resistance of asphalt mixtures (Yin et al., 2021). Figure 2.25 shows the test setup, where the specimen is cut in several places and glued to two steel plates. One plate is fixed, while the other moves back and forth. A crack propagates from the bottom of the specimen where it meets both plates, allowing β to be measured. The lower β is, the better cracking resistance a mixture has.

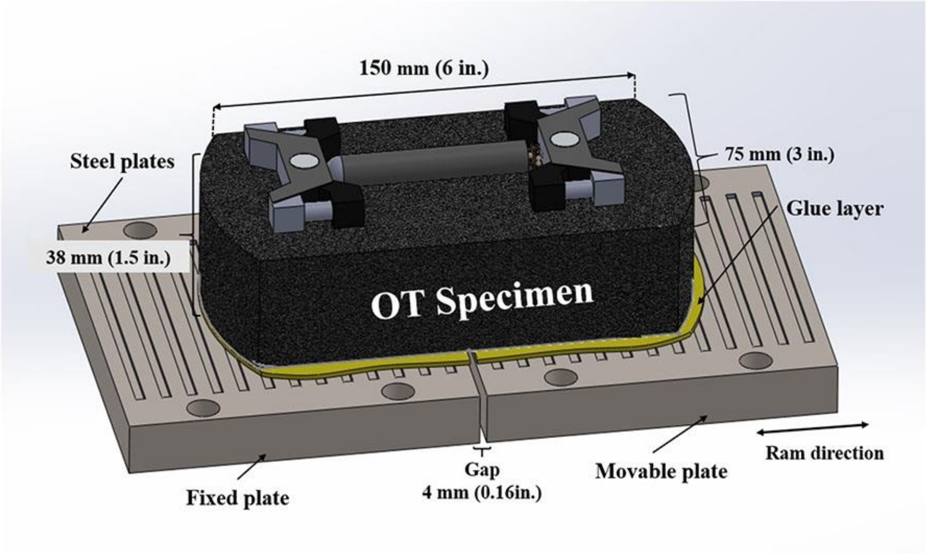

Figure 2.25: OT Setup (“Center for Transportation Infrastructure Systems,” 2021)

Using the same wet process rPE incorporation as in the IDEAL-CT experiment, Yin et al. (2021) conducted an OT experiment involving several different asphalt mixtures. The mixtures were the same as in the IDEAL-CT experiment, except in the OT experiment all mixtures were long-term aged. It was determined that the control mixture “had a lower average β value than the three modified mixtures,” which can be seen in Figure 2.26, but it was also noted that “the difference was not statistically significant if considering the variability of the OT results” (Yin et al., 2021). The findings show that using rPE or rPE+RET as additives “did not seem to affect the reflective cracking resistance of asphalt mixtures after long-term aging” (Yin et al., 2021).

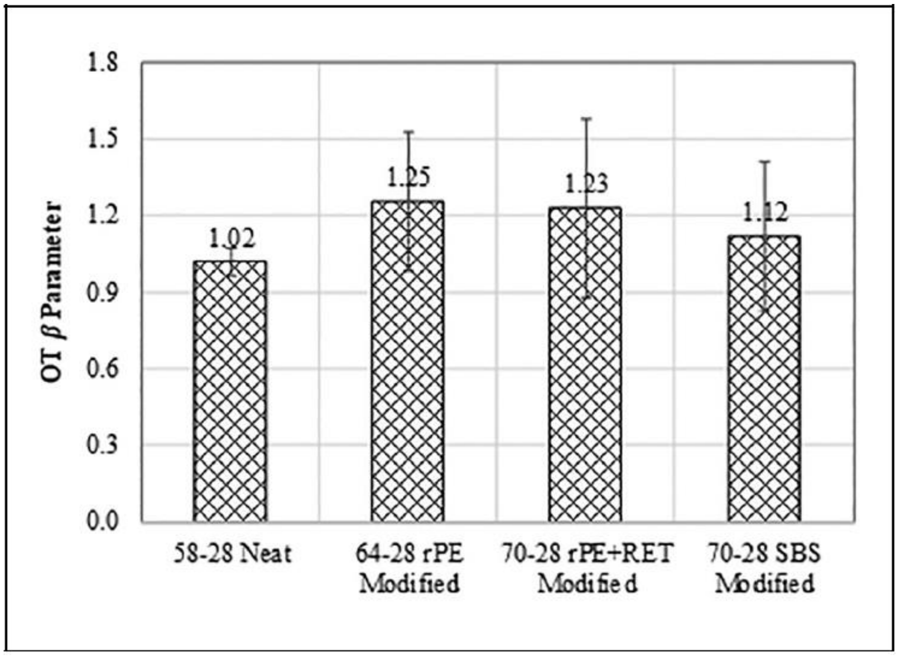

Figure 2.26: OT β Results of Long-Term Aged Asphalt Mixtures (Yin et al., 2021)

From the laboratory and field experiments presented in this literature review, it is clear that more testing needs to be conducted on mixtures utilizing the new additive types. Some of the existing test results agree on whether the additives improve cracking resistance, while others disagree. For example, it appears that tests such as the I-FIT, IDEAL-CT, and E* agree that GTR decreases the cracking resistance of a mixture, even though some researchers claim that this trend is inconsistent with field performance. However, the SCB test has shown that dry process GTR can increase the cracking resistance of a mixture. For rPE, the I-FIT and IDEAL-CT agree that it decreases the cracking resistance of a mixture, but the OT test has shown that wet process rPE might not affect the cracking resistance of a mixture. For synthetic fibers, though, the general consensus of the IDEAL-CT, SCB, and E* is that they do not affect the cracking resistance of mixtures at low or manufacturer dosages. However, some tests have shown that cracking resistance is increased when fibers are included at higher dosages.

2.4 Additive Group Experiment Phase I: Methodology and Publicly Available Results

As mentioned in Chapter 1, Phase I of the AG Experiment involved preliminary efforts, such as limited laboratory characterization and predictive structural analyses for several experimental and control mixtures. That effort is presented here as part of the publicly available information that sponsors agreed to share in an anonymous fashion. Due to NDAs within Phase I, the particular technologies that were used will not be identified in this literature review to preserve anonymity, and each additive will be referred to by the random number assigned to it in a previous study (Timm et al., 2022).

For this investigation, a typical dense-graded mixture design was used to make 12 mixtures. Two of the mixtures were used as controls, with one using PG 67-22 unmodified asphalt binder and the other using PG 76-22 SBS modified asphalt binder. The remaining mixtures were experimental, each utilizing a different new asphalt additive. Two of the additive modified mixtures were plant produced and had their own respective control mixtures. E* and Cyclic Fatigue tests were conducted on each mixture to determine its stiffness and fatigue damage characteristics (Timm et al., 2022). The results of these tests were then used as inputs in the WESLEA for Windows Version 3.0 and FlexPAVE™ 1.1 programs for pavement structural design analysis using a pavement cross-section that was planned for the full-scale accelerated pavement evaluation on the NCAT Test Track (Timm et al., 2022). The WESLEA analysis yielded a predicted the number of cycles to bottom-up fatigue cracking failure. The FlexPAVE™ analysis resulted in a predicted percent damage (% damage) value due to bottom-up fatigue cracking as well as top-down cracking (Timm et al., 2022). Both analyses were then iterated with varying pavement thickness until equivalent layer thicknesses and provisional structural coefficients (a_1) were determined for each additive modified mixture relative to the SBS modified control mixture (Timm et al., 2022). Figure 2.27 presents a flow chart for this AG Phase I methodology. From all the laboratory and predictive structural analysis data, sponsors were able to compare the various additive modified mixtures to the control mixtures and make informed decisions about which additive modified test sections to construct at the NCAT Test Track.

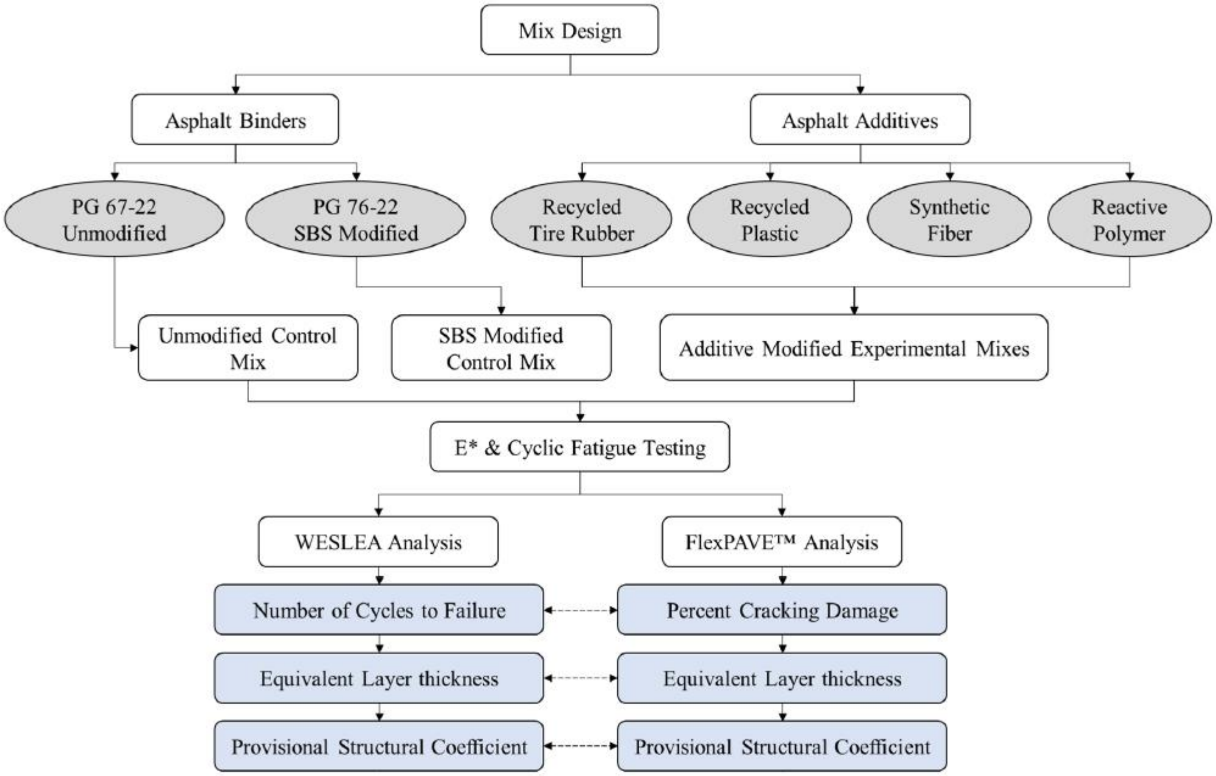

Figure 2.27: AG Phase I Methodology Flow Chart (Timm et al., 2022)

As documented by Timm et al. (2022), a 12.5 mm nominal maximum aggregate size (NMAS) dense-graded mixture was used for mixture design. The mixture included a blend of granite and manufactured sand as well as 20% RAP Baghouse fines were also added at 1.0% by weight of aggregate to account for potential aggregate breakdown during production. The mixture design was first created with PG 76-22 SBS modified asphalt binder. It was found that the performance optimum binder content (OBC) of the mixture was 5.6%. At OBC, the mixture had 4.4% air voids and 15.9% voids in the mineral aggregate (VMA) at a design compaction effort (N_{design}) of 60 gyrations. The OBC was selected using a BMD approach involving the IDEAL-CT and the Hamburg Wheel Tracking Test (HWTT) (AASHTO T 324). The IDEAL-CT and HWTT were conducted on short-term aged for 4 hours at 135˚C (AASHTO R 30). The IDEAL-CT was performed at 25˚C to evaluate intermediate temperature cracking resistance. The HWTT was conducted at 50˚C to evaluate rutting resistance. The mixture at OBC had an average CT_{Index} of 54.1 and an average rut depth of 2.5 mm at 20,000 passes with no signs of stripping.

As further documented by Timm et al. (2022), E* testing was conducted on small-size cylindrical gyratory specimens using an Asphalt Mixture Performance Tester (AMPT). Triplicate specimens were prepared according to AASHTO PP 99-19, and each was tested with nine temperature-loading frequency combinations, which included three test temperatures (i.e., 4, 20, and 40°C) and three loading frequencies (i.e., 10, 1, and 0.1 Hz). An E* master curve was then constructed via the process outlined in AASHTO R 84-17. Also, the modulus value at 20˚C and 10 Hz was used as an index parameter to compare the asphalt mixtures. Table 2.2 compiles the E* master curve coefficients of the 12 laboratory mixtures, including the PG 67-22, PG 76-22 control, and ten additive modified experimental mixtures. It should be noted that the two other plant produced additive modified mixtures and their respective control mixtures are not included in the table to preserve anonymity. Figure 2.28 shows the E* master curves for the PG 67-22 and PG 76-22 control mixtures for visualization purposes. Figure 2.29 presents all the modulus values determined from E* testing at 20C and 10 Hz. In Figure 2.29, error bars represent one standard deviation. An ANOVA analysis (α = 0.05) with Tukey pairwise statistical groupings was conducted to statistically rank the E* results, with the resulting groups being shown in Figure 2.29. Mixtures that do not share a letter are significantly different, so the differences in E* stiffness values at 20°C and 10 Hz between the experimental and control mixes are mainly due to the effect of the additives.

Table 2.2: E* Master Curve Fitting Coefficients (Timm et al., 2022)

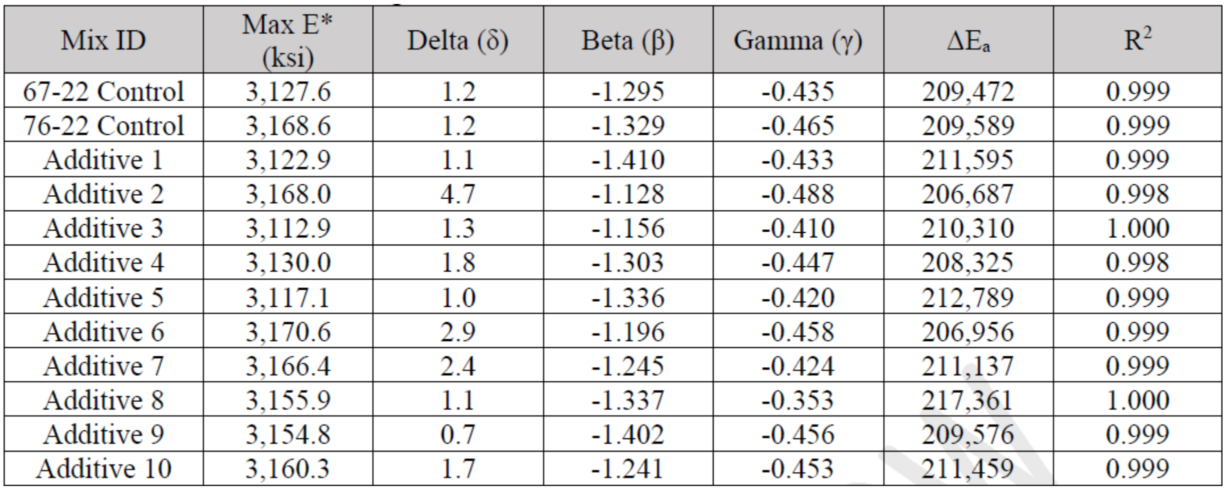

Mix ID	Max E* (ksi)	Delta (δ)	Beta (β)	Gamma (γ)	ΔE_a	R^2
67-22 Control	3,127.6	1.2	-1.295	-0.435	209,472	0.999
76-22 Control	3,168.6	1.2	-1.329	-0.465	209,589	0.999
Additive 1	3,122.9	1.1	-1.410	-0.433	211,595	0.999
Additive 2	3,168.0	4.7	-1.128	-0.488	206,687	0.998
Additive 3	3,112.9	1.3	-1.156	-0.410	210,310	1.000
Additive 4	3,130.0	1.8	-1.303	-0.447	208,325	0.998
Additive 5	3,117.1	1.0	-1.336	-0.420	212,789	0.999
Additive 6	3,170.6	2.9	-1.196	-0.458	206,956	0.999
Additive 7	3,166.4	2.4	-1.245	-0.424	211,137	0.999
Additive 8	3,155.9	1.1	-1.337	-0.353	217,361	1.000
Additive 9	3,154.8	0.7	-1.402	-0.456	209,576	0.999
Additive 10	3,160.3	1.7	-1.241	-0.453	211,459	0.999

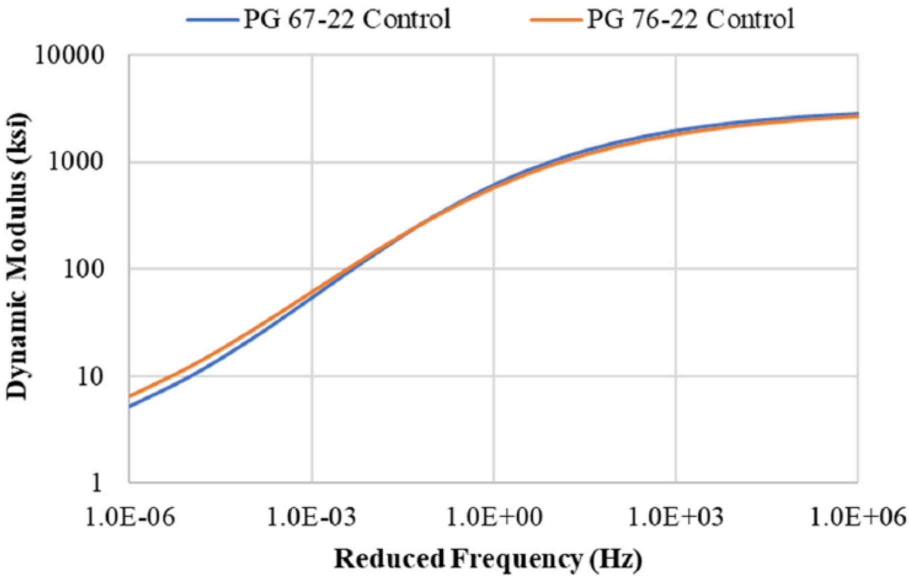

Figure 2.28: E* Master Curves of PG 67-22 and PG 76-22 Control Mixtures (Timm et al., 2022)

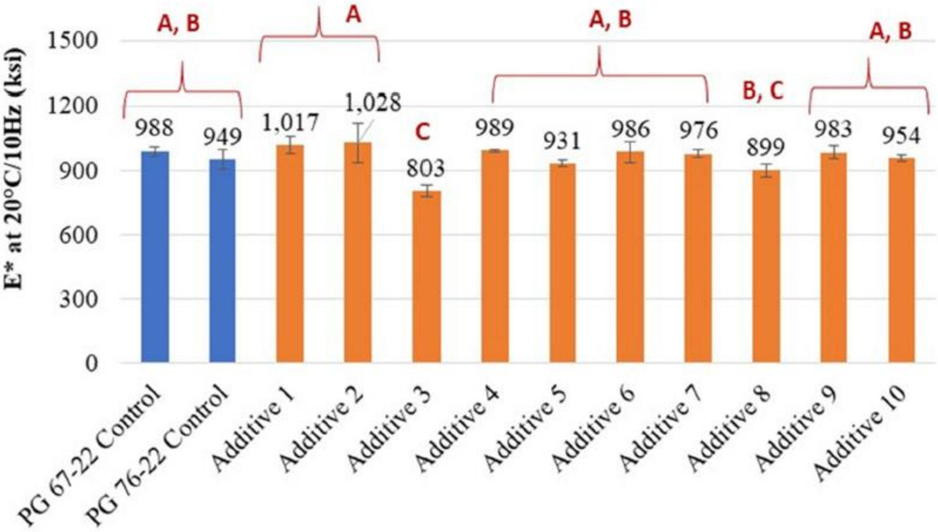

Figure 2.29: E* Values at 20˚C and 10 Hz (Timm et al., 2022)

The Cyclic Fatigue test was also conducted on small-size cylindrical gyratory specimens using an AMPT. As described by Timm et al. (2022), triplicate specimens were again prepared, and each was tested according to AASHTO TP 133-19. The test temperature of 21˚C was chosen based on the climate high-temperature grade requirement of the mix design, and the frequency was held constant at 10 Hz. The main output was a plot of mixture modulus and phase angle versus the number of loading cycles, with specimen failure being determined by the point where the phase angle peaked and started to drop off. The corresponding number of cycles at this failure point was designated as the number of cycles to failure (N_f). For analysis of this data, a damage characteristic curve was constructed by plotting the mixture pseudo-stiffness as a material integrity parameter (C) on the y- axis against the damage parameter (S) on the x-axis. This C-versus-S curve represents the fundamental damage characteristics of the mixture, which is independent of test temperature and loading frequency. The predicted N_f at strain levels varying from 100 to 600 microstrain (μƐ) at 20˚C was determined by applying the simplified viscoelastic continuum damage (S-VECD) model to the test data. These predicted N_f values were then fitted with a power function trendline to construct the predicted N_f-versus-Strain curves. Table 2.3 summarizes the fitting coefficients of the C-versus-S and Nf-versus-Strain curves from the Cyclic Fatigue test. Figure 2.30 and Figure 2.31 show the the C-versus-S and Nf-versus-Strain curves, respectively, of the PG 67-22 and PG 76-22 control mixtures for visualization purposes (Timm et al., 2022). In Figure 2.30, the C-versus-S curve of the PG 76-22 control mixture was longer and plotted above the curve of the PG 67-22 control mixture, which indicates that the PG 67-22 control mixture was more susceptible to fatigue damage in direct tension. This inference can also be made from Figure 2.31, where the PG 76-22 control mixture yielded consistently higher predicted N_f values at all strain levels and, therefore, was expected to have better fatigue damage resistance than the PG 67-22 control mixture.

Table 2.3: Cyclic Fatigue C-versus-S and Nf-versus-Strain Curve Fitting Coefficients (Timm et al., 2022)

Mix ID	C-versus-S Curve			N_f-versus-Strain Curve	
	C_{11}	C_{12}	S_{max}	A	B
PG 67-22 Control	0.00228	0.486	160,000	2.61E+21	7.085
PG 76-22 Control	0.00235	0.477	200,000	1.06E+23	7.553
Additive 1	0.00206	0.487	200,000	1.30E+22	7.245
Additive 2	0.00221	0.473	280,000	6.38E+23	7.774
Additive 3	0.00226	0.496	160,000	3.54E+23	7.862
Additive 4	0.00179	0.506	170,000	7.18E+21	7.303
Additive 5	0.00207	0.496	160,000	6.38E+22	7.550
Additive 6	0.00236	0.472	210,000	2.05E+23	7.649
Additive 7	0.00226	0.480	240,000	7.40E+23	7.819
Additive 8	0.00271	0.460	220,000	2.57E+25	8.477
Additive 9	0.00207	0.496	160,000	7.13E+20	6.849
Additive 10	0.00186	0.499	180,000	3.81E+22	7.490

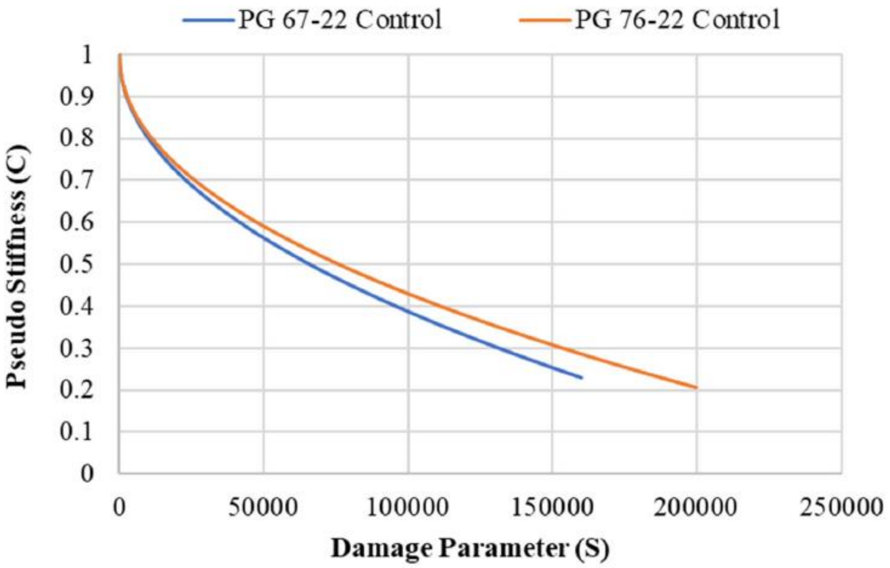

Figure 2.30: Cyclic Fatigue C-versus-S Curve for PG 67-22 and PG 76-22 Control Mixtures (Timm et al., 2022)

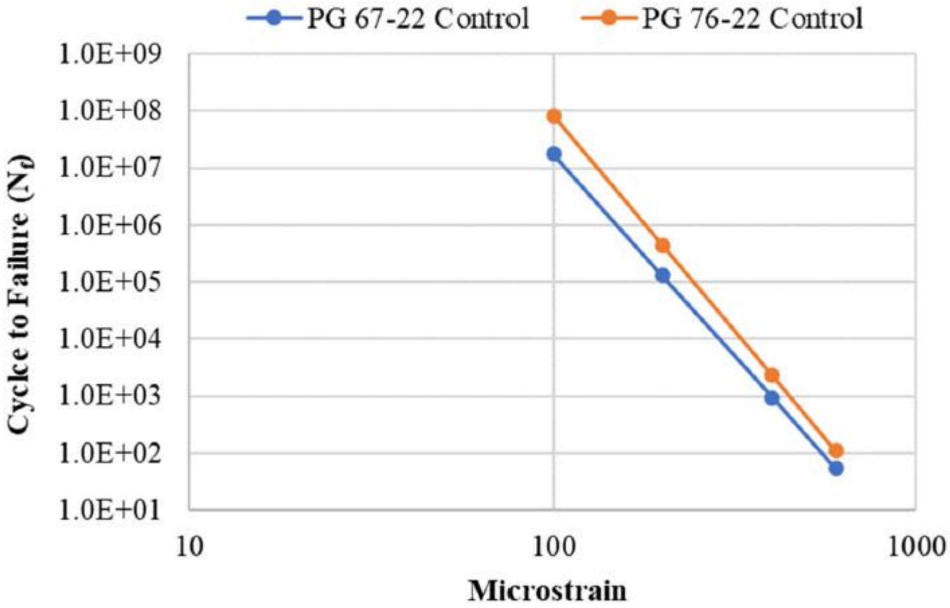

Figure 2.31: Cyclic Fatigue N_f-versus-Strain Curve for PG 67-22 and PG 76-22 Control Mixtures (Timm et al., 2022)

The WESLEA analysis used layered elastic analysis to determine tensile strain levels at the bottom of the asphalt concrete (AC) layer in each of the analyzed cross sections as described by Timm et al., (2022). These cross sections included the two control mixtures (PG 67-22 unmodified binder and PG 76-22 SBS modified binder) and the experimental additive modified mixture. Granular base (GB) and subgrade layer properties were held constant. Figure 2.32 shows one of the experimental additive modified pavement cross sections alongside the two control cross sections.

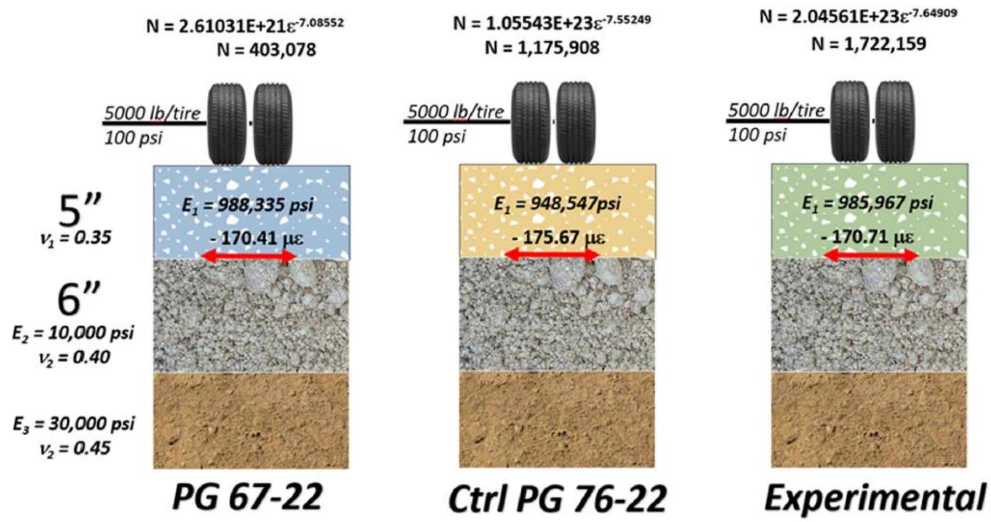

Figure 2.32: WESLEA Cross-Sections (Timm et al., 2022)

The moduli (E) of the subgrade and GB layer unbound materials, which can be found in Figure 2.32, were based on representative values obtained through backcalculation of FWD data from previous research cycles at the Test Track (Taylor and Timm, 2009). Typical Poisson ratios were assumed for the materials and can also be found in Figure 2.32, and the moduli of the asphalt layers were based on the E* testing at 20°C and 10 Hz (Timm et al., 2022). 20˚C was selected due to it being in the middle of the expected temperature range of the asphalt layer at the NCAT Test Track, it is near the cyclic fatigue test temperature (21°C), and it corresponds to the AASHTO reference temperature of 68°F used for asphalt structural layer coefficients. The cross sections were modeled as 5 inches of AC over 6 inches of GB to simulate the planned AG cross sections at the NCAT Test Track. Simulated loadings were 20,000 lb per axle or 5,000 lb per tire with an inflation pressure of approximately 100 psi, which is meant to mimic the weight of the single axles on the trucks at the NCAT Test Track (Timm et al., 2022).

The tensile strain at the bottom of the AC was then determined from WESLEA analysis. The strain values were used in the transfer functions, which were generated from AMPT cyclic fatigue testing, and N_f was estimated for each section (Timm et al., 2022). Examples of the transfer functions and N_f values are shown above the cross sections in Figure 2.32, and Figure 2.33 presents all the N_f values. It should be noted that the N_f values do not include lab-to-field shift factors, so they are only used to compare to other N_f values and against % damage predictions made via FlexPAVE™ analysis (Timm et al., 2022).

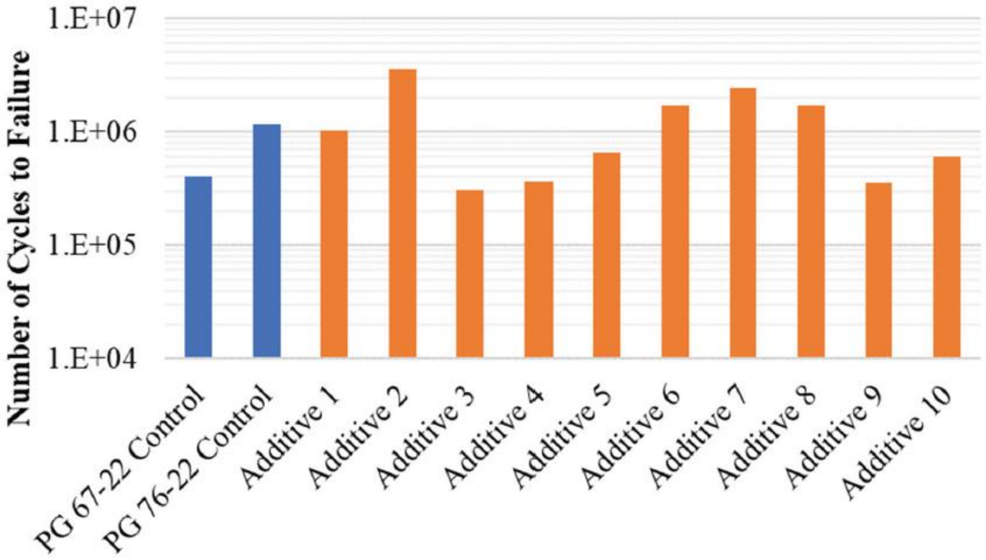

Figure 2.33: WESLEA N_f Values (Timm et al., 2022)

WESLEA was then used to conduct additional simulations to determine the required thickness to the nearest 0.1 inch of the unmodified PG 67-22 control and additive modified experimental cross sections to yield approximately the same N_f as the PG 76-22 control cross section (Timm et al., 2022). The material properties were held constant, except for the AC layer thicknesses of the PG 67-22 control and additive modified experimental cross sections. Figure 2.34 shows all the equivalent AC thickness values. The determined thicknesses ranged from 4.5 to 5.7 inches, and as expected, the mixtures with the highest predicted N_f values translated to the thinnest equivalent AC thicknesses.

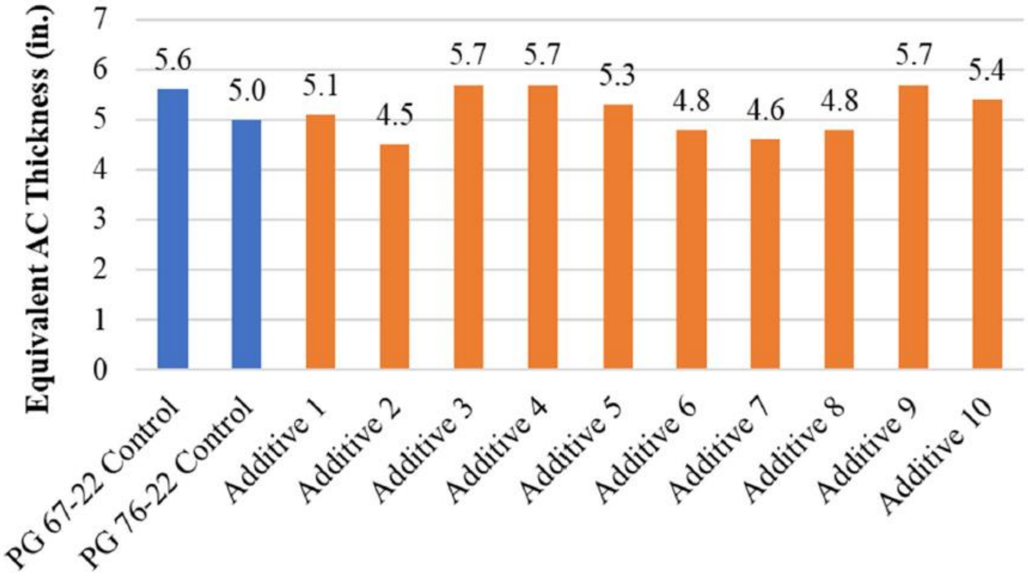

Figure 2.34: WESLEA Equivalent AC Thicknesses (Timm et al., 2022)

The resulting equivalent thicknesses were then used to calculate a_1 values for use in the AASHTO 1993 Design Guide of Pavement Structures (Timm et al., 2022). An a_1 of 0.54 was assumed for the PG 76-22 control cross section since it is the current value used for this material by the Alabama Department of Transportation. When this a_1 is multiplied by the AC layer thickness of 5 inches, a structural number (SN) of 2.7 is determined for the AC layer (Timm et al., 2022). Structural coefficients for the PG 67-22 control and additive modified experimental cross sections were then determined by "dividing 2.7 by the corresponding estimated thicknesses from the WESLEA simulations" since they were "designed as structurally equivalent (i.e., SN = 2.7). Figure 2.35 presents all the a_1 values. The determined a_1 values ranged from 0.47 to 0.60, and as expected, the mixtures with the highest predicted N_f values and thinnest equivalent AC thicknesses translated to the highest structural coefficients. What was unexpected, however, was the fact that the structural coefficients all exceeded the commonly used value of 0.44 but were well below the maximum reported value from the American Association of State Highway Officials (AASHO) Road Test, which was 0.83 (Highway Research Board, 1962).

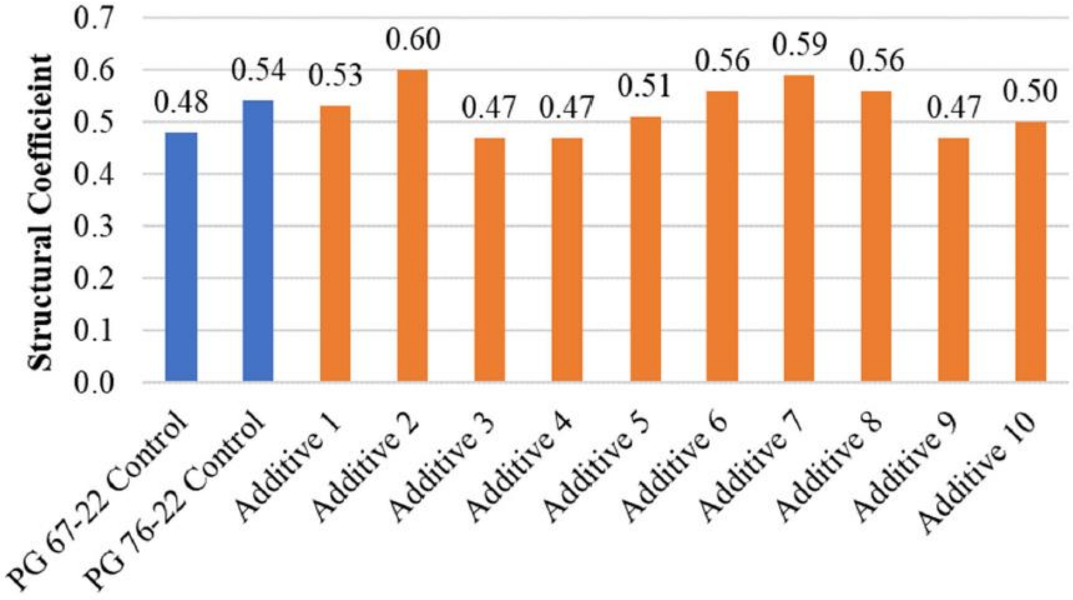

Figure 2.35: WESLEA a_1 Values (Timm et al., 2022)

As documented by Timm et al. (2022), the FlexPAVE™ analysis used viscoelastic continuum damage theory to account for the effects of loading rate and temperature on the asphalt pavement response and distress mechanisms and three-dimensional finite element analysis with moving loads to compute the mechanical response under various traffic loads. The Enhanced Integrated Climatic Model (EICM) is incorporated into FlexPAVE™ to provide realistic climatic conditions for pavement response calculations and performance predictions.

The inputs used for the FlexPAVE™ fatigue cracking analysis were selected to closely mimic the traffic, climate, and subgrade conditions of the NCAT Test Track as well as the anticipated pavement structure of the AG experiment (Timm et al., 2022). The inputs were aligned with WESLEA inputs when possible to minimize differences between the analyses. Table 2.4 summarizes the FlexPAVE™ inputs.

Table 2.4: FlexPAVE™ Inputs (Timm et al., 2022)

Pavement type	new pavement
Analysis option	pavement performance analysis (fatigue cracking only)
Pavement design life	2 years
Pavement structure	3-layer pavement
AC layer	varying thickness, using E* and Cyclic Fatigue test results as material inputs
GB layer	6 inches, modulus = 10,000 psi, Poisson's ratio = 0.40
Subgrade layer	infinite layer, modulus = 30,000 psi, Poisson's ratio = 0.45
Climate data	EICM temperature profile for Troy, AL (closest location to Auburn, AL in FlexPAVE™)
Traffic data	single axle, dual tires 18-kip axle load, design speed = 45 mph, daily ESAL = 13,699 (to simulate 10 million ESALs over 2 years), no traffic growth

Examples of the resulting % damage values obtained via FlexPAVE™ analysis can be seen in Figure 2.36. From the curves, it is evident that % damage decreases as the AC layer thickness increases, which is due to enhanced structural capacity of the pavement (Timm et al., 2022). Figure 2.37 shows the % damage values for all the mixtures. Of the ten additive-modified experimental mixtures, four were predicted to outperform the PG 76-22 SBS control mixture in terms of the predicted cracking performance as determined by FlexPAVE™. All the experimental mixtures except one (i.e., Additive 9) had a lower predicted percent damage, and therefore better predicted cracking performance, than the PG 67-22 control mixture.

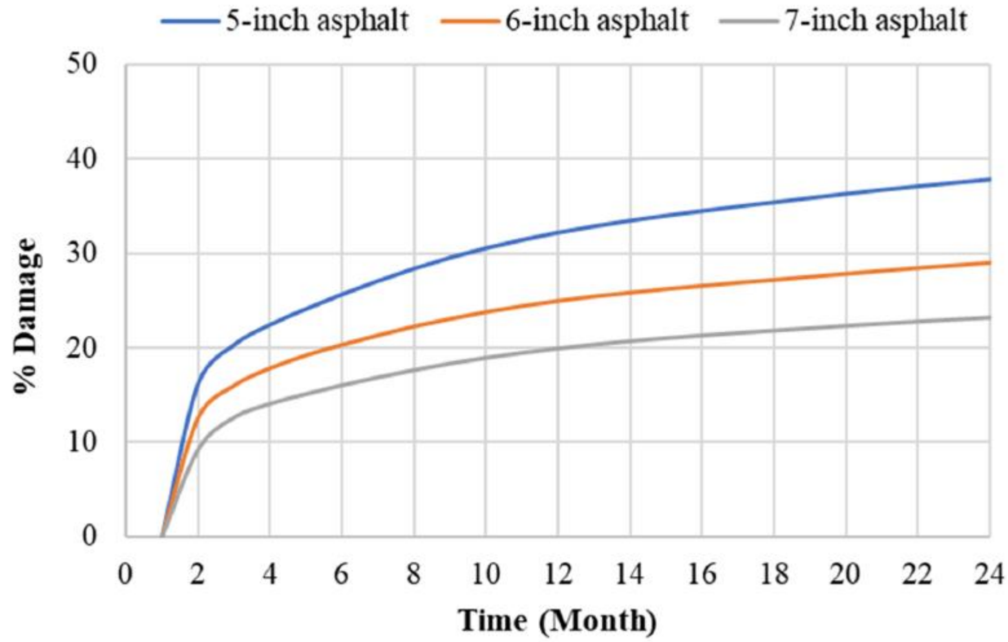

Figure 2.36: FlexPAVE™ Example Predicted % Damage Curves (Timm et al., 2022)

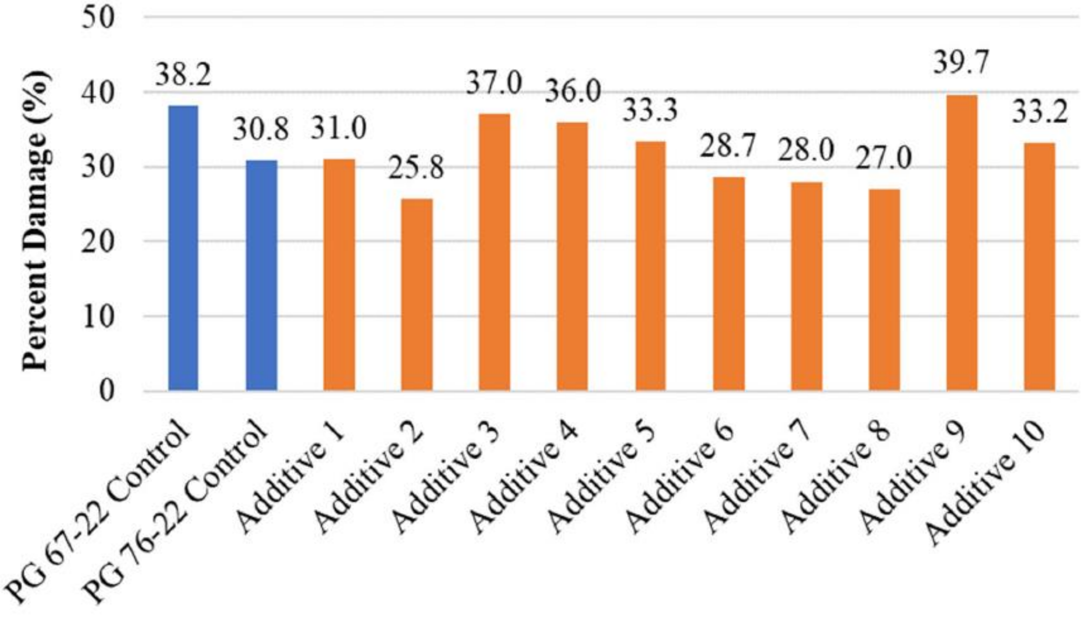

Figure 2.37: FlexPAVE™ % Damage Values (Timm et al., 2022)

Similar to the WESLEA analysis, iterative FlexPAVE™ simulations were conducted using varying AC layer thicknesses for the PG 67-22 control and additive modified experimental cross sections until an equivalent thickness to the PG 76-22 control cross section was determined (Timm et al., 2022). However, instead of N_f, the % damage of the PG 76-22 control cross section was the target value for the iterative FlexPAVE™ simulations. Figure 2.38 presents the equivalent AC thickness values. Then the provisional a_1 was computed using the same methodology as in the WESLEA analysis (Timm et al., 2022). Figure 2.39 shows the calculated a_1 values. The equivalent AC layer thicknesses of the experimental mixtures varied from 4.3 to 5.8 inches, while the provisional a_1 values varied from 0.47 to 0.67. Overall, the results indicate that many of the asphalt additives evaluated have the potential to improve the structural capacity of asphalt mixtures, based on the predicted cracking performance in FlexPAVE™. However, the degree of difference from the control mixtures seems to vary greatly from additive to additive.

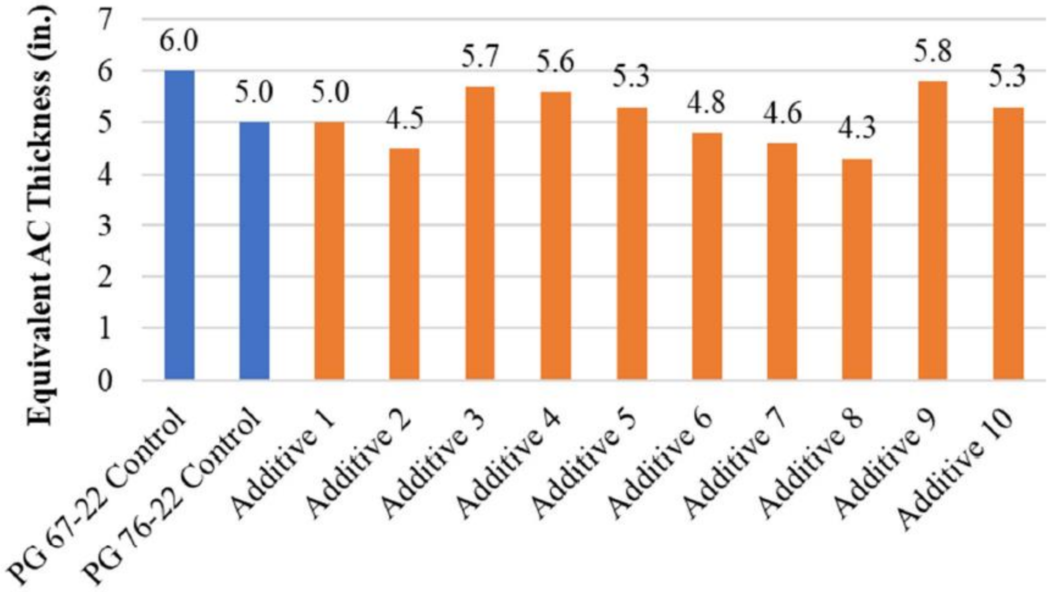

Figure 2.38: FlexPAVE™ Equivalent AC Thicknesses (Timm et al., 2022)

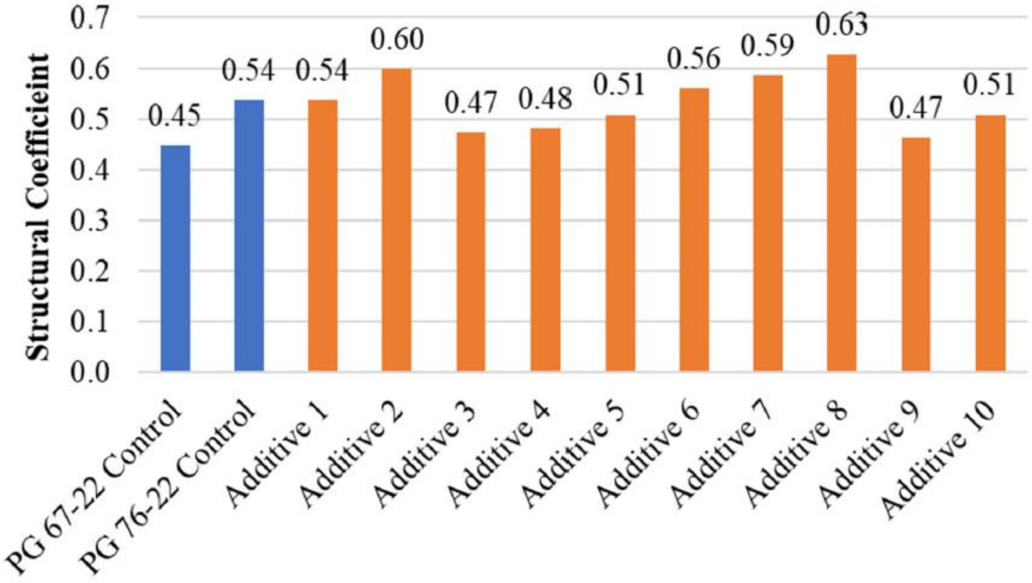

Figure 2.39: FlexPAVE™ a_1 Values (Timm et al., 2022)

After both WESLEA and FlexPAVE™ analyses were conducted on the mixtures, similarities between the results were noticed. Direct comparisons, which can be seen in Figures 2.40, 2.41, and 2.42, were then made to more clearly understand the relationship between the two distinctly different analysis methods. It should be noted that the figures include data from the four plant produced mixtures that were not presented previously (Timm et al., 2022). From the figures, it is evident that all comparisons show relatively strong correlations ($R^2 \geq 0.86$). The researchers noted that the two analysis methods, working from the same set of laboratory data but using very different performance prediction approaches arrived at a strong and reasonable (i.e., % fatigue damage decreases with increasing number of cycles to failure) correlation (Timm et al., 2022). The regression equation in Figure 2.40 can be used as a way to predict FlexPAVE™ % damage from the WESLEA N_f analysis and vice versa over the range of conditions that were evaluated in this study. Figure 2.41 shows the equivalent AC thicknesses determined via the two methodologies, with a linear regression trendline forced through a 0-inch y-intercept. On average, the two methods produce almost the same equivalent thickness. Again, this is interesting given that the two approaches are extremely different in terms of complexity. Similar statements can be made regarding Figure 2.42, where the structural coefficients are compared between the two approaches. The linear trendline once again indicates that the results from the FlexPAVE™

and WESLEA analyses are nearly identical. However, the data in Figure 2.42 is not surprising, given Figure 2.41, since it is simply transformed from equivalent thicknesses to a_1 values by dividing a constant number by the equivalent thicknesses.

Also, even though they show nearly identical results in Figures 2.41 and 2.42, two mixtures fall relatively farther from the linear trendlines. It is not known why this is the case, but it will be addressed as part of the AG Experiment.

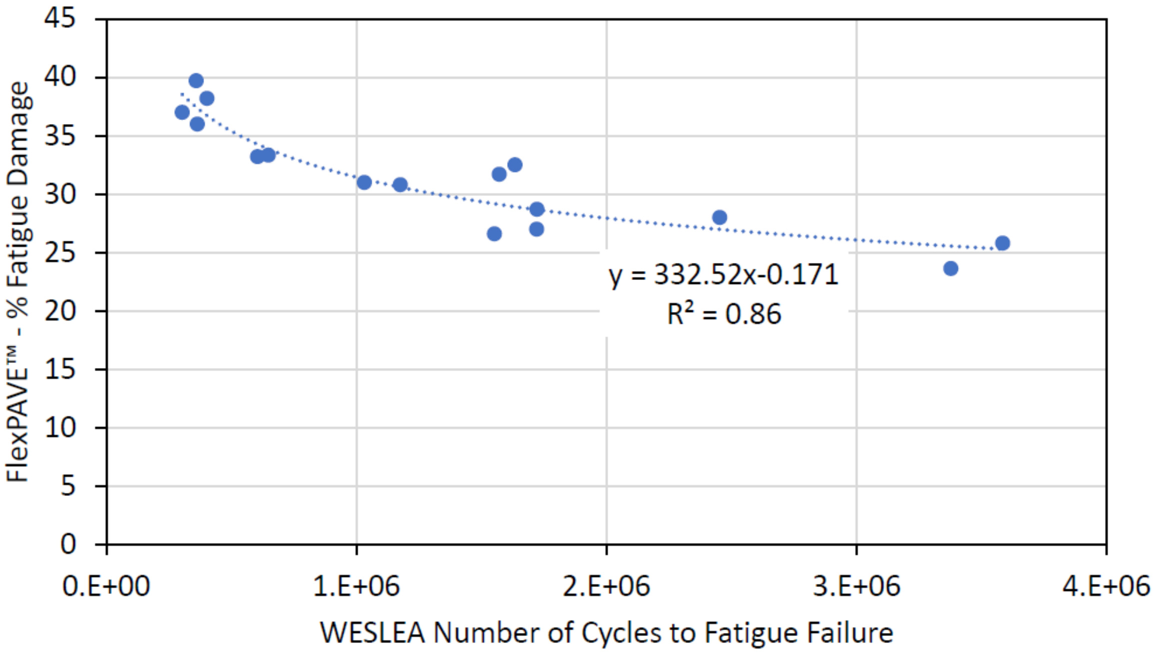

Figure 2.40: FlexPAVE™ % Damage versus WESLEA Nf (Timm et al., 2022)

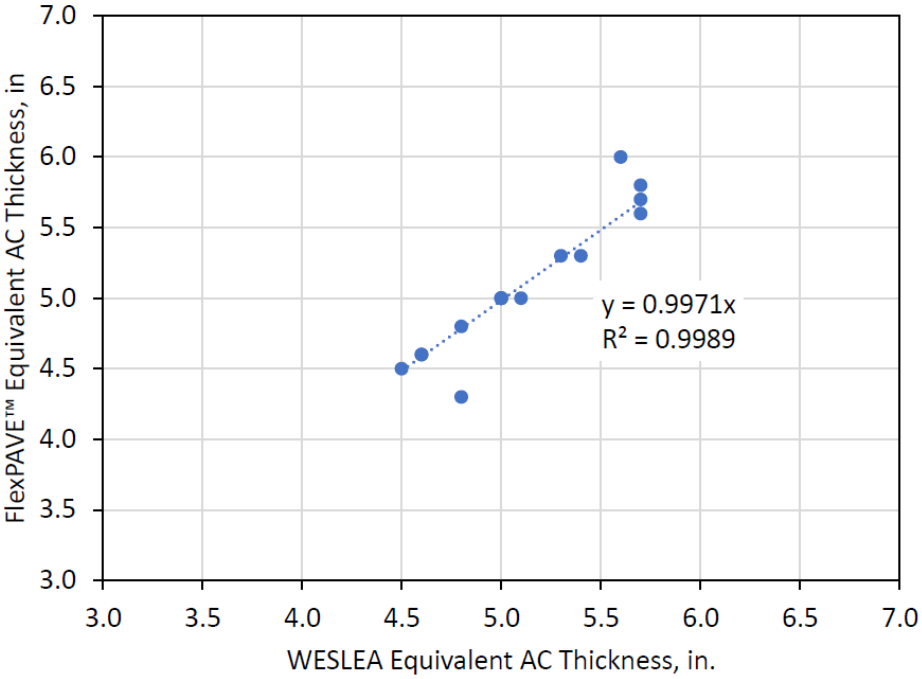

Figure 2.41: FlexPAVE™ versus WESLEA Equivalent AC Thicknesses (Timm et al., 2022)

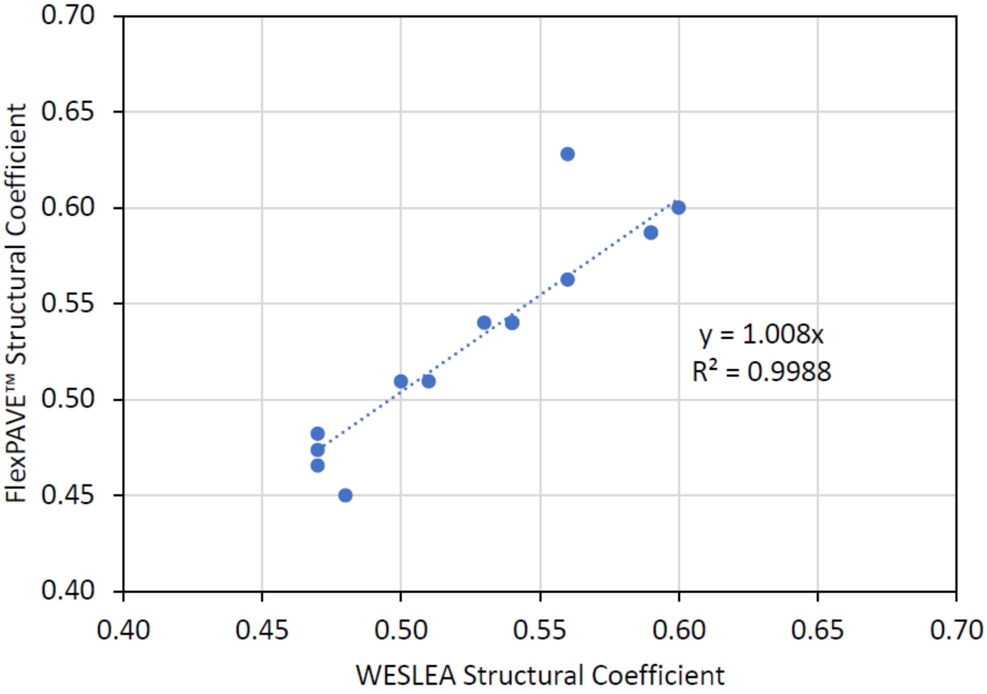

Figure 2.42: FlexPAVE™ versus WESLEA a_1 Values (Timm et al., 2022)

Due to these strong correlations, a framework could be established to rapidly predict and evaluate the performance of additive modified mixtures using one or both of the analysis methods. Another goal of Phases II, IIIa, and IIIb of the AG Experiment is to determine whether this possibility is viable or if the methods should be refined.

2.5 Summary

This literature review introduced the new asphalt additive technologies that are relevant to the AG Experiment, listed and discussed potential benefits and concerns of each of the new asphalt additive technologies, presented some previous testing and studies involving the new asphalt additive technologies, and stated and discussed the methods and publicly available results of the AG Experiment: Phase I study.

It was found from reviewing literature about laboratory and field studies that more testing needs to be conducted on mixtures utilizing the new additive types. The various studies conflicted regarding the roles of GTR and rPE in altering mixture cracking performance. However, it is generally agreed that synthetic fibers do not affect the cracking resistance of mixtures at low or manufacturer dosages. Some tests show that synthetic fibers may increase mixture cracking resistance when included at higher dosages, though.

From reviewing the publicly available results of Phase I, it was determined that N_f and % damage values for the additive modified mixtures, which were derived from WESLEA and FlexPAVE™ structural analyses, varied in terms of degree of change from the control mixtures. The same trend, as well as the expected trend of decreasing equivalent AC thickness and increasing a_1 as N_f increased and % damage decreased, was observed in the calculated values for the additive modified mixtures. What was unexpected, however, was the fact that the values determined from the WESLEA and FlexPAVE™ analyses and values calculated from them correlated extremely well ($R^2 \geq 0.86$). This was not expected due to the vastly different approaches and differing levels of complexity associated with the analysis methods. Regardless, both methods may potentially allow for the rapid evaluation of additive modified mixture performance. To this end, a goal of Phases II, IIIa, and IIIb of the AG Experiment is to determine the viability of the different structural analysis methods.

CHAPTER 3

Additive Group Experiment Phase II: Construction

Once the preliminary work of Phase I was completed, the sponsors chose five new asphalt additives to include in the construction of test sections at the NCAT Test Track. The chosen additives are presented in Table 3.1, along with their section designations and descriptions. From this point on, the sections will be referred to in this thesis by their respective descriptions and section numbers for brevity.

Table 3.1: AG Experiment Test Section Information

Section	**Non-SBS Additive Technology**	**Description**
N1	SmartMIX™ (Liberty Tire Recycling)	GTRDry
N2	Terminal Blended (TB) Rubber Binder (Entech, Inc.)	GTRWet
N5	ACE XP™ (Surface Tech™)	Aramid
N7	N/A	Ctrl
S5	Generic Post-Consumer Recycled (PCR) Plastics	DryPlastic
S6	LLDPE+ELVALOY™ RET (Dow®)	WetPlastic

As discussed previously, full-scale testing is necessary to comprehensively characterize and evaluate the additive modified mixtures. So, the sections were constructed and instrumented with asphalt strain gauges (ASGs), earth pressure cells (EPCs), and thermocouple temperature probes to monitor the sections’ performance over time and as accelerated loading is applied. This chapter presents the instrumentation process and overall construction of the AG Experiment sections.

3.1 Instrumentation

3.1.1 Layout and Purpose

The various instruments embedded within the sections all measure a flexible pavement's response to traffic and the environment. ASGs measure the horizontal strain response of the pavement, EPCs measure the vertical pressure that the pavement experiences, and thermocouple temperature probes measure the temperature of the pavement. The instrumentation scheme and installation process was consistent with recent NCAT Test Track construction cycles and was implemented into the 2021 research cycle with few modifications (Timm et al., 2009; McCarty, 2020). For instance, the one notable difference between the 2021 Test Track cycle construction and previous cycle construction is that pandemic-related supply chain issues delayed the shipment of many ASGs. This delay caused several ASGs that were intended to be used on another project to be utilized in the 2021 Test Track cycle construction. Therefore, some sections were instrumented with ASGs from different batches, but all met the quality standards for the Test Track. The primary difference was the length of wires attached to the gauge itself, which did not prove problematic.

In each section, twelve ASGs were placed at the bottom of the asphalt concrete (AC) layer, an EPC was placed at the top of the granular base (GB) layer, and another EPC was placed at the top of the subgrade soil to measure the structural response of the pavement sections. A bundle of thermocouple temperature probes was also assembled to measure temperatures at the top, middle, and bottom of the AC layer and 3 inches into the GB layer. This probe was inserted into the sections to capture the temperature gradient through the depth of the pavement. The ASGs consisted of the Geocomp 4" x 6" model with 30-foot leads as well as 150-foot leads. The EPCs were all the Geokon® 3500-2-250KPA model semiconductor with 30-foot leads. Finally, the thermocouple temperature probes were all the Campbell Scientific® 108-U-L30-PT model with permanent temperature measurement and type J thermocouples. These ASGs, EPCs, and thermocouple temperature probes are shown in Figures 3.1, 3.2, and 3.3, respectively.

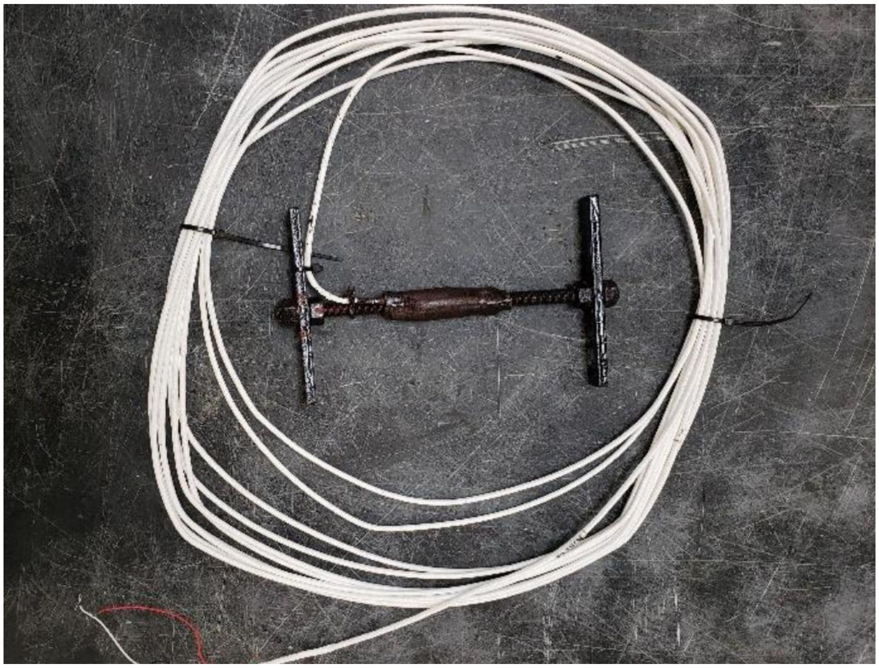

Figure 3.1: Geocomp ASG (McCarty, 2020)

Figure 3.2: Geokon® EPC (McCarty, 2020)

Figure 3.3: Campbell Scientific® Thermocouple Temperature Probe Bundle (McCarty, 2020)

Figure 3.4 depicts and numbers the ASG and EPC layout in plan view. The ASGs were assigned to channels 1 through 12, while the EPCs were assigned to channels 13 and 14 in the DATAQ data acquisition system. The instrument layout, or gauge array, was centered over the outside wheel path (OWP) to ensure that peak responses of truck passes were captured and that natural wheel wander was taken into account. The gauges within the gauge array were spaced from center at 2-foot increments. However, gauge 14 was an exception since it was spaced from center at 4 feet from the nearest ASG to provide sufficient spacing for the EPC transducer. Also, based on past Test Track measurements illustrating that the maximum tensile strain came from responses in the direction of traffic (i.e., longitudinal strain), the ASGs were only oriented longitudinally in all of the AG Experiment sections (Timm and Priest, 2008).

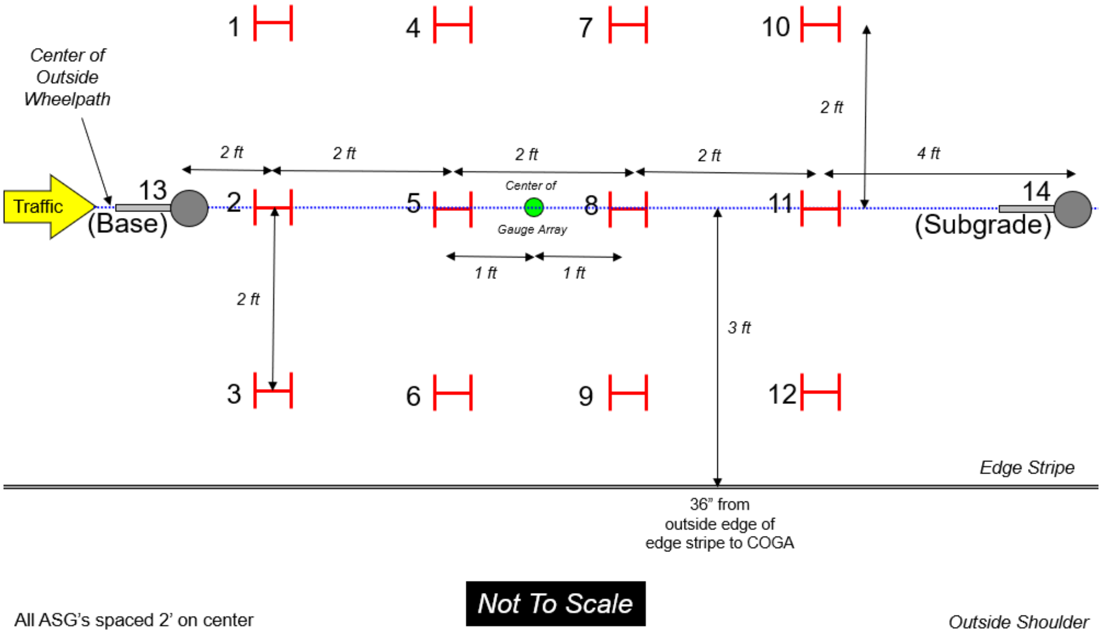

Figure 3.4: Gauge Array for AG Experiment Sections

3.1.2 Calibration

The ASG and EPC local calibration procedures, as documented by McCarty (2020), were utilized for the gauges in the AG Experiment sections. The ASG calibration procedure involves ensuring gauge functionality and obtains a voltage-to-strain calibration factor. Each ASG was wired into the DATAQ data acquisition system to record voltage signals and mounted into a calibration jig to apply tension to the ASG. Displacement values were noted as tension is applied, allowing strain to be calculated. Two loading and unloading cycles were applied as a repeatability check. The gauge factor was then determined from the slope of the linear trendline of the plotted microstrain versus voltage points. Individual gauge factors were determined, but the ASG gauge factors were typically around 500 microstrain/Volt.

The EPC calibration process also involves ensuring gauge functionality. Each EPC was wired into the DATAQ to record voltage signals and placed into the water-filled chamber to apply compressive stress to the EPC. Pressure values were recorded as compressive stress was applied. Two loading and unloading cycles were again applied as a repeatability check. The gauge factor was then determined from the slope of the linear trendline of the plotted pressure versus voltage points. The EPC gauge factors are typically around 7.2 psi/Volt.

The detailed calibration data for each gauge in the AG Experiment sections can be seen in Appendix A. The resulting calibration factor of each gauge for the sections can be viewed in Appendix B, along with the gauge assignments for each test section.

3.1.3 Installation

After all the gauges were calibrated, installation within the AG Experiment sections commenced in coordination with the pavement construction schedule. Installation of the gauges was similar to that of previous test cycles. For each section, the subgrade EPC was installed first. The gauge's wire was threaded into flexible conduit to ensure that it did not get pinched or cut by aggregate or equipment during construction. Next, the gauge and conduit were placed on the subgrade according to the layout pictured in Figure 3.4. Spray paint was then used to mark the placement, allowing the gauge and conduit to be removed. A trench was then dug in the subgrade along the spray paint guidelines for the conduit to lie in, as seen in Figure 3.5. A shallow hole was also dug for the EPC itself. Subgrade soil was sieved through a #8 and a #16 sieve for placement underneath the EPC to make it level with the subgrade surface and provide a layer of protection from larger stones. The -#8 material was placed first, followed by a thin layer of finer -#16 material. Figure 3.6 shows a leveled subgrade EPC from one of the sections. Once leveled, the location of the EPC was documented by a surveyor with a total station. The EPC was then covered with more -#16 and -#8 subgrade material. The conduit was also placed in the trench and covered and compacted with subgrade material that had large aggregate removed with a ¼" screen. The installed and covered subgrade EPC can be seen in Figure 3.7. Finally, an aggregate base was placed, graded, and compacted on top of the subgrade. Construction equipment was used to dump and work loads of aggregate base material on top of the covered subgrade EPC, as seen in Figure 3.8.

Figure 3.5: Subgrade Trench Digging

Figure 3.6: Leveled Subgrade EPC

Figure 3.7: Installed and Covered Subgrade EPC

Figure 3.8: Aggregate Base Material Covering the Subgrade EPC

After the aggregate base was placed and met moisture and density requirements, the base layer EPC and ASGs were installed. The installation of the base layer EPC was exactly the same as the installation of the subgrade EPC, except that aggregate base material was dug into and used as backfill instead of subgrade material.

ASG installation was also similar, but some aspects varied. The gauge wires were again threaded into protective flexible conduit. This process proved to be challenging and time-consuming for the ASGs with 150-foot leads. Thus, these ASGs were prepped using fish tape beforehand and placed into buckets for transportability, which can be seen in Figure 3.9. Then the gauges and conduits were placed on the aggregate base according to the layout pictured in Figure 3.4. Spray paint was again used to mark the placement, allowing the gauges and conduit to be removed. Figure 3.10 shows the gauges before removal. Trenches were then dug in the aggregate base along the spray paint guidelines for the conduit to fit in, as seen in Figure 3.11. The conduit was then placed in the trench and covered and compacted with aggregate base material that had large aggregate sieved from it using a ¼” screen. The installed ASGs, as well as base layer EPC, can be seen in Figure 3.12 having locations documented by a surveyor with a total station.

Figure 3.9: Buckets Used to Prep and Transport 150-foot Lead ASGs

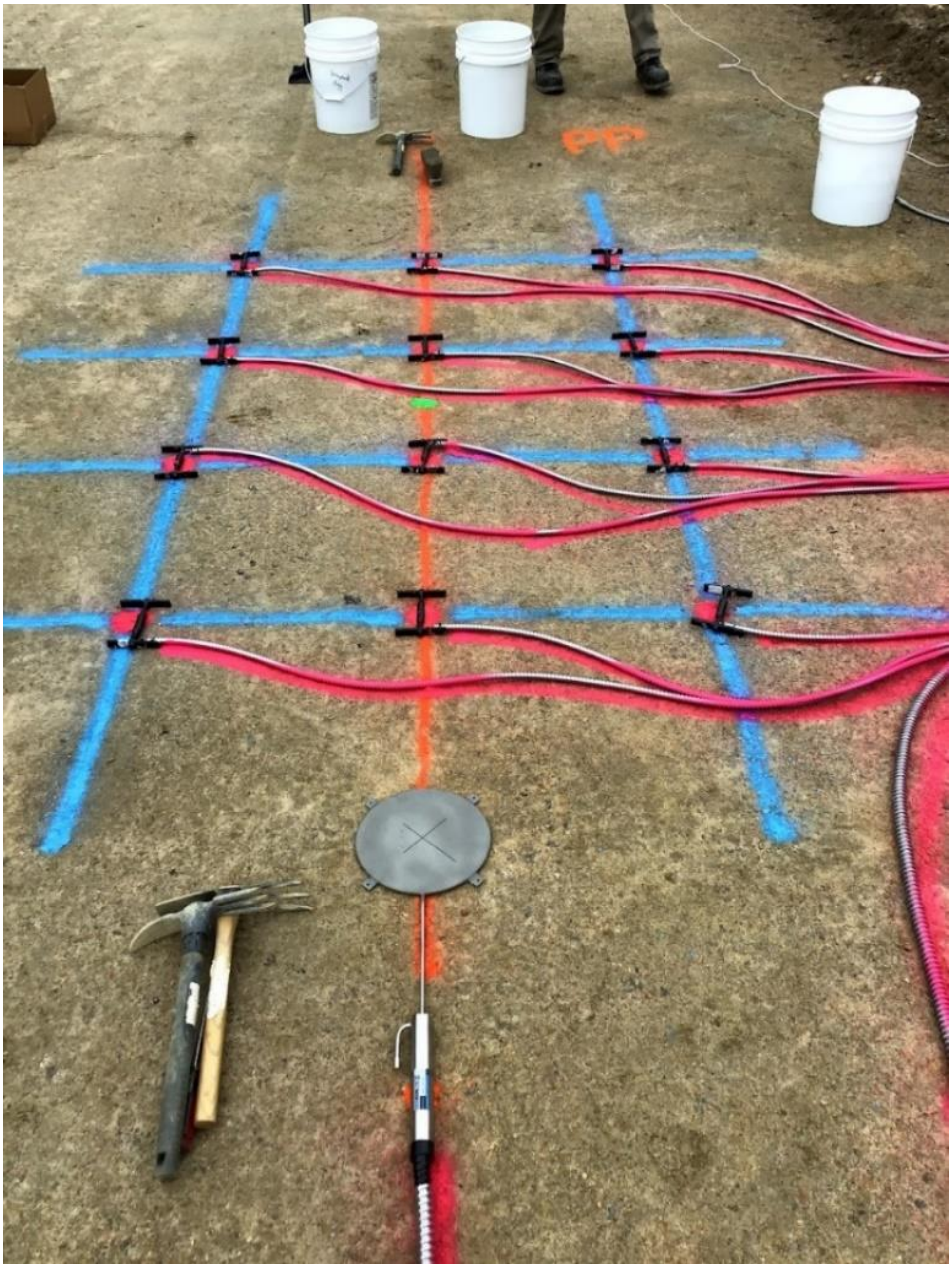

Figure 3.10: ASGs in Layout Before Trenches Were Dug

Figure 3.11: Digging Aggregate Base Trenches

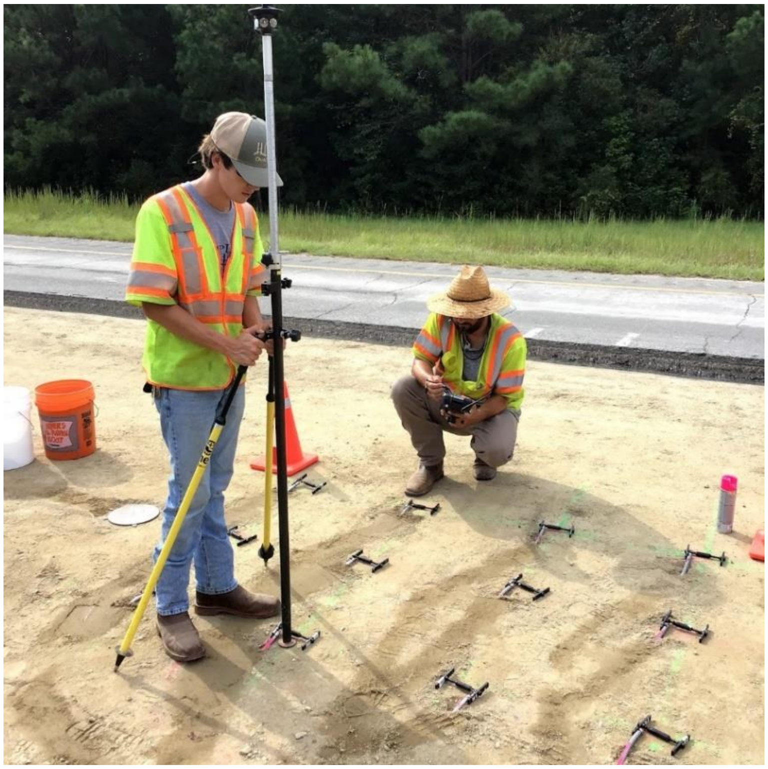

Figure 3.12: Surveying Installed ASGs and Base Layer EPC

After all the gauges were installed in the subgrade and aggregate base layers, paving of the Hot Mix Asphalt (HMA) layer began. Details about the different mixtures as well as the various conditions associated with paving the AG Experiment sections are discussed in later sections of this chapter. The remainder of this section, however, focuses on how the ASGs and base layer EPC were handled and monitored during paving.

As with previous Test Track cycles, the ASGs were first tacked to the aggregate base using a blend of heated asphalt binder from the mixture being placed and sand, as seen in Figure 3.13. This prevents the ASGs from moving from their documented locations during paving. Next, mix was taken from the paver and sieved to remove large aggregate using a ¼” screen. The sieved mix material was then used to cover the gauges in an effort to ensure the paver and compactors did not pull them out of the base layer or adversely affect their survivability. When covering the gauges, compressive force was applied to the mix over the ASGs to pre-strain them. It is believed that this helps them endure the extreme tensile strains that occur as the construction equipment passes over. Finally, the mix was carefully compacted with a tamping plate using constant pressure and a rocking motion. The pre-straining process, the compaction of the covering mix, and the paving-ready gauges are shown in Figures 3.14, 3.15, and 3.16, respectively.

Figure 3.13: Tacked Down ASG

Figure 3.14: ASG Pre-Straining Process

Figure 3.15: Compaction of the Gauge-Covering Mix

Figure 3.16: Paving-Ready Gauges

After the sections were paved and compacted, smoothness was deemed to be inadequate. This was expected since only a single thick lift was used rather than the more conventional multilift approach. Therefore, all sections underwent precision grinding surface treatments. The thick-lift topic and method will be discussed in detail later in this chapter. However, after all the sections were ground to a suitable smoothness and final AC layer thicknesses were established, they were each retrofitted with a thermocouple temperature probe. Based on past Test Track cycles, thermocouple temperature probes were found useful to structural integrity research due to the high correlations with AC mid-depth temperature, AC strain levels, and AC elastic modulus determined from backcalculation (Timm and Priest, 2008). The probe was installed in the shoulder of the roadway to avoid being run over by trucks and so that a hole was not cut in the middle of the section. Pictures were not taken during the installation of the AG Experiment section thermocouple temperature probes, however, pictures taken during an earlier Test Track reconstruction cycle installation are shown for demonstrative purposes. The process began by saw cutting transversely from the pavement edge to about a foot into the shoulder and vertically about an inch into the pavement, as seen in Figure 3.17. This cut was then repeated at an offset of about an inch. A vibrating hammer drill was then used to chisel out the AC between the cuts, creating a shallow slot for the probe wires. Next, a vertical hole was drilled into the pavement deep and wide enough so that the probes fit and that the top of the probe was flush with the pavement surface. Figures 3.18 and 3.19 show the drilling and the hole, respectively. The probe and wires were then inserted into the hole and slot, as shown in Figure 3.20. Finally, the probes were inserted into the hole and slot using roofing cement, which can be seen in Figure 3.21.

Figure 3.17: Saw Cutting Probe Slot (McCarty, 2020)

Figure 3.18: Drilling Probe Hole (McCarty, 2020)

Figure 3.19: Probe Hole (McCarty, 2020)

Figure 3.20: Probe in Hole and Slot (McCarty, 2020)

Figure 3.21: Roofing Cement Application Process (McCarty, 2020)

3.1.4 Survivability

Following paving, all EPCs and ASGs within the AG Experiment sections were checked to see if they produced viable signals. Table 3.2 presents these results as well as survivability rates for each section. A green cell means that the gauge was found to be working properly, while a red cell with an X means that the gauge was found to be inoperable.

Table 3.2: Gauge Survivability for the AG Experiment Sections

Channel	**N1** **GTRDry**	**N2** **GTRWet**	**N5** **Aramid**	**N7** **Ctrl**	**S5** **DryPlastic**	**S6** **WetPlastic**
1	🟩	🟩	🟩	🟥 X	🟩	🟩
2	🟩	🟥 X	🟩	🟥 X	🟩	🟩
3	🟩	🟩	🟩	🟥 X	🟥 X	🟩
4	🟩	🟩	🟥 X	🟩	🟩	🟥 X
5	🟩	🟩	🟥 X	🟩	🟥 X	🟥 X
6	🟥 X	🟩	🟥 X	🟩	🟩	🟥 X
7	🟩	🟩	🟥 X	🟩	🟩	🟩
8	🟩	🟩	🟩	🟥 X	🟥 X	🟩
9	🟩	🟩	🟩	🟥 X	🟩	🟩
10	🟩	🟥 X	🟥 X	🟩	🟥 X	🟩
11	🟩	🟩	🟩	🟥 X	🟥 X	🟩
12	🟩	🟩	🟩	🟥 X	🟥 X	🟥 X
13	🟩	🟩	🟩	🟩	🟩	🟩
14	🟩	🟩	🟩	🟩	🟩	🟩
Survivability Rate	93%	86%	64%	50%	57%	71%

Although some of the sections have low gauge survivability rates, this is believed to be a nonissue due to the redundancy in the gauge array as well as statistical checks that are built into the data processing system, which will be explained in detail later in this thesis. Regardless, all EPCs are operable, and at least one ASG to the left, center, and right of the OWP is working properly for all AG Experiment sections.

3.2 Mixture Designs

As described earlier in this thesis, the mixtures for the AG Experiment sections were designed using Balanced Mixture Design (BMD) and were dense graded. Each mix design is presented later in this chapter. However, the plant configuration settings used to target the mixture designs can be viewed in Table 3.3. Summaries of all the construction data are also included in Appendix C.

Table 3.3: Plant Configuration Settings

Component	**% Setting**					
	N1 GTRDry	**N2 GTRWet**	**N5 Aramid**	**N7 Ctrl**	**S5 DryPlastic**	**S6 WetPlastic**
Binder Content	5.7	6.1	5.9	5.9	5.9	5.9
78 Granite	39.0					
Sand	23.0					
89 Granite	18.0					
Processed RAP	20.0					
Evotherm P25	0.5					
Dry Additive / Fiber	12.0 (% by Total Binder)	N/A	2.1 oz/ton	N/A	0.5 (% by Aggregate)	N/A

The binder content plant settings for the N1-GTRDry and N2-GTRWet sections differ from the rest of the sections because they were dry and wet processes that were paved consecutively on the same day from the same production plant. Adjustments had to be made in the plant settings to ensure that the quality control (QC) binder content data was within tolerance. Also, the plant configurations for the mixtures add up to greater than 100% because East Alabama Paving Company, which is the plant that produced the mixtures, operates the plant based on aggregate weight instead of on the total mixture weight. This results in 100% for the sum of aggregate percentages. Also, the Evotherm P25 additive is based on the weight of the binder content instead of the weight of the mixture or aggregate.

The various asphalt binder performance grades (PG) that were utilized in these sections are presented in Table 3.4. All sections used a PG 67-22 base asphalt binder. The N2-GTRWet and S6-WetPlastic sections utilized Entech, Inc. and Dow® wet process asphalt additives, respectively, to modify the base binders to achieve PG 76-22 binders. The N5-Aramid, N7-Ctrl, and S5-DryPlastic sections all utilized styrene-butadiene-styrene (SBS) to modify the base binders to achieve PG 76-22 binders. The modified asphalt binders were delivered to the production plant pre-blended, so the binder contents detailed in Table 3.3 are associated with the blended binders. However, the N1-GTRDry section is slightly different from the other sections in that it does not utilize a modifier or wet process additive and consequently has a lower graded high temperature, meaning that the binder is softer. The decision to leave the base binder unmodified in this section was based on the expected grade bump provided by the SmartMIX™ dry additive.

Table 3.4: Asphalt Binder Performance Grades

	N1 GTRDry	**N2 GTRWet**	**N5 Aramid**	**N7 Ctrl**	**S5 DryPlastic**	**S6 WetPlastic**
PG	67-22	76-22	76-22	76-22	76-22	76-22
Modifier / Wet Additive	N/A	Entech, Inc.	SBS	SBS	SBS	Dow®

The granite, sand, and Reclaimed Asphalt Pavement (RAP) used in the mixtures were considered local to the Test Track, coming from nearby quarries and roadway projects. Evotherm P25 was also utilized in the mixtures. This is a warm mix additive (WMA), which can lower the temperatures required for paving. However, another purpose is to improve the workability of the mixture, which was the reason why it was used in the AG Experiment sections. The improved workability likely aided compaction.

3.3 Use of Thick-Lift Paving

Thick-lift paving was utilized for all the AG Experiment sections. This method was chosen based on previous research conducted at the Test Track (McCarty, 2020). In this research, a section was paved about 8 inches thick in one pass. The section achieved adequate density but had issues regarding smoothness and took a considerable amount of time to cool since it was paved in the middle of the day. Precision grinding had to be used to improve the smoothness to an acceptable level, and it was determined that thick-lift sections needed to be paved at night to allow for faster cooling.

The advantages of thick-lift paving outweighed the disadvantages, though, for an experiment of this kind. Thick-lift pavements can be constructed in one lift, which eliminates the possibility of slippage failure between lifts. This concept was crucial to the design of the AG Experiment sections, as the intended mode of failure was bottom-up fatigue cracking. Failures at lift interfaces would prohibit the experiment from running as expected and could interfere with the comparability of the sections and additives. Therefore, the AG Experiment sections were designed and constructed as 5.5 inch thick-lift pavements. Smoothness was an issue again, so precision grinding was completed after paving all the sections.

3.4 Paving Conditions

Environmental conditions on the day of paving can have a large impact on the quality of an asphalt pavement. Low air temperatures expedite the cooling process, which could negatively affect compaction. High air temperatures have the opposite effect. Also, rain can be detrimental to an asphalt pavement. If paving occurs when a significant amount of rain has fallen, the aggregate base may be weakened by the water it traps. Stripping and other moisture-related AC issues may follow as well. The conditions that were prevalent while paving the AG Experiment sections are summarized in Table 3.5.

Table 3.5: Paving Conditions

	N1 GTRDry	**N2 GTRWet**	**N5 Aramid**	**N7 Ctrl**	**S5 DryPlastic**	**S6 WetPlastic**
Completion Date	14-Sep-21	14-Sep-21	23-Sep-21	3-Sep-21	21-Sep-21	22-Sep-21
24 Hour High Temperature (˚F)	88	88	76	86	90	82
24 Hour Low Temperature (˚F)	70	70	55	69	73	64
24 Hour Rainfall (in)	0	0	0.03	0	0.06	1.15
Approx. Avg. Temperature at Plant (˚F)	330					

All the sections were paved during the month of September and experienced similar temperatures. However, the S6-WetPlastic section experienced more rain on the day of paving than the other sections. This could have impacts on the construction quality and structural behavior of the section. Also, all the mixtures placed had an approximate average production temperature of 330˚F at the plant. The East Alabama Paving Company plant is located in Opelika, AL, which is only 6 miles from the Test Track. This short distance allowed for the quick distribution and placement of the mixtures, which likely helped compaction.

3.4.1 Paving Equipment

The AG Experiment sections were all placed using conventional equipment used in the construction of past research cycle sections. Several truckloads of each mix were first delivered to the Test Track. The mixtures were then transferred from trucks into a Roadtec material transfer vehicle, or Shuttle Buggy®, and then loaded into a Vogele paver. This process, which can be visualized in Figure 3.22, was utilized so that the trucks did not have to drive over the gauges. The Shuttle Buggy® instead swung over the section and into the paver, which straddled the gauges as it placed the mixture.

Figure 3.22: Paving Equipment

3.4.2 Roller Patterns and Equipment

The sections were compacted with a similar roller and rolling pattern as previous Test Track cycles. The steel-wheel roller was a Hamm tandem roller and can be seen in Figures 3.23 and 3.24. The roller's steel drums vibrated to compact the sections to adequate densities, which will be discussed later in this chapter, and to leave a smooth pavement surface behind.

In Figure 3.23, the roller is beginning its three passes down section N7 (AG Ctrl) and back. The first of the passes compacts the inside lane part of the section (left in Figures 3.23 and 3.24). The second of the passes compacts the middle, and the third of the passes compacts the outside lane part (right in Figures 3.23 and 3.24). The three passes are then repeated twice more, resulting in a pavement like in Figure 3.24.

Figure 3.23: Start of Roller Compaction

Figure 3.24: End of Roller Compaction

3.5 As-Built Properties

Once the AG Experiment sections were placed and compacted, the mixture designs were compared to the as-built AC to quality control (QC) the materials used. Table 3.6 presents the mixture designs and QC checks for the AG Experiment sections. The slight deviations seen in the table were considered within the acceptable tolerance of normal construction practice.

Table 3.6: Mixture Design Targets versus As-Built Properties

Section-Description		**N1 GTRDry**		**N2 GTRWet**		**N5 Aramid**		**N7 Ctrl**		**S5 DryPlastic**		**S6 WetPlastic**	
		Target	**QC**	**Target**	**QC**	**Target**	**QC**	**Target**	**QC**	**Target**	**QC**	**Target**	**QC**
Gradation (Sieve Size)	25 mm (1")	100	100	100	100	100	100	100	100	100	100	100	100
	19 mm (3/4")	100	100	100	100	100	100	100	100	100	100	100	100
	12.5 mm (1/2")	98	97	98	97	98	98	98	97	98	97	98	97
	9.5 mm (3/8")	89	87	89	86	89	84	89	84	89	87	89	86
	4.75 mm (#4)	55	59	55	57	55	54	55	54	55	56	55	56
	2.36 mm (#8)	41	44	41	42	41	40	41	41	41	43	41	42
	1.18 mm (#16)	33	34	33	32	33	31	33	32	33	33	33	32
	0.60 mm (#30)	22	20	22	19	22	18	22	20	22	20	22	20
	0.30 mm (#50)	12	10	12	10	12	9	12	10	12	9	12	10
	0.15 mm (#100)	7	7	7	6	7	6	7	6	7	6	7	6
	0.075 mm (#200)	4.5	4.3	4.5	4.1	4.5	3.8	4.5	4	4.5	3.8	4.5	4
Volumetrics	Binder Content (Pb)	5.6	5.6	5.6	5.8	5.6	5.5	5.6	5.7	5.6	5.8	5.6	5.7
	Eff. Binder Content (Pbe)	5	5	4.9	5.2	5	4.9	5	5	5	5.1	5	5
	Dust-to-Eff. Binder Ratio	0.9	0.9	0.9	0.8	0.9	0.8	0.9	0.8	0.9	0.7	0.9	0.8
	RAP Binder Replacement (%)	21	20	21	19	21	20	21	20	21	19	21	20
	RAS Binder Replacement (%)	0	0	0	0	0	0	0	0	0	0	0	0
	Total Binder Replacement (%)	21	20	21	19	21	20	21	20	21	19	21	20
	Rice Gravity (Gmm)	2.453	2.449	2.457	2.453	2.453	2.465	2.453	2.455	2.453	2.439	2.453	2.463
	Bulk Gravity (Gmb)	2.344	2.328	2.314	2.351	2.344	2.35	2.344	2.369	2.344	2.359	2.344	2.333
	Air Voids (Va)	4.4	4.9	5.8	4.2	4.4	4.7	4.4	3.5	4.4	3.3	4.4	5.3
	Aggregate Gravity (Gsb)	2.627	2.622	2.627	2.636	2.627	2.639	2.627	2.632	2.627	2.616	2.627	2.641
	VMA (via Gsb)	15.8	16.2	16.8	16	15.8	15.8	15.8	15.1	15.8	15	15.8	16.7
	VFA	72	69	65	74	72	71	72	77	72	78	72	68

3.5.1 In-Place Density

The AG Experiment sections were also checked with a nuclear density gauge to see if adequate compaction was reached. Four random locations were tested at three offsets (inside, between, and outside wheelpath) with the nuclear density gauge set in backscatter mode. Then 3 field cores were extracted from the end transition zone of the section to calibrate the density gauge. The resulting average section compaction values are shown in Table 3.7. Evidently, density was not an issue for the AG Experiment sections, given that all compactions are greater than 92%. However, it should be noted that the N7-Ctrl section had a considerably greater density than the rest of the sections.

Table 3.7: AG Experiment Section Compaction

Section Description	**N1 GTRDry**	**N2 GTRWet**	**N5 Aramid**	**N7 Ctrl**	**S5 DryPlastic**	**S6 WetPlastic**
Avg. Measured Mat Compaction (% of G_{mm})	93.7%	94.1%	94.2%	95.9%	93.5%	93.9%

3.5.2 Roughness

The thick-lift AG Experiment sections were relatively rough after paving, so precision grinding was employed, as it has been used in South Carolina and at the Test Track for years to improve the smoothness and International Roughness Index (IRI) for pavements (McCarty, 2020). Figure 3.25 shows the N7-Ctrl section shortly after precision grinding. Table 3.8 presents the pre- and post-grind IRI data for the sections. From the table, it is evident that IRI greatly improved with the precision grinding of each section.

Figure 3.25: N7-Ctrl Section After Precision Grinding

Table 3.8: AG Experiment Section Pre- and Post-Grind IRI Data

Section and Description	IRI (in/mile)	
	Pre-Grind	Post-Grind
N1-GTRDry	175.96	72.96
N2-GTRWet	179.72	82.83
N5-Aramid	214.42	155.80
N7-Ctrl	238.18	125.00
S5-DryPlastic	178.88	96.74
S6-WetPlastic	152.03	79.61

3.5.3 Post-Grind Thicknesses

The post-grind thicknesses for the AG Experiment sections can be found in Tables 3.9 and 3.10. Table 3.9 presents the averages and standard deviations for the AC layer thicknesses surveyed in the gauge array, outside of the gauge array, and overall. Table 3.10 shows the percent difference of the overall AC layer thicknesses from the design thickness of 5.5 inches. Table 3.11 shows the averages and standard deviations for the GB layer thicknesses surveyed throughout the sections as well as the percent difference of the overall

GB layer thicknesses from the design thickness of 6 inches. Comprehensive post-grind thickness data can be found in Appendix D.

Table 3.9: Post-Grind Asphalt Concrete Thicknesses

Section Description	**N1 GTRDry**	**N2 GTRWet**	**N5 Aramid**	**N7 Ctrl**	**S5 DryPlastic**	**S6 WetPlastic**
All, Avg (in)	5.70	5.74	5.60	5.68	5.28	5.73
All Std Dev (in)	0.25	0.23	0.23	0.25	0.24	0.23
Non-Gauge Avg (in)	5.58	5.55	5.56	5.82	5.42	5.79
Non-Gauge Std Dev (in)	0.21	0.18	0.25	0.28	0.20	0.19
Gauge Avg (in)	5.81	5.90	5.63	5.56	5.16	5.69
Gauge Std Dev (in)	0.24	0.11	0.20	0.14	0.21	0.25

Table 3.10: Percent Difference of AC Thicknesses from Design Thickness

Section	**All, Avg (in)**	**% Difference from Design (5.5 in)**
N1-GTRDry	5.70	3.72%
N2-GTRWet	5.74	4.34%
N5-Aramid	5.60	1.81%
N7-Ctrl	5.68	3.23%
S5-DryPlastic	5.28	-3.97%
S6-WetPlastic	5.73	4.27%

Table 3.11: GB Thicknesses and Percent Difference from Design Thickness

Section	**All, Avg (in)**	**All Std Dev (in)**	**% Difference from Design (6 in)**
N1-GTRDry	6.00	0.07	0.00%
N2-GTRWet	6.04	0.10	0.61%
N5-Aramid	5.98	0.08	-0.31%
N7-Ctrl	5.99	0.11	-0.15%
S5-DryPlastic	6.02	0.15	0.30%
S6-WetPlastic	5.97	0.08	-0.43%

From the tables, it is evident that the AC thicknesses differed by various degrees from the design thickness, which was expected given the innate variability associated with different aspects of construction and the fact that the thick-lift paving method was used. The Aramid section differed the least at 1.81%, while the GTRWet section differed the most at 4.34%. Due to this variability of AC thickness, a normalization process was employed to fairly compare the sections and their respective performances in terms of measured strain response. This normalization process is discussed in detail later in this thesis. The GB thicknesses, however, varied much less than the AC thicknesses with percent difference from the design thickness being less than a percent for each section. Figure 3.26 shows visual representations of the as-built cross sections.

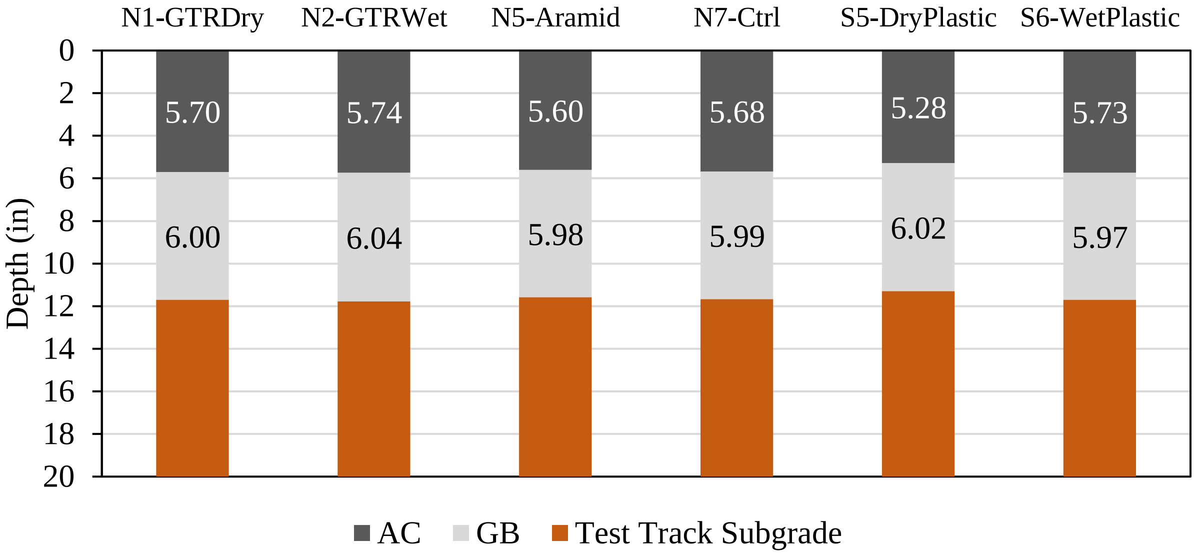

Figure 3.26: AG Experiment As-Built Cross Sections

3.6 Summary

Full-scale testing is necessary to comprehensively characterize and evaluate the additive modified mixtures for their resistance to bottom-up fatigue cracking. Therefore, five additive modified sections and one control section were constructed at the Test Track for study. To structurally analyze the pavement sections, twelve ASGs, two EPCs, and one temperature probe were installed in each section. Each gauge was subjected to local calibration procedures prior to installation. However, some did not survive the construction process. After construction, QC checks showed that the deviations between the mixture design targets and the as-built properties were considered within the acceptable tolerance of normal construction practice. It was also determined that the sections achieved adequate density but had issues regarding smoothness. Precision grinding was used to remedy the roughness issue and produced pavements that had adequate IRI values. Post-grind thicknesses were then surveyed and documented.

Once all the sections were constructed, accelerated trafficking began. Monitoring of the sections as well as performance analyses and evaluations also commenced. The following chapters discuss the trafficking, monitoring, early surface performance, and early structural behavior of the AG Experiment sections.

CHAPTER 4

Additive Group Experiment Phase IIIa: Early Surface Performance

As discussed earlier, field testing is necessary to truly characterize and evaluate the performance of an additive modified pavement. However, field performance evaluation can be time-consuming when real-world traffic is utilized. To minimize this issue and expedite field testing, the AG Experiment sections constructed at the Test Track were subjected to accelerated trafficking.

The accelerated traffic was applied to the sections by using multiple triple-trailer trucks, one of which can be seen in Figure 4.1. The NCAT Test Track operates on three-year research cycles. The first year is reserved for the planning and construction of new test sections. The second and third years are designated for the trafficking and forensic analysis of the in-place test sections. During trafficking, the trucks run five days per week for nearly 16 hours a day to apply 10 million equivalent single axle loads (ESALs), lapping the Test Track roughly 200 times per day at approximately 45 mph, over the two-year experimental period.

Figure 4.1: Test Track Truck Configuration (McCarty, 2020)

The tractor and trailer combinations were changed as necessary to maximize trafficking productivity. The tractors had a steer axle and a drive tandem axle, while the trailers together had five single axles. The weight range for each axle is detailed below in Table 4.1.

Table 4.1: Axle Weight Ranges

Steer (lbs)	Tandem (lbs/axle)	Single (lbs)
9,900 – 13,500	19,750 – 22,050	17,600 – 22,450

For the 2021 research cycle, traffic began on November 10, 2021. This thesis includes data from the start of traffic until March 15, 2022, accumulating approximately 956,884.2 ESALs. This is approximately 10% of the total traffic the sections will experience during this research cycle.

Once accelerated trafficking began on the AG Experiment sections, surface performance data collection commenced. Cracking, rutting, and roughness field performance measurements were taken every two weeks to monitor the sections' performance over time and due to the accelerated traffic. The remainder of this chapter presents and discusses these early surface performance measurements for the AG Experiment sections. Comparisons are also made between the additive modified and control AG Experiment sections.

4.1 Cracking

Cracking was determined via visual inspection and an automated crack imaging system. For visual inspection, the sections were walked every two weeks by a team of 2 to 4 people, with each looking closely for signs of cracking. The automated crack imaging system was more complex. The system involved using a PathRunner data collection vehicle to assess the sections' cracking conditions on a weekly basis at normal highway speeds. An on-board front-facing super high-definition camera and a three-dimensional automated crack detection software worked in tandem to locate cracks on the surface of the sections. Even though the two methods for detecting cracking varied in terms of complexity, they both arrived at the same conclusion. From the beginning of accelerated traffic application, which was November 10, 2021, through March 15, 2022, all AG Experiment sections had no cracking. Figures 4.2 to 4.7 show the sections as of March 14, 2022. The analysis timeframe is relatively short, though, and the expected mode of failure is bottom-up fatigue cracking, so cracking should continue to be monitored throughout the research cycle.

Figure 4.2: N1-GTRDry Section as of March 14, 2022

Figure 4.3: N2-GTRWet Section as of March 14, 2022

Figure 4.4: N5-Aramid Section as of March 14, 2022

Figure 4.5: N7-Ctrl Section as of March 14, 2022

Figure 4.6: S5-DryPlastic Section as of March 14, 2022

Figure 4.7: S6-WetPlastic Section as of March 14, 2022

4.2 Rutting

Rutting was determined for the AG Experiment sections using the Dynatest® Mark IV road surface profiler bar mounted on a van, which was manufactured by Pathways. Figure 4.8 shows the rutting that was measured in each section over the timeframe. As seen in the figure, all sections show that rut depth increases at about the same rate as time passes and accelerated traffic is applied. Some rutting is to be expected due to the additional compaction caused by the trucks early on as well as due to increases in temperature. However, as of March 14, 2022, the rutting in all sections was less than the commonly used failure point of 0.5 inches. The rut depths for the N2-GTRWet section were greater than the other sections, though, which could possibly be due to it having more binder in the mix. Also, the moduli of all sections will be determined and analyzed in Chapter 5. The results will be checked to see whether the N2-GTRWet section has a lower AC layer modulus than the rest, which could also be a reason for the higher rutting values. Regardless, this analysis timeframe is relatively short, so monitoring should continue throughout the research cycle to determine the impact of more time, more traffic, and greater temperature ranges on the sections.

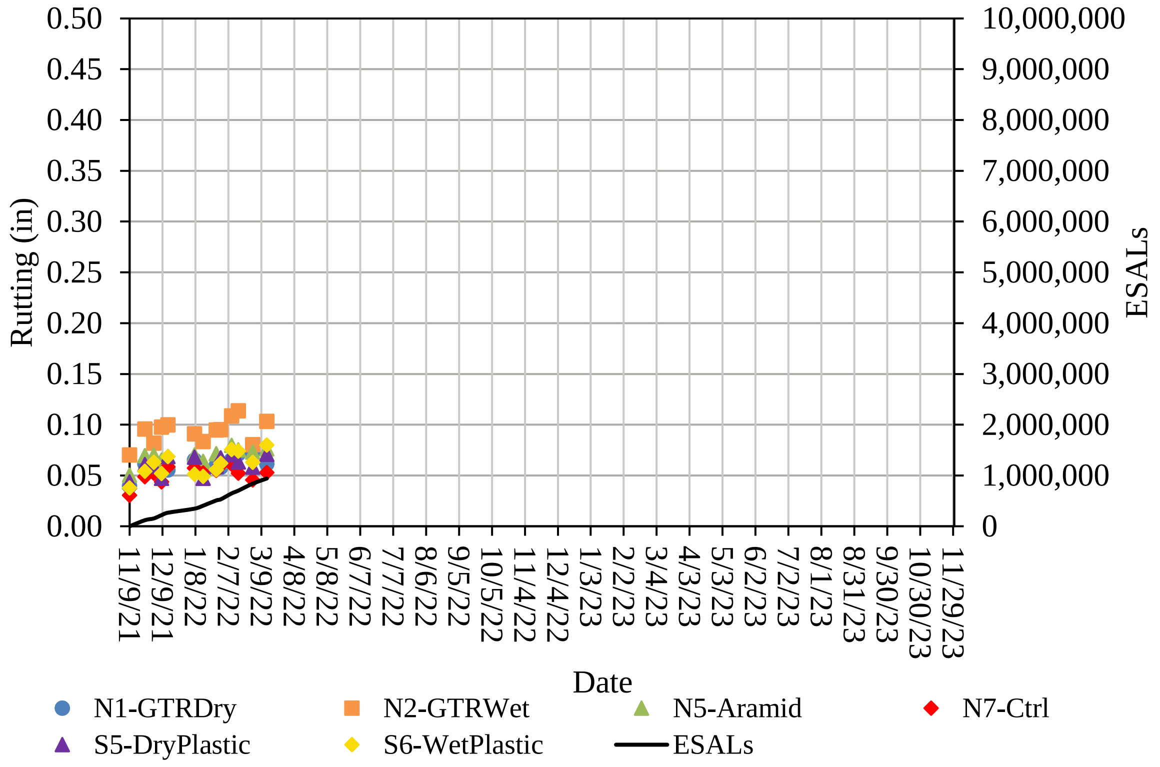

Figure 4.8: AG Experiment Section Rutting

4.3 Roughness

The International Roughness Index (IRI) was also determined for the AG Experiment sections using the Dynatest® Mark IV road surface profiler bar mounted on the van that was manufactured by Pathways. Figure 4.9 presents the IRI measured in each section over the timeframe. The pre-grind IRI values of the sections, which were presented in Chapter 3, and the associated significant decreases in IRI are not shown in Figure 4.9 due to the improvements not being caused by traffic or time passing. The post-grind IRI values that are presented in Figure 4.9 show decreases over time and as traffic is applied, which was determined by the slightly negative slope of the linear trendlines. Slight decreases in IRI are expected since applied traffic wears down the surface texture of pavements. So, the smoothness of the sections remains relatively steady with no obvious signs of distress. The exceptions to this are the N7-Ctrl and S5-DryPlastic sections. They both have slightly positive linear trendline slopes, meaning that IRI is increasing or the pavement is getting rougher. However, no cracking or extreme rutting was observed in these sections. So, the reason behind the increasing IRI values is not yet known. Since the R^2 values are all relatively low, the trendlines therefore do not fit the data well. It is probable that as IRI data is collected and points are added to the plot, the slopes will fluctuate and potentially change signs, which would reverse the interpretation of the data. The IRI of the sections with slightly positive trendline slopes as well as the rest of the sections should continue to be monitored throughout the research cycle to determine the impact of more time and traffic.

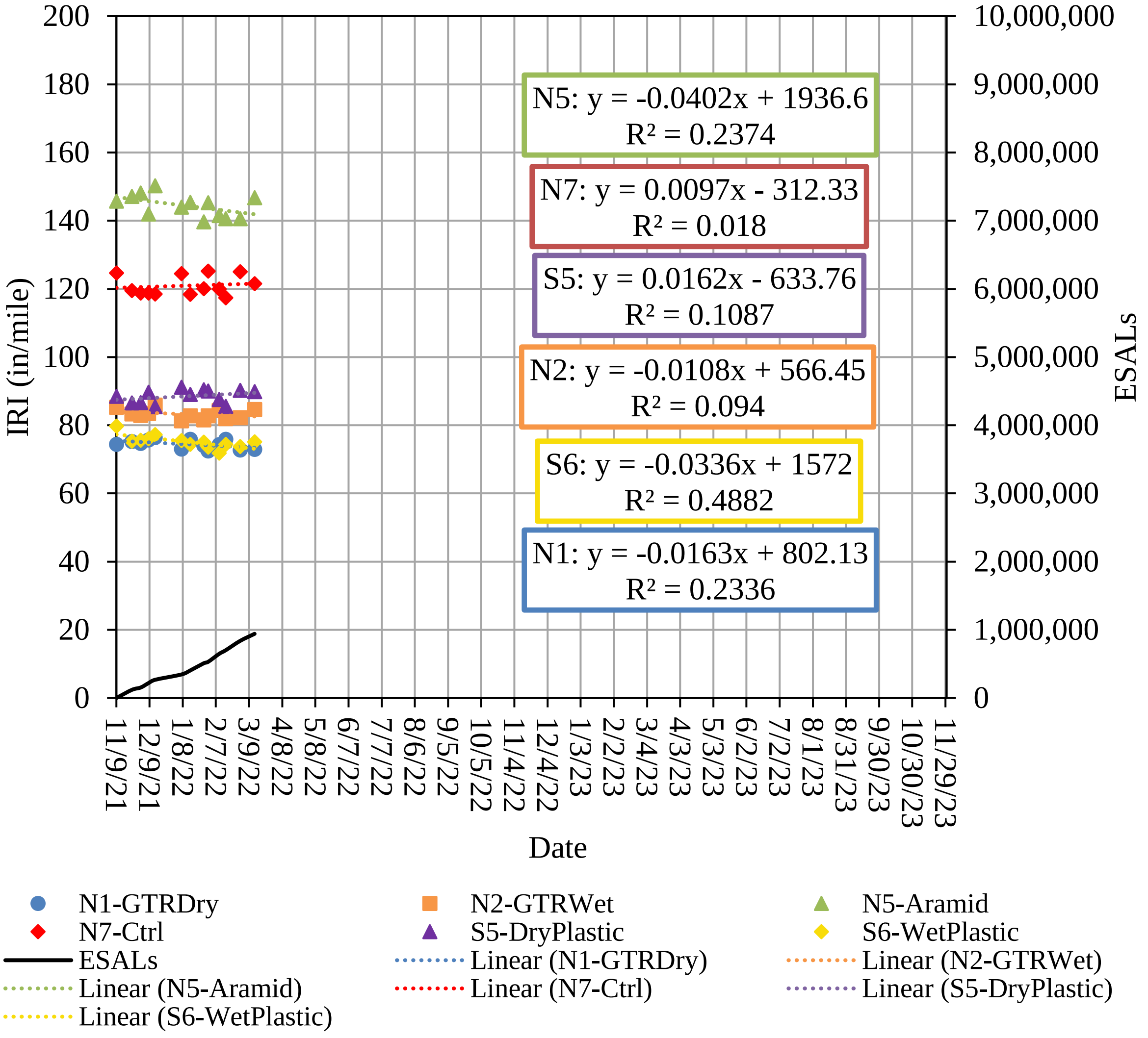

Figure 4.9: AG Experiment Section IRI

4.4 Summary

Field testing is necessary to comprehensively characterize and evaluate the additive modified mixtures, but this can be extremely time consuming. The NCAT Test Track utilizes accelerated trafficking to expedite the process. Multiple heavy tractor, triple-trailer combination trucks run five days per week for nearly 16 hours a day to apply 10 million ESALs over the two-year experimental period. For the 2021 research cycle, traffic began on November 10, 2021. The timeframe for this thesis is from this start date to March 15, 2022, which amounts to approximately 956,884.2 ESALs being applied to the AG Experiment sections.

Cracking, rutting, and roughness field measurements were taken for the AG Experiment sections throughout the timeframe to monitor their surface performance due to the accelerated traffic. From visual inspection and an automated crack imaging system, it was determined that none of the AG Experiment sections showed signs of cracking. Some rutting, which increased at about the same rate for all sections, was observed. However, all rutting in the sections is well below the commonly used failure threshold of 0.5 inches. The rut depths for the N2-GTRWet section are greater than the other sections, though, which could possibly be due to it having more binder in the mix. The AC layer modulus of this section will be determined and analyzed against the other sections to see whether it has a lower value than the rest, which could also be a reason for the higher rutting values. All section IRI values, except for the Ctrl and DryPlastic sections, decreased slightly. So, the smoothness of most sections remains relatively steady and shows no signs of distress. However, no cracking or extreme rutting was observed in the two sections with slightly increasing IRI, so the reason for it is not yet known. Since the R^2 values are all relatively low, it is probable that as more IRI data is collected, the slopes will fluctuate and potentially change signs. This would reverse the interpretation of the data. It is recommended to continue monitoring the sections in terms of cracking, rutting, and IRI throughout the research cycle to determine the impact of more time, more traffic, and greater temperature ranges on the sections.

In addition to the early surface performance characterization presented in this chapter, the early structural behavior of the sections was analyzed. Field measured and determined values were used to characterize the structural health of the sections. Chapter 5 focuses on this aspect of Phase IIIa of the AG Experiment.

CHAPTER 5

Additive Group Experiment Phase IIIa: Early Structural Behavior

Before adopting routine use of any additive, agencies need to understand their performance and structural characteristics in a full-scale environment. Early performance was discussed in the previous chapter and this chapter focuses on in situ structural characterization. To document this process, this chapter first describes the data collection and processing procedures. Then the processed data from the embedded instruments and Falling Weight Deflectometer (FWD) testing is analyzed, and the structural characterization of each AG Experiment section is presented. Finally, the additive modified AG Experiment sections are compared to the control AG Experiment section.

5.1 Dynamic Data Collection and Processing

As described in Chapter 3, each AG Experiment section was embedded with 12 asphalt strain gauges (ASGs) and 2 earth pressure cells (EPCs). Data from each of the functioning gauges was collected weekly, with collection times alternating from morning (beginning at 8:00 am) to afternoon (beginning at 2:00 pm) to ensure the data included varying ambient and mid-depth AC temperatures. As the NCAT trucks passed over the sections during collection times, the gauges experienced stress and strain, which the computer would register as raw voltage versus time. From the raw voltage data, each truck event and the strain and stress that each of their axles caused on the sections were captured, as seen in Figures 5.1 and 5.2. The data in the figures are from one truck event passing over one gauge. Each peak from the data was induced by an axle from the truck event, which is why there are eight peaks in Figures 5.1 and 5.2.

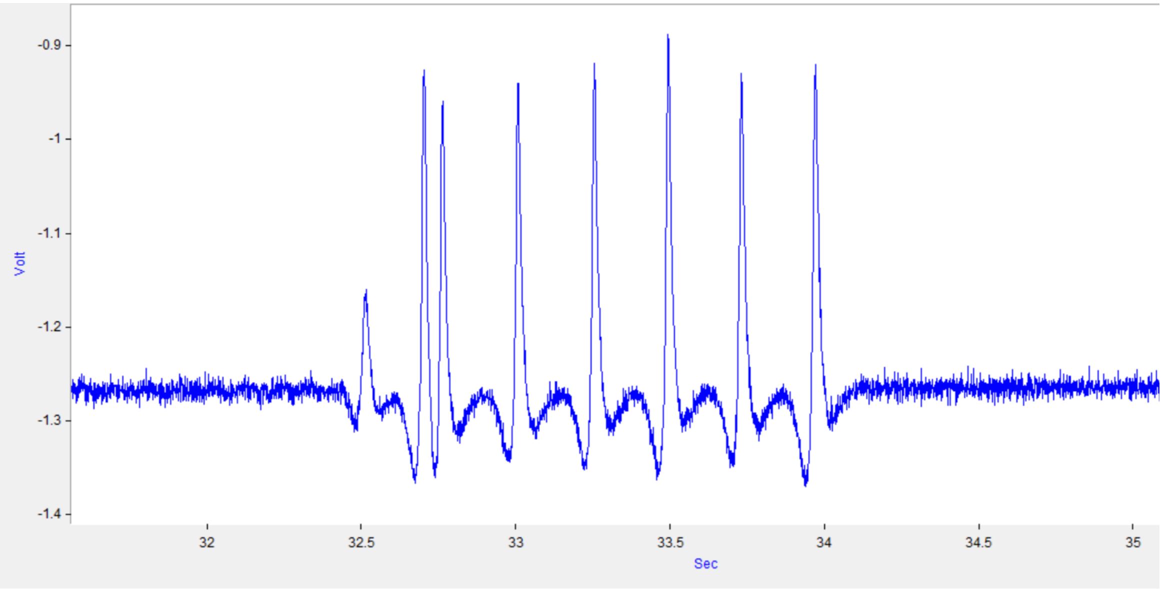

Figure 5.1: Example of ASG Raw Voltage Versus Time Data

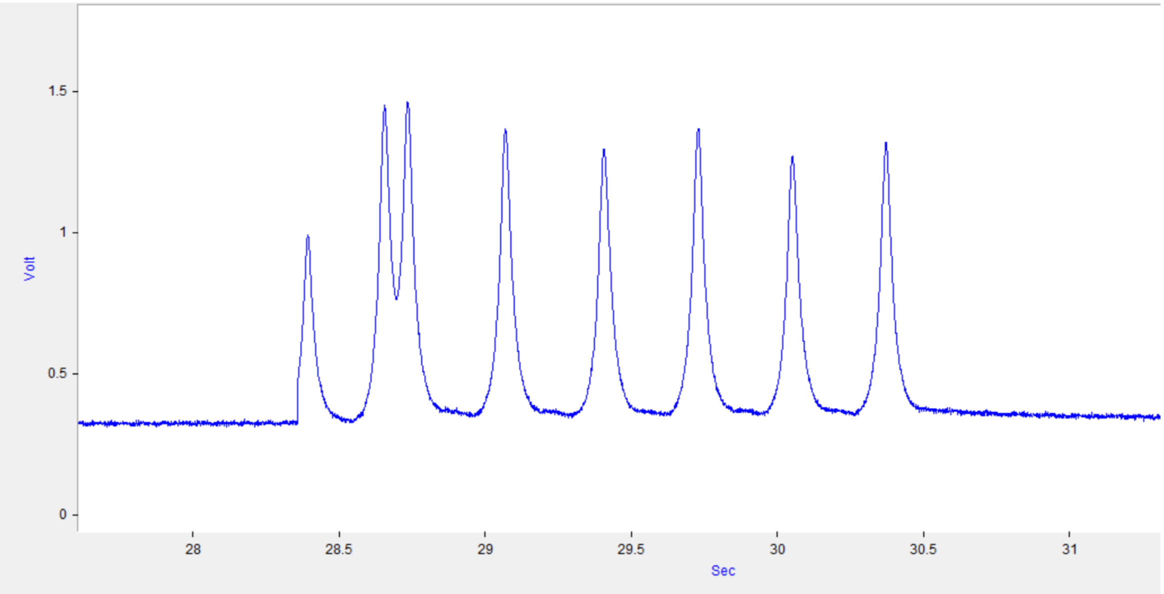

Figure 5.2: Example of EPC Raw Voltage Versus Time Data

For the ASG signals, voltages above the baseline represent tension and voltages below the baseline represent compression. For the EPC signals, it is the opposite. Voltages above the baseline represent compression, while voltages below the baseline represent tension. The EPCs should not experience tension, though, as this would mean that they are being pulled upward instead of being pushed down as trucks pass over. Therefore, changes in EPC voltages are always above the baseline meaning compressive stress, as seen in Figure 5.2, unless an error has occurred. However, ASGs experience both tension and compression due to the compressive waves that the pavement experiences just before and after an axle passes over a gauge as well as the tension that the pavement experiences as an axle is directly over a gauge. This mode reversal from compression to tension and then back to compression as an axle passes over can be seen in Figure 5.1.

Next, the raw voltage data were loaded into DADiSP® 2002, which is a visual spreadsheet program designed for handling time-series data. Customized algorithms within the program then extracted the peak responses from the EPC signals as seen in Figure 5.3. The process is slightly different for ASG signals, though. Since the greatest tensile strain at the bottom of the asphalt layer is most critical for pavement design, the entire strain response, which is essentially the strain associated with the mode reversal caused by an axle pass, was extracted from the ASG raw voltage data. Customized algorithms within DADiSP® 2002 does so by finding and documenting inflection and peak points in the data, which are illustrated in Figures 5.4 and 5.5. This process has been documented elsewhere (Timm, 2016).

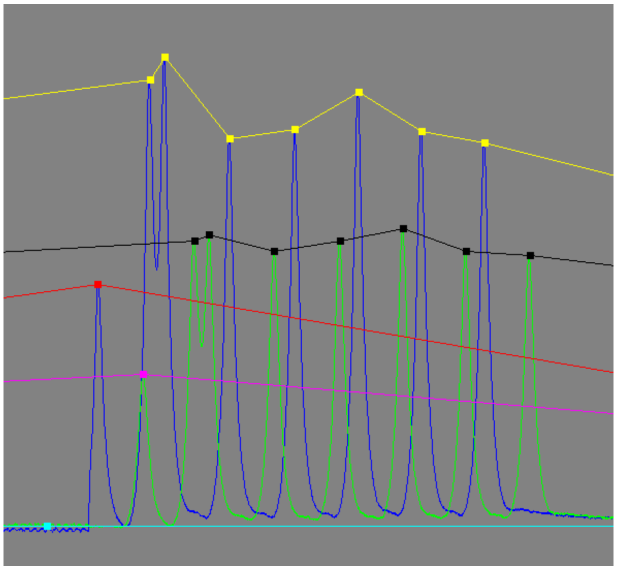

Figure 5.3: Example of DADiSP® 2002 EPC Peak Responses

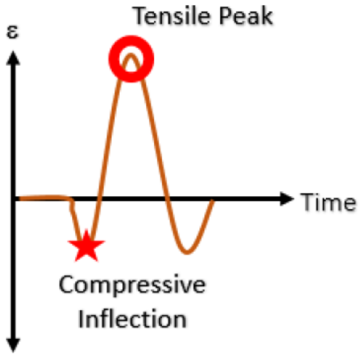

Figure 5.4: Illustration of ASG Strain Response (Timm and Foshee, 2022)

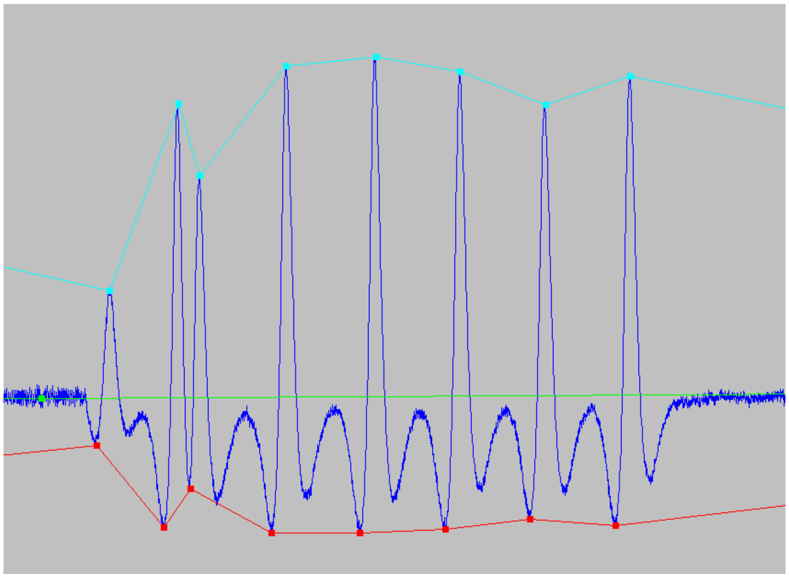

Figure 5.5: Example of DADiSP® 2002 ASG Strain Responses

The data were then grouped by axle type (steer, tandem, or single). The ASG and EPC data used in this analysis was from the five trailing single axles, which represent the vast majority of loading events. Also, the 95th percentile response for both the ASGs and EPCs was determined. Based on prior research at the Test Track, the 95th percentile of the "best hit" from each day's collection was the best data to use in structural characterization analyses (Willis et al., 2009).

As discussed in Chapter 3, the AG Experiment sections also had thermocouple temperature probes installed. From these thermocouple temperature probes, the mid-depth temperature (T2) of the sections was measured and documented during each collection period. These mid-depth temperatures were then used during the structural analysis of the sections, which will be discussed in detail later in this chapter.

5.2 FWD Data Collection and Processing

Deflection data were collected from four longitudinal locations within each AG Experiment section multiple times per month using a Dynatest® Model 8000 FWD. The four locations were chosen at random within the 200 ft sections, and each included three lateral offsets. The lateral offsets were the inside wheelpath (IWP), outside wheelpath (OWP), and between wheelpath (BWP). It is also important to note that location 4 is always in the center of the gauge array (COGA). An example of this location as well as its offsets can be seen in Figure 5.6. Each FWD test included three drops at each location using three different load levels (6,000 lb., 9,000 lb., and 12,000 lb.), with the radius of the testing plate being 5.91 inches. The nine FWD sensors were spaced at 0, 8, 12, 18, 24, 36, 48, 60, and 72 inches from the load center, respectively.

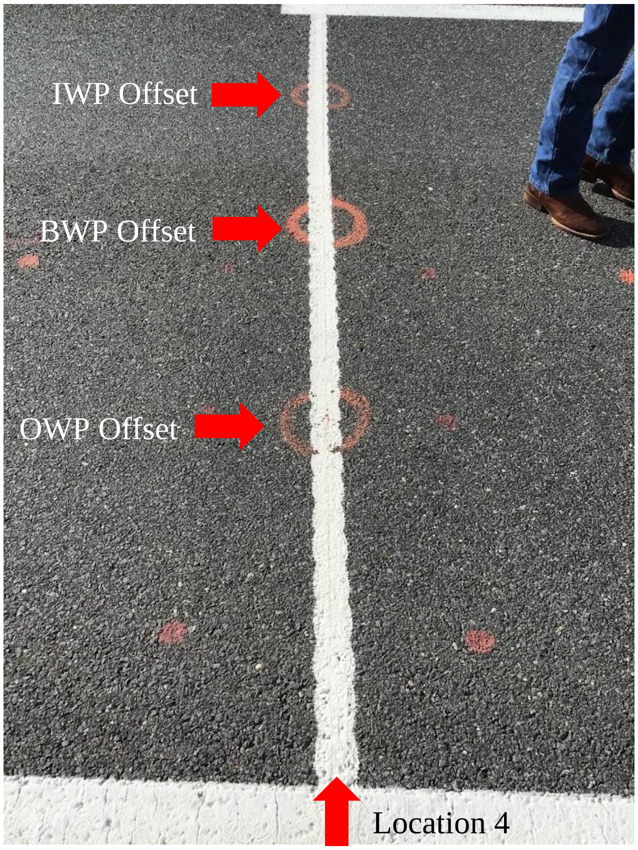

Figure 5.6: Example of FWD Testing Location 4 and Lateral Offsets

EVERCALC 5.0 was then used to backcalculate the pavement layer moduli using a trial-and-error method that minimized the root mean square error (RMSE) for each measured versus predicted deflection basin. Based on past research at the Test Track, a backcalculation pseudo-base layer of 16 inches was necessary to add to the original as-built granular base (GB) thickness to facilitate optimum backcalculation through the entire pavement cross-section (Timm and Tutu, 2017). Therefore, the backcalculation cross-section shown in Figure 5.7 was used within EVERCALC 5.0. Example values for AC and GB thickness are shown in the figure.

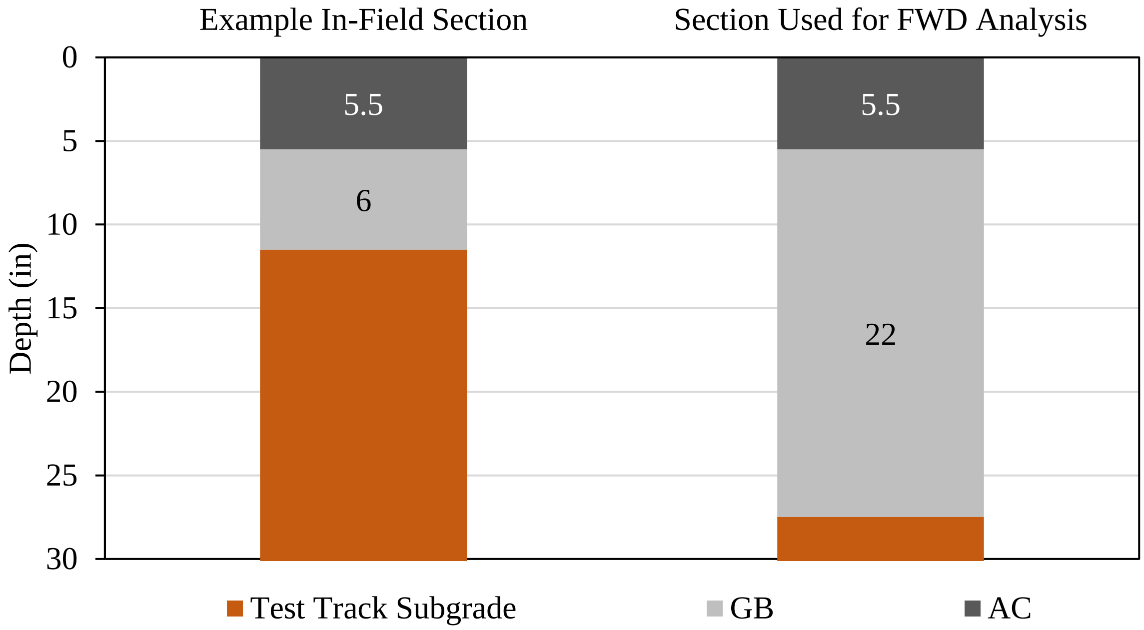

Figure 5.7: Cross-Section Comparison Used for FWD Backcalculation

5.3 Early Structural Characterization

5.3.1 Dynamic Data Analysis Methods and Results

The instruments embedded within the AG Experiment sections were utilized to measure the structural characteristics and health of the sections. The ASGs measured horizontal bending tensile strain at the bottom of the AC layer, which can aid in the prediction or identification of bottom-up fatigue cracking. If relatively high strains are measured, cracking may soon occur or has already begun. The EPCs measured the compressive stress at the top of the GB and subgrade, which can help predict or identify structural rutting. If relatively high stresses are measured, rutting may soon occur or has already begun.

The strain measured at the bottom of the AC layer depends on the thickness of the layer. Since the thickness of the AG Experiment sections varied due to normal construction tolerances, it was necessary to normalize the strain values for thickness so that the sections could be fairly compared. To this end, a thickness correction factor was applied to the strain values measured for each section. It is generally understood that for a given set of conditions, pavement strain is related to thickness by 1/thickness^2. So, small deviations from a measured thickness can be adjusted to a normalized thickness without compromising the integrity of the data. This approach was previously documented by Vargas-Nordcbeck (2012). Equation 5.1 shows how the correction factors were calculated, and Equation 5.2 demonstrates how to apply the correction factor to the measured strain values. Since AC layer thicknesses were surveyed in multiple locations within each section, it was decided to use the average of thicknesses measured in the ASG gauge array, which can be viewed in Table 5.1, in these calculations. This decision was based on the desire to involve all thicknesses within the ASG array since all ASGs were used to measure strain. It was also decided to normalize the strain measurements to the thickness of the N7-Ctrl section for ease of comparison. Therefore, H_{ref} was 5.53 inches and the corresponding correction factors are also listed in Table 5.1. For example, measured strain values in the N1-GTRDry section would be multiplied by 1.09 to account for the fact that it was slightly thicker than the N7-Ctrl section and would have had higher strain levels if it had been constructed at 5.53 inches instead of 5.77 inches.

$$CF = \frac{{H_{meas}}^2}{{H_{ref}}^2} \qquad \text{(Equation 5.1)}$$

Where:

CF = correction factor

H_{meas} = average AC layer thickness in ASG gauge array for the section, in

H_{ref} = average AC layer thickness in ASG gauge array for the N7-Ctrl section, in

$$\varepsilon_{corrected} = CF * \varepsilon_{uncorrected} \qquad \text{(Equation 5.2)}$$

Where:

$\varepsilon_{\text{corrected}}$ = thickness corrected tensile microstrain

CF = correction factor

$\varepsilon_{\text{uncorrected}}$ = measured tensile microstrain

Table 5.1: Average AC Layer Thickness in ASG Gauge Array and Correction Factors

Section Description	**N1 GTRDry**	**N2 GTRWet**	**N5 Aramid**	**N7 Ctrl**	**S5 DryPlastic**	**S6 WetPlastic**
Average AC Layer Height (in)	5.77	5.90	5.59	5.53	5.14	5.64
CF	1.09	1.14	1.02	1.00	0.86	1.04

Figures 5.8 to 5.13 show the measured and thickness corrected tensile microstrain values of the sections plotted versus time. From the figures, it is clear that from the months of November to March, strain generally increased for all sections except for S5-DryPlastic and S6-WetPlastic. The increase in strain is due to the temperature dependency of asphalt binder and the increasing temperatures experienced at the Test Track as the spring season begins. This topic will be discussed further in the next paragraph. However, the S5-DryPlastic and S6-WetPlastic sections show possibly decreasing or constant strain as time passes. This might be a result of the recycled plastics stiffening the AC layer. This pattern should continue to be studied. It is also evident that the strains were either decreased or increased by the thickness corrections. This is due to the sections having a lower or higher average AC layer thickness in the ASG gauge array, respectively, than the N7-Ctrl section. If the strains had not been corrected for thickness, the thinner S5-DryPlastic section, for example, would have been unfairly compared to the thicker N7-Ctrl section. The rest of the additive modified sections were thicker than the N7-Ctrl section on average in the ASG gauge array, so the strains were increased due to the thickness correction. The remaining discussion of strain in this chapter refers to measurements that have been corrected for thickness.

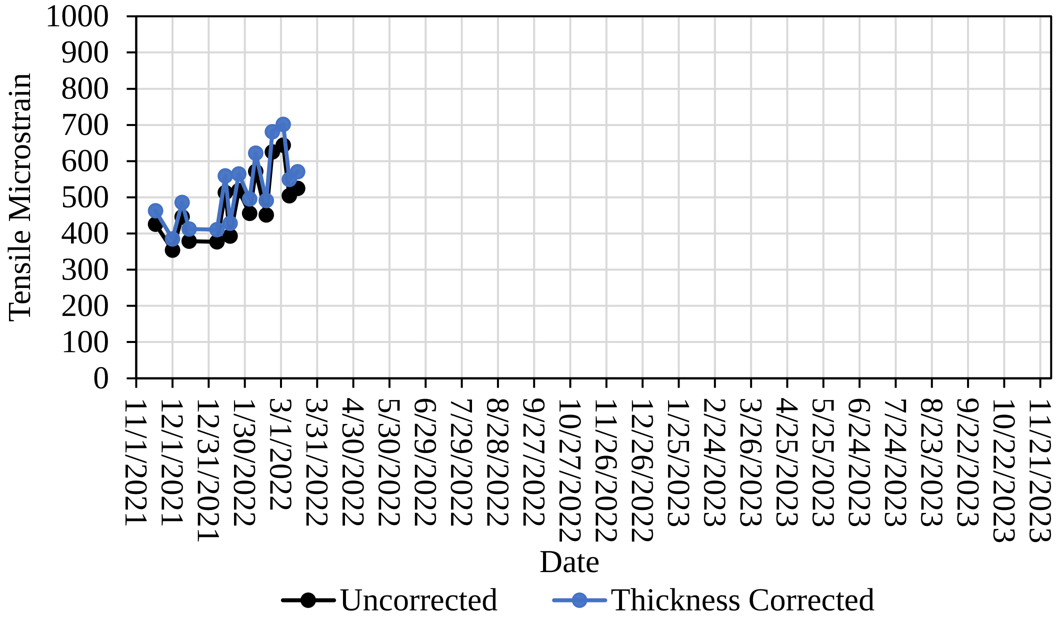

Figure 5.8: N1-GTRDry Section Measured and Thickness Corrected Strain Versus Time

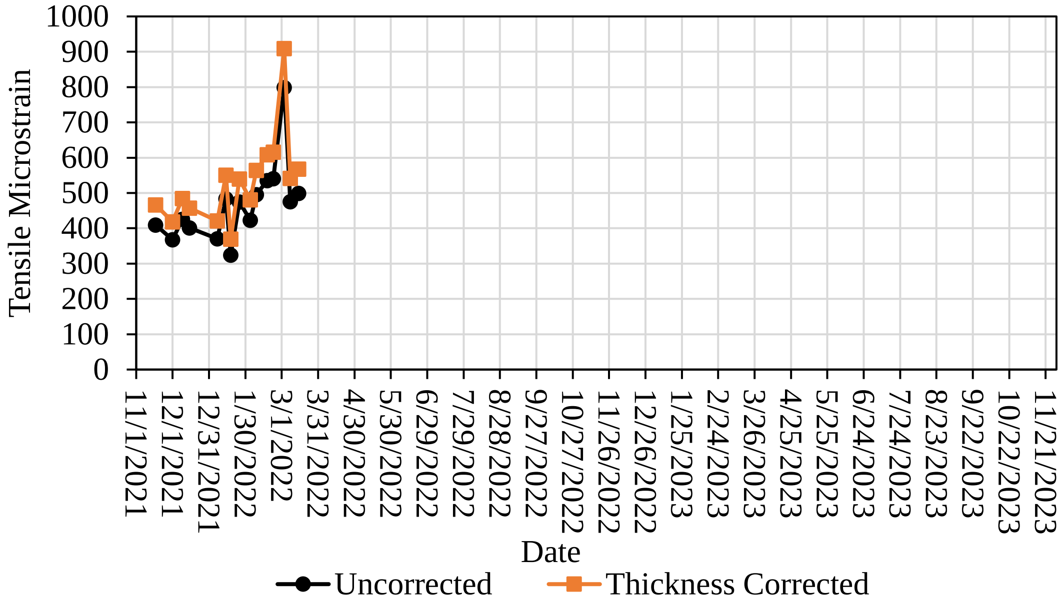

Figure 5.9: N2-GTRWet Section Measured and Thickness Corrected Strain Versus Time

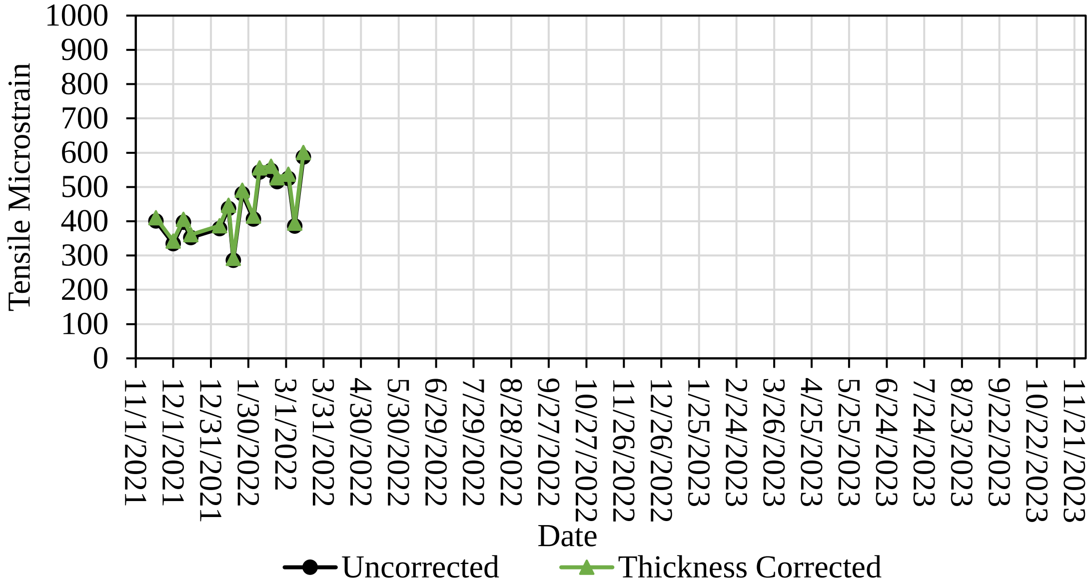

Figure 5.10: N5-Aramid Section Measured and Thickness Corrected Strain Versus Time

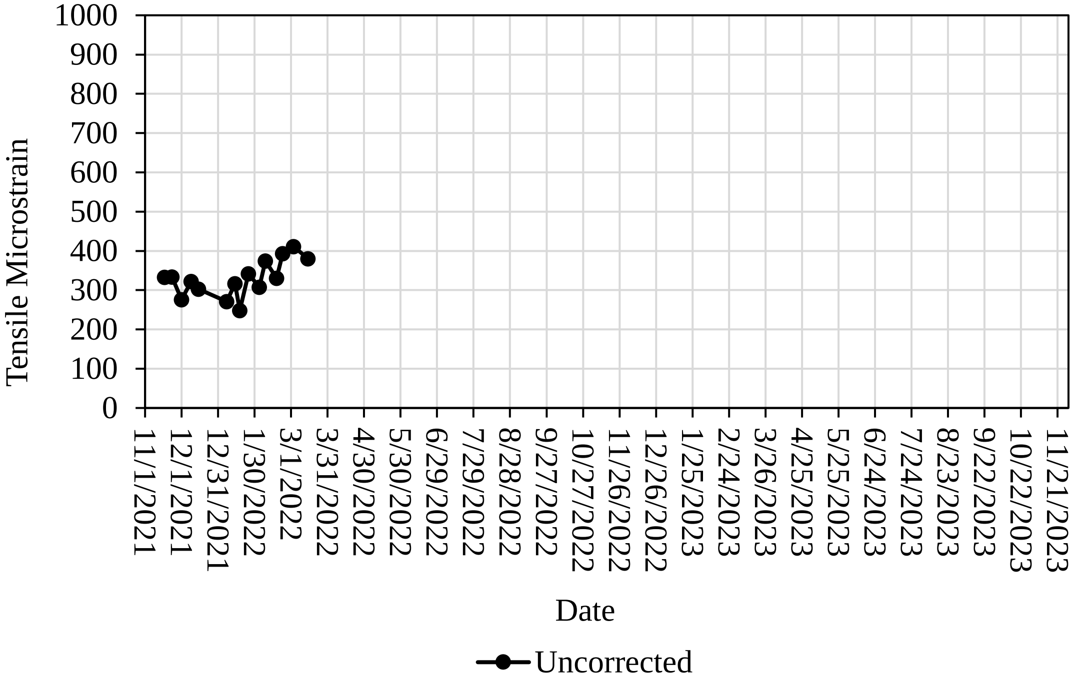

Figure 5.11: N7-Ctrl Section Measured and Thickness Corrected Strain Versus Time

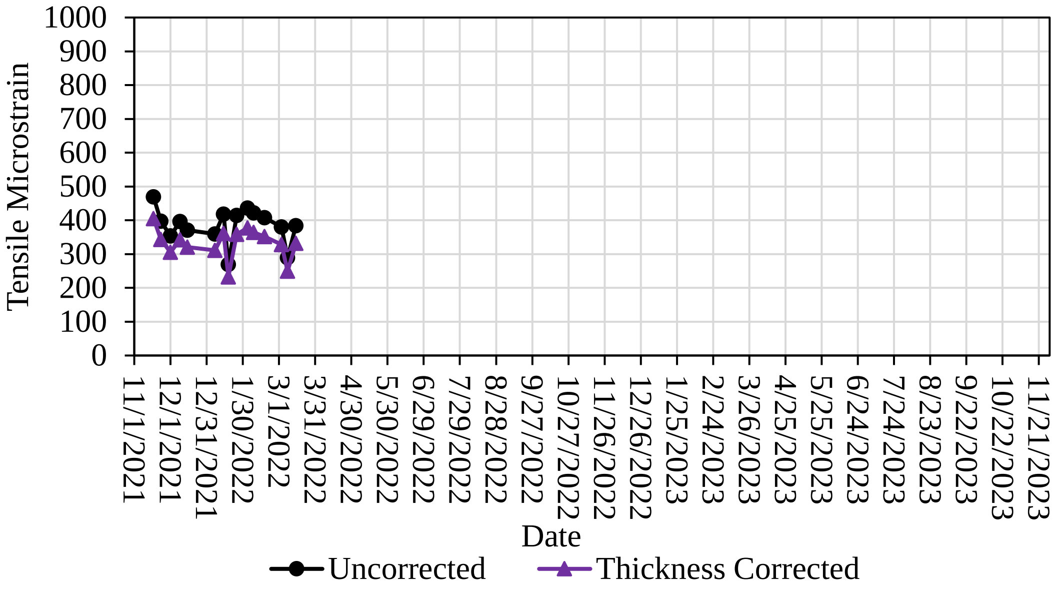

Figure 5.12: S5-DryPlastic Section Measured and Thickness Corrected Strain Versus Time

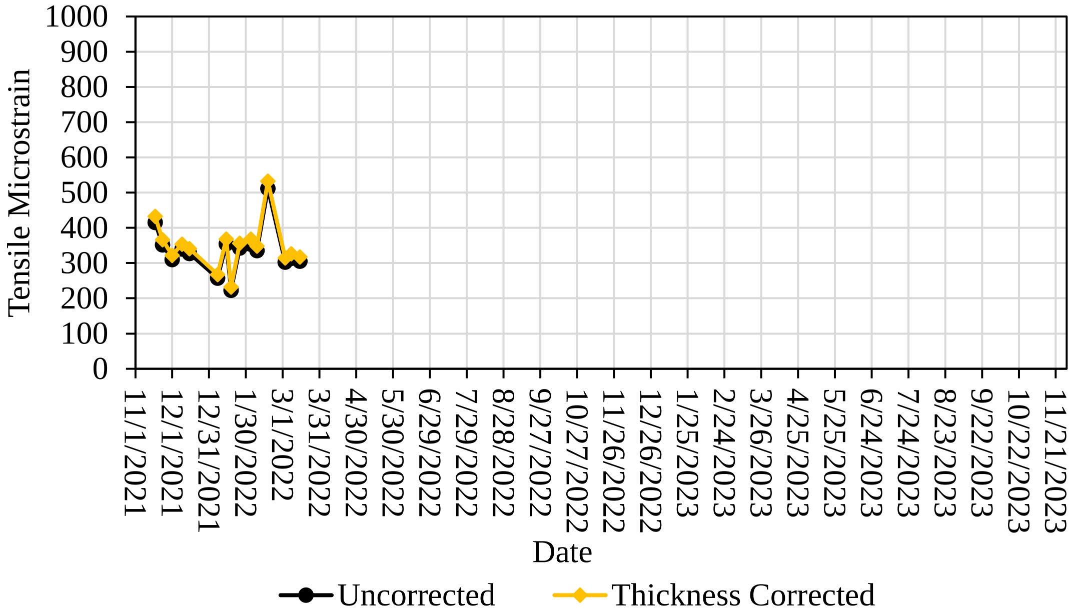

Figure 5.13: S6-WetPlastic Section Measured and Thickness Corrected Strain Versus Time

As alluded to in the previous paragraph, asphalt binder properties are largely dependent on temperature. At higher temperatures, the binder is less viscous and softer, which yields higher strain values in the AC layer. As temperature decreases, the binder is more viscous and stiffer, which yields lower strain values in the AC layer. And since the AG Experiment sections were constructed in a real-world environment at the Test Track, they experience a wide range of temperatures as the seasons progress. To further compare the sections, the strain values needed to be corrected again, but this time for temperature. The process for doing so first involved plotting the thickness corrected tensile microstrain versus the measured mid-depth AC temperature, which can be seen in Figure 5.14 for the N7-Ctrl section. The figure shows the expected temperature range at the Test Track, which is 20˚F to 140˚F. From this point in the thesis on, only plots for the N7-Ctrl section are shown, unless it is beneficial for discussion to plot all section data on the same graph. The remaining AG Experiment section plots can be found in Appendix E.

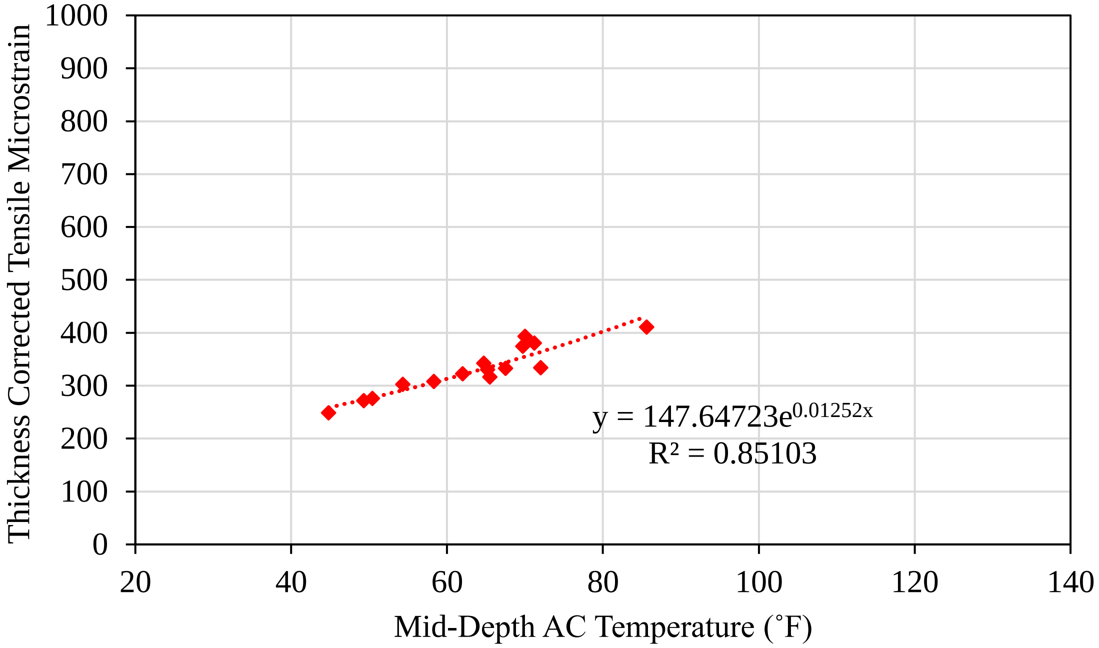

Figure 5.14: N7-Ctrl Section Thickness Corrected Tensile Microstrain Versus Temperature

From Figure 5.14, it is evident that thickness corrected tensile microstrain varies exponentially with temperature according to Equation 5.3. It should be noted that due to the relatively short data collection timeframe, higher summer temperatures were not measured in the field. So, the figure and trendline approximately present the lower half of the temperature range. The R^2 value for the trendline is therefore lower than it would be if more data points from warmer months were included. Regardless, the exponential regression coefficients were documented for each section and can be found in Table 5.2. Larger k_2 values show that the section is more dependent on temperature. So, the N1-GTRDry section is most sensitive to temperature changes, while the S5-DryPlastic section is least sensitive to temperature changes. However, the R^2 values for the exponential trendlines are all relatively low, so it is probable that as more data points are collected, they will improve and k_2 values will change.

$$\mathcal{E}_T = k_1 e^{k_2 T} \qquad \text{(Equation 5.3)}$$

Where:

$\mathcal{E}_T$ = thickness corrected tensile microstrain

k_1, k_2 = regression coefficients (see values in Table 5.2)

T = mid-depth pavement temperature (˚F)

Table 5.2: Thickness Corrected Tensile Microstrain Versus Temperature Exponential Regression Coefficients

Section and Description	k_1	k_2	R^2
N1-AG GTRDry	167.68	0.01929	0.77
N2-AG GTRWet	175.35	0.01865	0.64
N5-AG Aramid	153.55	0.01752	0.57
N7-AG Ctrl	147.65	0.01252	0.85
S5-AG DryPlastic	173.12	0.01107	0.34
S6-AG WetPlastic	135.90	0.01572	0.34

Once the exponential regression coefficients were determined, temperature correction to 68˚F commenced according to standard American Association of State Highway and Transportation Officials (AASHTO) practice. Equations 5.4 and 5.5 step through the process and show how to correct strain values for temperature.

$$\frac{\varepsilon_{68^\circ F}}{\varepsilon_T} = \frac{k_1 e^{k_2 68^\circ F}}{k_1 e^{k_2 T}} \qquad \text{(Equation 5.4)}$$

Where:

$\varepsilon_{68^\circ F}$ = temperature and thickness corrected tensile microstrain at 68˚F

ε_T = thickness corrected tensile microstrain

k_1, k_2 = regression coefficients (see values in Table 5.2)

T = mid-depth pavement temperature (˚F)

Simplifying Equation 5.4 by canceling the k_1 terms and grouping the exponential coefficients results in Equation 5.5:

$$\varepsilon_{68^\circ F} = \varepsilon_T e^{k_2 (68^\circ F - T)} \qquad \text{(Equation 5.5)}$$

Where:

$\varepsilon_{68^\circ F}$ = temperature and thickness corrected tensile microstrain at 68˚F

ε_T = thickness corrected tensile microstrain

k_2 = regression coefficient (see values in Table 5.2)

T = mid-depth pavement temperature (˚F)

Figure 5.15 shows the temperature and thickness corrected strain values for the N7-Ctrl section. The flat trendline and low R^2 value show that the thickness and temperature corrected microstrain values do not vary with temperature, which was intended and expected.

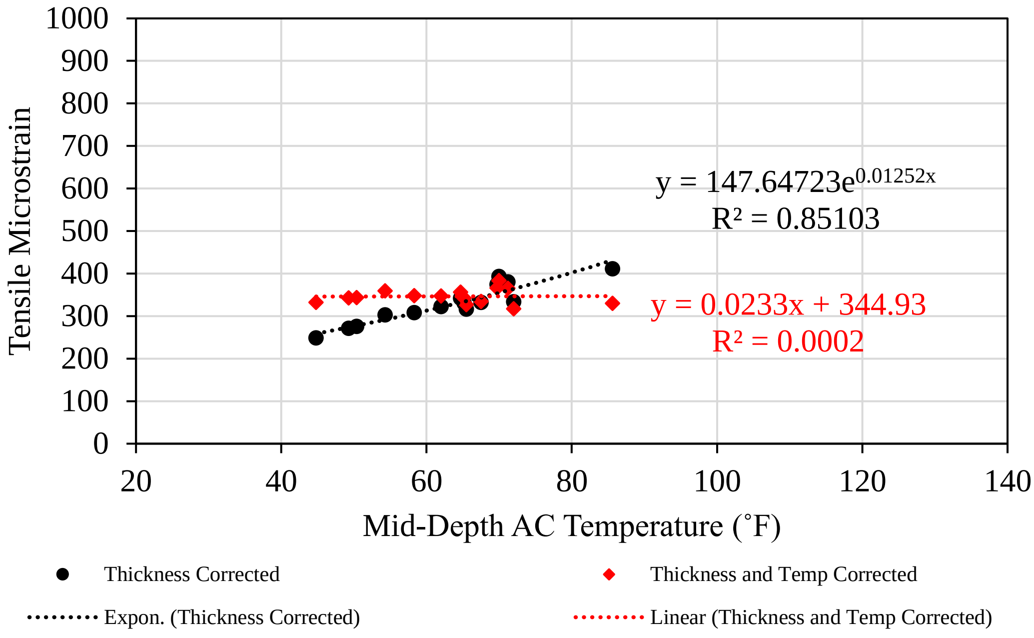

Figure 5.15: N7-Ctrl Section Thickness and Temperature Corrected Tensile Microstrain Versus Temperature

The thickness and temperature corrected microstrain values were then plotted versus collection date, as seen in Figure 5.16, to compare the strains between sections as well as check for any preliminary indications of distress. As seen in the figure, most of the sections have strain values that are steady and R^2 values that are relatively low. This indicates that the sections are not changing over time, which is a sign of good structural health as expected this early in the trafficking cycle. However, some of the R^2 values are large when compared to the others, which is the case for the N1-GTRDry and N5-Aramid sections. These sections both have R^2 values over 0.2 and show strain increasing as time passes, which might mean that fatigue cracking is possible. However, since cracking was not observed at the surface of the sections during this timeframe, monitoring of the cracking and strain of the sections should continue.

It was also noted that the N7-Ctrl section had the lowest strain values, while the N1-GTRDry and N2-GTRWet sections had the highest strain values. The N7-Ctrl section's low strain could possibly be a result of it having the greatest compacted density, which was presented in Chapter 3. Also, further structural analysis will be presented later in this chapter that investigates the modulus values of the sections. Due the fact that strain increases as modulus decreases, the modulus of the N7-Ctrl section is expected to be high and the moduli of the N1-GTRDry and N2-GTRWet sections are expected to be low.

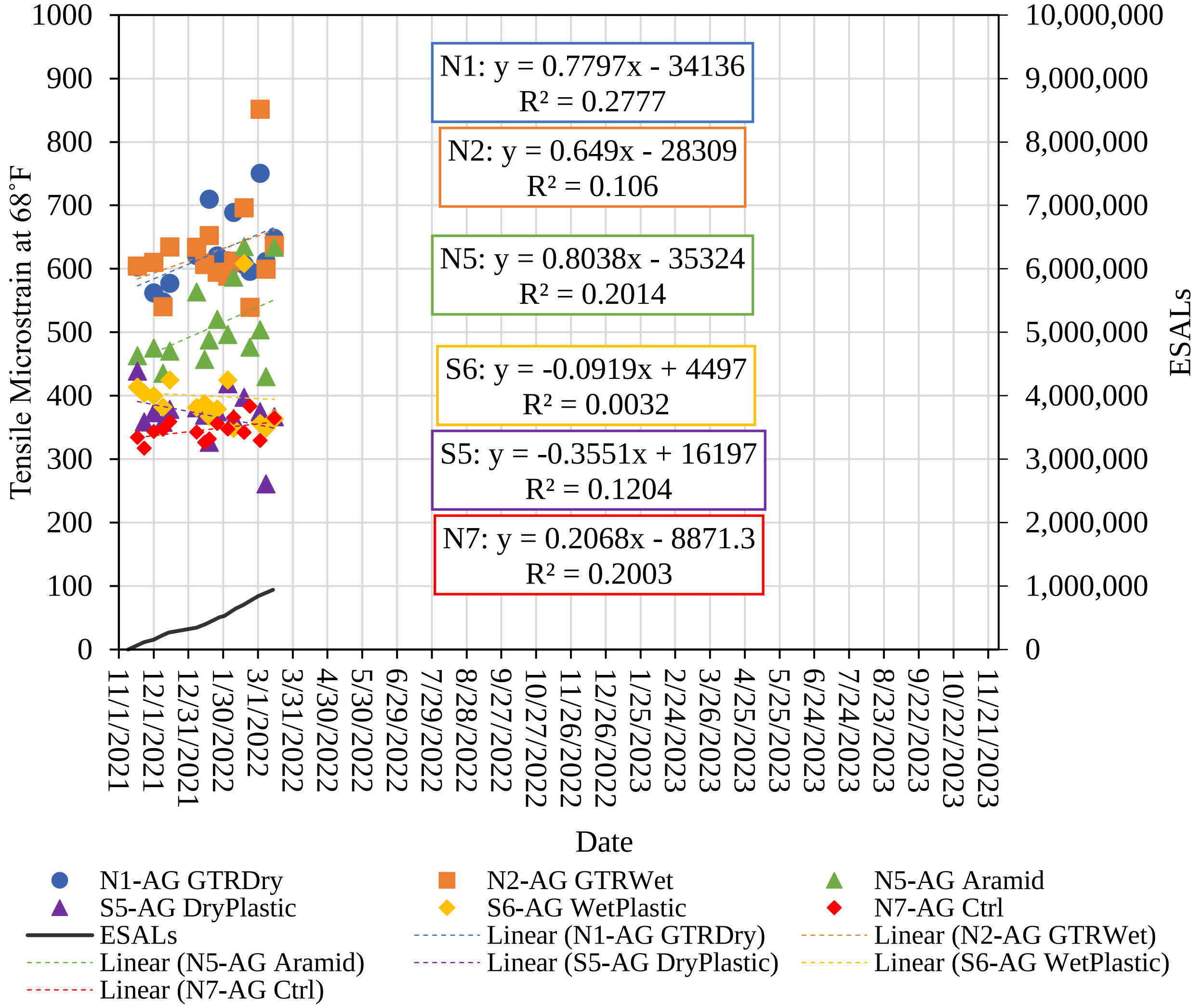

Figure 5.16: Thickness and Temperature Corrected Tensile Microstrain Versus Date

Figure 5.16 also shows fairly distinct grouping of the various AG Experiment sections in terms of strain. By visual inspection, it appears that N1-GTRDry and N2-GTRWet sections experienced very similar strains. It is possible that N7-Ctrl, S5-DryPlastic, and S6-WetPlastic sections also experienced similar strains. However, N5-Aramid section strains were not visually similar to any of the other sections and were between the other two groups.

Statistical analyses were then performed to further investigate the strain groupings. A single factor analysis of variance (ANOVA) was first conducted in Excel using a significance level (α) of 0.05 and according to the following hypotheses:

$$H_0\colon \mu_{N1-GTRDry} = \mu_{N2-GTRWet} = \mu_{N5-Aramid} = \mu_{N7-Ctrl} = \mu_{S5-DryPlastic} = \mu_{S6-WetPlastic}$$

$$H_a\colon Not\ all\ means\ are\ equal$$

Where:

H_0 = null hypothesis

H_a = alternative hypothesis

μ = mean of thickness and temperature corrected microstrain

Complete ANOVA analysis information can be found in Appendix F, but the p-value was determined to be extremely close to 0, which can be seen in Table 5.3. Since the p-value was less than α, the null hypothesis was rejected. Therefore, the mean values of the thickness and temperature corrected microstrain are not all equal. Further analysis in the form of a Tukey-Kramer multiple comparison test was warranted to compare the means of each section's microstrain values to that of each of the other sections. The Tukey-Kramer test was also completed in Excel with an α of 0.05. The first of the hypothesis pairs in this test can be seen below. The rest of the hypothesis pairs are the same, except the sections vary.

$$H_0\colon \mu_{N1-GTRDry} = \mu_{N2-GTRWet}$$

$$H_a\colon \mu_{N1-GTRDry} \neq \mu_{N2-GTRWet}$$

Where:

H_0 = null hypothesis

H_a = alternative hypothesis

μ = mean of thickness and temperature corrected microstrain

Table 5.3: Microstrain Statistical Results

Statistical Test	**p-value**
ANOVA	7.2015E-30
Tukey-Kramer: N1-AG GTRDry, N2-AG GTRWet	0.999997
Tukey-Kramer: N7-AG Ctrl, S5-AG DryPlastic	0.861137
Tukey-Kramer: N7-AG Ctrl, S6-AG WetPlastic	0.106879
Tukey-Kramer: S5-AG DryPlastic, S6-AG WetPlastic	0.688873

Comprehensive Tukey-Kramer analysis information can be found in Appendix F, but the p-values for the N1-GTRDry and N2-GTRWet sections, the N7-Ctrl and S5-DryPlastic sections, the N7-Ctrl and S6-WetPlastic sections, and the S5-DryPlastic and S6-WetPlastic sections hypothesis pairs were all greater than α, which can be seen in Table 5.3. So, the null hypothesis was not rejected and the mean values of the thickness and temperature corrected microstrain are statistically the same within the pairs. Figure 5.17 shows a graph of the means as well as the statistically determined section groupings. Error bars are also shown at one standard deviation. The conclusions from this statistical analysis confirm what was visually seen in the microstrain data.

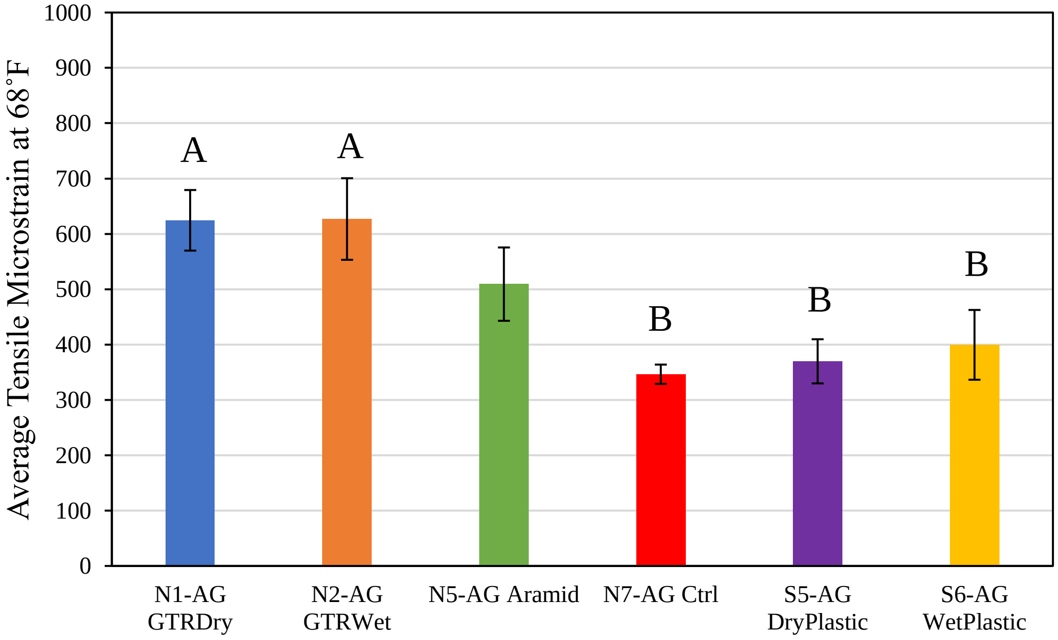

Figure 5.17: Average Thickness and Temperature Corrected Tensile Microstrain By Section

The EPC measured pressures were also analyzed to evaluate the structural behavior of the granular base (GB) and subgrade layers for the AG Experiment sections. The pressures were first plotted versus temperature to see if a dependency existed. Figures 5.18 and 5.19 show the measured pressure versus temperature for N7-Ctrl in the GB and subgrade, respectively.

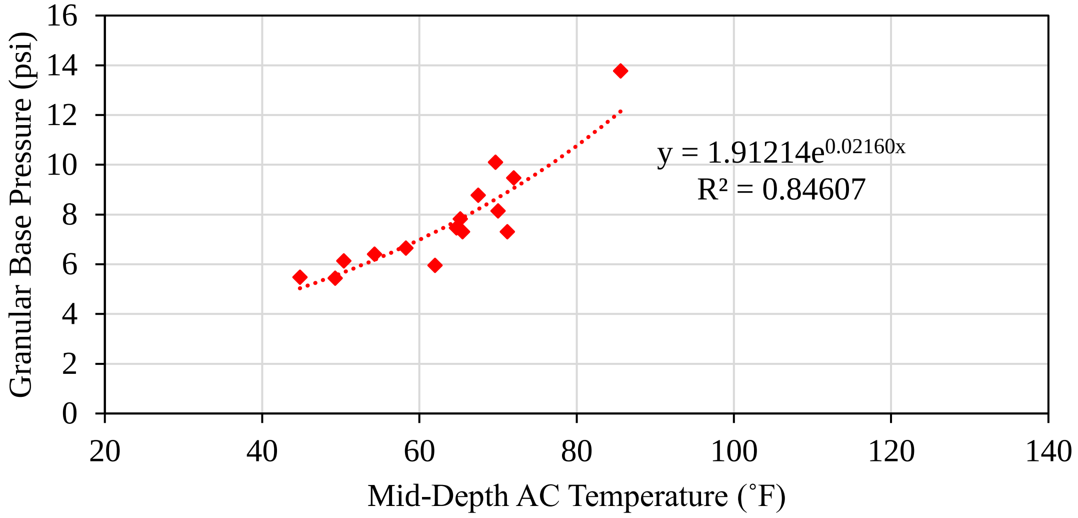

Figure 5.18: N7-Ctrl Section Measured Granular Base Pressure Versus Temperature

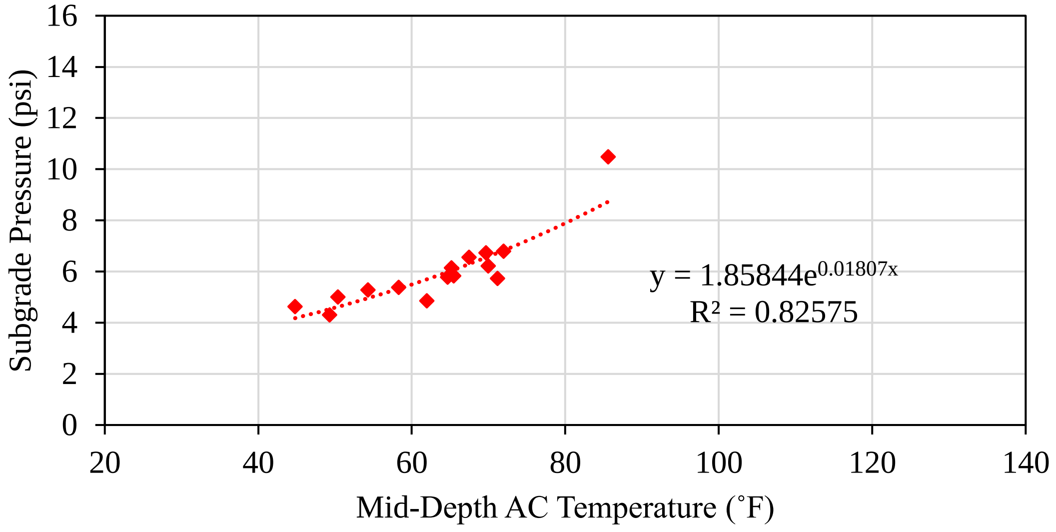

Figure 5.19: N7-Ctrl Section Measured Subgrade Pressure Versus Temperature

From the figures, it is evident that the measured pressures vary exponentially with temperature. The exponential regression coefficients were determined and documented for each section via the same process outlined earlier in this chapter and can be found in Table 5.4. This temperature dependence is likely due to the AC layer moduli changing as a function of temperature above them. For example, since the AC layer strains and deforms more in warm temperatures, the GB and Subgrade layers are subjected to more pressure. It should also be noted that pressure is greater in the GB than in the Subgrade in the figure, which is expected for a section that distributes stress properly.

Table 5.4: Measured Granular Base and Subgrade Pressure Versus Temperature Exponential Regression Coefficients

Section and Description	**GB**			**Subgrade**		
	k_1	**k_2**	**R^2**	**k_1**	**k_2**	**R^2**
N1-AG GTRDry	2.39121	0.01988	0.65	2.10437	0.01554	0.56
N2-AG GTRWet	2.16149	0.02374	0.73	2.11893	0.01634	0.79
N5-AG Aramid	1.7594	0.02525	0.60	1.84244	0.01767	0.53
N7-AG Ctrl	1.91214	0.02160	0.85	1.85844	0.01807	0.83
S5-AG DryPlastic	1.30763	0.02949	0.58	1.94727	0.01471	0.54
S6-AG WetPlastic	1.16983	0.02966	0.93	1.25696	0.01969	0.81

Once the exponential regression coefficients were determined, temperature correction to 68˚F commenced using the exact same process as with strain, except the equations involved pressure. Figure 5.20 shows the measured and temperature corrected GB pressure values for the N7-Ctrl section, and Figure 5.21 shows the same for the subgrade. The flat trendlines and low R^2 values show that the temperature corrected pressure values do not vary with temperature, which was expected.

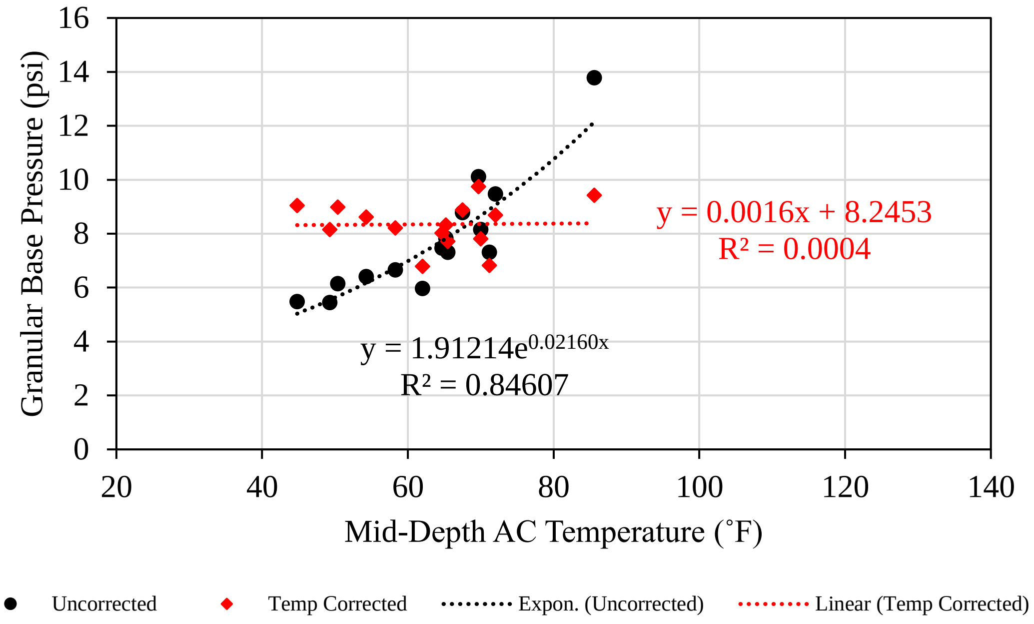

Figure 5.20: N7-Ctrl Section Measured and Temperature Corrected GB Pressure Versus Temperature

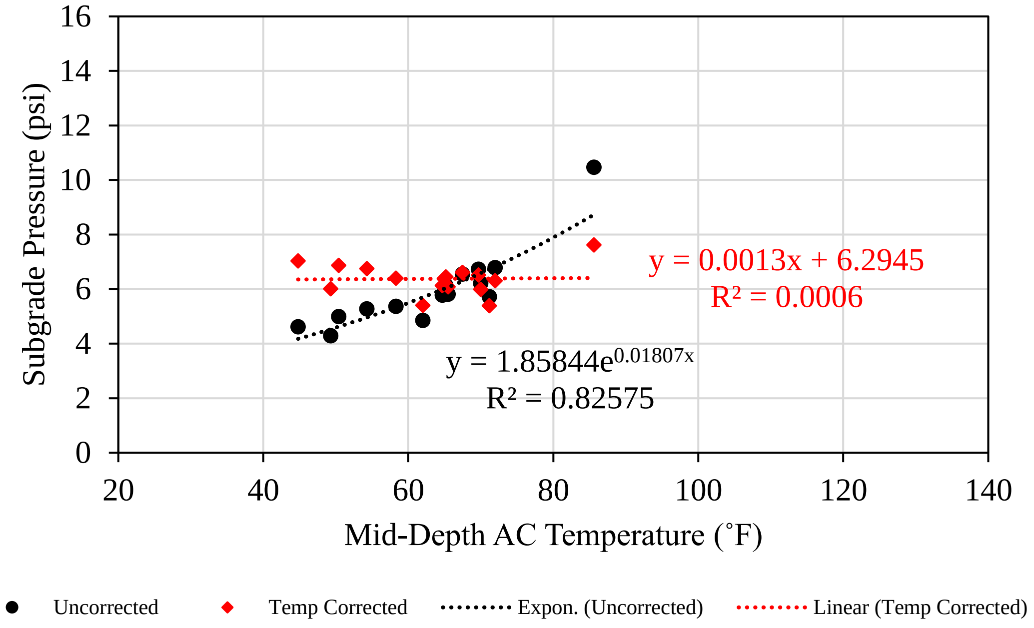

Figure 5.21: N7-Ctrl Section Measured and Temperature Corrected Subgrade Pressure Versus Temperature

The temperature corrected GB and Subgrade pressure values were then plotted versus collection date, as seen in Figures 5.22 and 5.23, respectively, to compare the section pressures as well as check for any indications of distress.

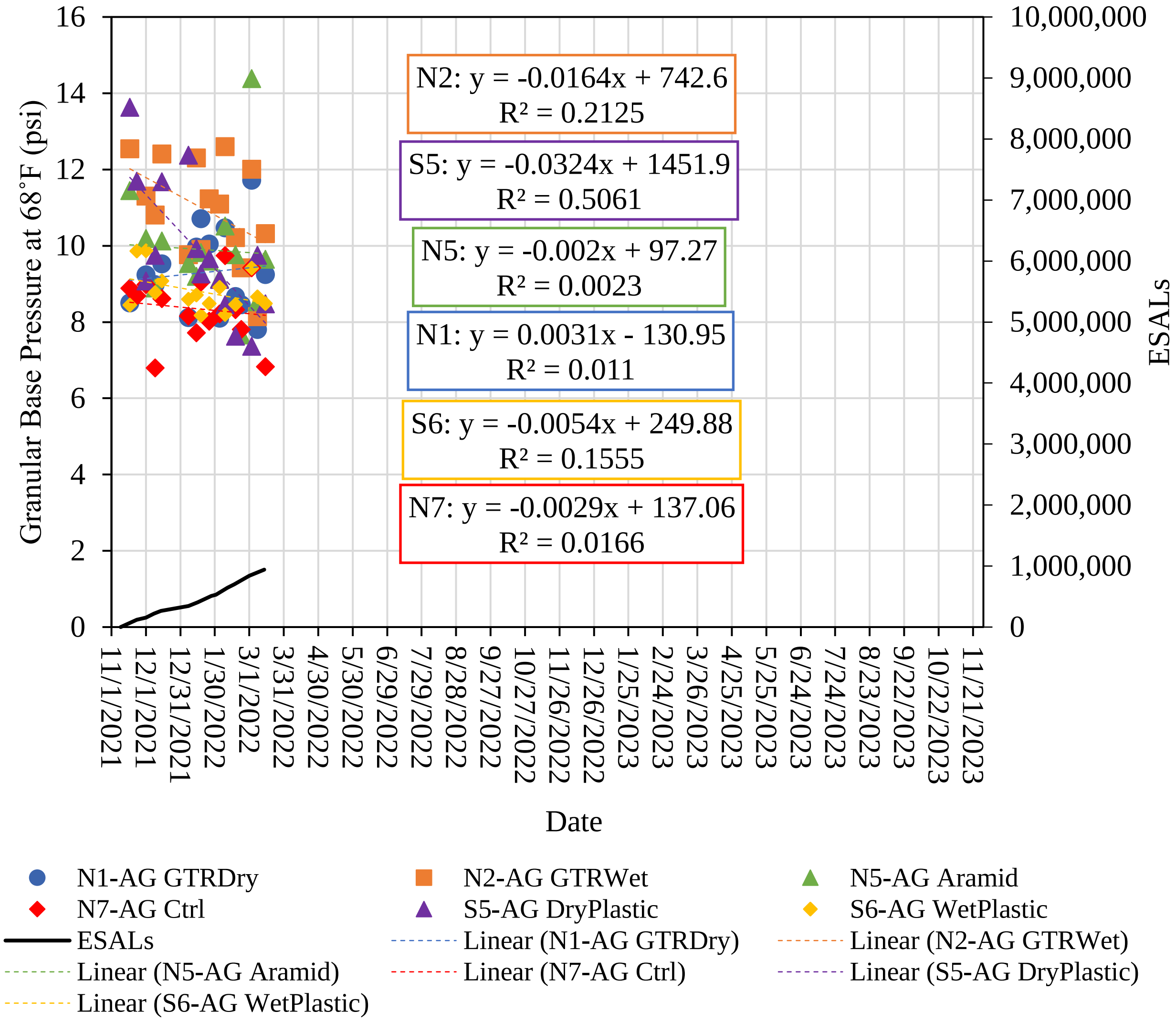

Figure 5.22: Temperature Corrected GB Pressure Versus Date

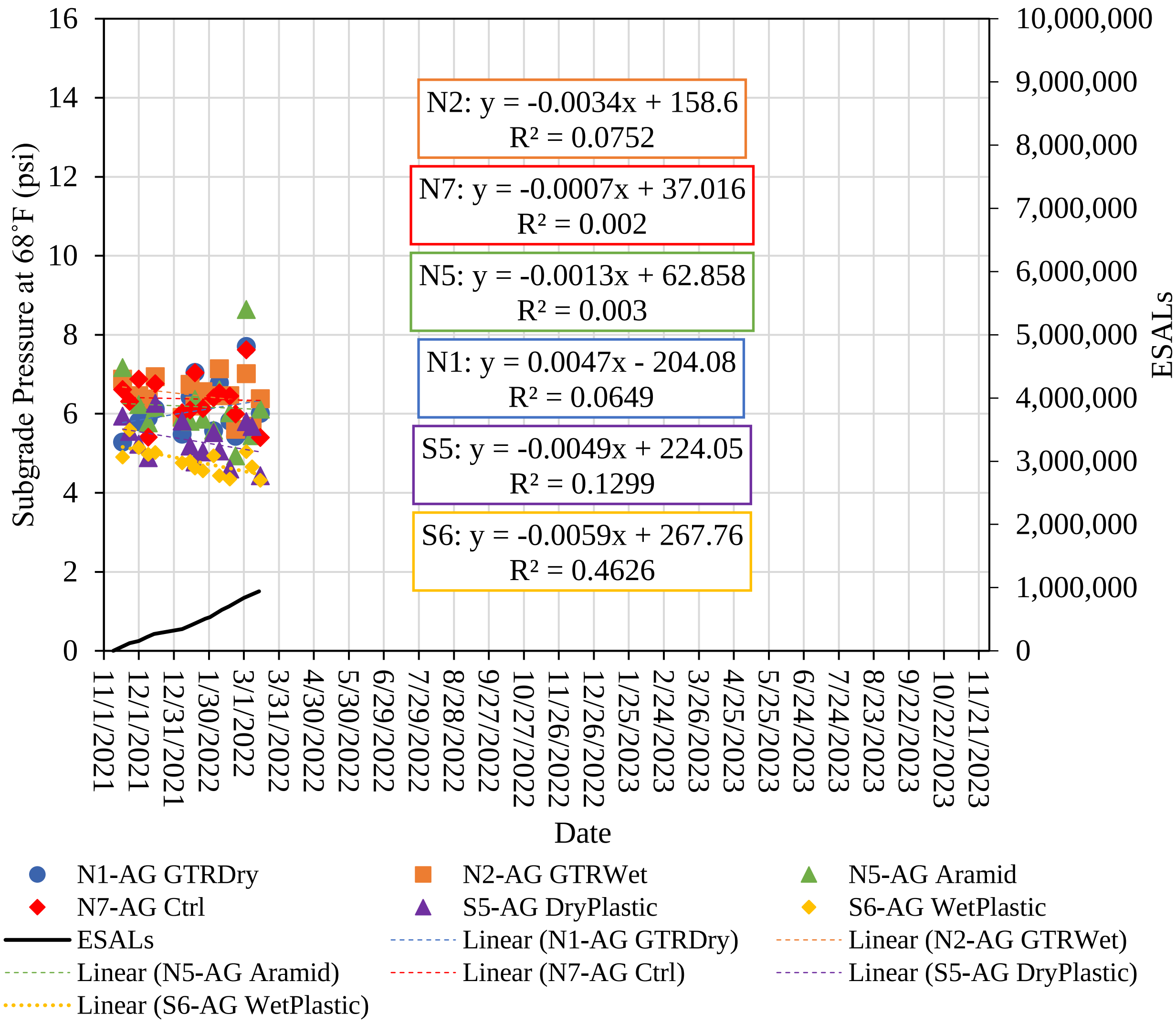

Figure 5.23: Temperature Corrected Subgrade Pressure Versus Date

From the figures, most of the sections' GB and subgrade pressures remained relatively constant or slightly decreased over time, which is a sign of good structural health. However, the GB pressure of the S5-DryPlastic section decreased at a higher rate and had a larger R^2 value than the rest of the sections. The trend is not observed in the subgrade pressure, though, so the reason for it is not yet known. The data should be monitored further and observed closely to see if the trend in GB pressure continues. It should also be noted from the previous figures as well as Figures 5.24 and 5.25, which show graphs of the GB and subgrade pressure means and error bars at one standard deviation, that the sections all experienced similar pressures. No obvious groupings are visible.

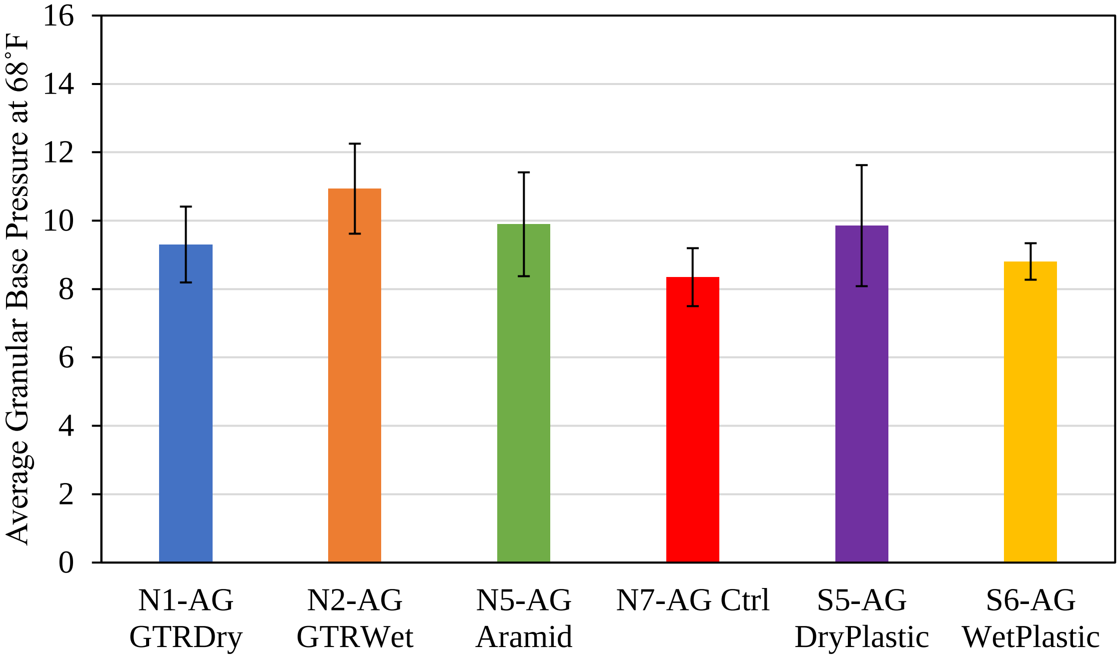

Figure 5.24: Average Temperature Corrected GB Pressure By Section

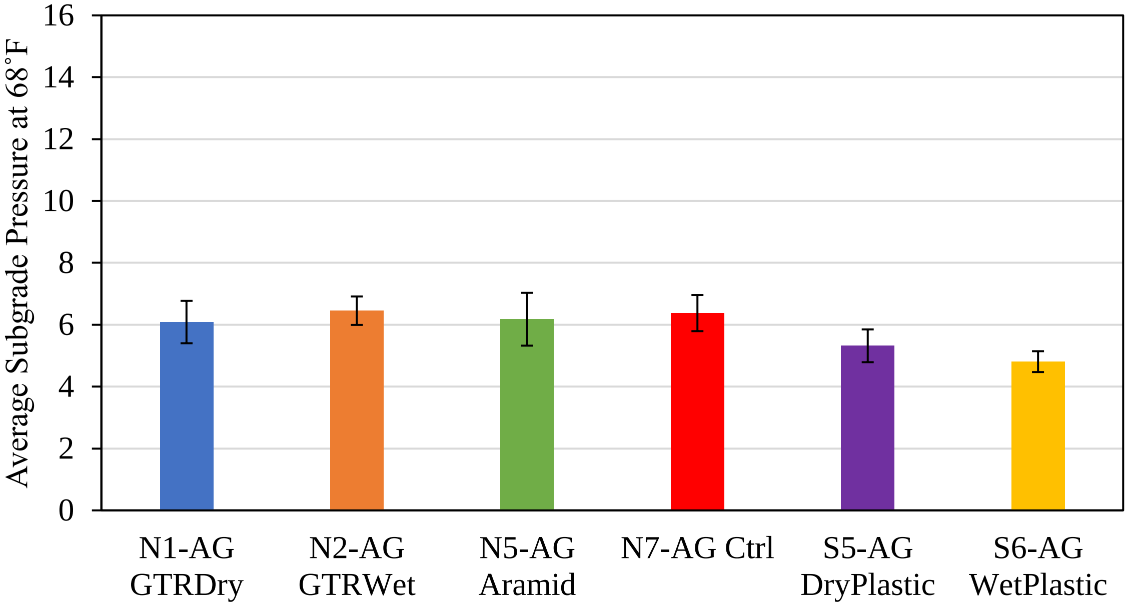

Figure 5.25: Average Temperature Corrected Subgrade Pressure By Section

From analyzing strain and pressure data, it was determined that strain values needed to be corrected for thickness and temperature, while pressure values only needed to be corrected for temperature. When corrected strain and pressure values were plotted versus time, it was found that the sections remained steady. Also, obvious groups were observed and proven to exist in the strain versus time plots. The mean strain of the N1-GTRDry and N2-GTRWet, N7-Ctrl and S5-DryPlastic, N7-Ctrl and S6-WetPlastic, and S5-DryPlastic and S6-WetPlastic sections are significantly the same. It was also determined that the N1-GTRDry and N2-GTRWet sections had the highest strains, while the N7-Ctrl section had the lowest strains.

5.3.2 FWD Data Analysis Methods and Results

The moduli of the pavement section layers were also used to evaluate the structural health of the AG Experiment sections. If modulus values decrease considerably over time, cracking may soon occur or has already begun.

For the modulus analysis presented in this thesis, only load levels between 8,000 lb and 10,000 lb were utilized. Also, backcalculation results with a RMSE of less than 3% were used to ensure that only valid modulus data would be analyzed. The calculated moduli for the AG Experiment sections did not need to be corrected for thickness, as depths were surveyed at each FWD drop location and used during the backcalculation process. However, as seen in Figure 5.24, the modulus values do vary with time where the beginning of seasonal trends in the data can be seen, even though the timeframe is relatively short. As temperatures drop in the winter, the AC layer modulus increases or becomes stiffer. And it is expected that as temperatures increase in the spring and summer, the AC layer modulus will decrease or become softer. So, it is necessary to correct the modulus values for temperature to see any signs of pavement distress over time.

Plotting the data for the N7-Ctrl section from Figure 5.26 versus temperature in Figure 5.27 clearly shows that the measured moduli vary exponentially with temperature. This was done for each section and the exponential regression coefficients were determined and documented for via the same process outlined earlier in this chapter and can be found in Table 5.5. From the table, it is evident that the N5-Aramid section has the largest k_2 value and is therefore the most sensitive to temperature, while the S5-DryPlastic section has the smallest k_2 value and is therefore the least sensitive to temperature. This is different from the determination made from the microstrain k_2 values. However, the R^2 values are greater in this instance, meaning that the data are better represented by the trendlines. More data needs to be analyzed to make conclusions, but the high R^2 values for the AC layer modulus k_2 values lend credibility to the N5-Aramid and S5-DryPlastic sections being the most and least temperature dependent, respectively.

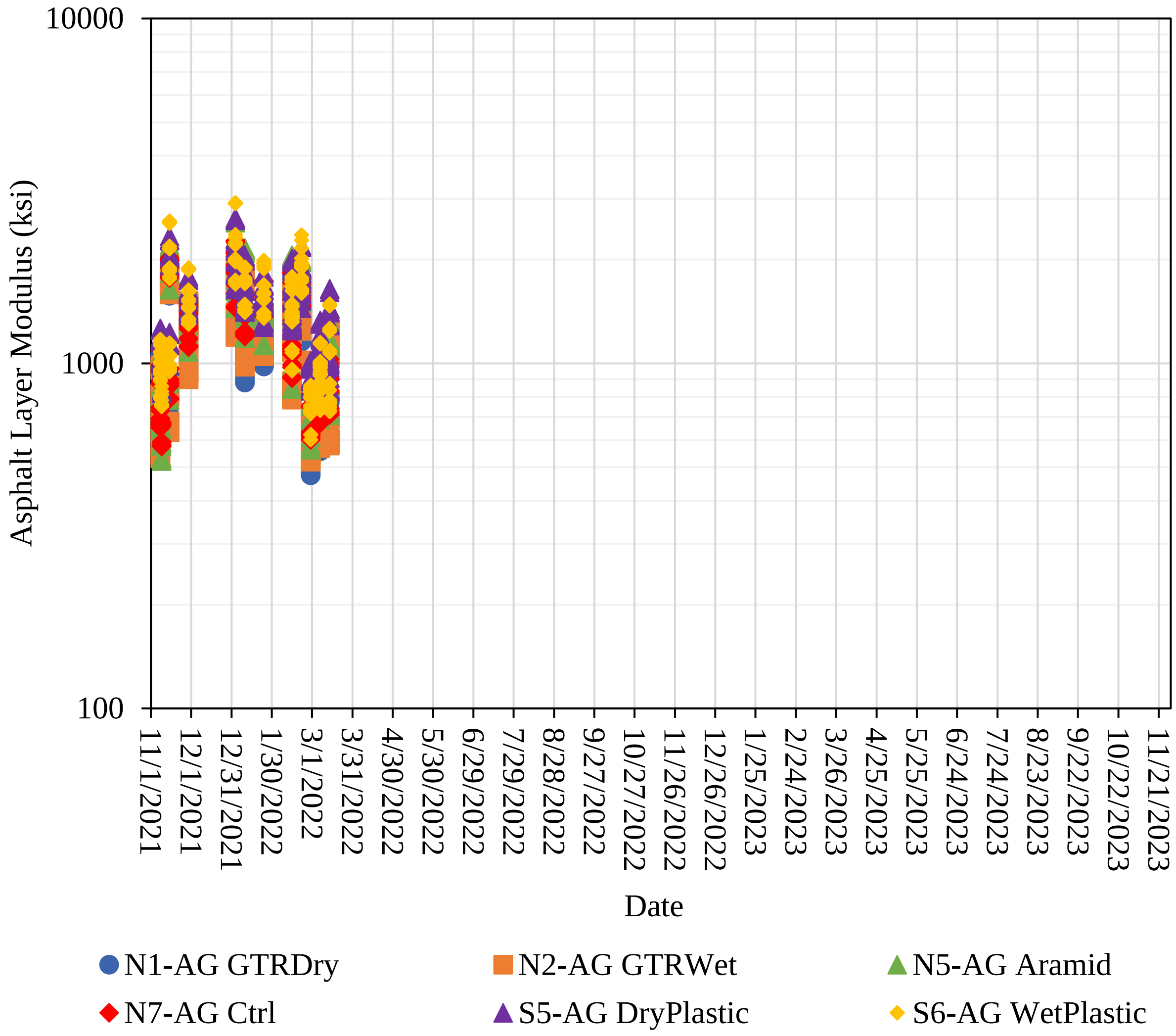

Figure 5.26: Asphalt Modulus Versus Date

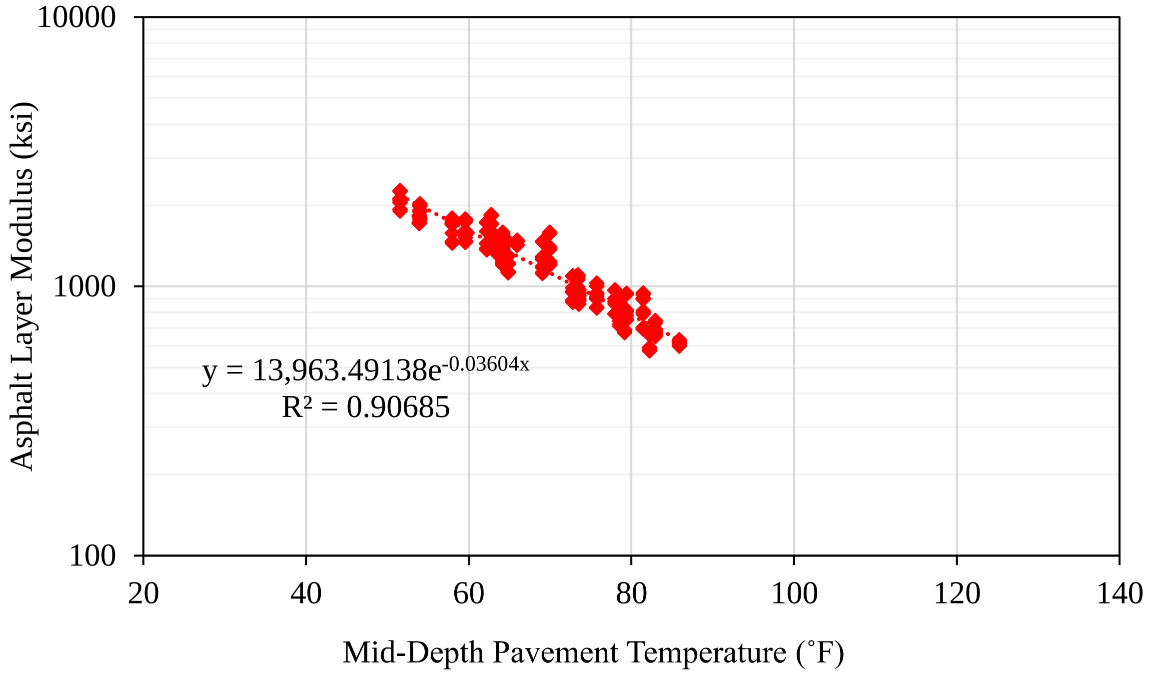

Figure 5.27: N7-Ctrl Asphalt Modulus Versus Temperature

Table 5.5: Asphalt Modulus Versus Temperature Exponential Regression Coefficients

Section and Description	**k_1**	**k_2**	**R^2**
N1-AG GTRDry	10993.09	-0.0369	0.93
N2-AG GTRWet	11299.84	-0.0372	0.91
N5-AG Aramid	14548.90	-0.0374	0.91
N7-AG Ctrl	13963.49	-0.0360	0.91
S5-AG DryPlastic	9376.65	-0.0277	0.89
S6-AG WetPlastic	12355.27	-0.0329	0.85

Once the exponential regression coefficients were determined, temperature correction to 68˚F commenced using the exact same process as with strain and pressure, except the equations involved modulus values. Figure 5.28 shows the uncorrected and temperature corrected AC layer modulus values for the N7-Ctrl section. The flat trendlines and low R^2

value shows that the temperature corrected modulus values do not vary with temperature, which was intended and expected.

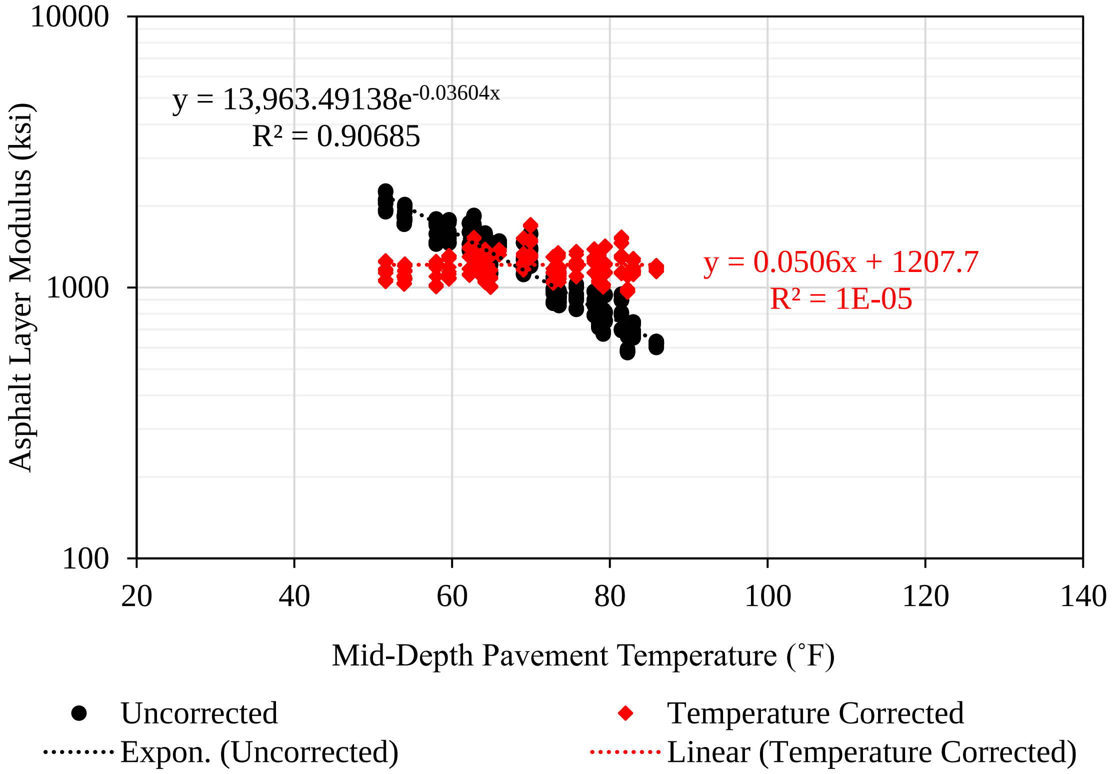

Figure 5.28: N7-Ctrl Section Uncorrected and Temperature Corrected Asphalt Modulus Versus Temperature

The temperature corrected AC layer modulus values were then plotted versus collection date, as seen in Figure 5.29, to compare the section moduli as well as check for any indications of distress. As seen in the figure, all the sections have modulus values that are steady and R^2 values that are relatively low. This indicates that the sections are not changing over time, which is a sign of good structural health.

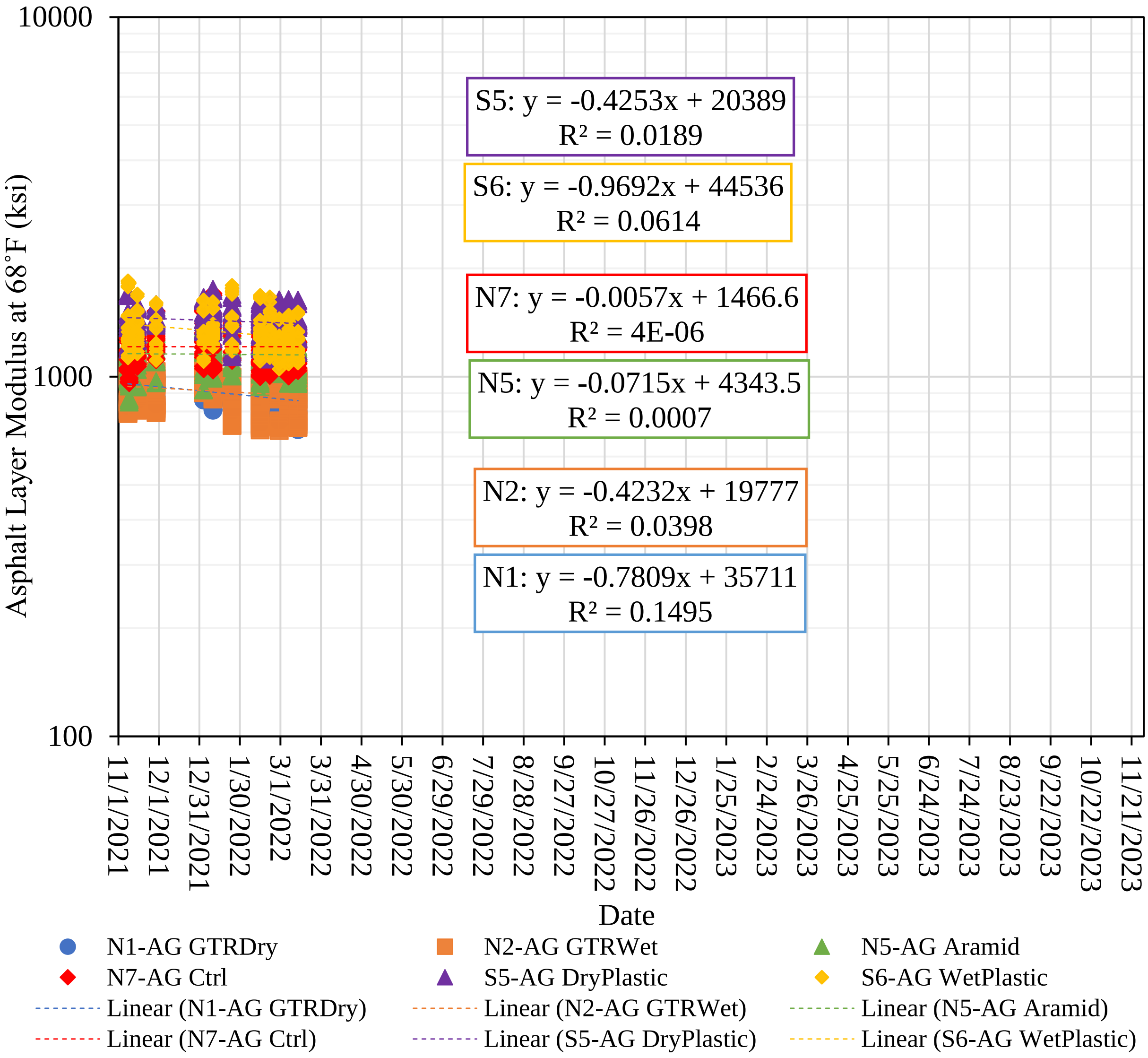

Figure 5.29: Temperature Corrected Asphalt Modulus Versus Date

It was also noted that the S5-DryPlastic section had the greatest modulus values, while the N1-GTRDry and N2-GTRWet sections had the lowest. A high S5-DryPlastic section modulus was expected, as it was presented in Chapter 2 that a potential concern of PCR plastic additives was that they would cause the mixture to be extremely stiff. Low N1-GTRDry and N2-GTRWet section moduli were also expected since the sections also had the highest strain values. From similar reasoning, the N7-Ctrl section should have a high modulus. Its modulus is high, but it is ranked only third highest when compared to the other sections, which was unexpected given that the N7-Ctrl section had the greatest compacted density and the lowest strain values. The strain and modulus data should continue to be monitored to further investigate the structural behavior of this section.

Figure 5.29 also shows fairly distinct grouping of the various AG Experiment sections in terms of modulus. By visual inspection, it appears that the N1-GTRDry and N2-GTRWet sections have similar moduli. It is also possible that the N5-Aramid and N7-Ctrl sections and the S5-DryPlastic and S6-WetPlastic sections have similar moduli. The same statistical analyses that were discussed earlier in this chapter were performed on the modulus data to further investigate the modulus groupings. Again, comprehensive statistical analysis information can be found in Appendix F. However, Table 5.6 presents a summary of the statistical results. From the ANOVA analysis, the resulting p-value was 0, meaning that the null hypothesis was rejected. Therefore, the mean values of the temperature corrected moduli are not all equal. Further analysis in the form of a Tukey-Kramer multiple comparison test was warranted to compare the means of each section's modulus values to that of each of the other sections. This analysis yielded that the p-value for the N1-GTRDry and N2-GTRWet section hypothesis pair was greater than α. So, the null hypothesis was not rejected, and the mean values of the temperature corrected modulus are statistically the same within the pair. Figure 5.30 shows a graph of the means as well as the statistically determined section groupings. Error bars are also shown at one standard deviation. The conclusions from this statistical analysis confirm what was visually seen in the modulus data.

Table 5.6: AC Layer Modulus Statistical Results

Statistical Test	p-value
ANOVA	0.00000
Tukey-Kramer: N1-AG GTRDry, N2-AG GTRWet	0.90044

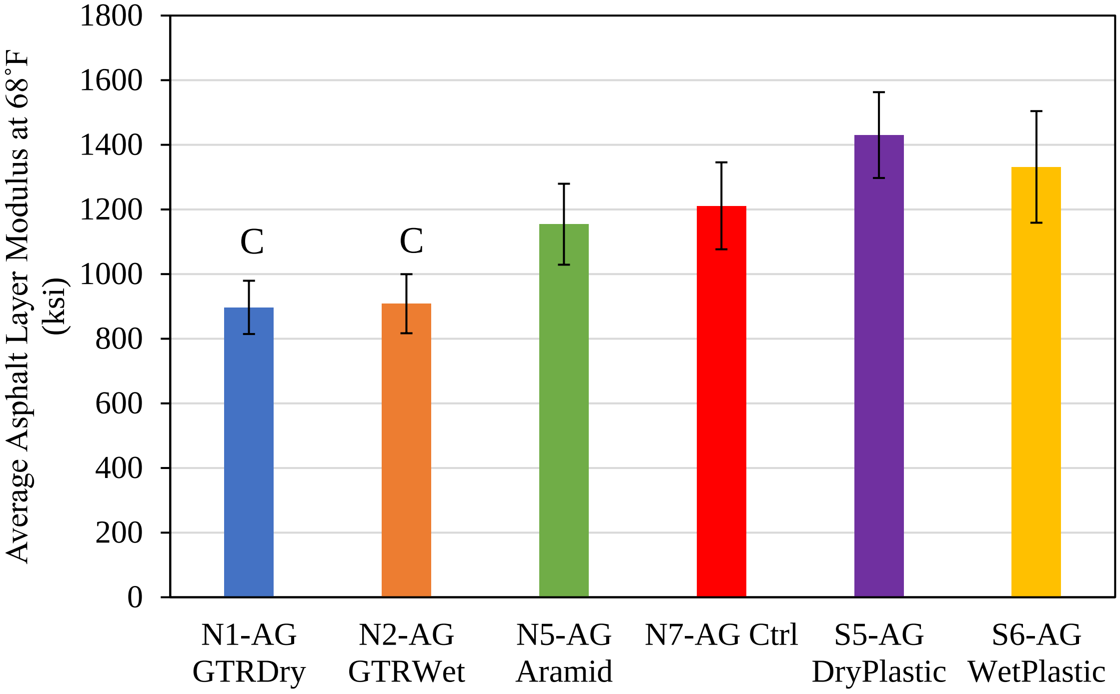

Figure 5.30: Average Temperature Corrected Moduli By Section

The temperature corrected modulus data was also analyzed by wheelpath, but no trends were revealed in the data. This is supported by the fact that the coefficient of variation (COV) values for the section moduli, which are presented in Table 5.7, are all 13 percent or less.

Table 5.7: AC Layer Modulus COV Values

Section and Description	COV
N1-AG GTRDry	9%
N2-AG GTRWet	10%
N5-AG Aramid	11%
N7-AG Ctrl	11%
S5-AG DryPlastic	9%
S6-AG WetPlastic	13%

The moduli of the GB and Subgrade layers were also analyzed to evaluate the structural behavior of the layers for the AG Experiment sections. Figure 5.31 shows the N7-Ctrl section

GB modulus versus temperature, and Figure 5.32 shows the N7-Ctrl section Subgrade modulus versus temperature. From the figures, it is evident that the layers do not vary with temperature, so a temperature correction is not necessary.

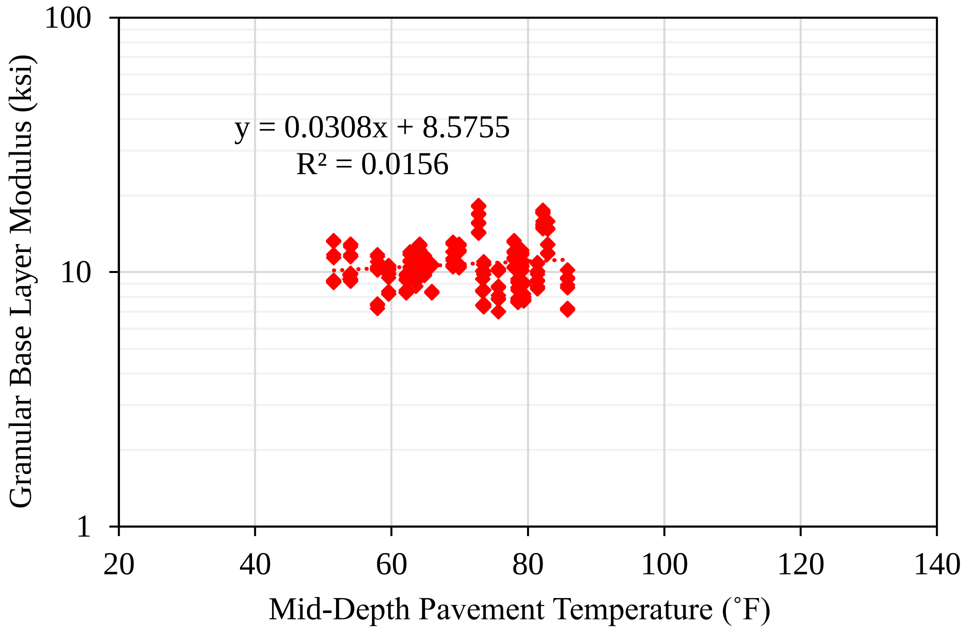

Figure 5.31: N7-Ctrl Section GB Modulus Versus Temperature

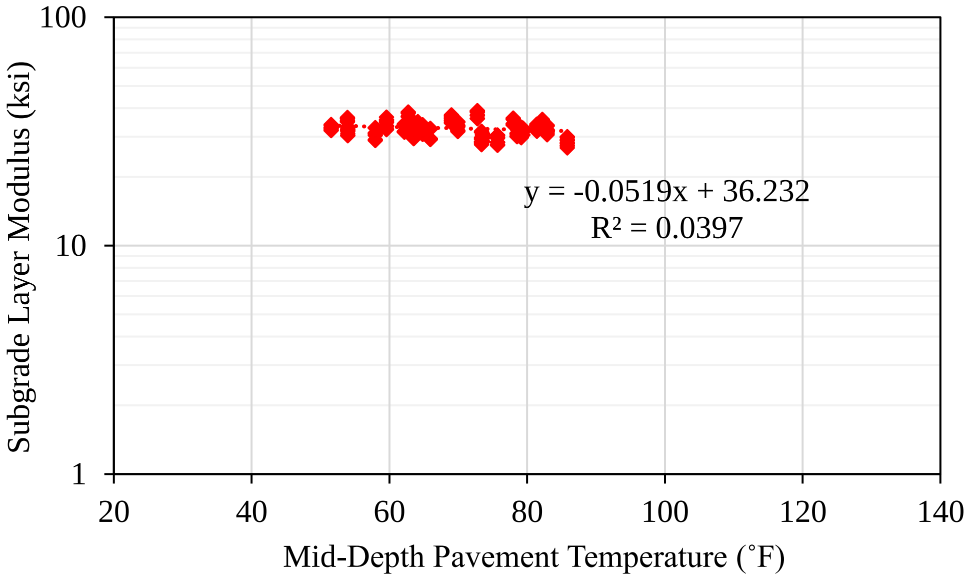

Figure 5.32: N7-Ctrl Section Subgrade Modulus Versus Temperature

The GB and subgrade layer moduli were then plotted versus date, as seen in Figures 5.33 and 5.34, respectively, to compare the section moduli as well as check for any indications of distress.

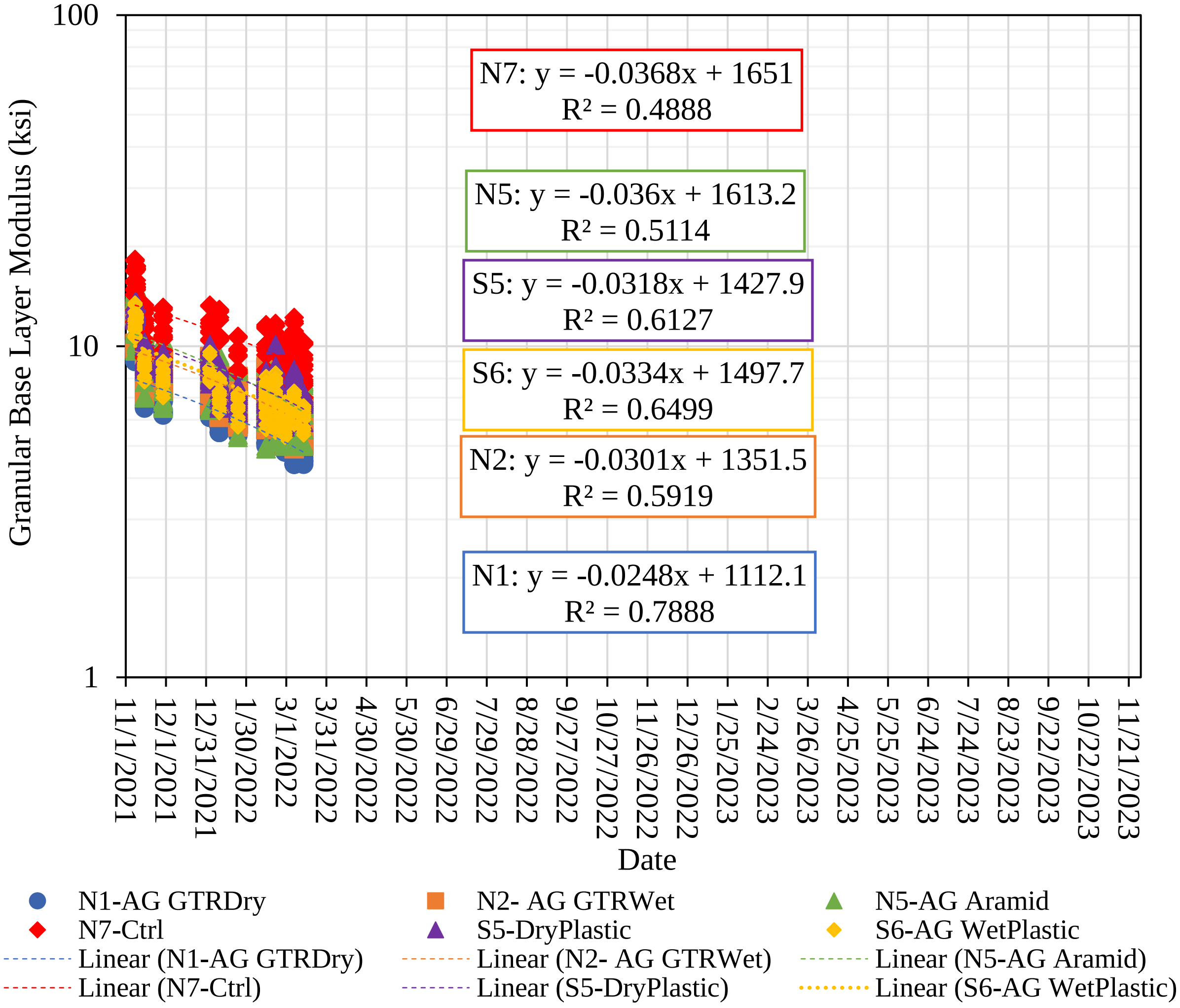

Figure 5.33: Granular Base Layer Modulus Versus Date

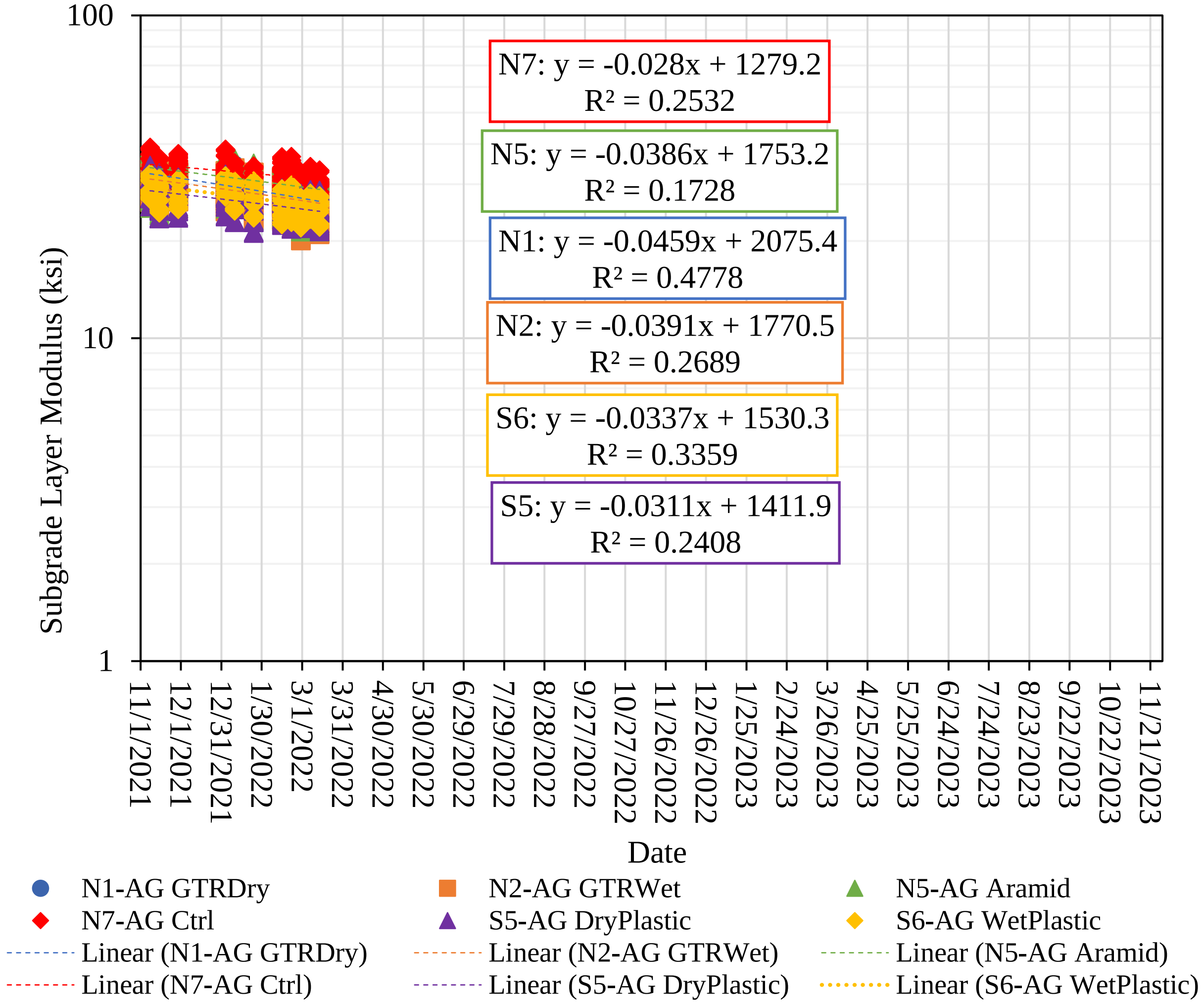

Figure 5.34: Subgrade Layer Modulus Versus Date

From the figures, it is evident that all the section layer modulus values are similar to each other. However, in Figure 5.33, the N7-Ctrl section has a slightly higher modulus, and the N1-GTRDry section has a slightly lower modulus. The same statistical analyses that were discussed earlier in this chapter were performed on the GB layer modulus data to further investigate the potential groupings. Again, comprehensive statistical analysis information can be found in Appendix F. However, Table 5.8 presents a summary of the statistical results. From the ANOVA analysis, the resulting p-value was 0, meaning that the null hypothesis was rejected. Therefore, the mean values of the GB layer moduli are not all equal. Further analysis in the form of a Tukey-Kramer multiple comparison test was warranted to compare the means of each section's GB layer modulus values to that of each of the other sections.

This analysis revealed that the p-values for the N2-GTRWet and S6-AG WetPlastic section and the N5-AG Aramid and S5-AG DryPlastic section hypothesis pairs were greater than α. So, the null hypothesis was not rejected, and the mean values of the GB layer modulus are statistically the same within each pair. Figure 5.35 shows a graph of the means as well as the statistically determined section groupings. Error bars are also shown at one standard deviation. The conclusions from this statistical analysis confirm what was visually seen in the modulus data. The N7-Ctrl and N1-GTRDry sections are both significantly different in terms of GB modulus means from the rest of the sections. These differences could possibly be due to construction variances.

Table 5.8: GB Layer Modulus Statistical Results

Statistical Test	p-value
ANOVA	1.7986E-159
Tukey-Kramer: N2-AG GTRWet, S6-AG WetPlastic	0.707801
Tukey-Kramer: N5-AG Aramid, S5-AG DryPlastic	0.944251

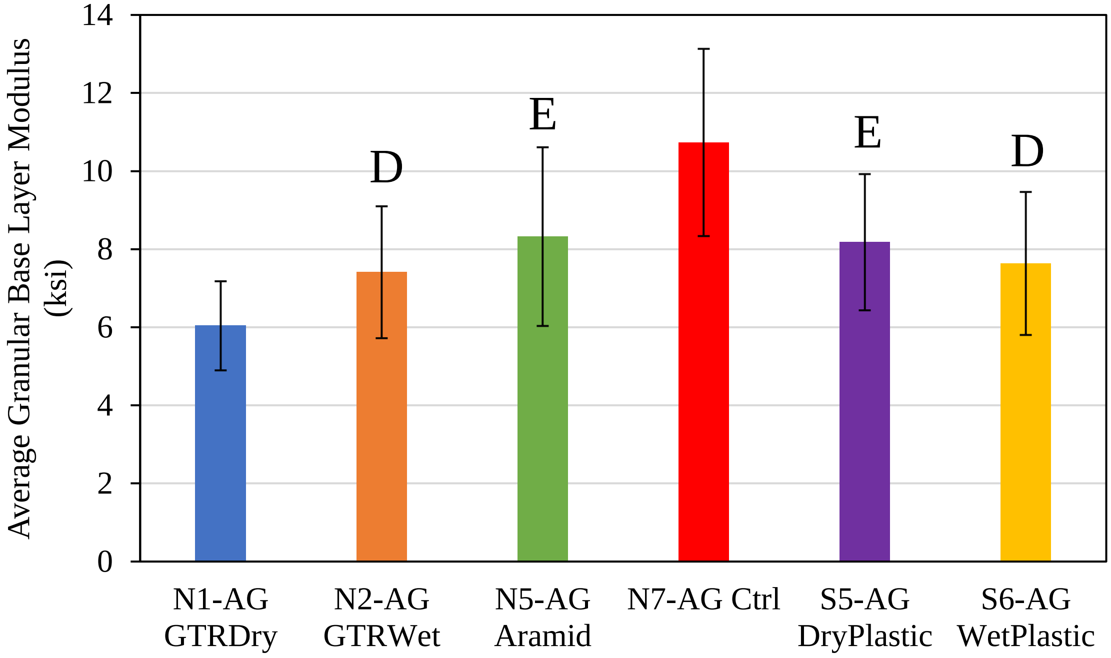

Figure 5.35: Average GB Layer Moduli By Section

It should also be noted that all the GB moduli are around 10 ksi, and all the Subgrade moduli are around 30 ksi. It is typical for the modulus to decrease with depth, as the deeper pavement layers usually do not have better structural capacity. However, the reverse of this is seen in Test Track data for years. The subgrade material that is native to the Test Track has great structural capacity (Taylor and Timm, 2009).

Even though obvious groupings in the subgrade layer modulus values were not seen, the same statistical analyses that were discussed earlier in this chapter were performed on the subgrade layer modulus data to investigate potential groupings. Again, comprehensive statistical analysis information can be found in Appendix F. However, Table 5.9 presents a summary of the statistical results. From the ANOVA analysis, the resulting p-value was essentially 0, meaning that the null hypothesis was rejected. Therefore, the mean values of the subgrade layer moduli are not all equal. Further analysis in the form of a Tukey-Kramer multiple comparison test was warranted to compare the means of each section's subgrade layer modulus values to that of each of the other sections. This analysis revealed that the p-values for the N1-GTRDry and N2-GTRWet section hypothesis pair was greater than α. So, the null hypothesis was not rejected, and the mean values of the subgrade layer modulus are statistically the same within the pair. Figure 5.36 shows a graph of the means as well as the statistically determined section grouping. Error bars are also shown at one standard deviation. The conclusions from this statistical analysis mostly confirm what was visually seen in the modulus data, with the exception being that the N1-GTRDry and N2-GTRWet section means are statistically the same.

Table 5.9: Subgrade Layer Modulus Statistical Results

Statistical Test	**p-value**
ANOVA	7.7865E-146
Tukey-Kramer: N1-AG GTRDry, N2-AG GTRWet	0.129648

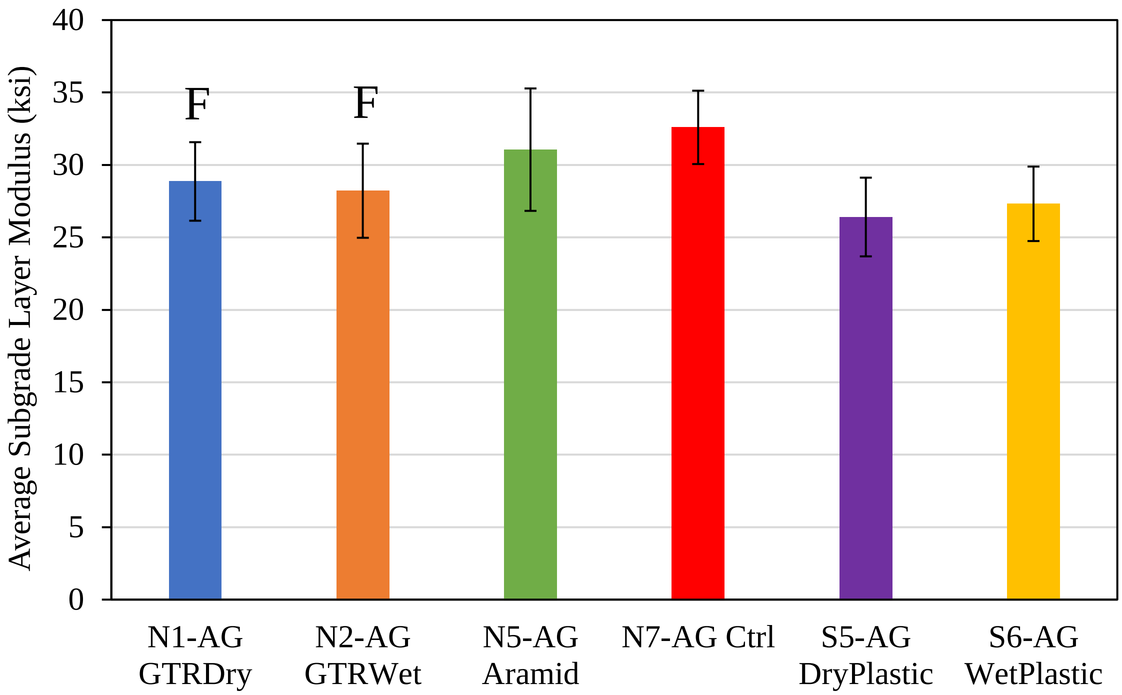

Figure 5.36: Average Subgrade Layer Moduli By Section

From analyzing modulus data, it was determined that the AC layer moduli needed to be corrected for temperature, while the GB and subgrade layer moduli did not need to be corrected at all. When the moduli were plotted versus time, it was found that the sections remained steady. Also, obvious groups were observed and proven in the AC layer modulus versus time plot and the GB layer modulus versus time plot. The mean AC layer modulus of the N1-GTRDry and N2-GTRWet sections are significantly the same. Also, the GB layer modulus of the N2-GTRWet and S6-AG WetPlastic sections and the N5-AG Aramid and S5-AG DryPlastic sections are significantly the same. Obvious groups were not observed in the subgrade layer modulus versus time plot, but the N1-GTRDry and N2-GTRWet section subgrade modulus values were nonetheless proven to be significantly the same. It was also determined that the N1-GTRDry and N2-GTRWet sections had the lowest AC layer modulus, while the N7-Ctrl section had the highest AC layer modulus.

5.4 Comparing Strain and Modulus Results

The next step that was taken to structurally characterize the AG Experiment sections was to compare the AC layer microstrain and modulus values. Theoretically, the parameters should correlate. As modulus increases, microstrain should decrease. So, the average thickness and temperature corrected microstrain values were plotted against the average temperature corrected modulus values, as seen in Figure 5.37. From the figure, it is clear that the theory holds based on the high R^2 value from the linear trendline.

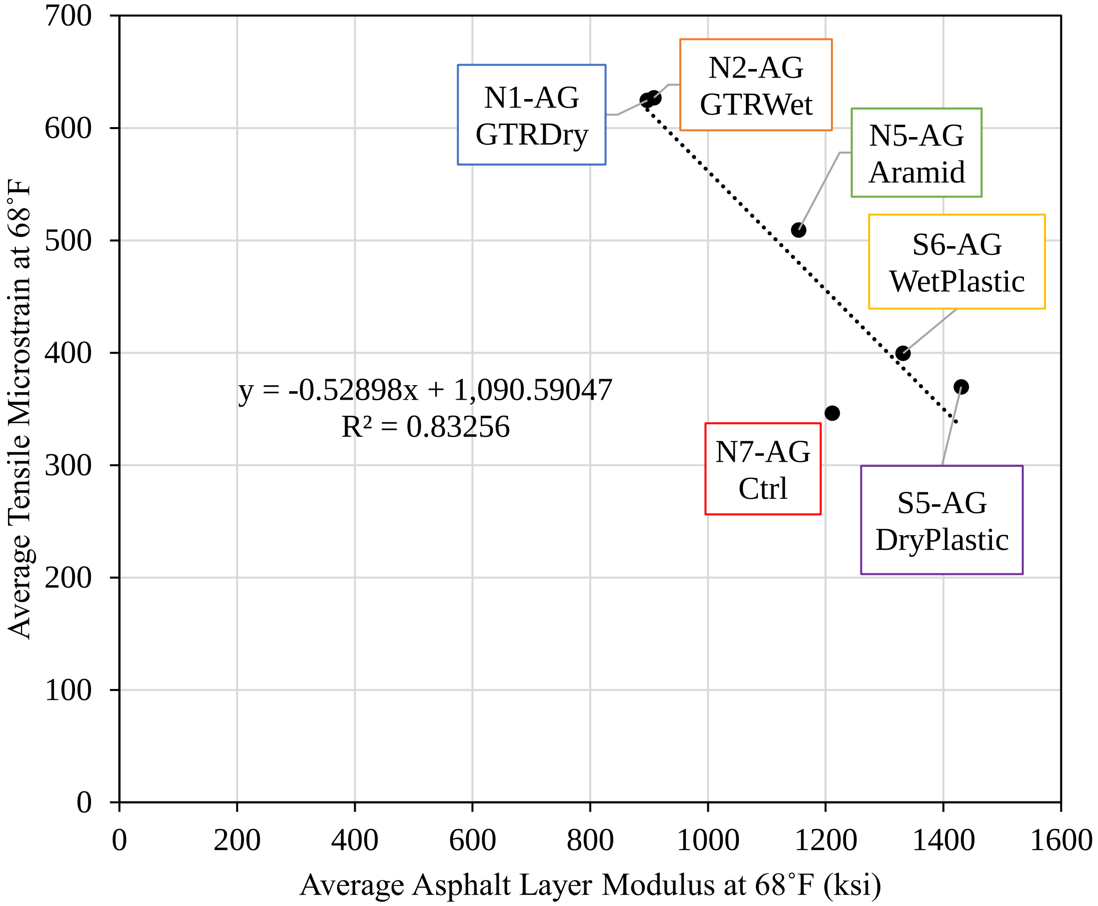

Figure 5.37: Field Measured Average Microstrain Versus Average Modulus

The R^2 value could have been higher, though, if the N7-Ctrl section was not acting as an outlier. The most obvious explanation for the section acting as an outlier was the fact that it had slightly greater GB and Subgrade moduli than the rest of the sections. So, it was necessary to determine if this behavior could be predicted and replicated. The WESLEA for Windows program was used to run simulations of the various in-situ AG Experiment sections to determine predicted strain values. The cross sections that were used in the simulations are summarized in Table 5.10. The average height of the N7-Ctrl section AC layer in the ASG gauge array was used for all sections since thickness corrections could not be applied to the strains. Figure 5.38 shows the resulting predicted average strain values versus the average modulus values. It is important to note that field measured strain values are usually higher than predicted, which is likely due to the prevalence of strain mode reversal in the field, so the values should only be compared relative to each other.

Table 5.10: WESLEA Simulation Cross Section Summary

Section and Description	E_{AC} (psi)	H_{AC} (in)	E_{GB} (psi)	H_{GB} (in)	E_{subg} (psi)
N1-AG GTRDry	896,978	5.53	6,038	22.00	28,861
N2-AG GTRWet	908,314	5.53	7,410	22.04	28,220
N5-AG Aramid	1,154,264	5.53	8,323	21.98	31,055
N7-AG Ctrl	1,211,224	5.53	10,711	21.99	32,655
S5-AG DryPlastic	1,430,165	5.53	8,179	22.02	26,406
S6-AG WetPlastic	1,331,590	5.53	7,635	21.97	27,317

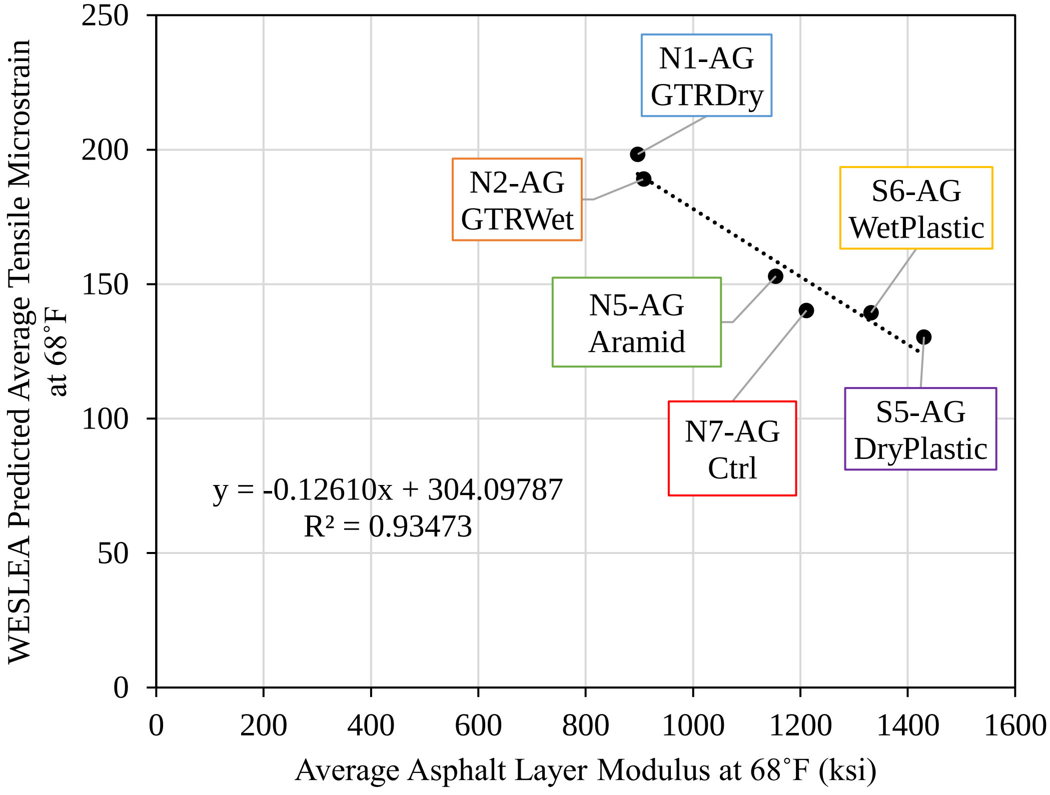

Figure 5.38: WESLEA Predicted Average Microstrain Versus Average Modulus

From the figure, it is evident that N7-Ctrl acting as a more significant outlier was not predicted, based on the extremely high R^2 value. This means that the field measured strain for the N7-Ctrl section was lower than the strain of the other sections than predicted. The reason for this is not yet known and should be investigated further. It could be that further monitoring through the entire temperature regime will resolve this issue.

5.5 Summary

To evaluate the structural health of the various asphalt additive modified sections in the AG Experiment over the timeframe and temperature range, the sections were subjected to an early field performance and structural characterization analysis. Stress and strain measurements at the top of the GB and subgrade layers as well as at the bottom of the AC layer were collected and recorded weekly via EPCs and ASGs, respectively. Modulus values were also determined for the sections' different layers via FWD field testing multiple times per month.

An early structural behavior analysis was performed on the field-measured data. But to fairly compare microstrain values of the various AG Experiment sections, they had to first be corrected for thickness. With the same goal in mind, it was also determined that microstrain, pressure, and AC layer modulus needed to be corrected for temperature. Once all corrections were completed, microstrain values were plotted against time. This revealed that the sections remained steady in terms of strain as time passed and that some sections behaved statistically similarly. These included: N1-GTRDry and N2-GTRWet sections and N7-Ctrl, S5-DryPlastic, and S6-WetPlastic sections. It was also found that N1-GTRDry and N2-GTRWet had the highest strains and that N7-Ctrl had the lowest strains. The GB and Subgrade pressure data were also analyzed and determined to have remained relatively constant with time. AC layer modulus was then plotted versus time. This revealed that the sections remained steady in terms of modulus as time passed and that two sections, N1-GTRDry and N2-GTRWet, behaved similarly. It was also determined that the two sections had the lowest modulus values, which was expected due to them also having the highest strains. However, it was also expected that N7-Ctrl would have the highest modulus, but analysis showed that it only had the third highest of the sections. The modulus of the GB and subgrade layers was also analyzed and determined to have remained relatively constant with time. One important discovery was the fact that the N7-Ctrl section had the highest GB modulus, though. The average GB moduli for the N7-Ctrl and N1-GTRDry sections were both found to be significantly different than the other sections. Also, the N1-GTRDry and N2-GTRWet sections were shown to have average subgrade modulus values that were statistically the same.

The AC layer strain and modulus values were then compared to each other to verify that as modulus increased, strain decreased. The correlation was found to be strong, however, the R^2 was lower than it could have been due to the N7-Ctrl section acting as an outlier of sorts. The initial thought was that the section's greater GB modulus differentiated it too much from the rest of the sections. So, the AG Experiment section in-field cross sections were simulated in WELSEA to determine whether the outlier behavior could be predicted and replicated. The results determined that the behavior was not predicted, which indicated that the field strains experienced by N7-Ctrl were lower than the rest of the sections than predicted. The reasons for this are not yet known. It is recommended to continue to monitor this section as well as the rest of the AG Experiment sections and complete further structural analysis once more data is collected.

CHAPTER 6

Conclusions and Recommendations

Full-scale construction of the Additive Group experiment allowed for various field measurements, such as percent cracking, rut depth, roughness, strain, pressure, and layer modulus, to be documented or determined for the sections. The field values were then used to conduct early surface performance evaluations as well as early structural behavior characterizations. Comparisons were also made between the additive modified sections' performance and behavior to those of the control section to determine whether the asphalt additives studied are viable alternatives to the conventional SBS polymer used in the control section. Based on the data presented in this thesis, the following conclusions and recommendations are made.

6.1 Conclusions

To monitor the surface performance of the sections due to accelerated trafficking and time, cracking, rutting, and roughness measurements were collected for the sections. At this point, it may be concluded that all the sections are exhibiting excellent performance through the first several months and approximately 1 million ESALs of trafficking. From visual inspection and an automated crack imaging system, it was determined that none of the AG Experiment sections showed signs of cracking during the timeframe. Minimal rutting was observed in the sections. This was not alarming, though, as slight initial rutting is expected, the rutting in all sections increased at roughly the same rate, and all rutting in the sections was well below the commonly used failure threshold of 0.5 inches. The rut depths for the N2-GTRWet section are greater than the other sections, though, which could possibly be due to it having more binder in the mix. The AC layer modulus of this section was computed and analyzed against the other sections to see whether it has a lower value than the rest because this could also be a reason for the higher rutting values. This analysis is discussed in the next paragraph. The International Roughness Index (IRI) parameter measurements were different for the sections in that most showed that roughness decreased slightly, while others (Ctrl and DryPlastic sections) showed slightly increasing roughness as time progressed and traffic was applied. Slight decreases in IRI are expected since applied traffic wears down the surface texture of pavements. Therefore, any increase in roughness is interesting, as it could imply that the pavement is experiencing a distress of some sort. However, no cracking or extreme rutting was observed in the two sections with slightly increasing IRI, so the reason for it is not yet known. Since the R^2 values are all relatively low, it is likely that as more IRI data is collected, the slopes will fluctuate and potentially change signs, which would reverse the interpretation of the data.

To monitor the structural behavior of the sections due to accelerated trafficking, time, and temperature, strain, pressure, and layer modulus values were measured or determined for the sections. From an early structural behavior analysis, it was concluded that the sections remained steady (and healthy) in terms of strain as time passed and that some sections behaved similarly. These included: N1-GTRDry and N2-GTRWet sections and N7-Ctrl, S5-DryPlastic, and S6-WetPlastic sections. It was also found that N1-GTRDry and N2-GTRWet had the highest strains and that N7-Ctrl had the lowest strains. The GB and Subgrade pressure data were also analyzed and determined to have remained relatively constant with time. The plotting of AC layer modulus versus time revealed that the sections remained steady (and healthy) in terms of modulus as time passed and that two sections, N1-GTRDry and N2-GTRWet, behaved similarly. It was also determined that the two sections had the lowest modulus values, which was expected due to them also having the highest strains. However, it was also expected that N7-Ctrl would have the highest modulus, but analysis showed that it only had the third highest of the sections. The modulus of the GB and subgrade layers was also analyzed and determined to have remained relatively constant with time. It is important to note that the N7-Ctrl section had the highest GB modulus, though. The average GB moduli for the N7-Ctrl and N1-GTRDry sections were both found to be significantly different than the other sections. Also, the N1-GTRDry and N2-GTRWet sections were shown to have average subgrade modulus values that were statistically the same.

The AC layer strain and modulus values were then compared to each other to verify that as modulus increased, strain decreased. The correlation was found to be strong, however, the R^2 was lower than it could have been due to the N7-Ctrl section acting as an outlier. The initial thought was that the section’s greater GB modulus differentiated it too much from the rest of the sections. So, the AG Experiment section in-situ cross sections were run through

WELSEA to determine whether the outlier behavior could be predicted and replicated. The results determined that the behavior was not predicted, which indicated that the field strains experienced by the N7-Ctrl section were lower than the rest of the sections than predicted. The reasons for this are not yet known but likely will become more evident with continued testing and monitoring through the remaining 9 million ESALs.

6.2 Recommendations

It is recommended to continue monitoring the sections in terms of cracking, rutting, and IRI throughout the research cycle to determine the impact of more time, more traffic, and greater temperature ranges on the sections. The expected mode of failure is bottom-up fatigue cracking, so percent cracking should be given close attention. Also, the IRI values of the N7-Ctrl and S5-DryPlastic sections should be observed carefully to determine the cause of the increased roughness.

It is also recommended to continue to monitor the AG Experiment sections in terms of strain, pressure, and modulus to complete further and possibly more complex structural analysis once more data is collected. Continuations of the structural analyses presented in this thesis should be completed, utilizing more data points and wider temperature ranges. This may help address concerns, such as the unexpected statistical outlier behavior of the N7-Ctrl section, that were raised in this thesis. The FlexPAVE™ software could be utilized to run more sophisticated structural analyses on the as-built AG Experiment cross sections to verify the conclusions presented in this thesis and also address concerns.

Regardless, more field data needs to be collected and time needs to pass to comprehensively characterize the performance of the AG Experiment sections. Also, no cracking has developed in these additive modified pavement sections, which means that the mechanisms behind bottom-up fatigue cracking has not yet been identified for the various additives. So, recommendations on the viability of the additives for use in real-world applications will not be made in this thesis.

6.3 Plans for Future Research

Accelerated trafficking, monitoring, and field data analysis of the AG Experiment sections will continue into Phase IIIb until approximately 10 million ESALs are accumulated. Further laboratory testing of the as-built mixtures will also be completed during Phase IIIb. From the information gathered in all three phases, the additive modified mixtures can continue to be directly compared to a well-known and studied control section and could also be used to calibrate a tool that agencies and contractors may use to efficiently and confidently decide what types of asphalt additives are viable for projects.

REFERENCES

Abdalfattah, I., Mogawer, W., and Stuart, K. “Recycled Polyethylene Modified Asphalt Binders and Mixtures: Performance Characteristics and Environmental Impact”. *Transportation Research Record: Journal of The Transportation Research Board*, January 6, 2022, pp. 1-23. *SAGE Publications*, DOI: 10.1177/03611981211065733.

Alfalah, A., Offenbacker, D., Ali, A., Decarlo, C., Lein, W., Mehta, Y., and Elshaer, M. “Assessment of the Impact of Fiber Types on the Performance of Fiber-Reinforced Hot Mix Asphalt”. *Transportation Research Record: Journal of The Transportation Research Board*, vol 2674, no. 4, March 10, 2020, pp. 337-347. *SAGE Publications*, DOI: 10.1177/0361198120912425.

Alidadi, M. and Khabiri, M. “Experimental Study on The Effect of Glass And Carbon Fibers on Physical And Micro-Structure Behavior of Asphalt”. *International Journal of Integrated Engineering*, vol. 8, no. 3, 2016, pp. 1-8.

"Asphalt Plus". *Asphalt Plus LLC*, 2015. asphaltplus.com/.

Baumgardner, G., Hand, A., and Aschenbrener, T. “Resource Responsible Use of Recycled Tire Rubber in Asphalt Pavements”. *U.S. Department of Transportation Federal Highway Administration*, report no. FHWA-HIF-20-043, April 2020, pp. 1-41.

Bressi, S., Fiorentini, N., Huang, J., and Losa, M. “Crumb Rubber Modifier in Road Asphalt Pavements: State of the Art and Statistics”. *Coatings*, Vol. 9, No. 6, 2019, p. 384.

“Center for Transportation Infrastructure Systems”. *UTEP*, 2021. https://www.utep.edu/engineering/ctis/research/Current%20Research1/TXDOT%20IAC-NTP11.html.

Environmental Protection Agency. “How Do I Recycle? Common Recyclables”. 2018. https://www.epa.gov/recycle/how-do-i-recycle-common-recyclables.

Federal Highway Administration. “FHWA Recycled Materials Policy”. 2015. https://www.fhwa.dot.gov/legsregs/directives/policy/recmatpolicy.htm.

FORTA. “Fiber Reinforced Asphalt Concrete (FRAC) Guide Specification for Highway Construction”. 2017. http://www.forta-fi.com/wp-content/uploads/2017/12/FORTAFI-FRAC-Guide-Specification.pdf

Highway Research Board. *The AASHO Road Test*. Report 5, Pavement Research Special Report 61E, National Academy of Sciences – National Research Council, Washington, DC, 1962.

“Ideal-Ct - Simple, Reliable, Efficient, Repeatable, Cost Effective”. *Texas A&M Transportation Institute,* February 7, 2022, https://tti.tamu.edu/researcher/ideal-ct-simple-reliable-efficient-repeatable-cost-effective/.

Jahromi, S. “Effect of Carbon Nanofiber On Mechanical Behavior Of Asphalt Concrete”. *International Journal of Sustainable Construction Engineering & Technology,* vol 6, no. 2, 2015, pp. 57-66.

Kadolph, S. *Textiles*. Prentice Hall, Upper Saddle River, N.J., 2002.

Kaloush, K., Biligiri, K., Zeiada, W., Rodezno, C., and Reed, J. “Evaluation of Fiber-Reinforced Asphalt Mixtures Using Advanced Material Characterization Tests”. *Journal of Testing and Evaluation*, vol 38, no. 4, 2010, pp. 400-411.

"Liberty Tire Recycling". *Liberty Tire*, 2021. libertytire.com/.

Mahrez, A. and Karim, M. “Fatigue Characteristics of Stone Mastic Asphalt Mix Reinforced with Fiber Glass”. *International Journal of the Physical Sciences*, vol. 5, No. 12, 2010, pp. 1840–1847.

Mahrez, A., Karim, M., and Katman, H. “Fatigue and Deformation Properties of Glass Fiber Reinforced Bituminous Mixes”. *Journal of the Eastern Asia Society for Transportation Studies*, vol 6, 2005, pp. 997-1007.

McCarty, C. “Early Characterization and Performance of A Flexible Thick Lift Pavement”. Master of Science Thesis. Auburn University, Auburn, AL. 2020.

McDaniel, R. “NCHRP Synthesis of Practice 475: Fiber Additives in Asphalt Mixtures”. *Transportation Research Board of the National Academies*, Washington, D.C., March 2015. DOI: 10.17226/22191.

"Micronized Rubber Powder (MRP)". *Lehigh Technologies,* 2022. www.lehightechnologies.com/.

Muftah, A., Bahadori, A., Bayomy, F., and Kassem, E. “Fiber-Reinforced Hot-Mix Asphalt: Idaho Case Study”. *Transportation Research Record: Journal of The Transportation Research Board*, vol 2633, no. 1, January 1, 2017, pp. 98-107. DOI: 10.3141/2633-12.

Mull, M., Othman, A., and Mohammad, L. “Fatigue Crack Propagation Analysis of Chemically Modified Crumb Rubber–Asphalt Mixtures”. *Journal of Elastomers and Plastics*, vol 37, no. 1, January 1, 2005, pp. 73-87. *SAGE Publications*, DOI: 10.1177/0095244305049898.

Musa, N., Aman, M., Shahadan, Z., Taher, M., and Noranai, Z. “Utilization of Synthetic Reinforced Fiber In Asphalt Concrete – A Review”. *International Journal of Civil*

Engineering and Technology (IJCIET), vol 10, no. 5, May 2019, pp. 678-694. IAEME Publication.

Presti, D. “Recycled Tyre Rubber Modified Bitumens for Road Asphalt Mixtures: A Literature Review”. *Construction and Building Materials*, Vol. 49, 2013, pp. 863–881. DOI: 10.1016/j.conbuildmat.2013.09.007.

Rath, P., Majidifard, H., Jahangiri, B., Chen, S., and Buttlar, W. “Laboratory and Field Evaluation of Pre-Treated Dry-Process Rubber-Modified Asphalt Binders and Dense-Graded Mixtures”. *Transportation Research Record: Journal of The Transportation Research Board*, May 10, 2021, pp. 1-14. *SAGE Publications*, DOI: 10.1177/03611981211011480.

"Research Needed on Using Recycled Plastics in Asphalt". 2021. www.eng.auburn.edu/research/centers/ncat/newsroom/2019-fall/plastics.html.

Rivera-Pérez, J., Ozer, H., Lambros, J., and Al-Qadi, I. “Illinois Flexibility Index Test: Effect of Specimen Geometry and Test Configuration on the Asphalt Concrete Damage Zone”. *Journal of Transportation Engineering, Part B: Pavements*, March 2021, pp. 1-14. *American Society of Civil Engineers*, DOI: 10.1061/JPEODX.0000243.

"Scrap Tires in Asphalt". *Asphalt Pavement Association of New Mexico*, 2021. apanm.org/scrap-tires-in-asphalt/.

"SmartMix". *Liberty Tire*, 2021. libertytire.com/our-product/smartmix/.

Souliman, M., Gc, H., Isied, M., Walubita, L., Sousa, J., and Bastola, N. “Mechanistic Analysis and Cost-Effectiveness Evaluation of Asphalt Rubber Mixtures”. *Road Materials and Pavement Design*, Vol. 21, Supplement 1, 2020, pp. S76–S90. DOI: 14680629.2020.1735492.

Tapkin, S. “The Effect of Polypropylene Fibers on Asphalt Performance”. *Building and Environment*, Vol. 43, No. 6, 2008. pp. 1065–1071.

Taylor, A. and Timm, D. “Mechanistic Characterization of Resilient Moduli for Unbound Pavement Layer Materials”. *National Center for Asphalt Technology*, Report No. 09-06, Auburn University, 2009.

Timm, D. “Design, Construction and Instrumentation of the 2006 Test Track Structural Study”. NCAT Report 09-01. February 2009.

Timm, D. “Key Concepts in Dynamic Signal Processing from Instrumented Pavement Sections,” 5th International Conference on Accelerated Pavement Testing, San Jose, Costa Rica, September 19 – 21, 2016.

Timm, D. and Foshee, M. “The Influence of Asphalt/Base Modulus Ratio on Strain Mode Reversal in Flexible Pavements”. International Conference on the Bearing Capacity of Roads, Railways and Airfields (BCRRA), In press, 2022.

Timm, D. and Priest, A. “Flexible Pavement Fatigue Cracking and Measured Strain Response at the NCAT Test Track” *Proceedings of the 87th Annual Transportation Research Board*, Washington, D.C., 2008.

Timm, D. and Tutu, K. "Determination of An Optimum Backcalculation Cross Section for Unconventional Pavement Profiles". *Transportation Research Record: Journal Of The Transportation Research Board*, vol 2641, no. 1, 2017, pp. 48-57. *SAGE Publications*, DOI:10.3141/2641-07.

Timm, D., Yin, F., Tran, N., Foshee, M., and Rodezno, C. “Relative Structural Characterization Methods for Additive-Modified Asphalt Materials”. *Transportation Research Record: Journal of The Transportation Research Board*, In press, 2022.

Vargas-Nordcbeck, A. “Physical and Structural Characterization of Sustainable Asphalt Pavement Sections at the NCAT Test Track”. Doctor of Philosophy Dissertation. Auburn University, Auburn, AL. 2012.

Walker, D. “PASER Asphalt Roads Manual”. *Transportation Information Center – University of Wisconsin-Madison*. 2002, pp. 1-32.

Wang, T., Xiao, F., Zhu, X., Huang, B., Wang, J., and Amirkhanian, S. “Energy Consumption and Environmental Impact of Rubberized Asphalt Pavement”. *Journal of Cleaner Production*, Vol. 180, 2018, pp. 139–158. DOI: 10.1016/j.jclepro.2018.01.086.

Williams, B., Willis, R., and Ross, C. “Asphalt Pavement Industry Survey on Recycled Materials and Warm-Mix Asphalt Usage: 2018”. Information Series 138, 9th edition, September 2019, pp. 1-46. DOI: 10.13140/RG.2.2.22077.61920.

Willis, R. “Use of Ground Tire Rubber in a Dense-Graded Asphalt Mixture on US 231 in Alabama: A Case Study”. *Airfield and Highway Pavement 2013: Sustainable and Efficient Pavements*, July 9, 2013, pp. 1192-1201. DOI: 10.1061/9780784413005.100.

Willis, R., Timm, D., West, R., Powell, B., Robbins, M., Taylor, A., Smit, A., Tran, N., Heitzman, M., and Bianchini, A. “PHASE III NCAT TEST TRACK FINDINGS”. NCAT Report 09-08. Auburn, 2009, http://eng.auburn.edu/research/centers/ncat/files/technical-reports/rep09-08.pdf

Willis, R., Yin, F., and Moraes, R. “Recycled Plastics in Asphalt Part A: State of the Knowledge”. *National Asphalt Pavement Association*, report no. NAPA - IS-142, October 2020, pp. 1-36.

Yin, F. “LLDPE-rich PCR Sample_Picture1”. *Photo*, 2022.

Yin, F., Fortunatus, M., Moraes, R., Elwardany, M., Tran, N., and Planche, J. “Performance Evaluation of Asphalt Mixtures Modified with Recycled Polyethylene via the Wet Process”. *Transportation Research Record: Journal of The Transportation Research Board*, vol 2675, no. 10, July 6, 2021, pp. 491–502. *SAGE Publications*, DOI: 10.1177/03611981211011650.

APPENDIX A

ASG and EPC Calibration Graphs for AG Experiment Section Gauges

N1-GTRDry Section

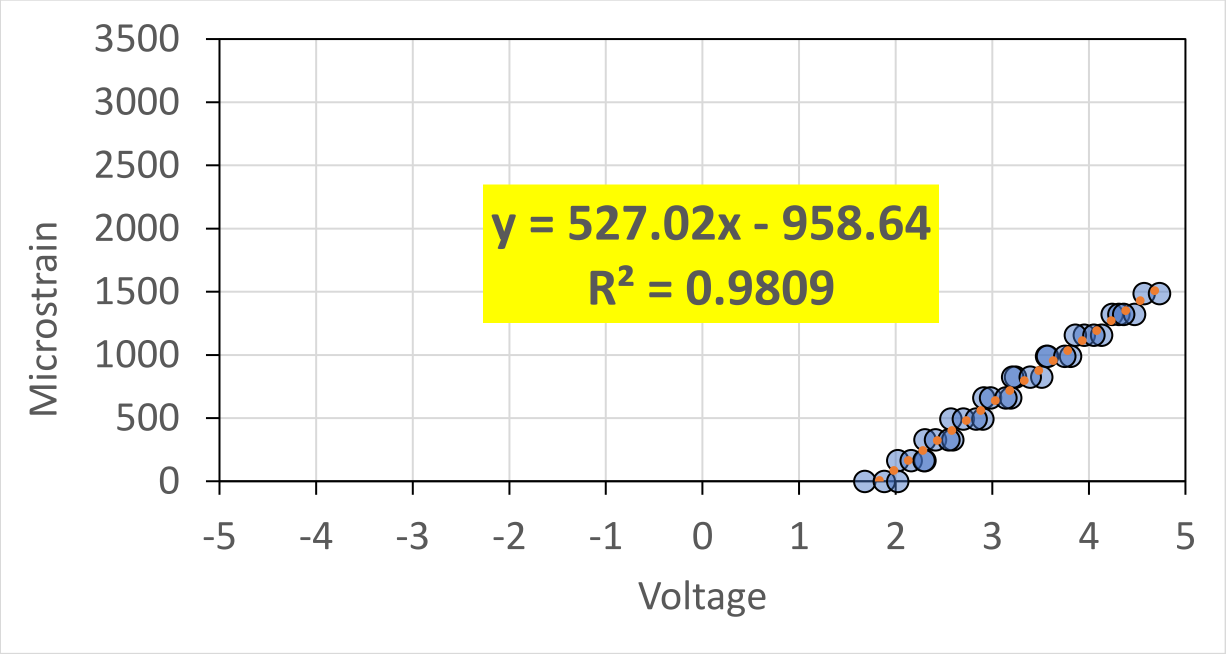

Figure A.1: ASG Channel 1 Calibration Graph

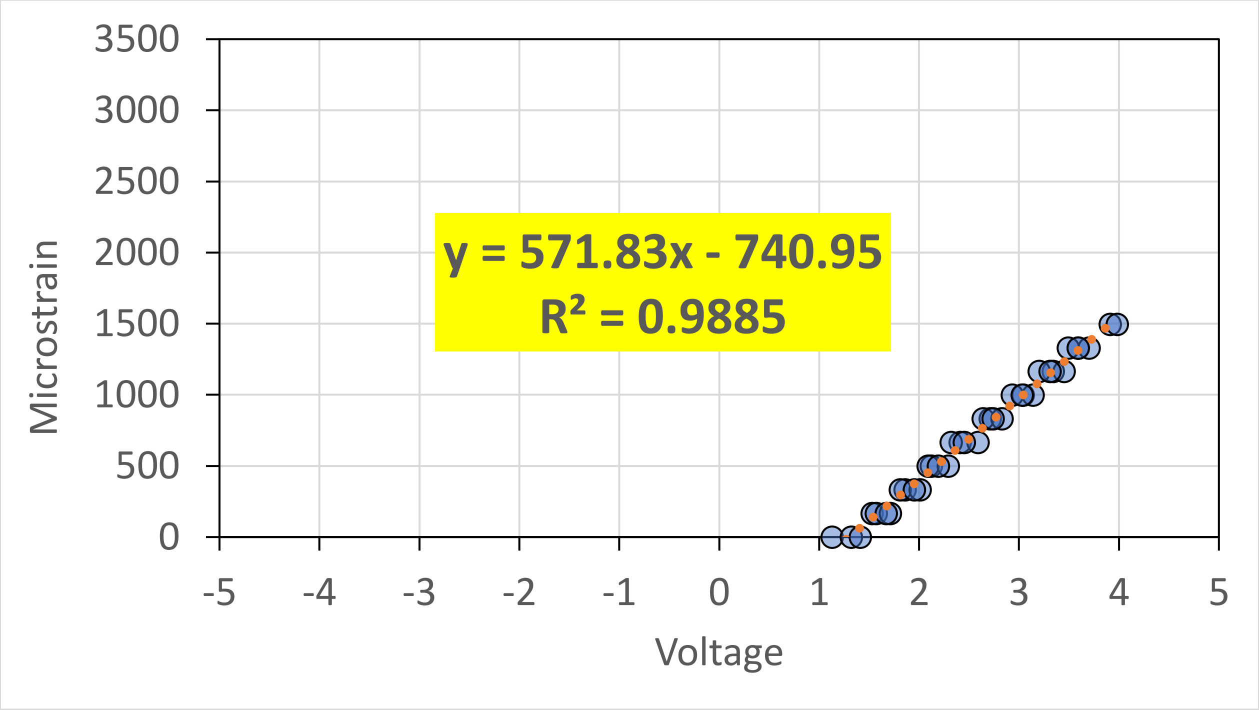

Figure A.2: ASG Channel 2 Calibration Graph

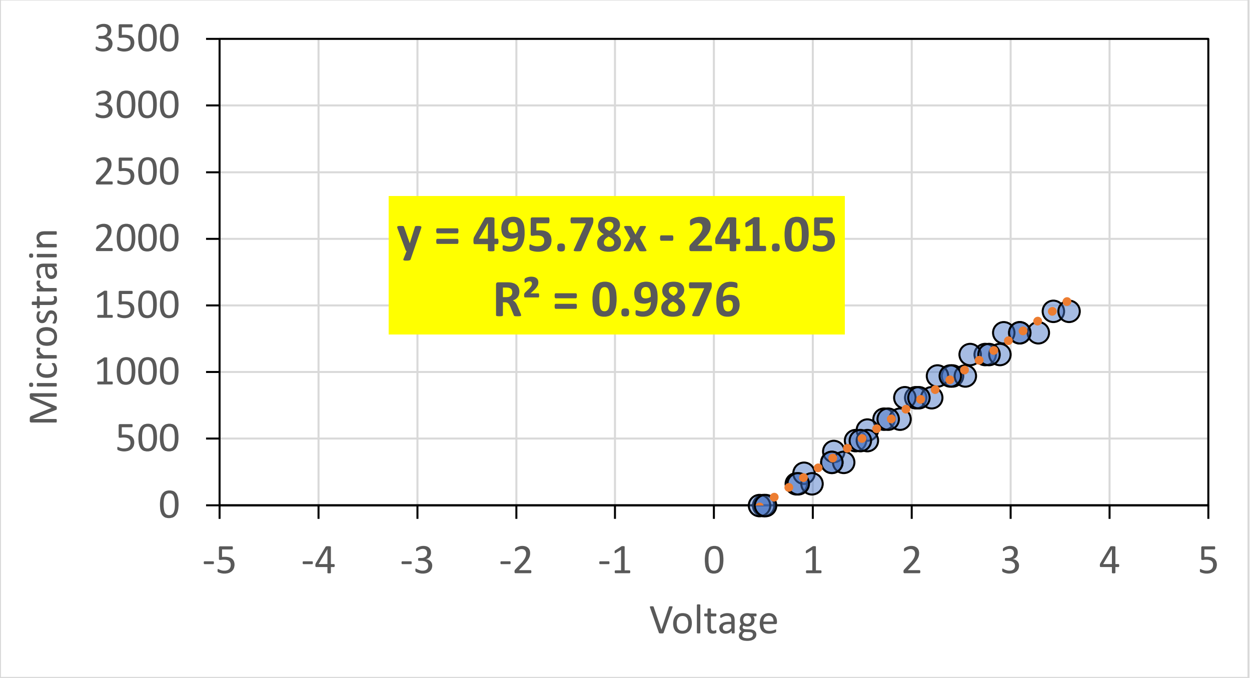

Figure A.3: ASG Channel 3 Calibration Graph

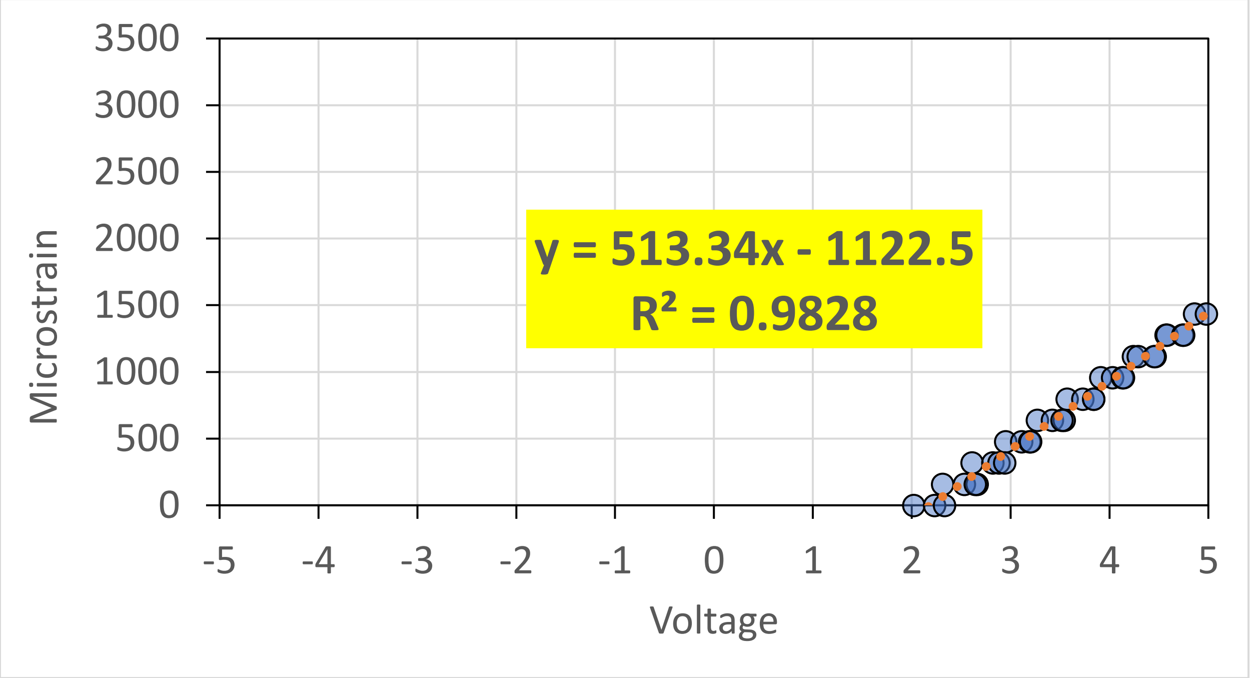

Figure A.4: ASG Channel 4 Calibration Graph

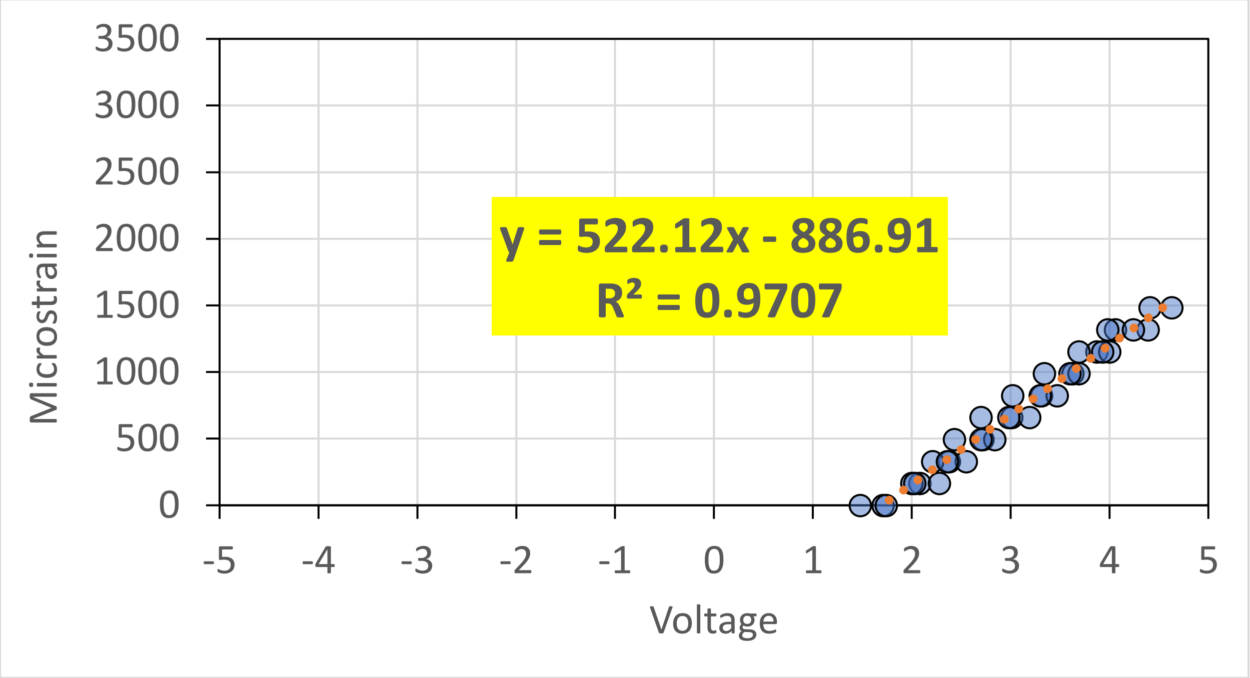

Figure A.5: ASG Channel 5 Calibration Graph

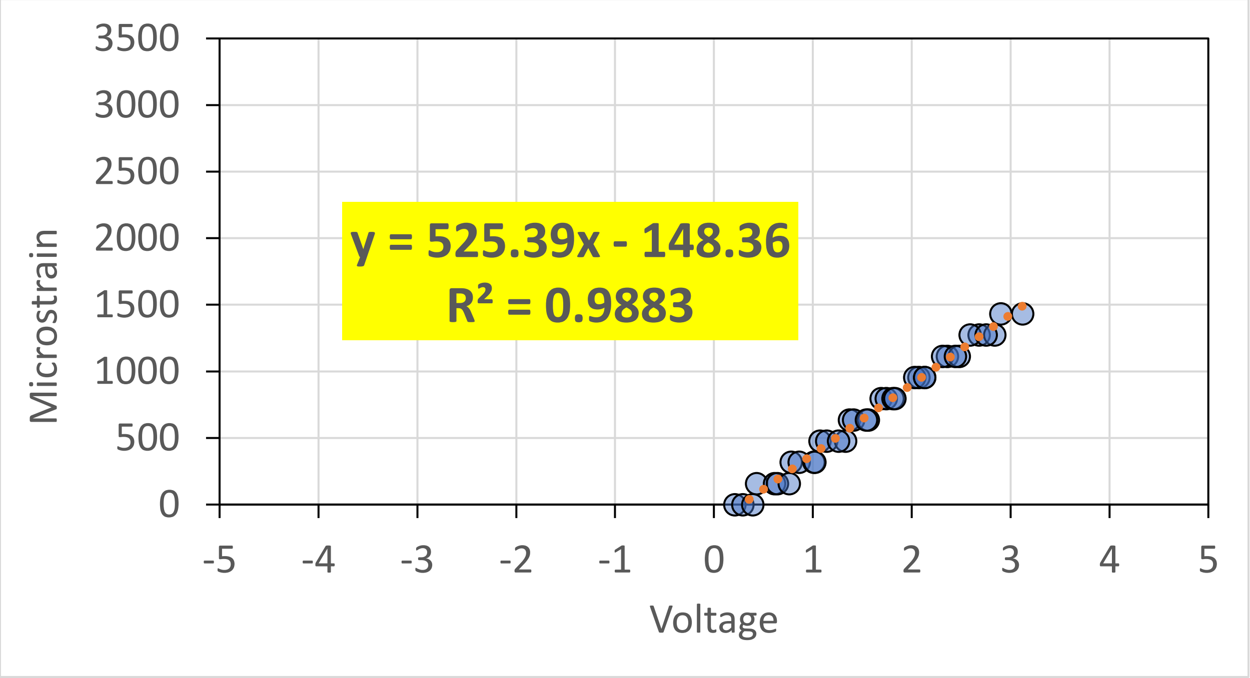

Figure A.6: ASG Channel 6 Calibration Graph

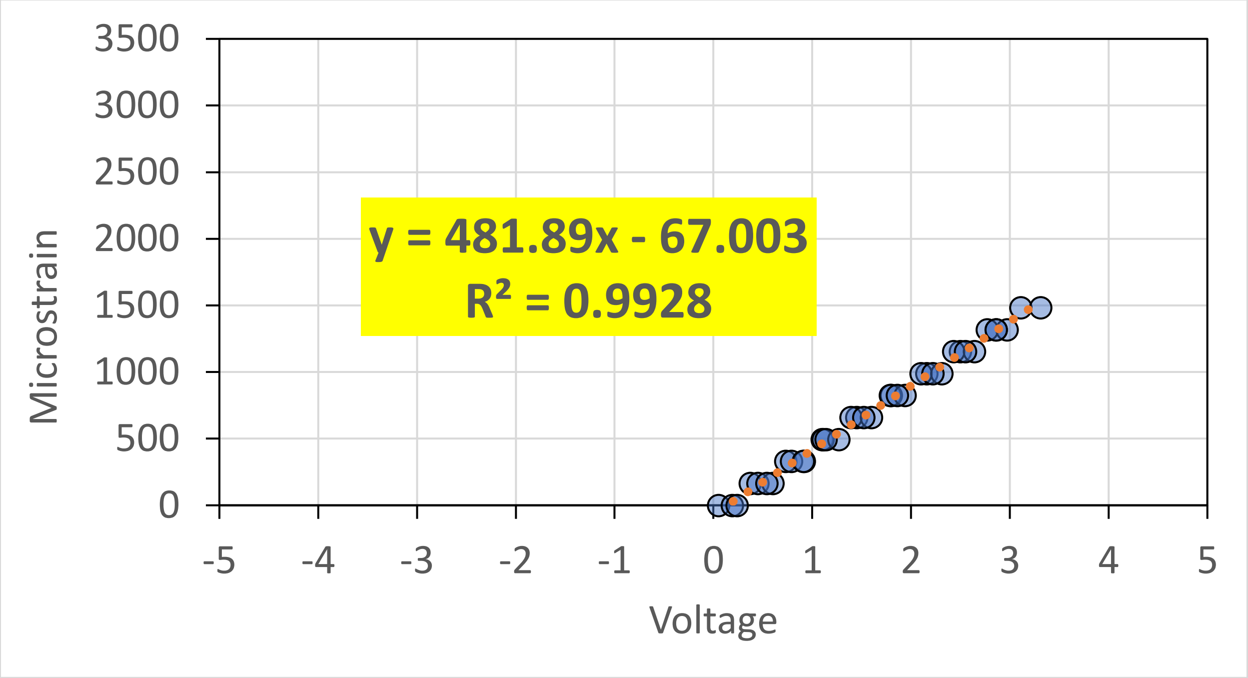

Figure A.7: ASG Channel 7 Calibration Graph

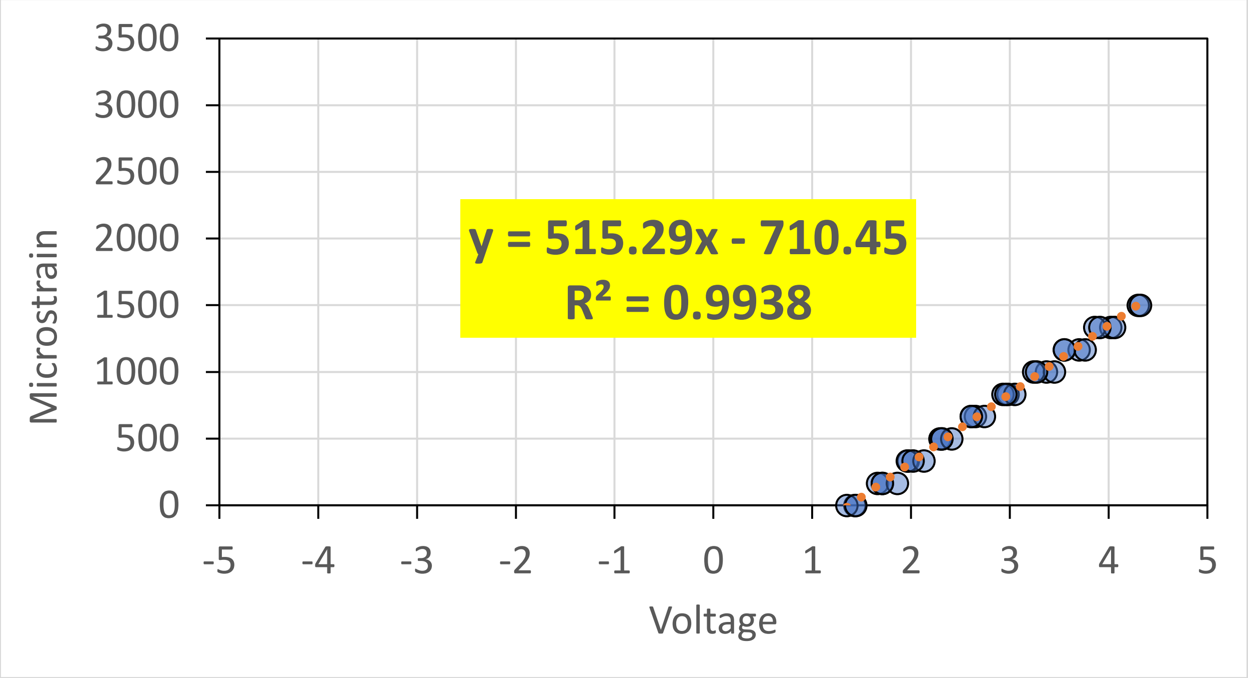

Figure A.8: ASG Channel 8 Calibration Graph

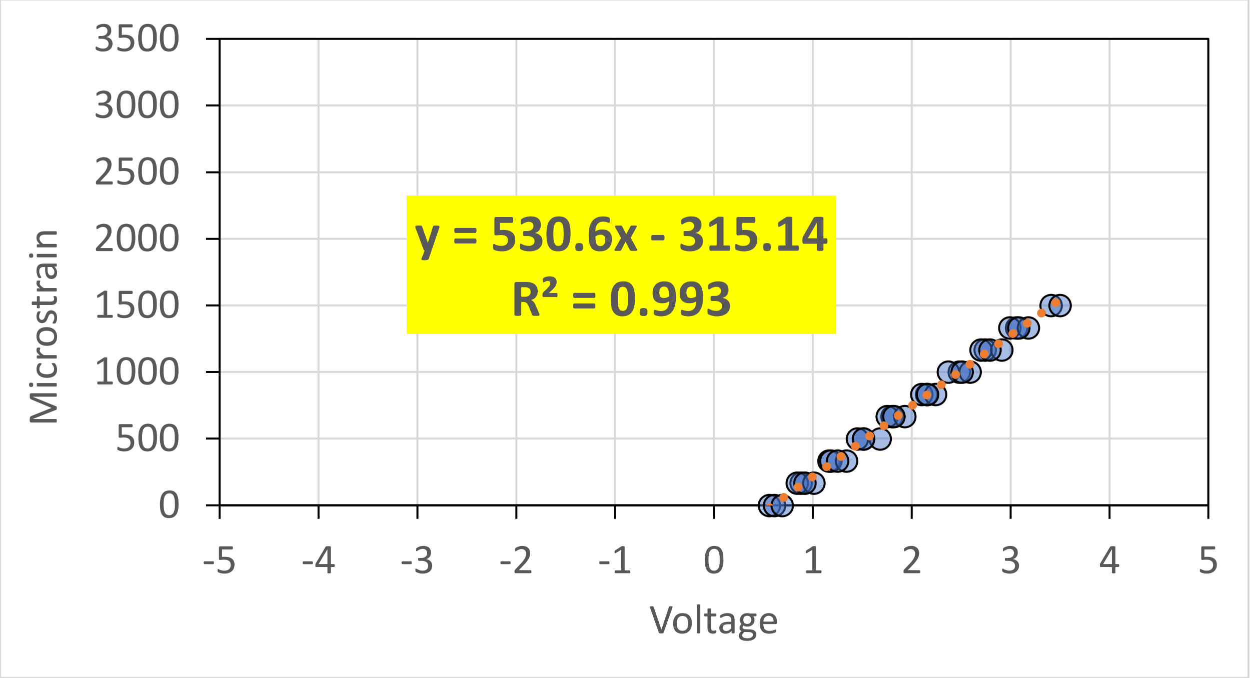

Figure A.9: ASG Channel 9 Calibration Graph

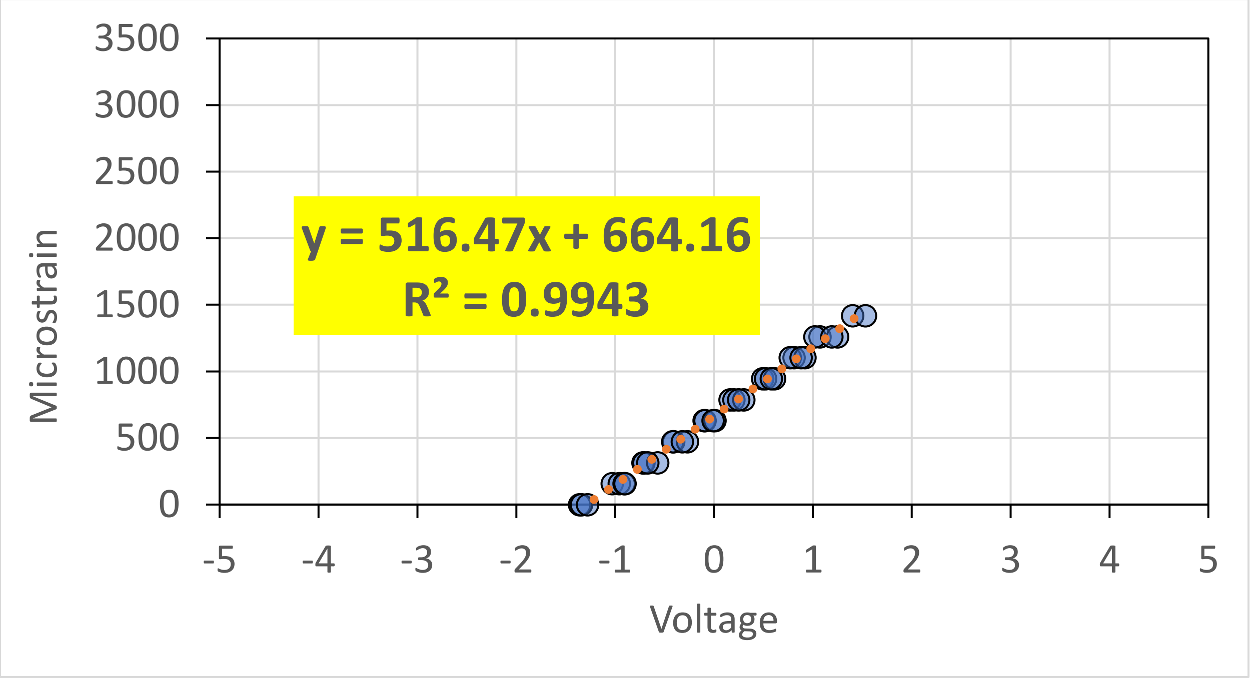

Figure A.10: ASG Channel 10 Calibration Graph

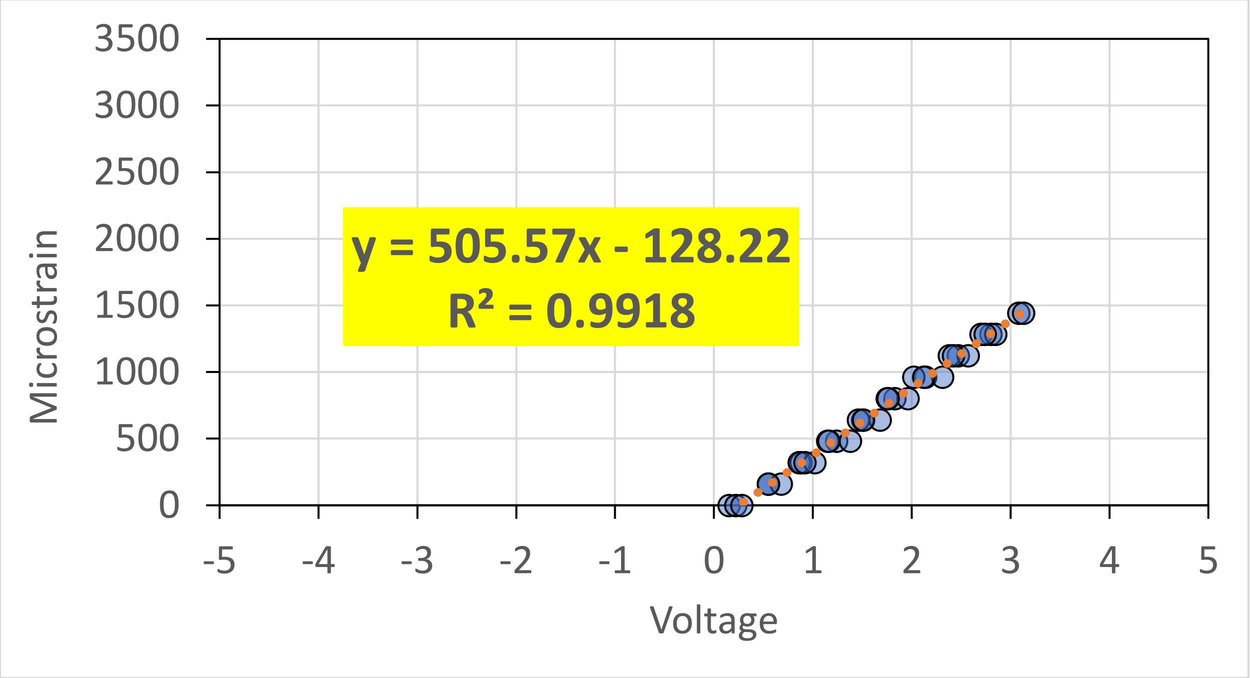

Figure A.11: ASG Channel 11 Calibration Graph

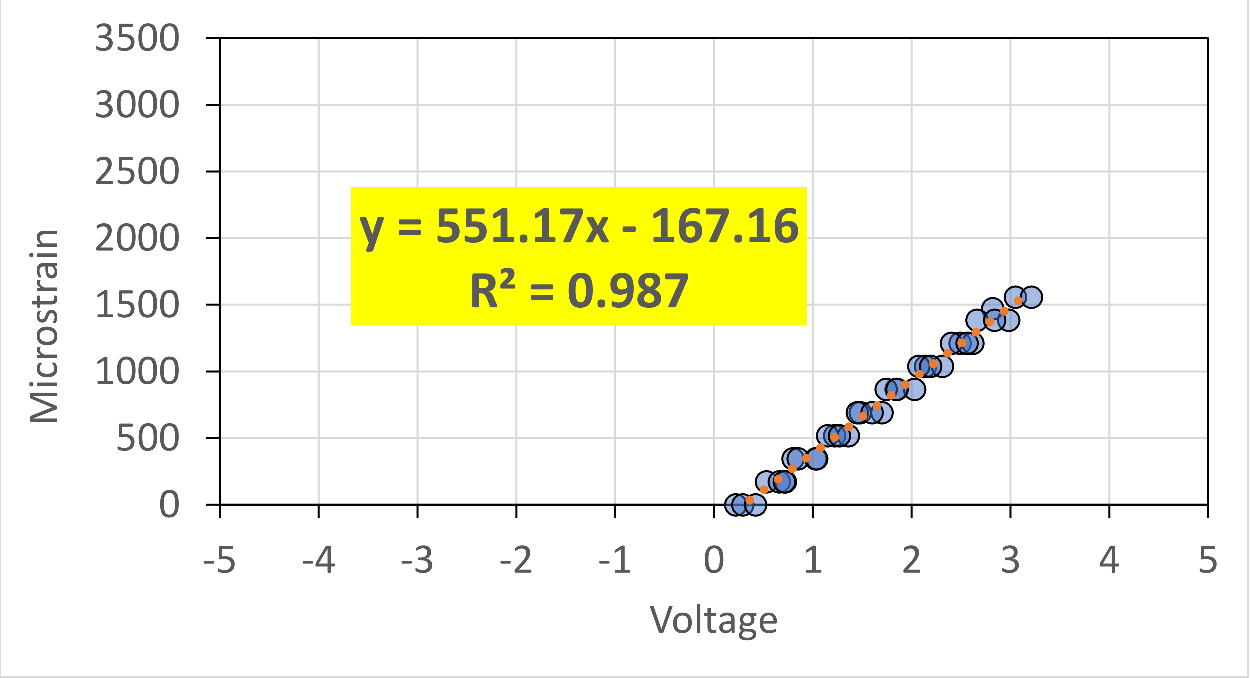

Figure A.12: ASG Channel 12 Calibration Graph

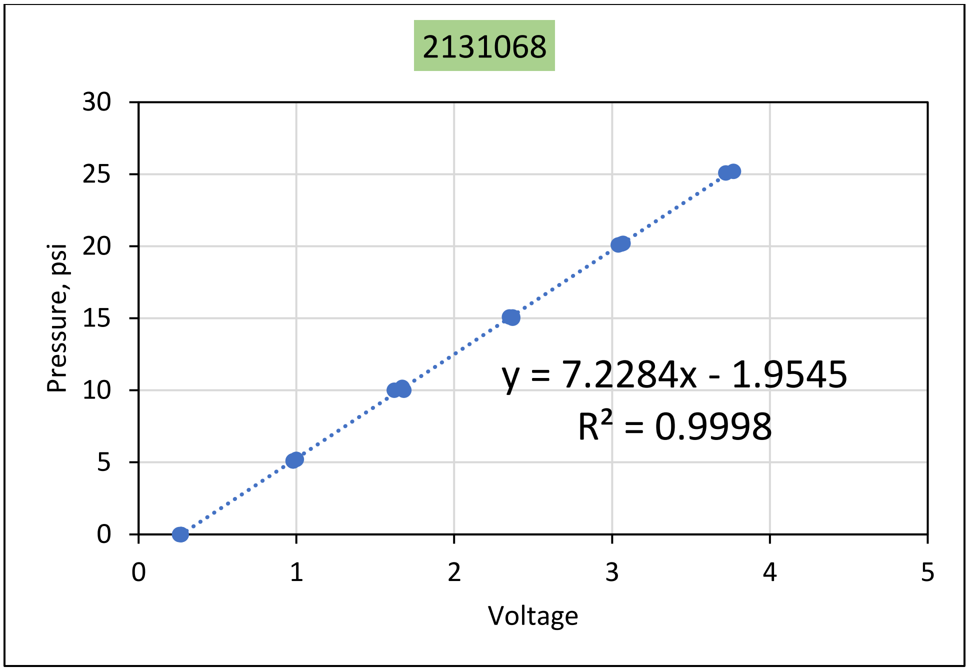

Figure A.13: EPC Channel 13 Calibration Graph

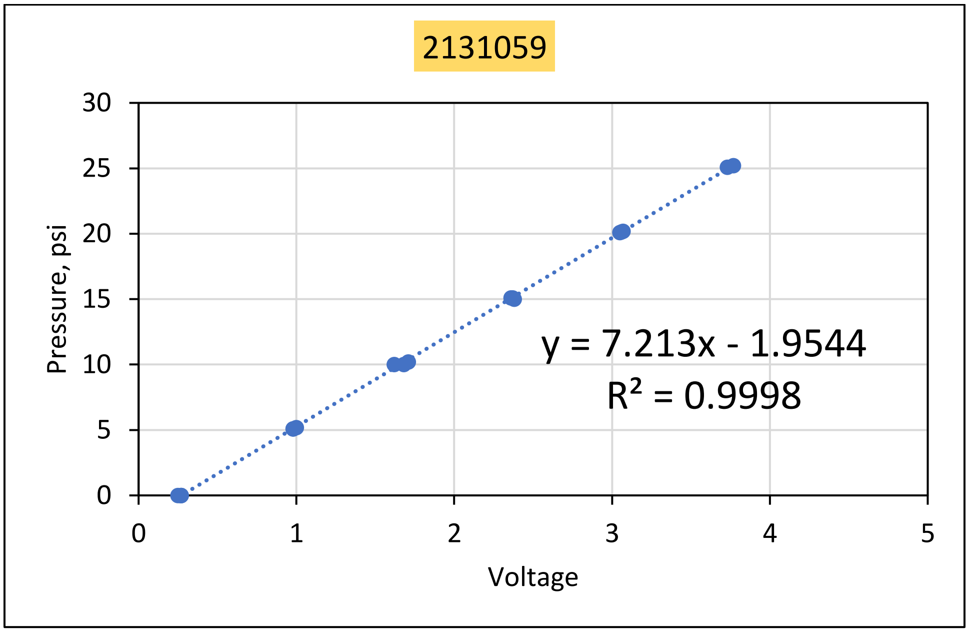

Figure A.14: EPC Channel 14 Calibration Graph

N2-GTRWet Section

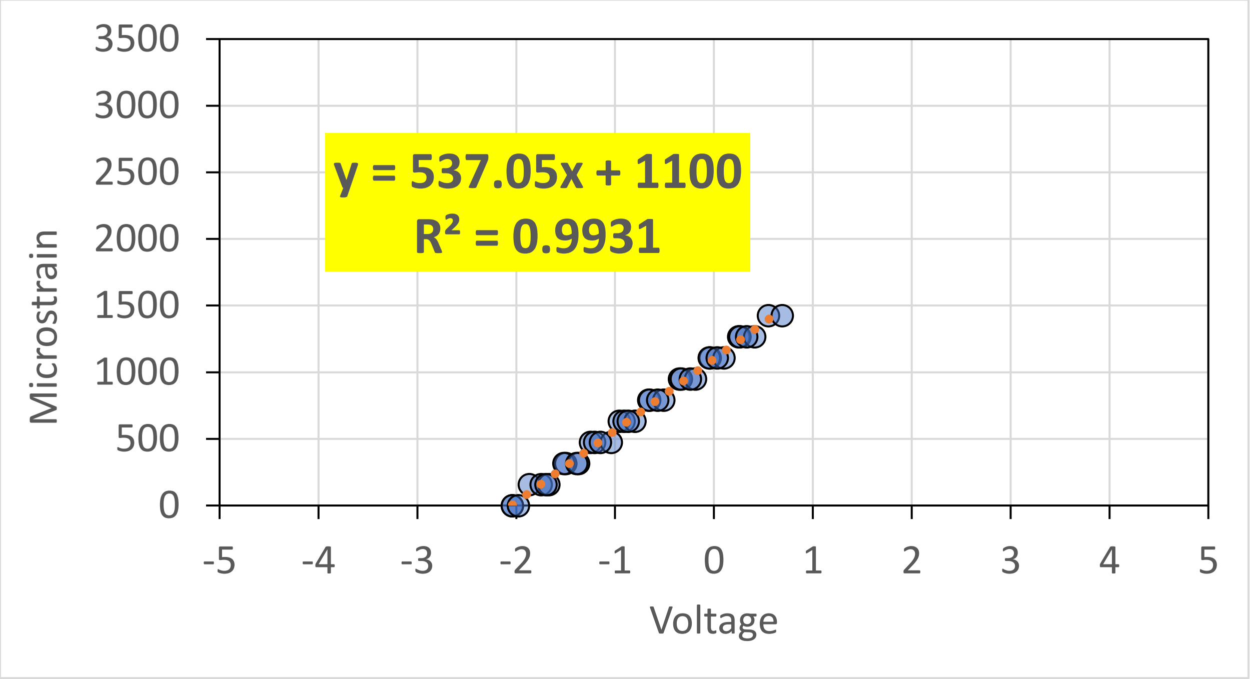

Figure A.15: ASG Channel 1 Calibration Graph

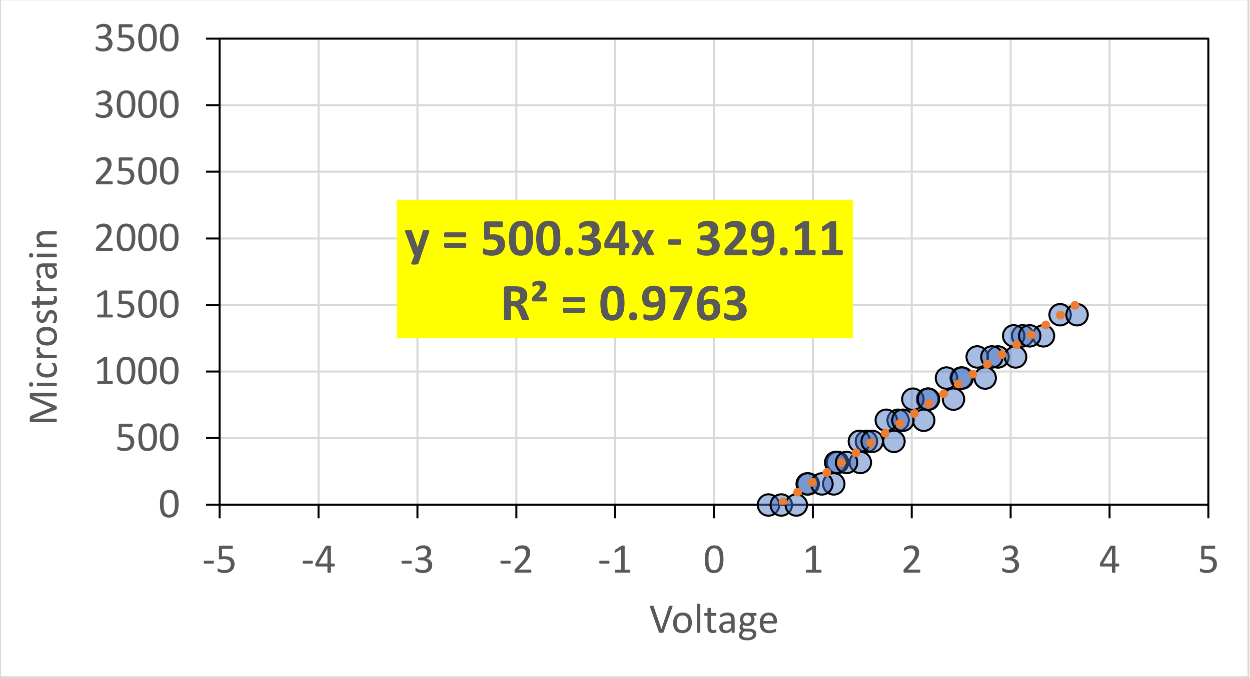

Figure A.16: ASG Channel 2 Calibration Graph

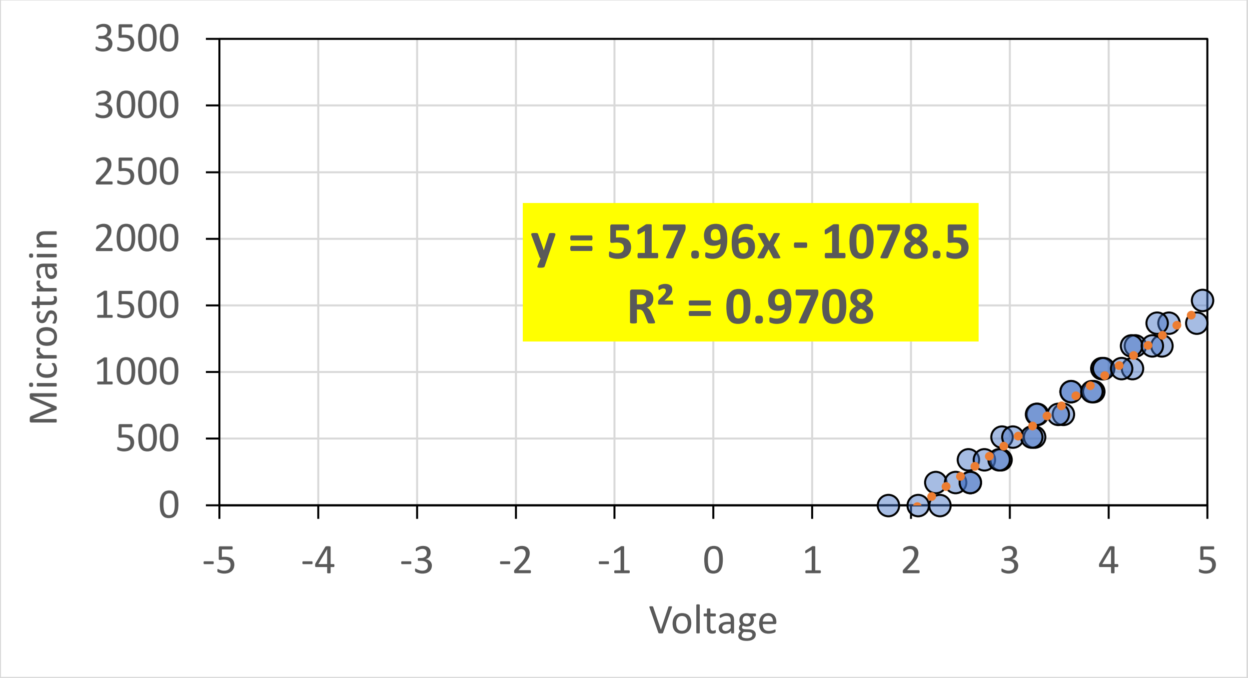

Figure A.17: ASG Channel 3 Calibration Graph

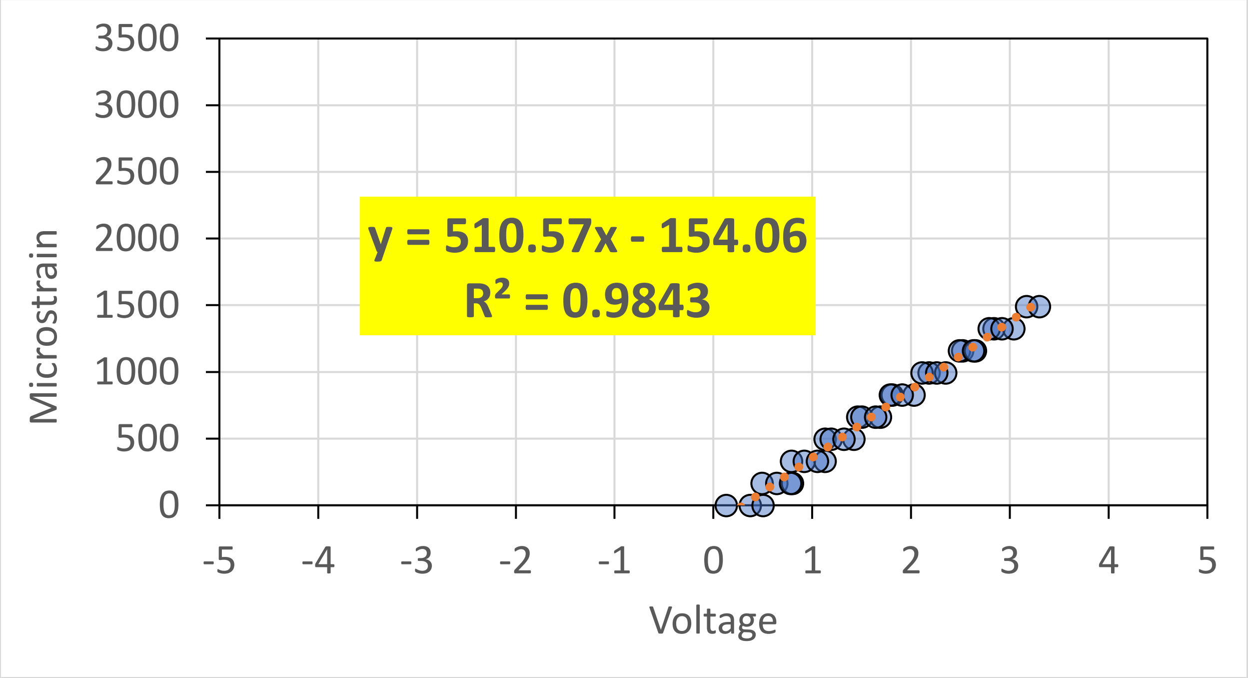

Figure A.18: ASG Channel 4 Calibration Graph

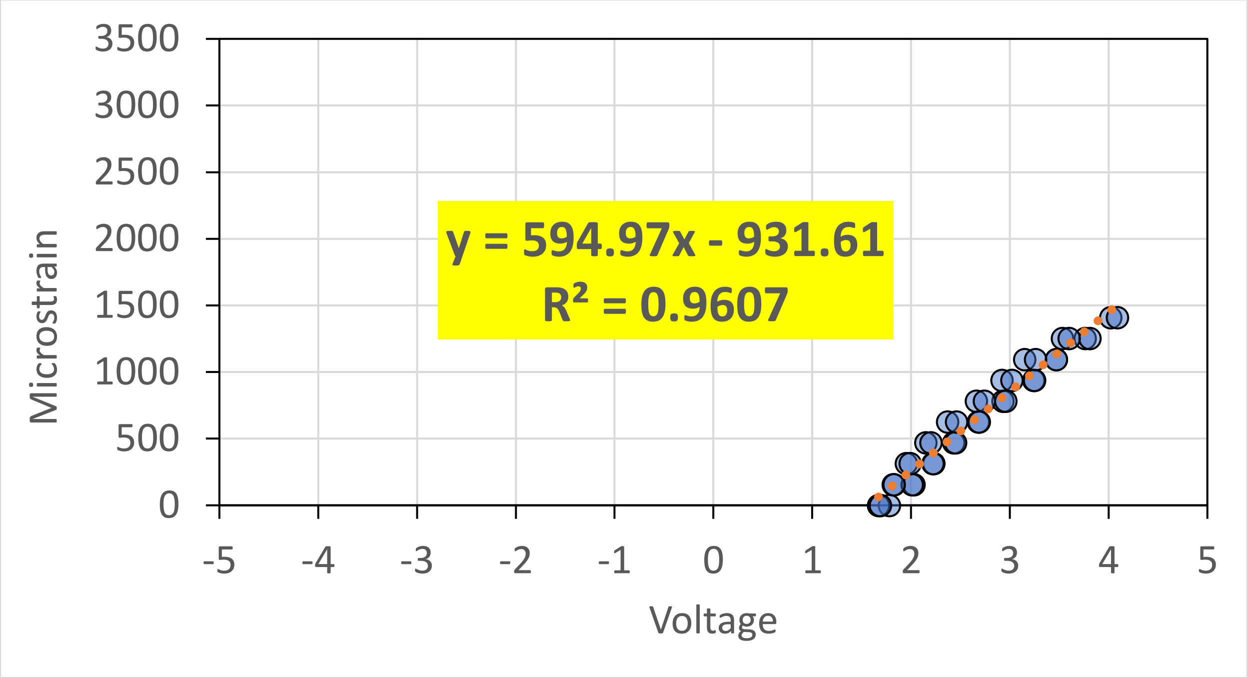

Figure A.19: ASG Channel 5 Calibration Graph

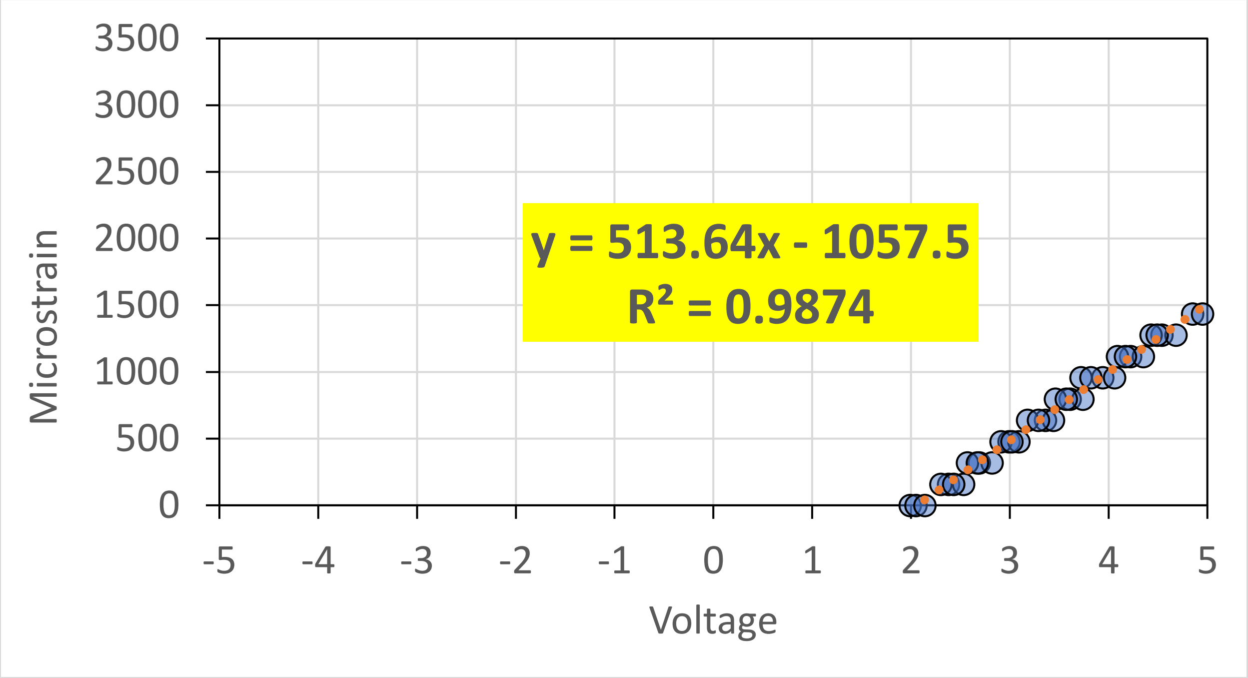

Figure A.20: ASG Channel 6 Calibration Graph

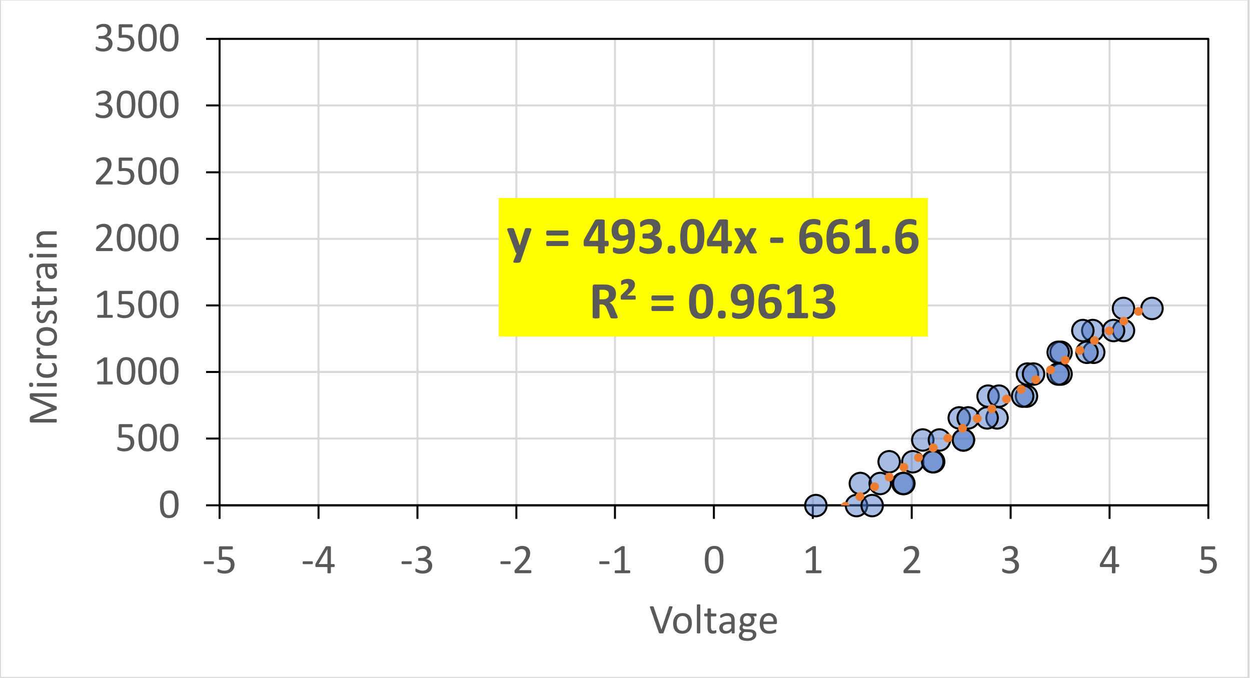

Figure A.21: ASG Channel 7 Calibration Graph

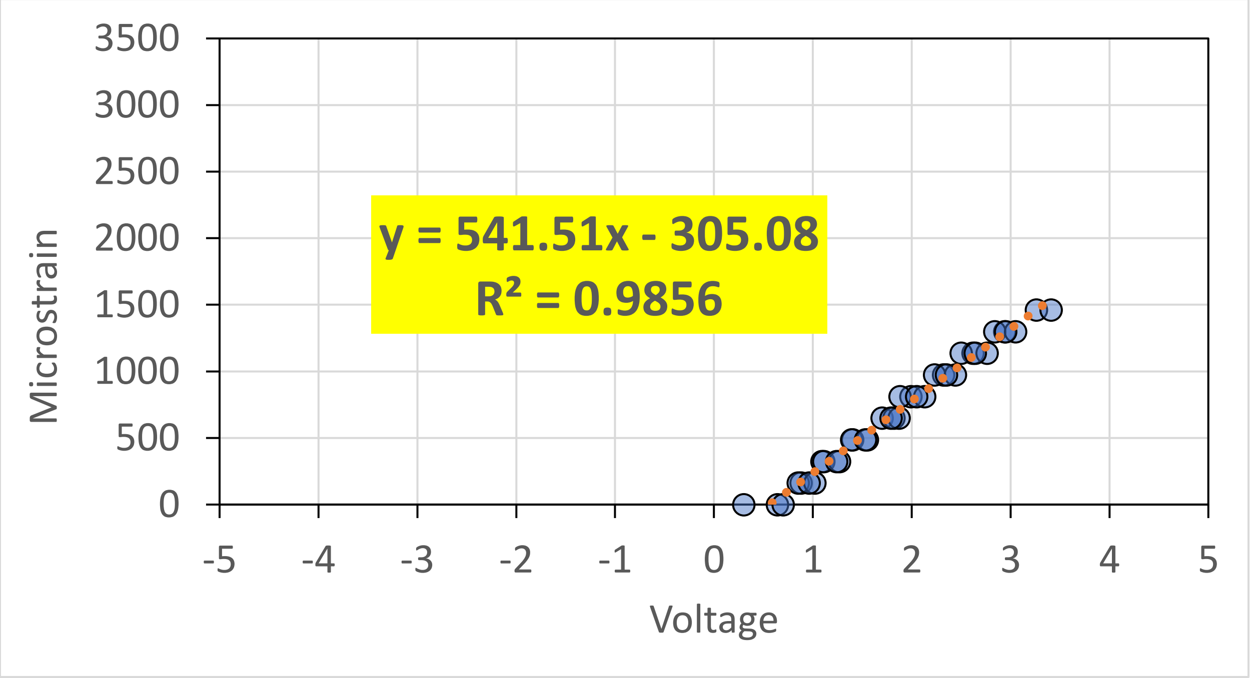

Figure A.22: ASG Channel 8 Calibration Graph

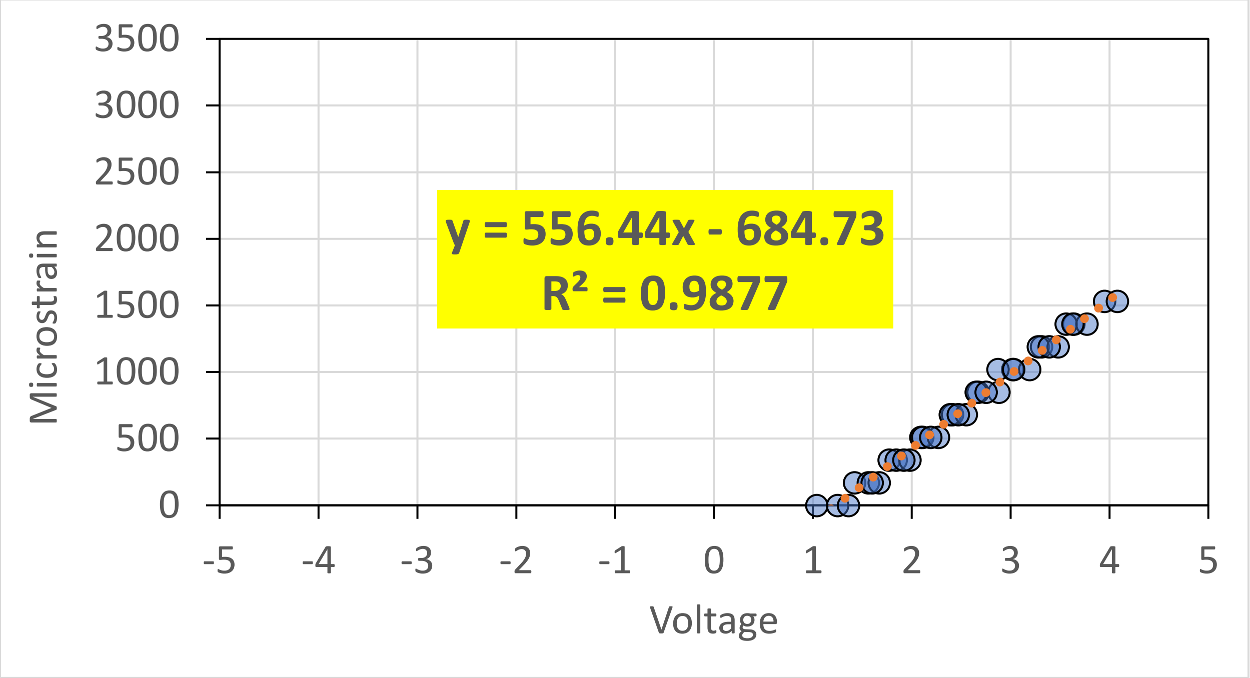

Figure A.23: ASG Channel 9 Calibration Graph

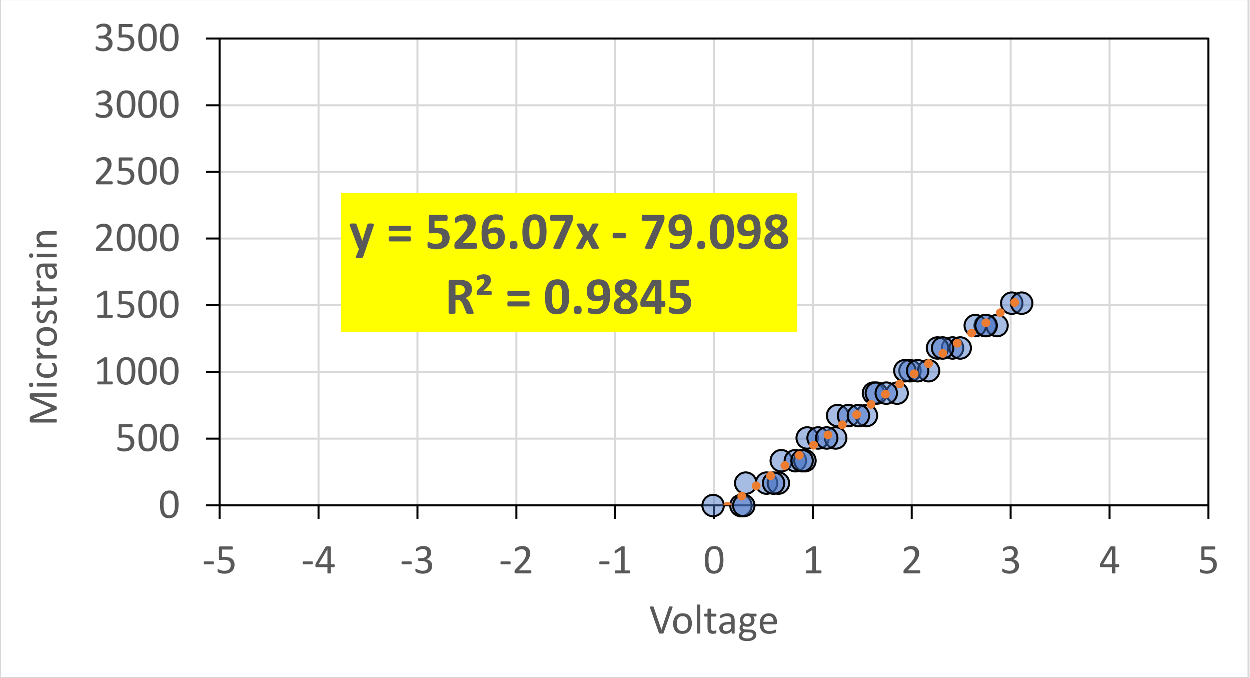

Figure A.24: ASG Channel 10 Calibration Graph

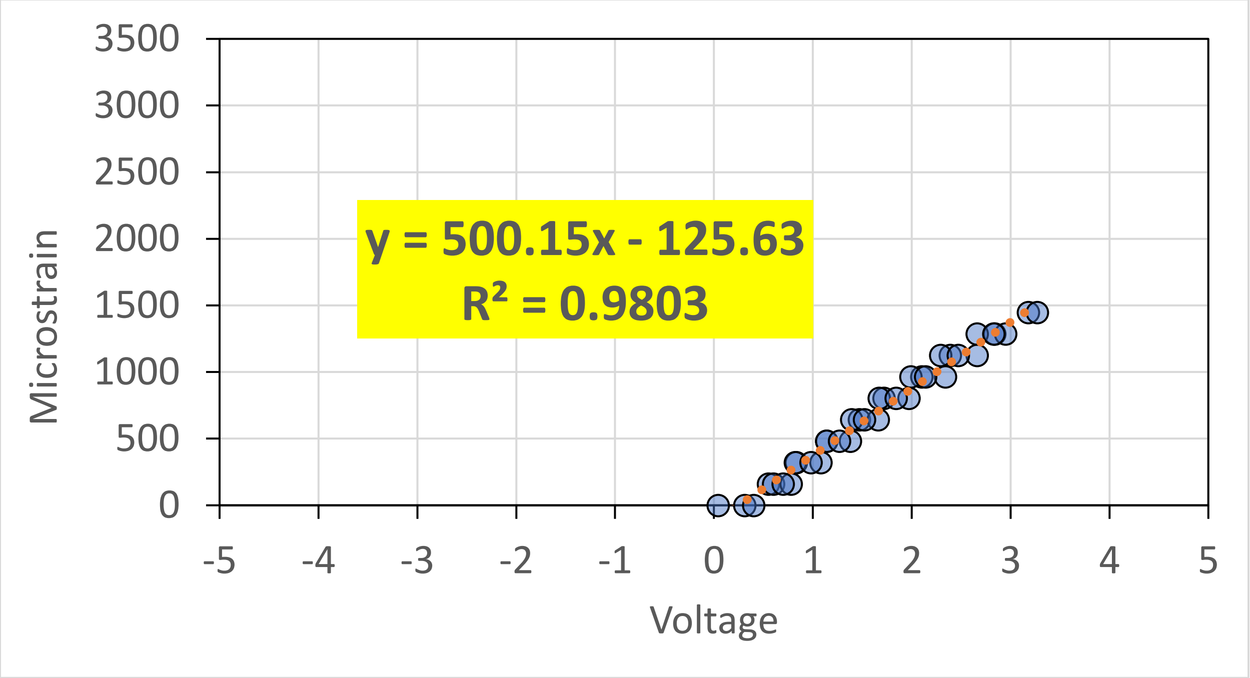

Figure A.25: ASG Channel 11 Calibration Graph

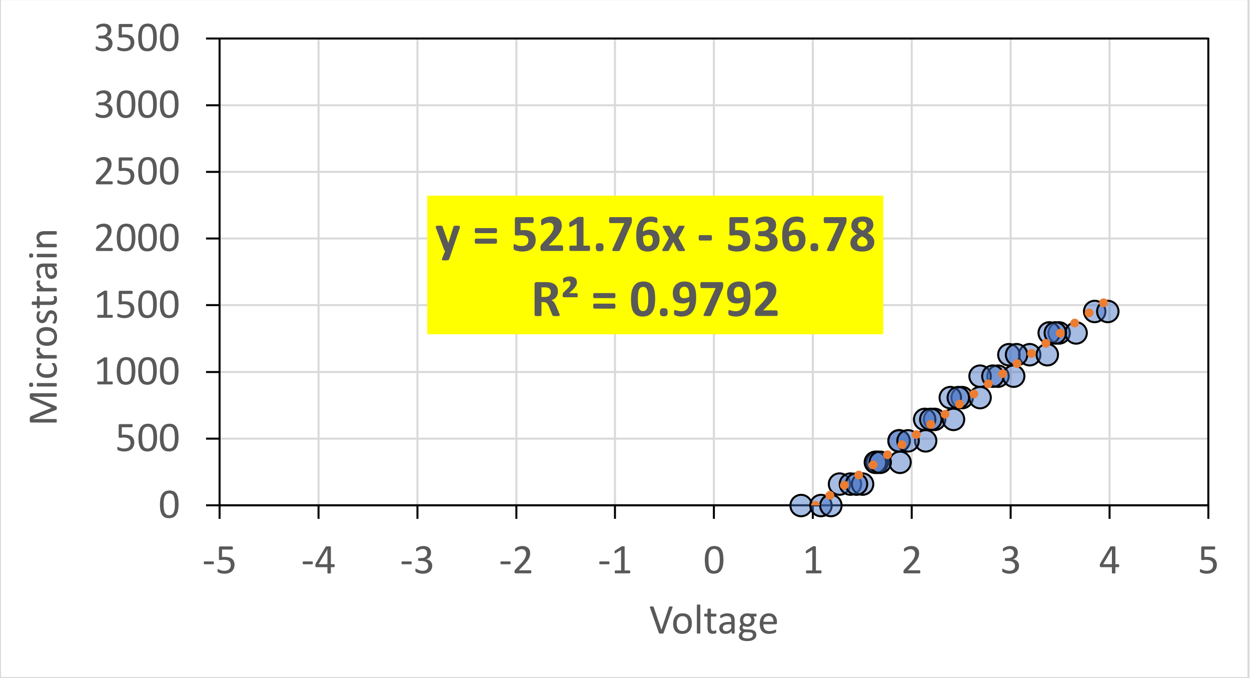

Figure A.26: ASG Channel 12 Calibration Graph

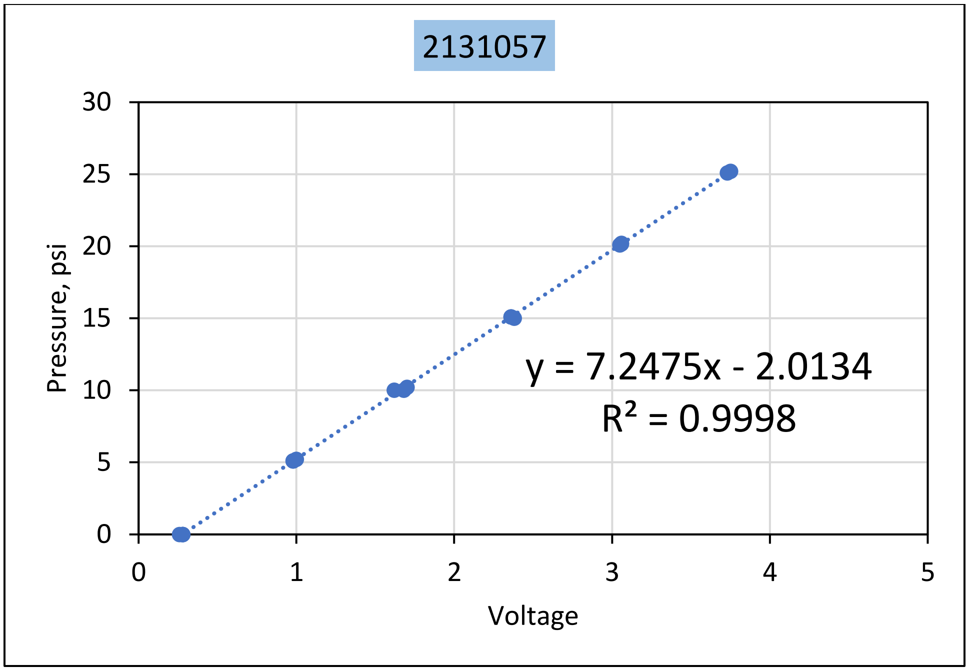

Figure A.27: EPC Channel 13 Calibration Graph

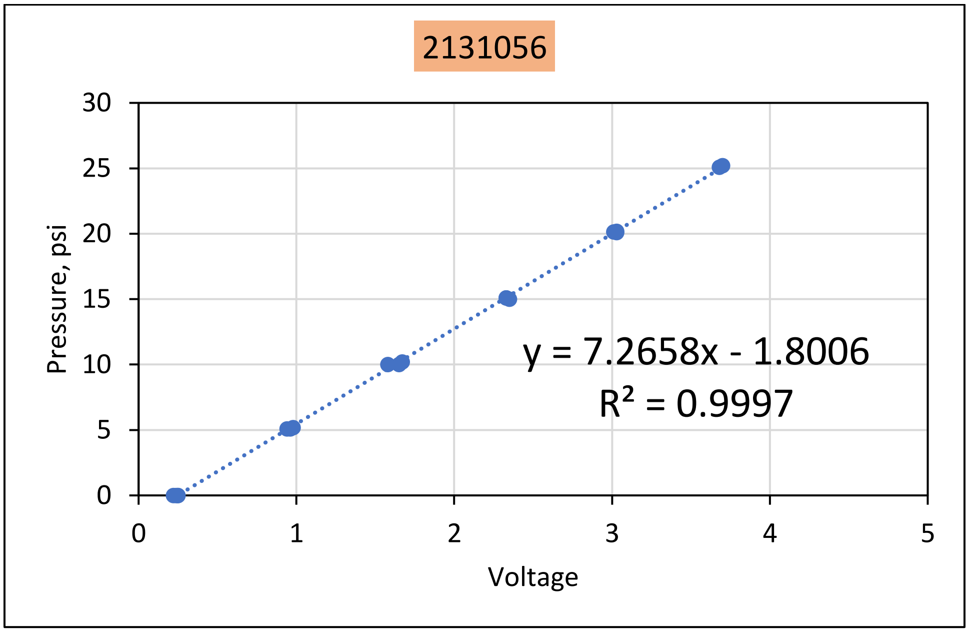

Figure A.28: EPC Channel 14 Calibration Graph

N5-Aramid Section

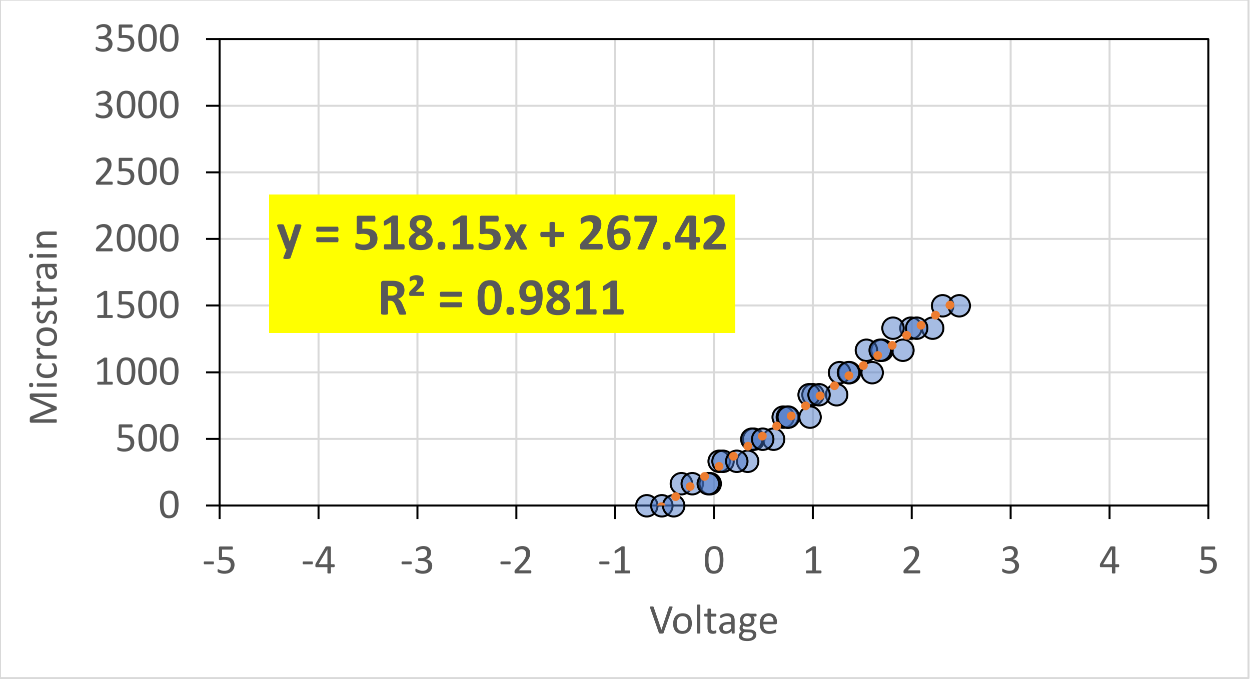

Figure A.29: ASG Channel 1 Calibration Graph

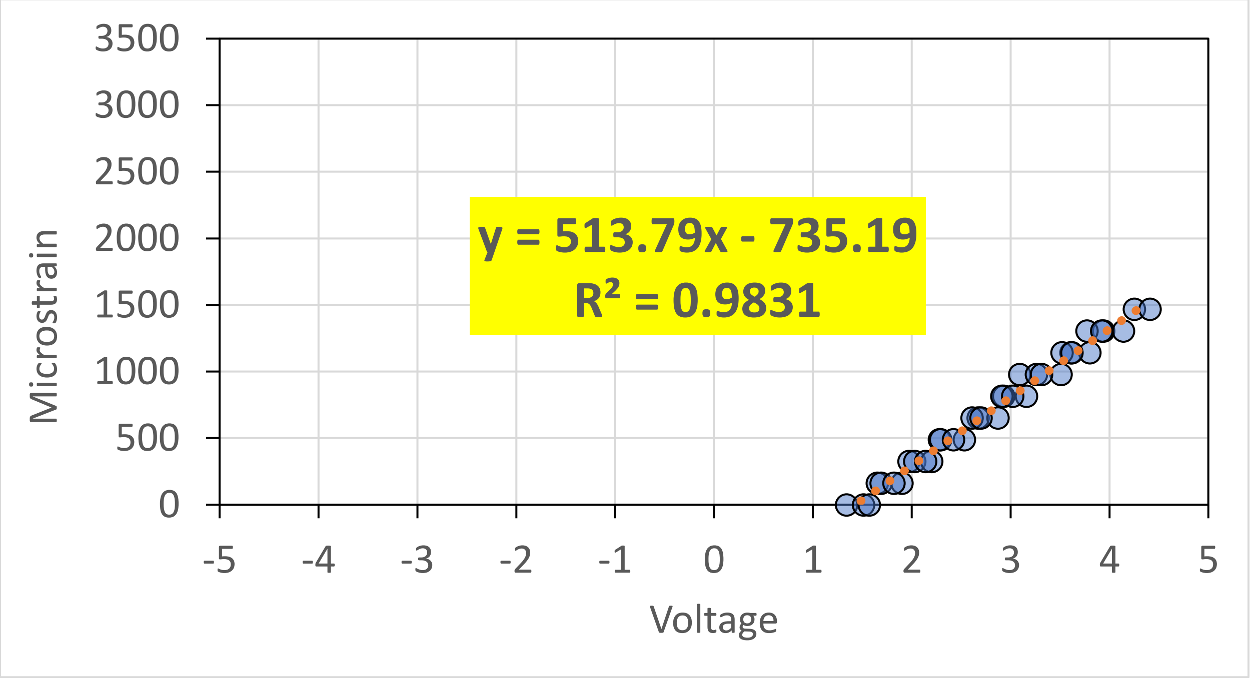

Figure A.30: ASG Channel 2 Calibration Graph

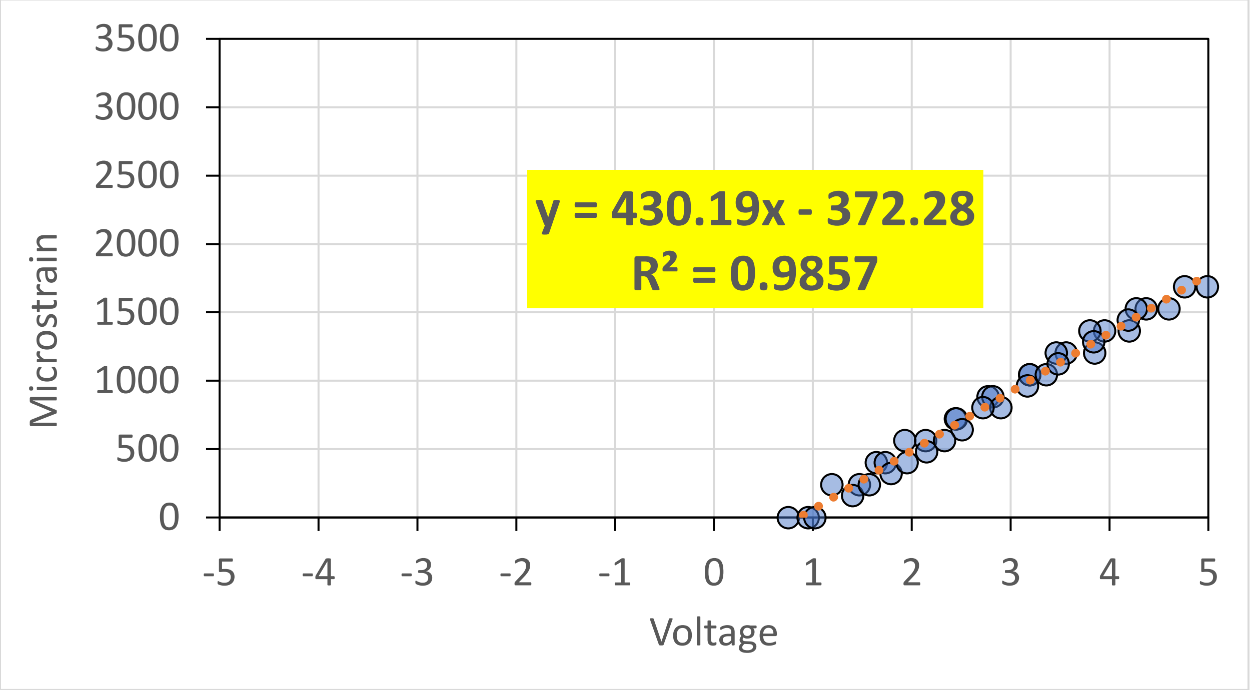

Figure A.31: ASG Channel 3 Calibration Graph

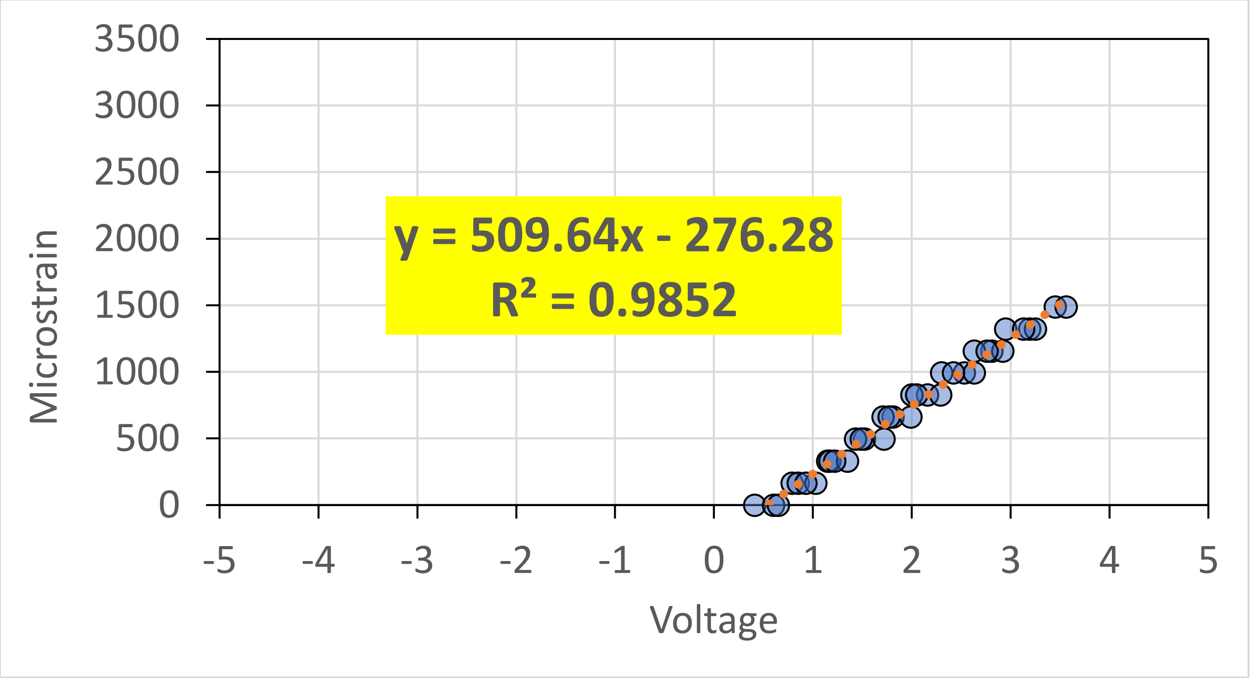

Figure A.32: ASG Channel 4 Calibration Graph

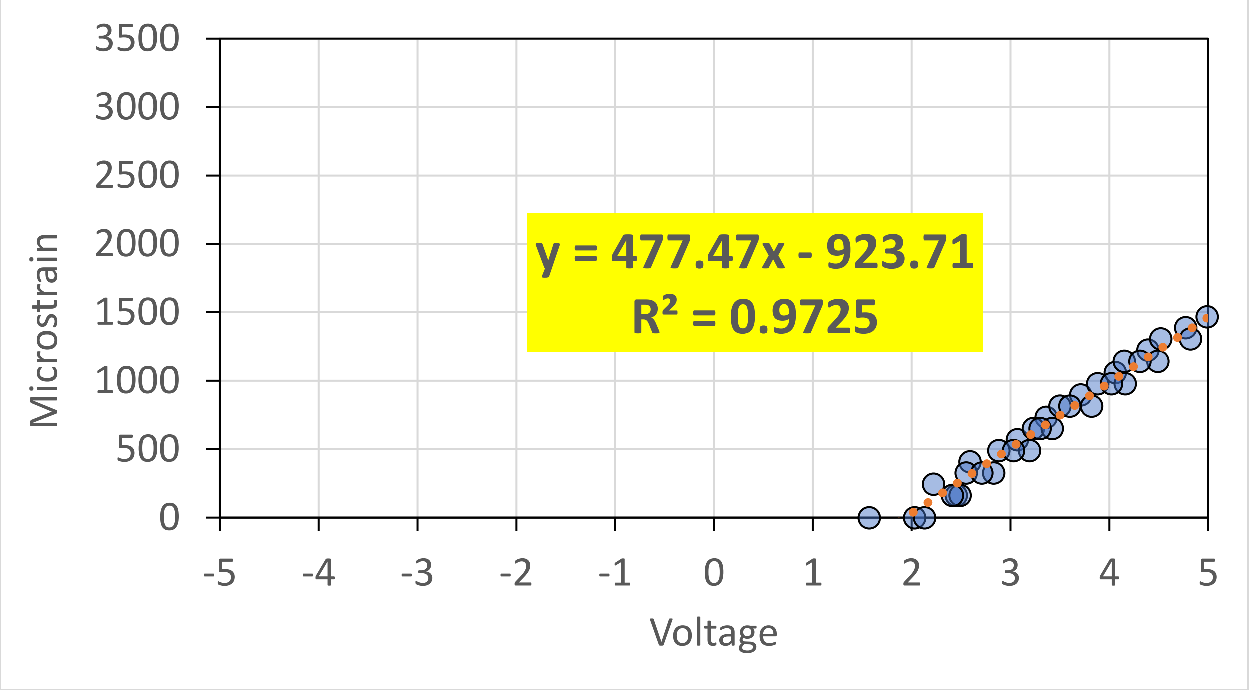

Figure A.33: ASG Channel 5 Calibration Graph

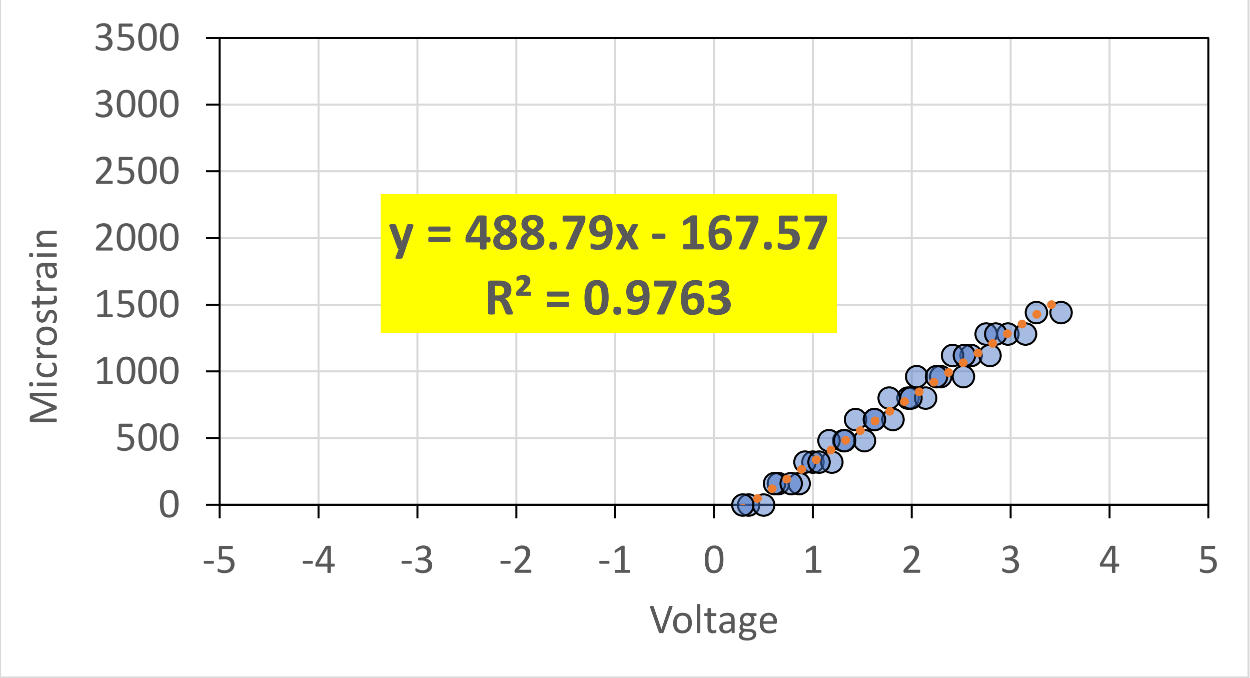

Figure A.34: ASG Channel 6 Calibration Graph

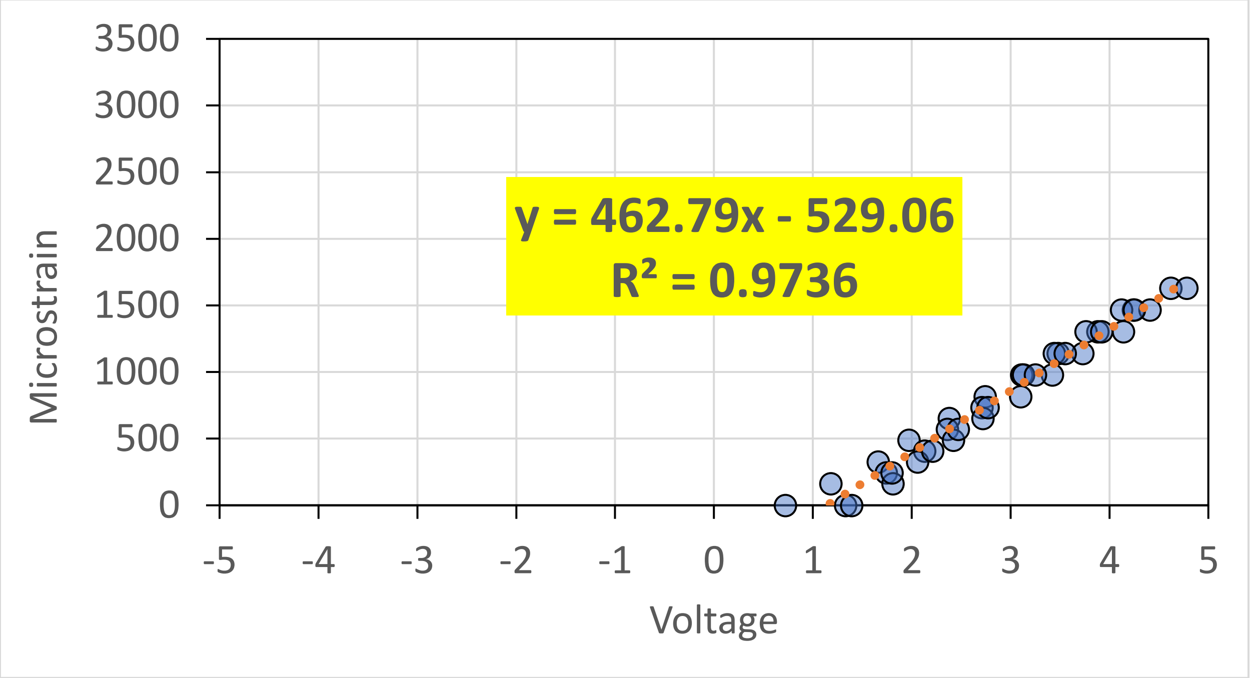

Figure A.35: ASG Channel 7 Calibration Graph

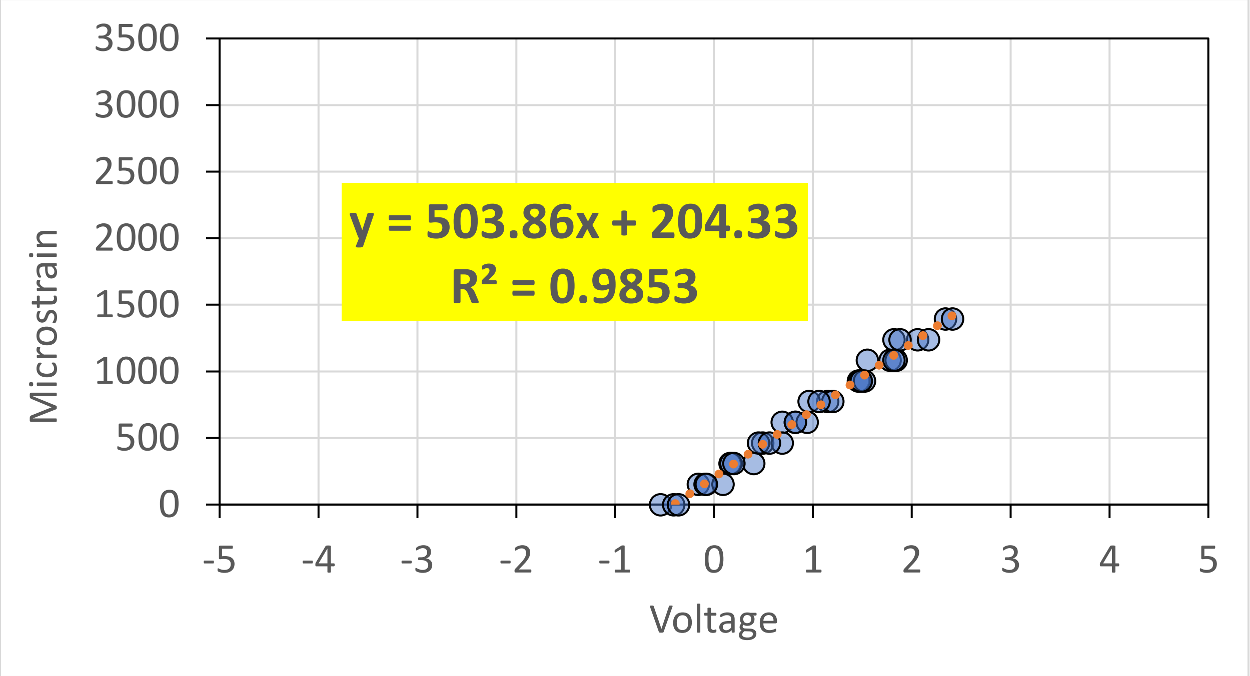

Figure A.36: ASG Channel 8 Calibration Graph

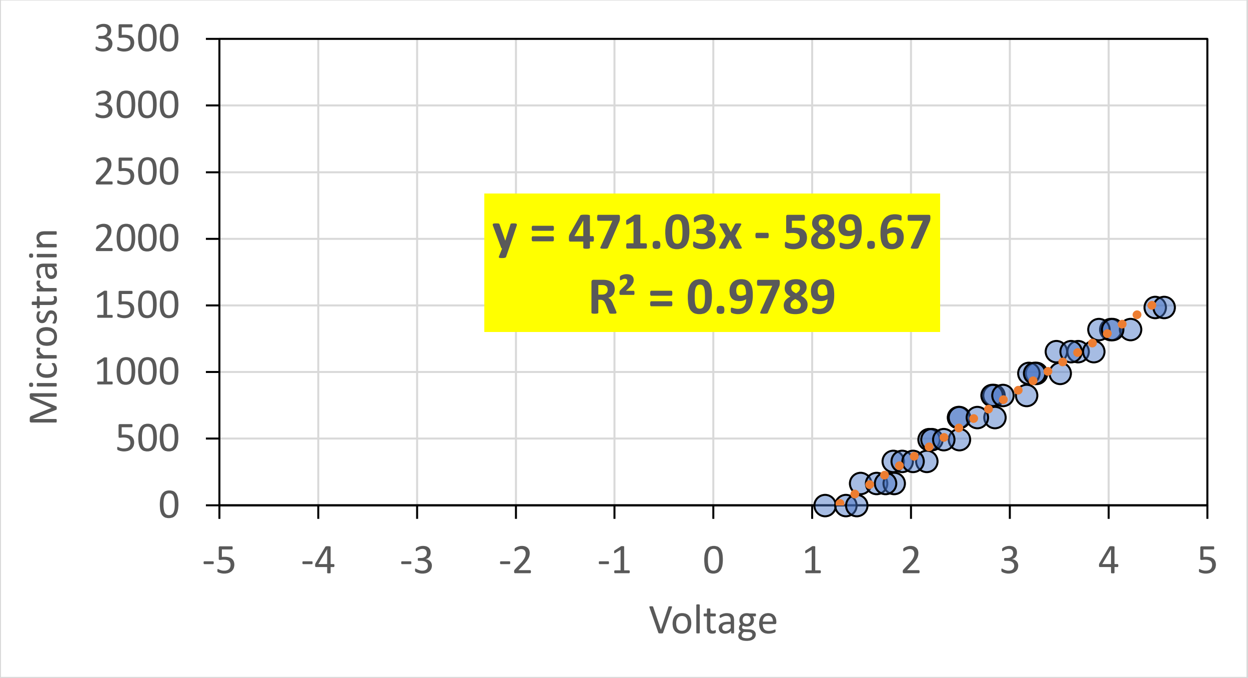

Figure A.37: ASG Channel 9 Calibration Graph

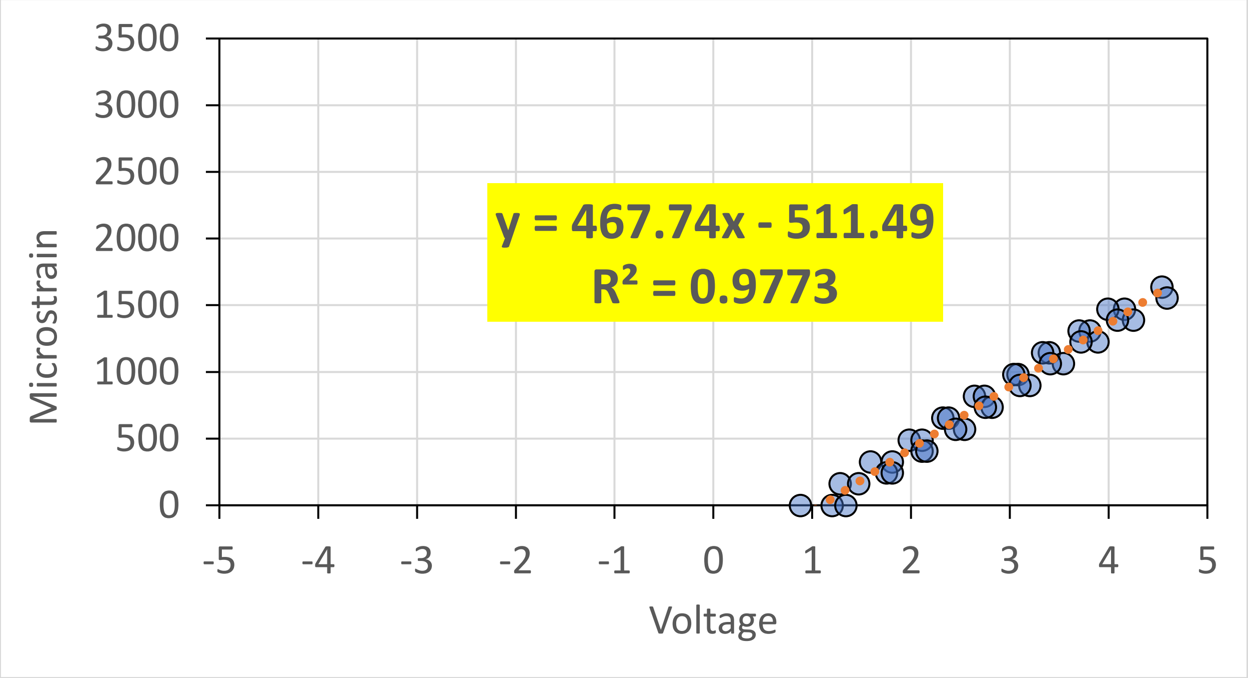

Figure A.38: ASG Channel 10 Calibration Graph

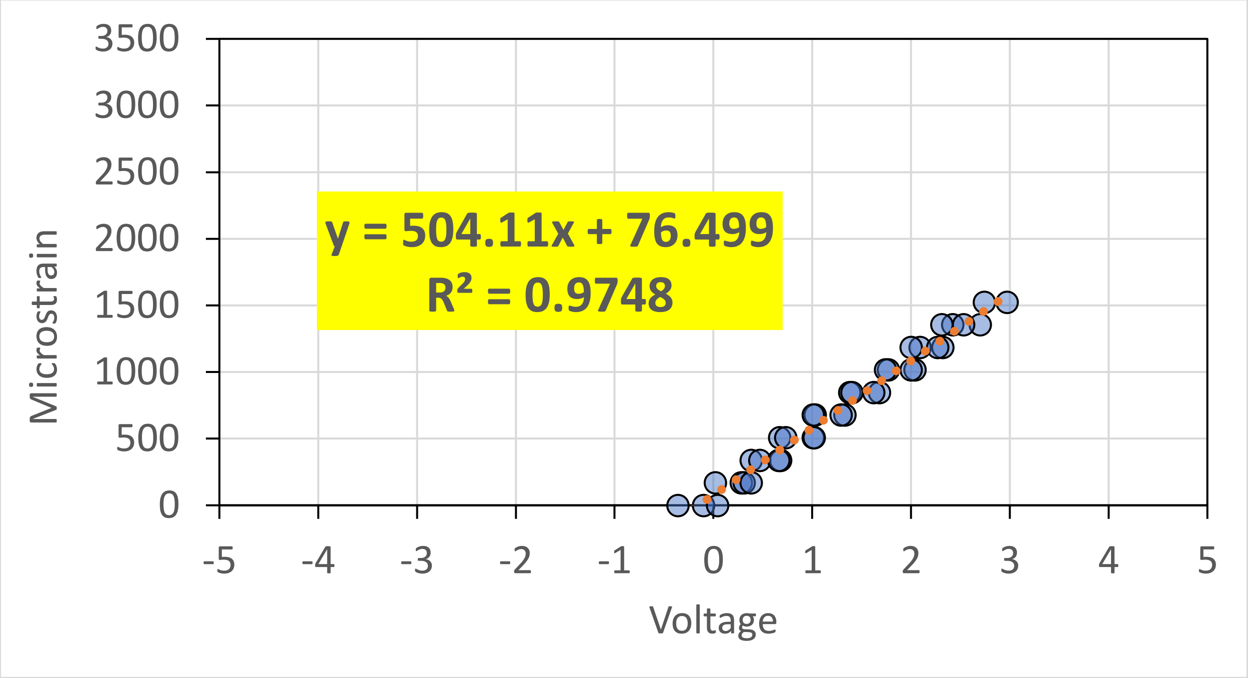

Figure A.39: ASG Channel 11 Calibration Graph

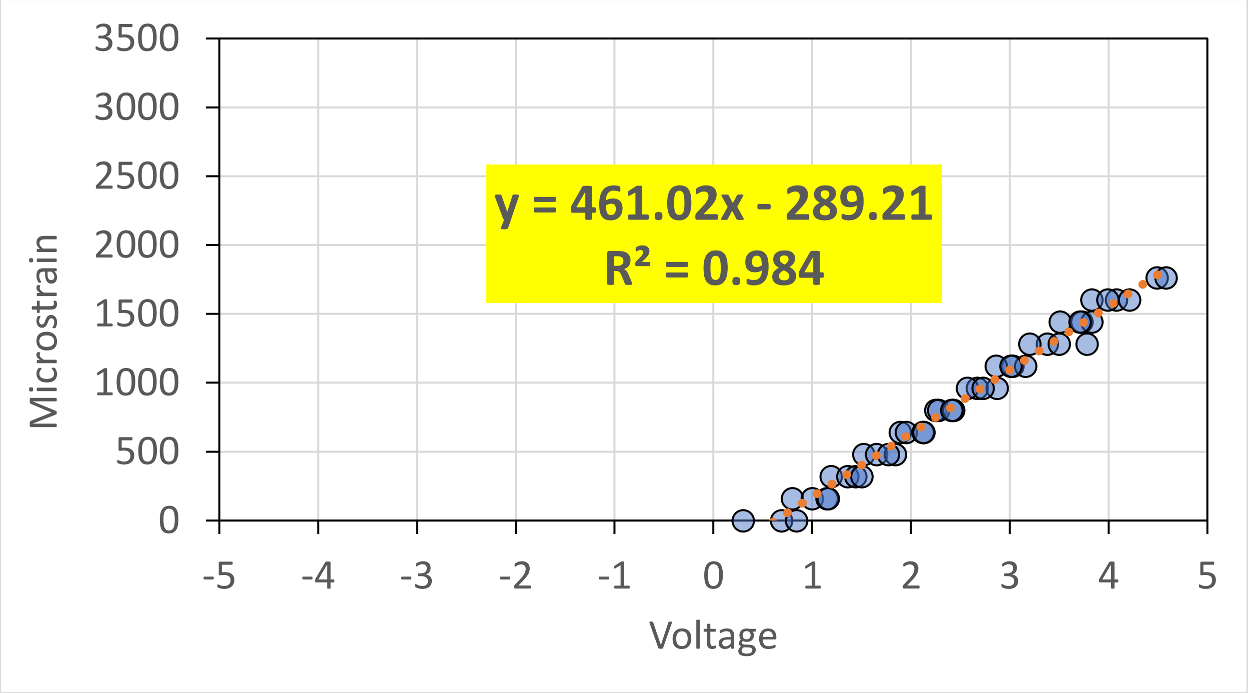

Figure A.40: ASG Channel 12 Calibration Graph

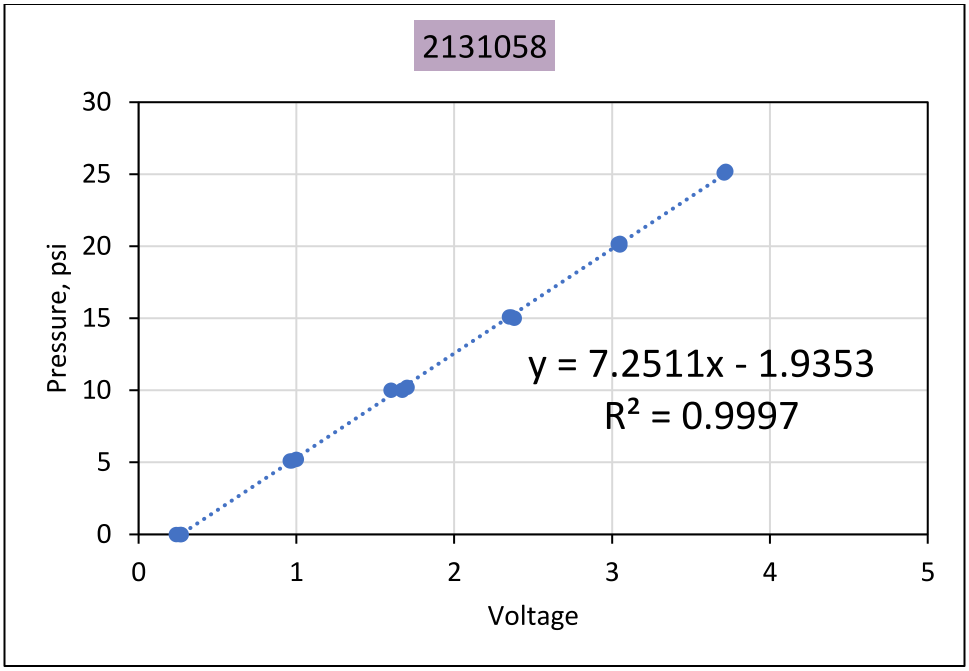

Figure A.41: EPC Channel 13 Calibration Graph

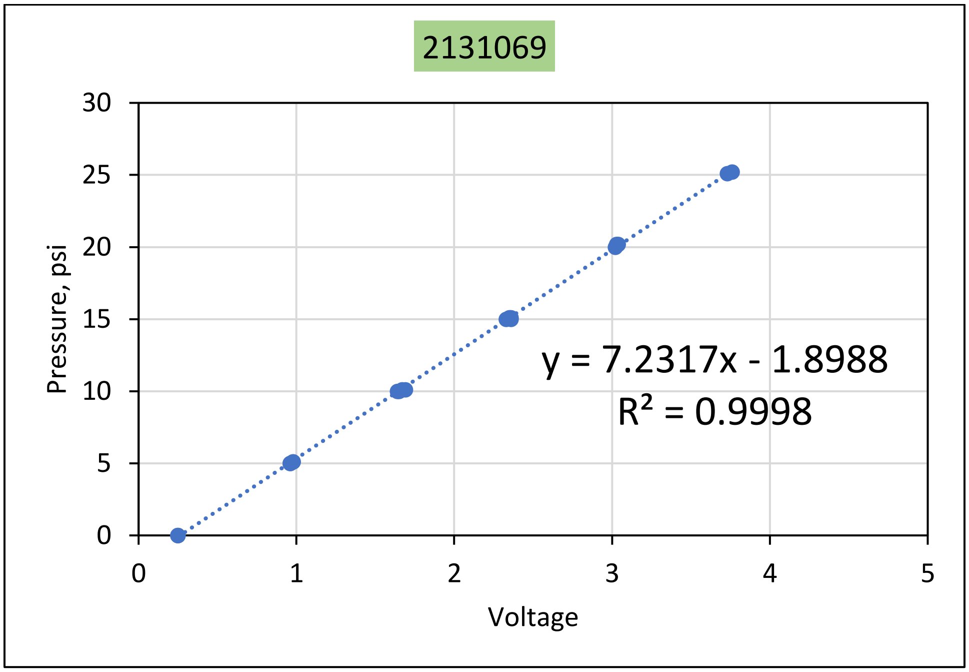

Figure A.42: EPC Channel 14 Calibration Graph

N7-Ctrl Section

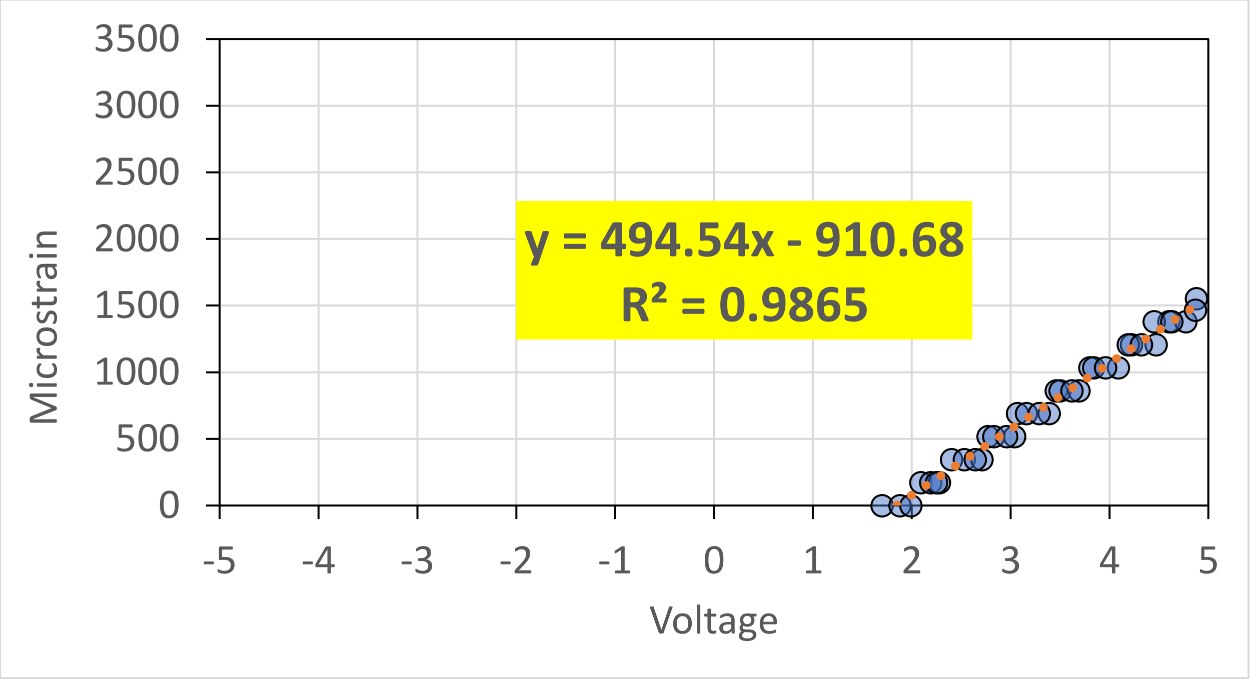

Figure A.43: ASG Channel 1 Calibration Graph

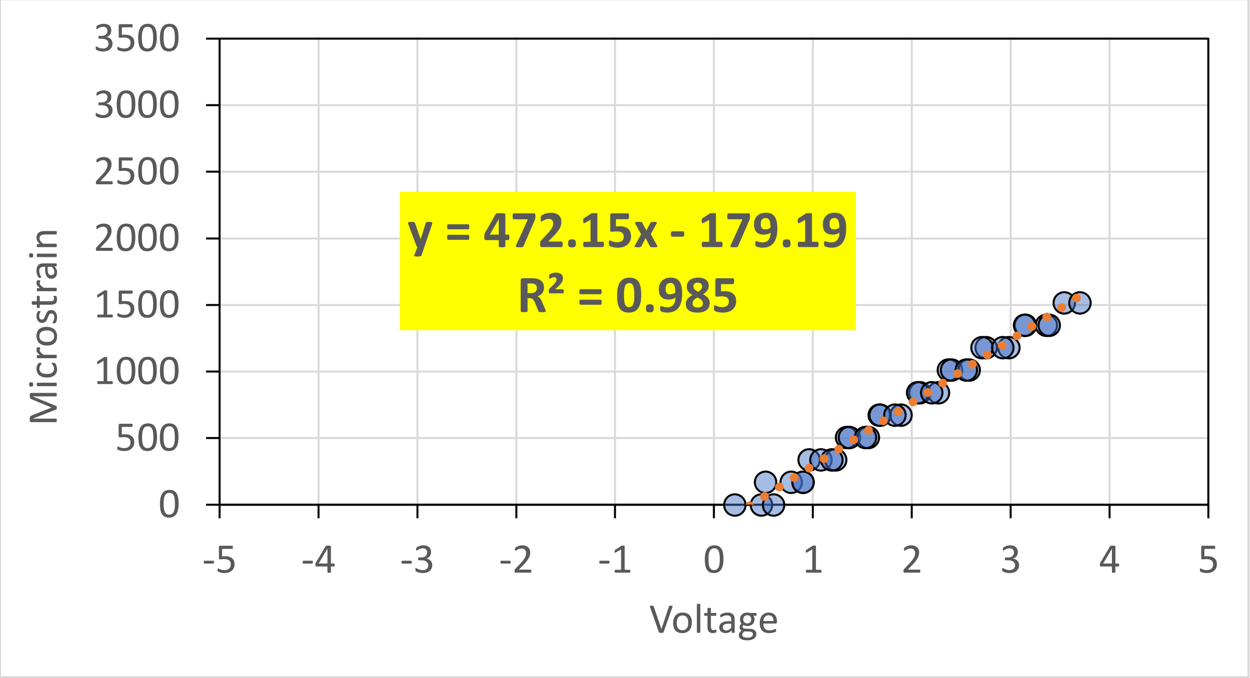

Figure A.44: ASG Channel 2 Calibration Graph

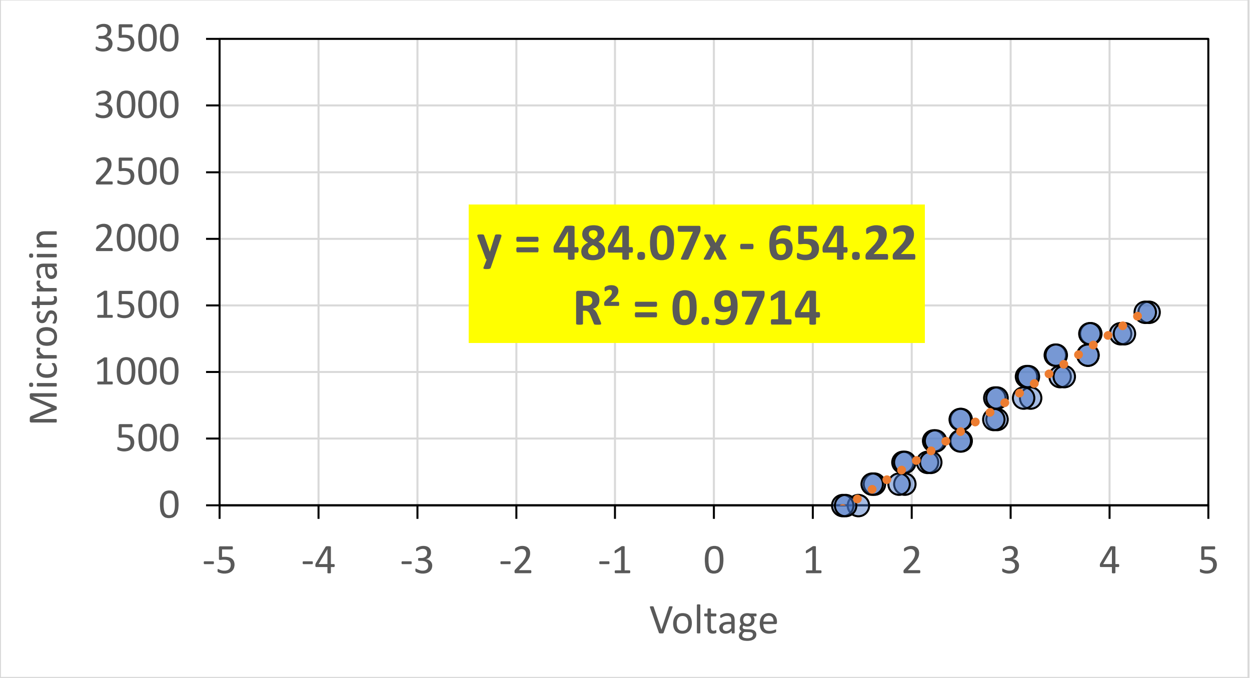

Figure A.45: ASG Channel 3 Calibration Graph

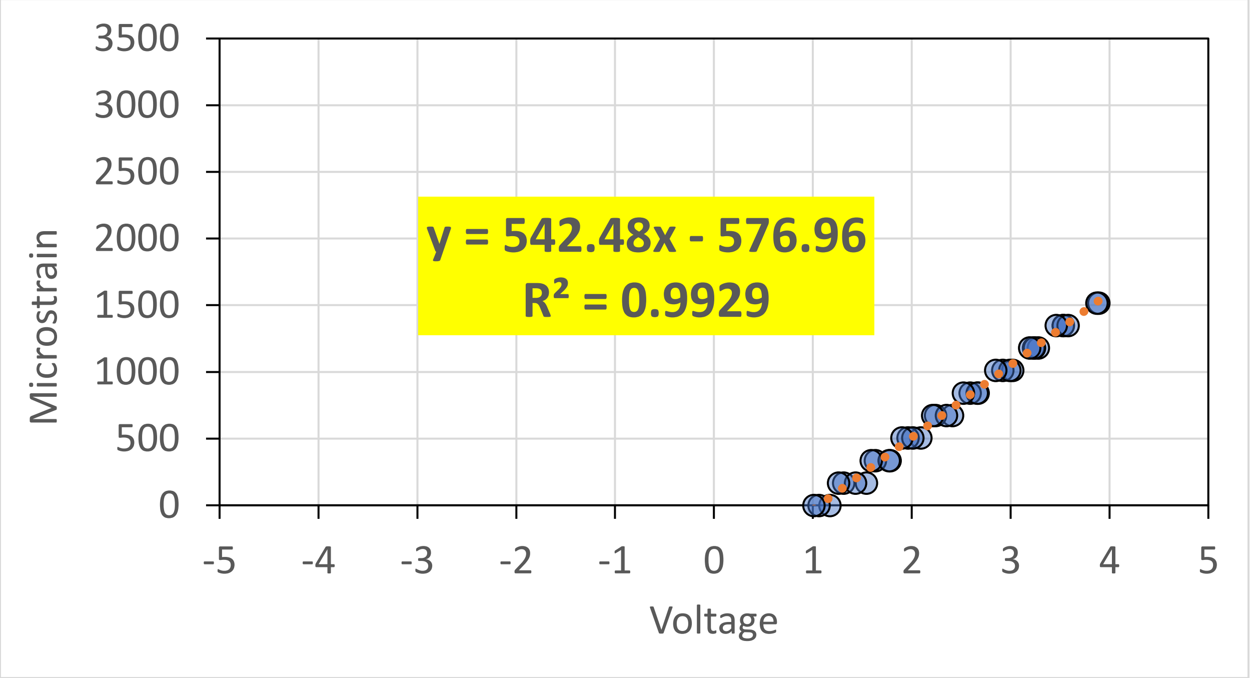

Figure A.46: ASG Channel 4 Calibration Graph

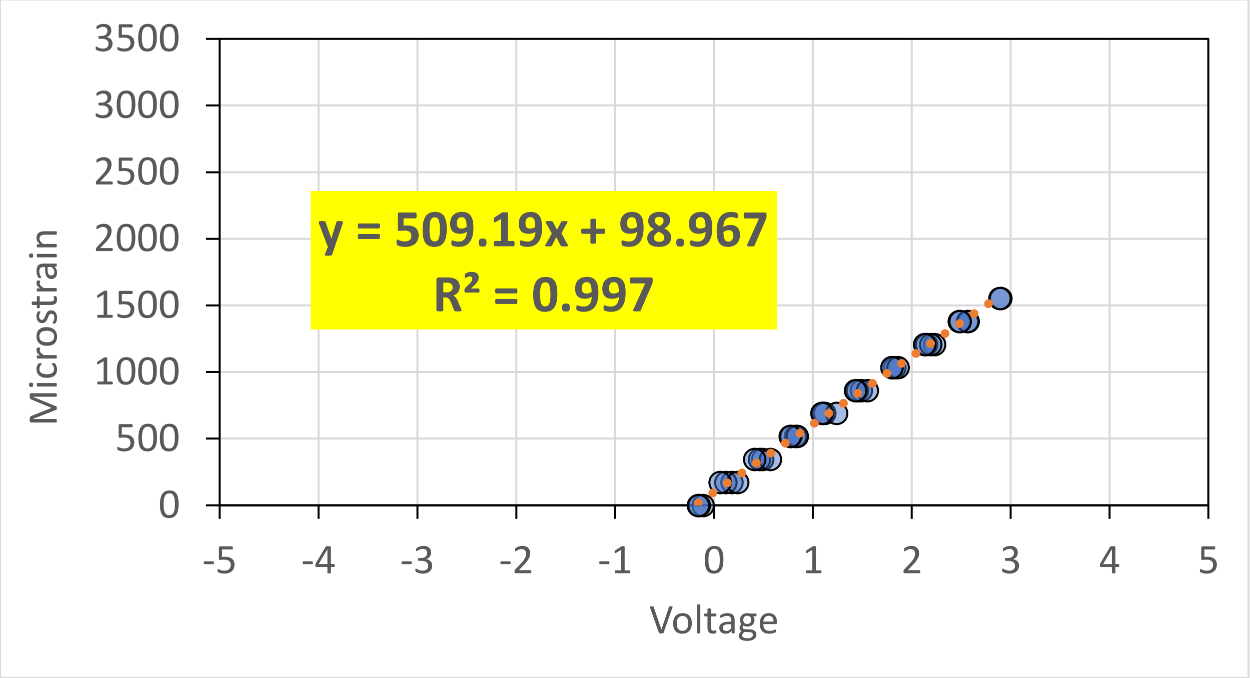

Figure A.47: ASG Channel 5 Calibration Graph

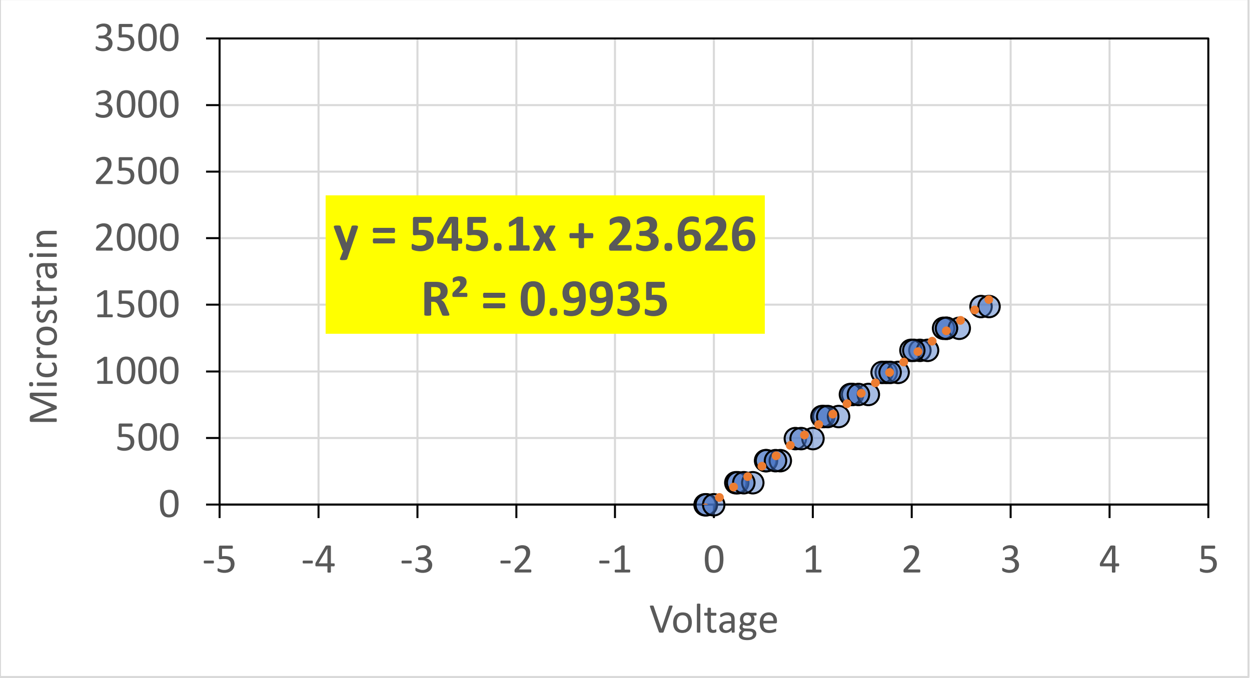

Figure A.48: ASG Channel 6 Calibration Graph

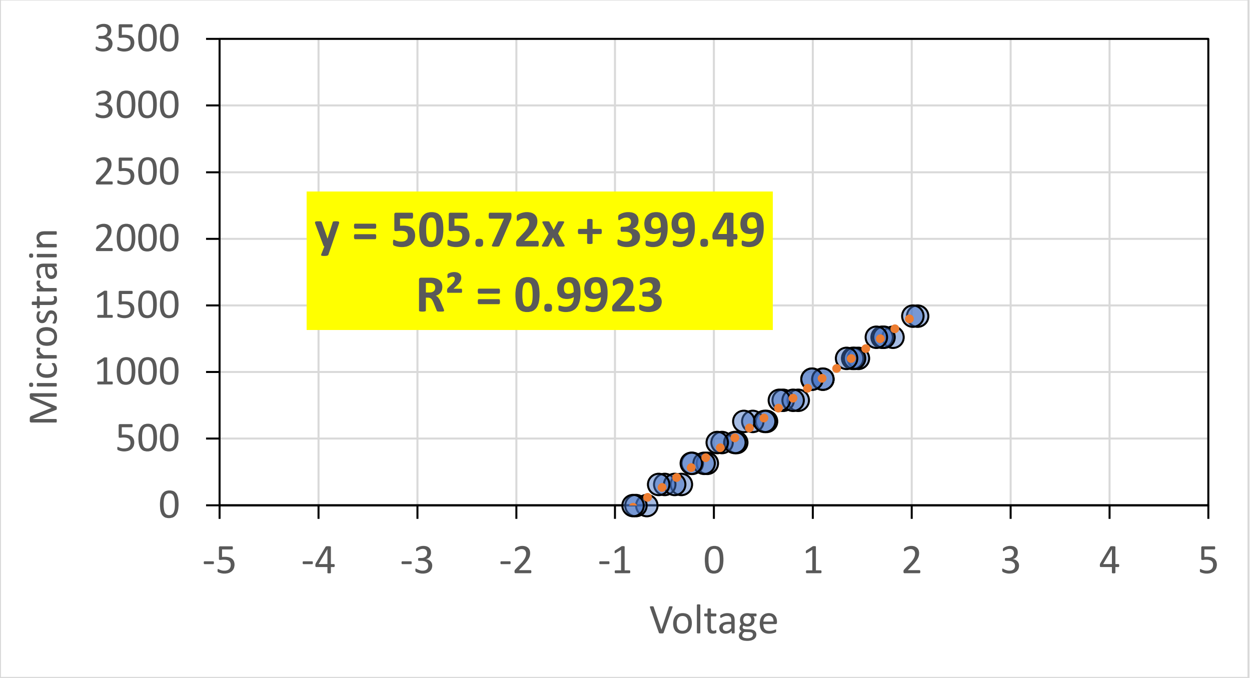

Figure A.49: ASG Channel 7 Calibration Graph

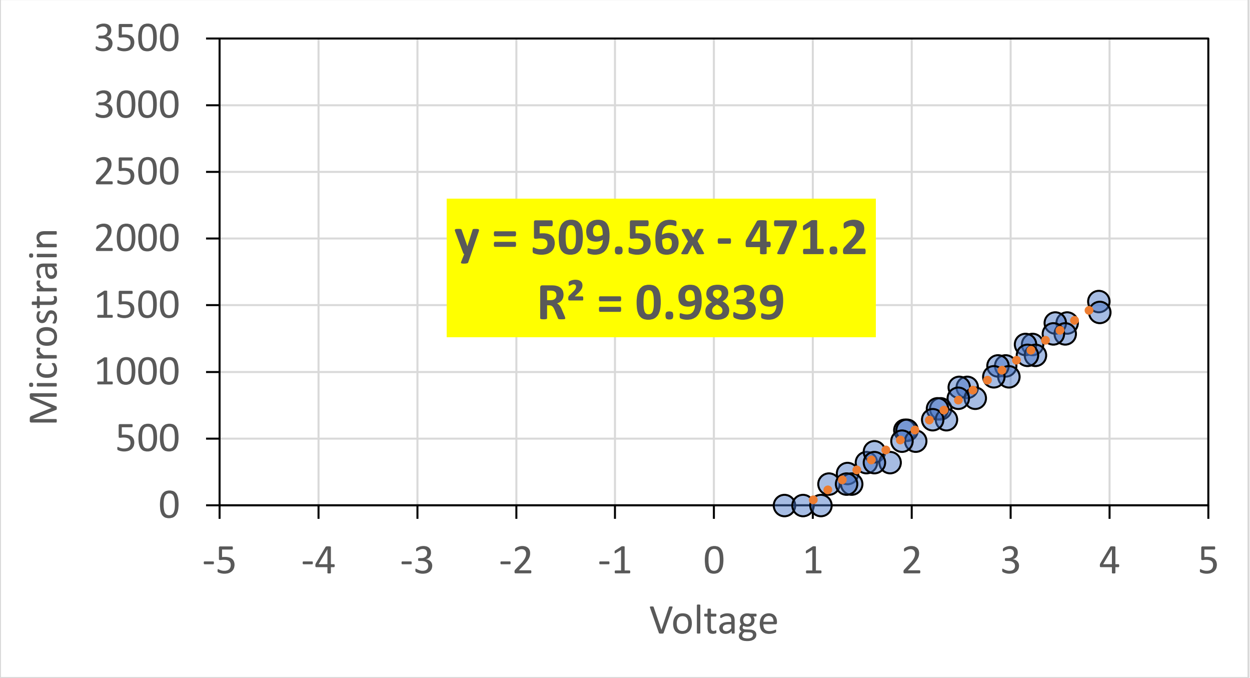

Figure A.50: ASG Channel 8 Calibration Graph

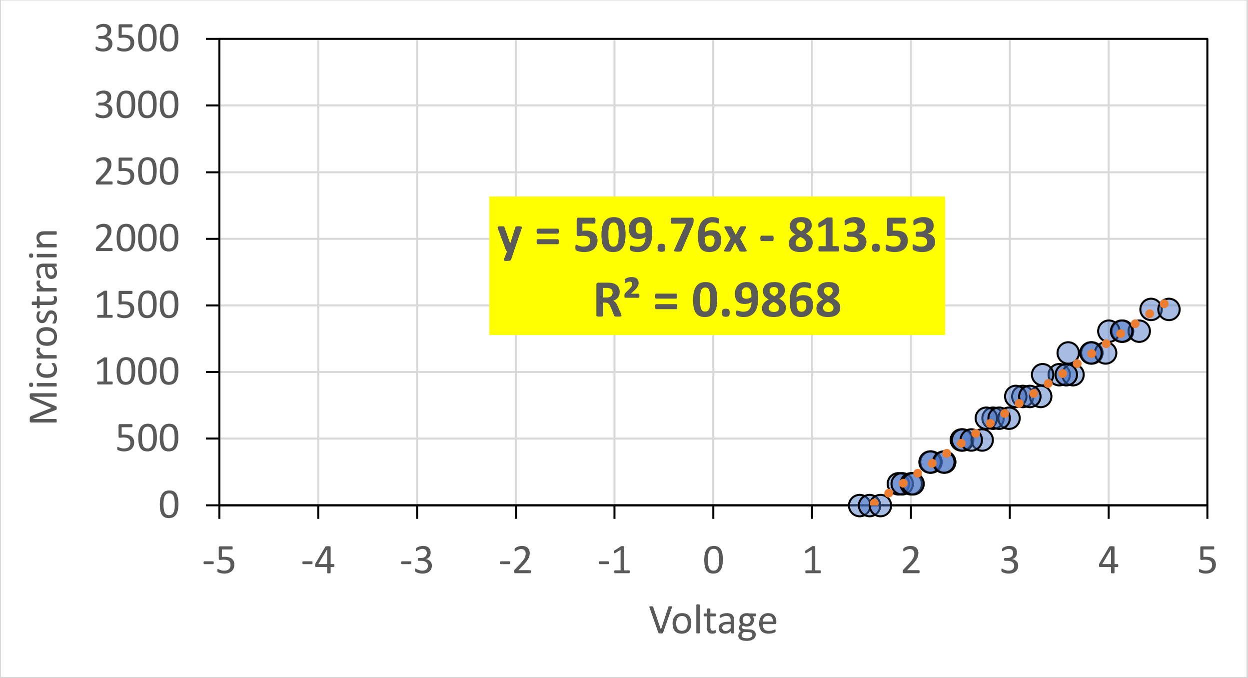

Figure A.51: ASG Channel 9 Calibration Graph

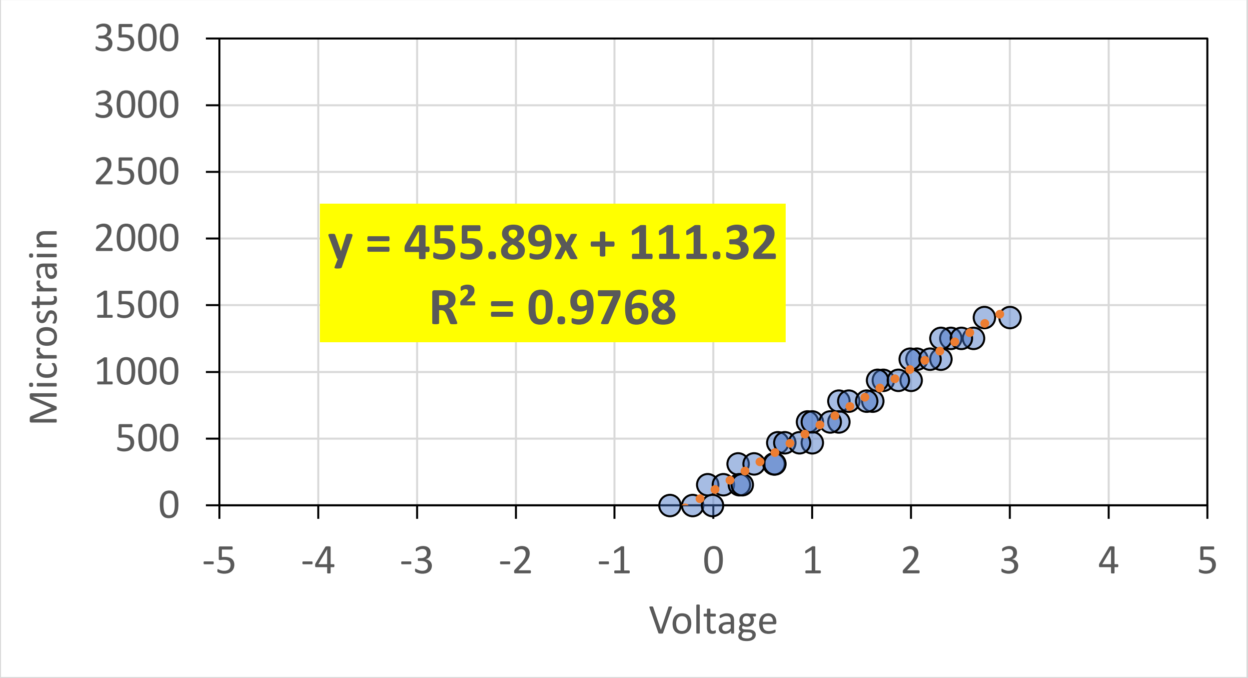

Figure A.52: ASG Channel 10 Calibration Graph

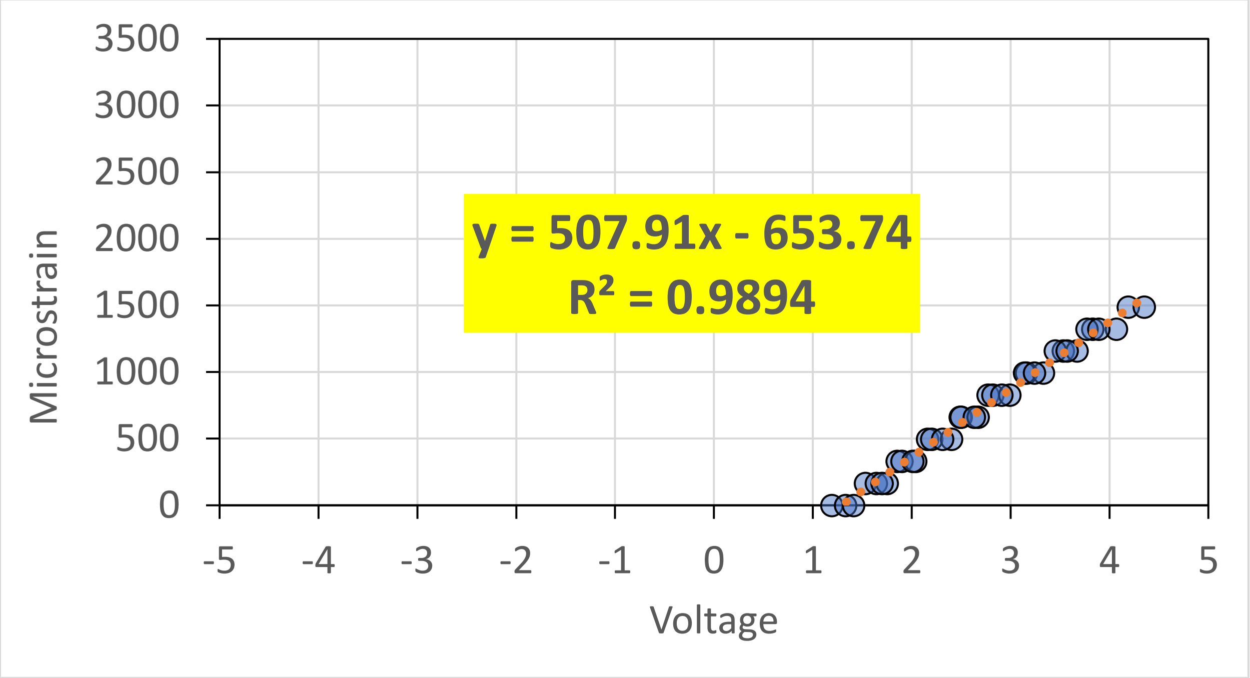

Figure A.53: ASG Channel 11 Calibration Graph

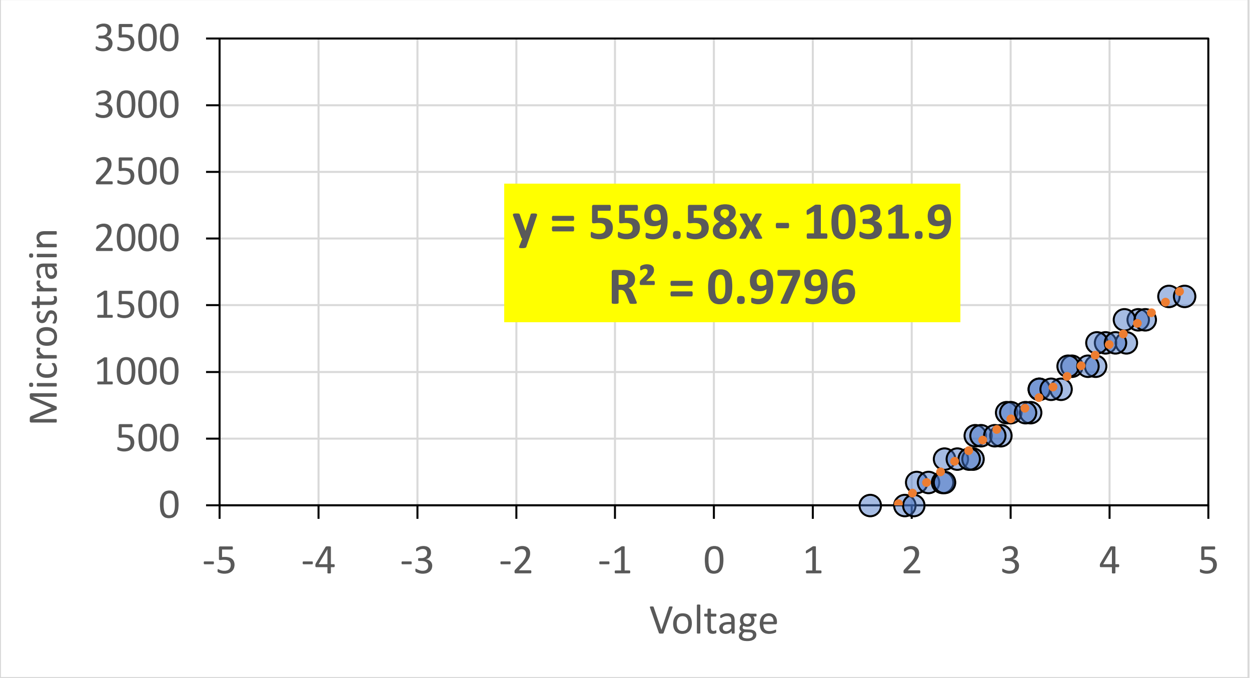

Figure A.54: ASG Channel 12 Calibration Graph

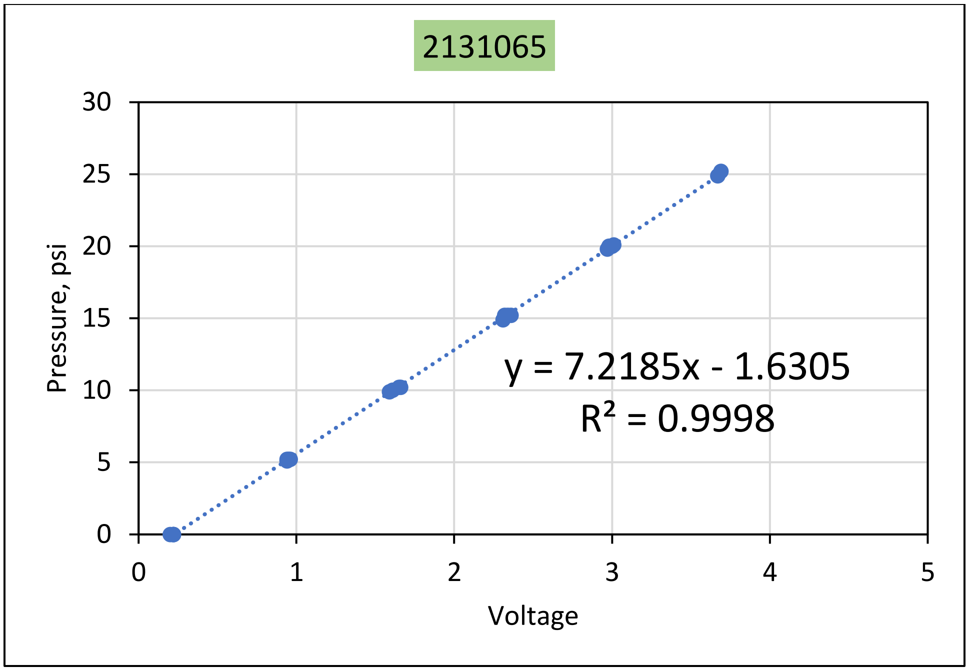

Figure A.55: EPC Channel 13 Calibration Graph

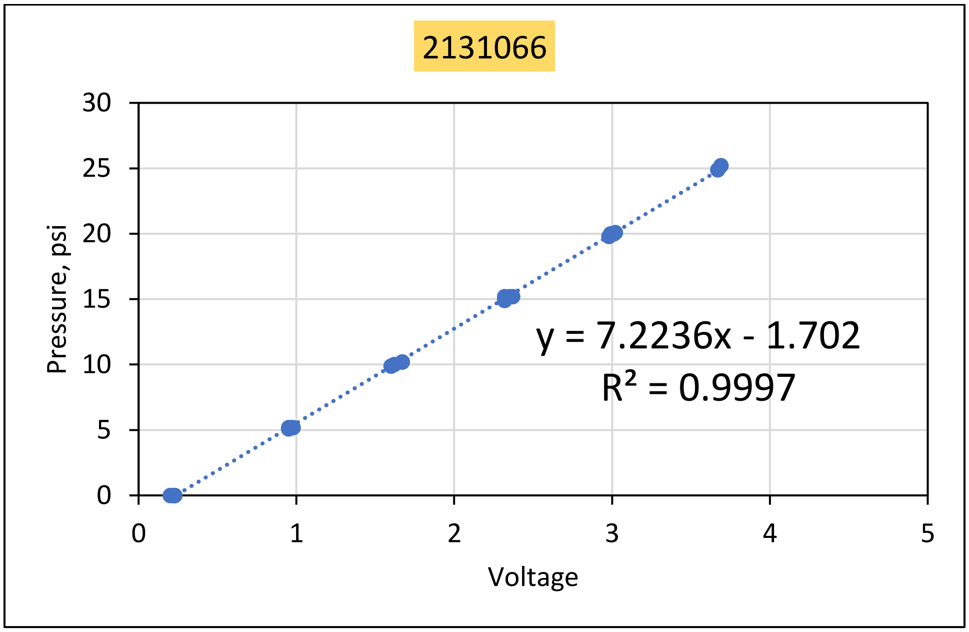

Figure A.56: EPC Channel 14 Calibration Graph

S5-DryPlastic Section

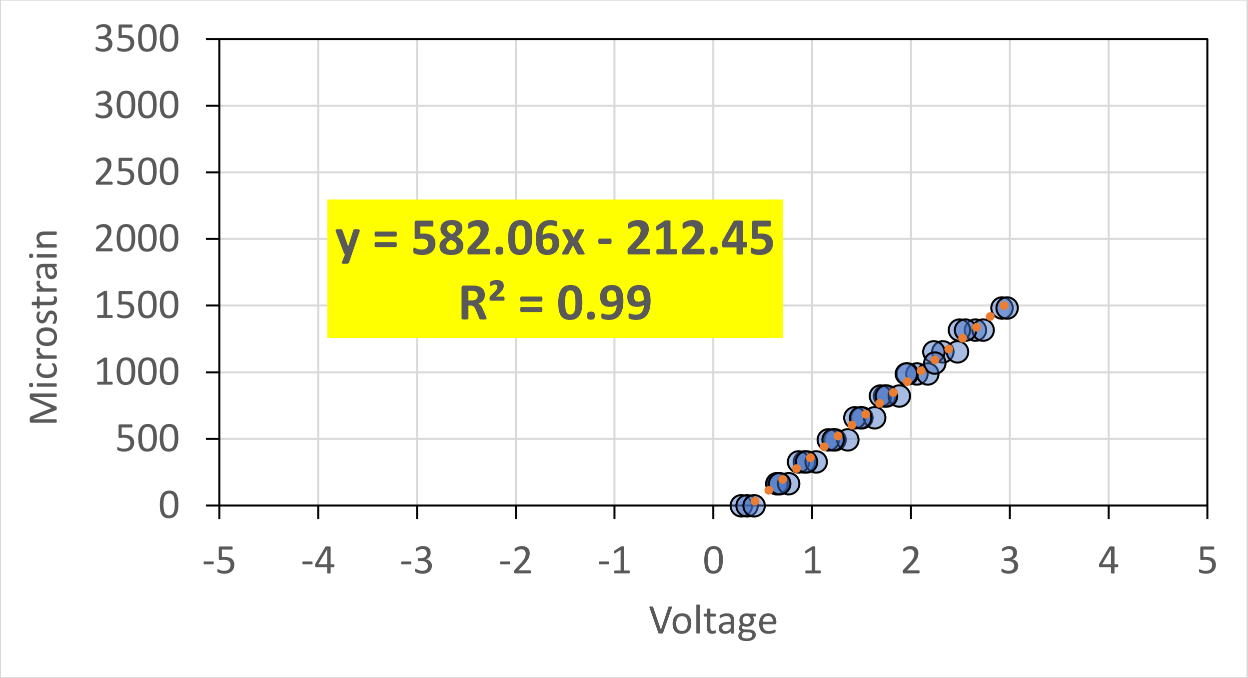

Figure A.57: ASG Channel 1 Calibration Graph

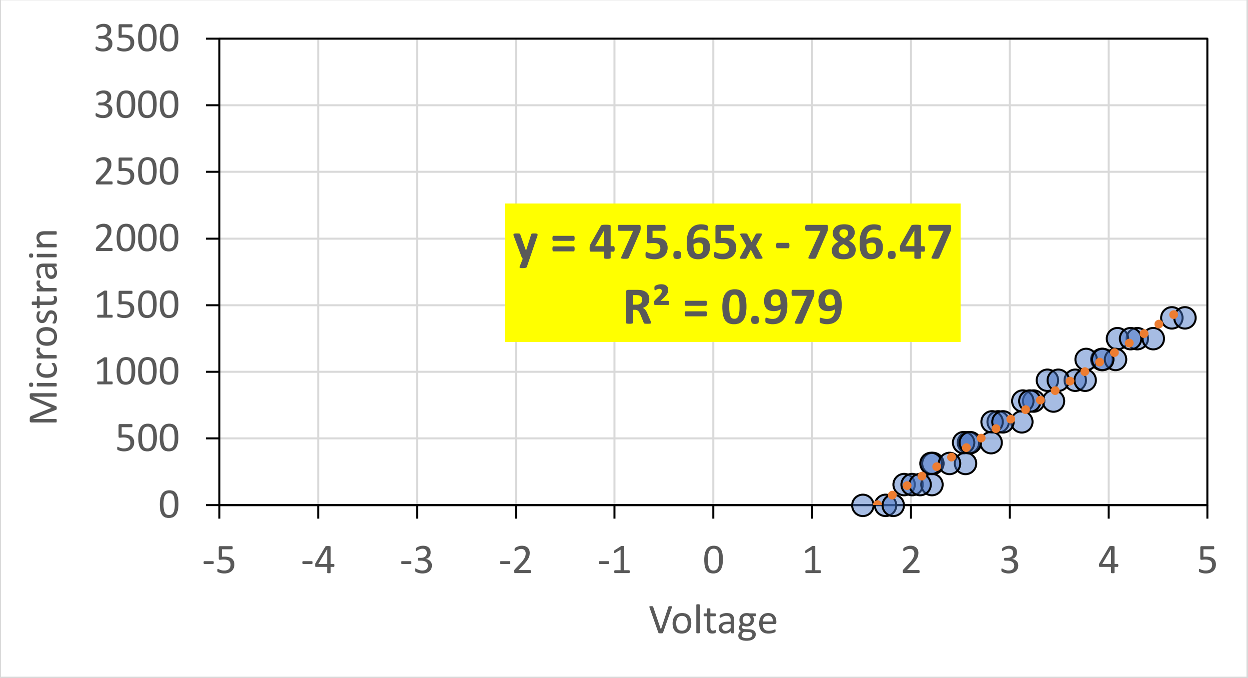

Figure A.58: ASG Channel 2 Calibration Graph

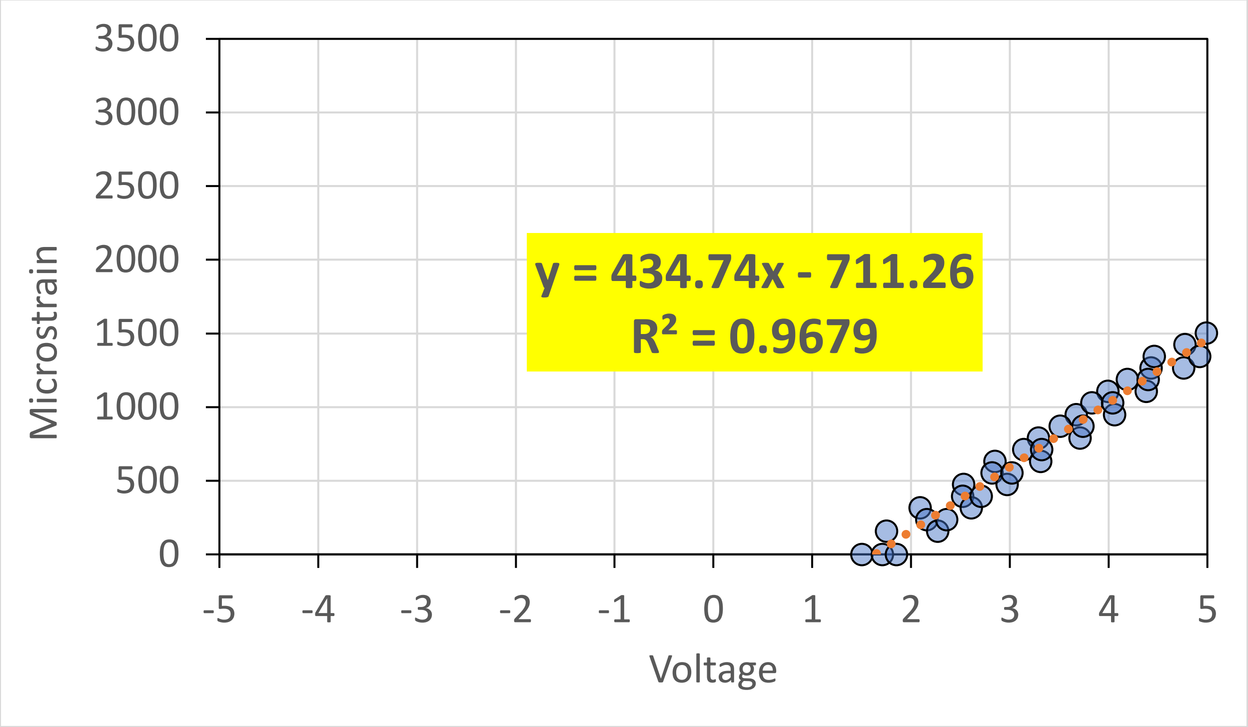

Figure A.59: ASG Channel 3 Calibration Graph

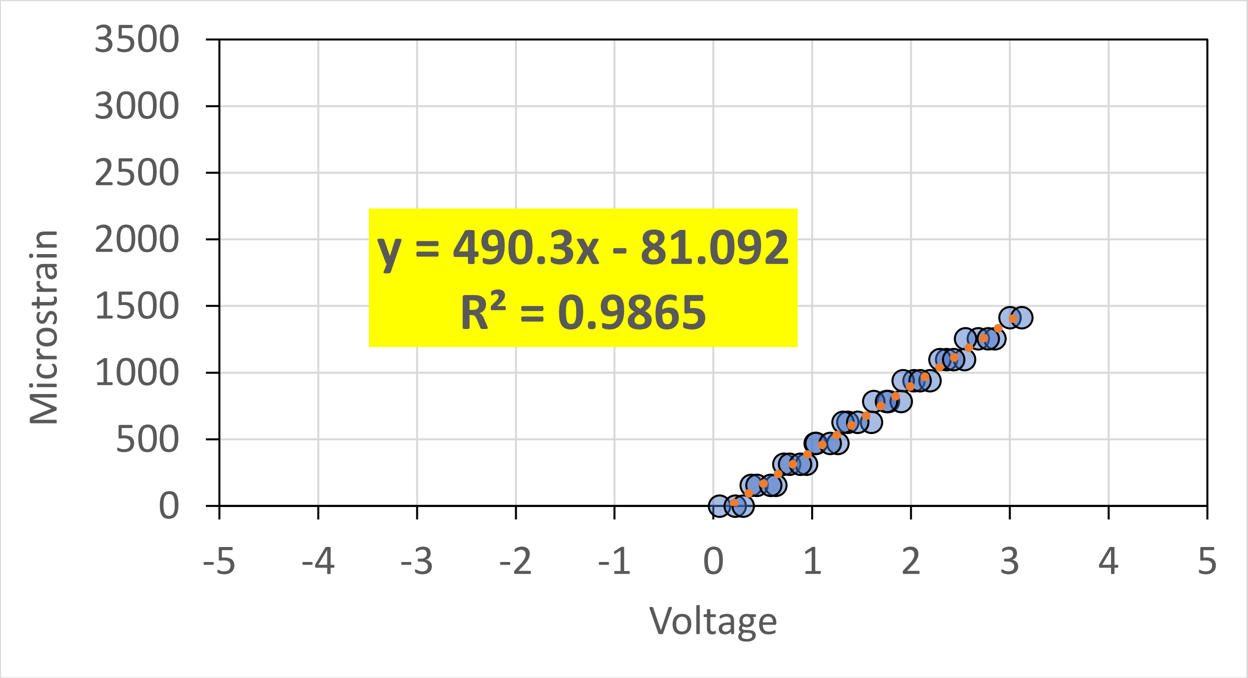

Figure A.60: ASG Channel 4 Calibration Graph

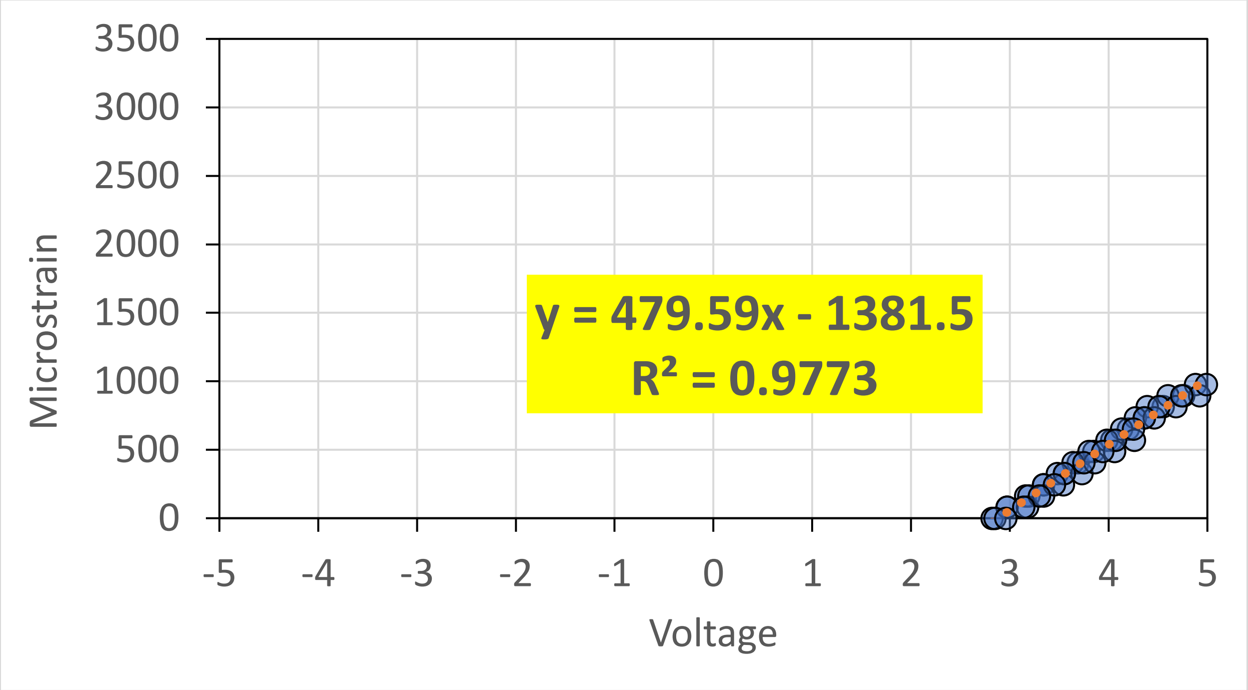

Figure A.61: ASG Channel 5 Calibration Graph

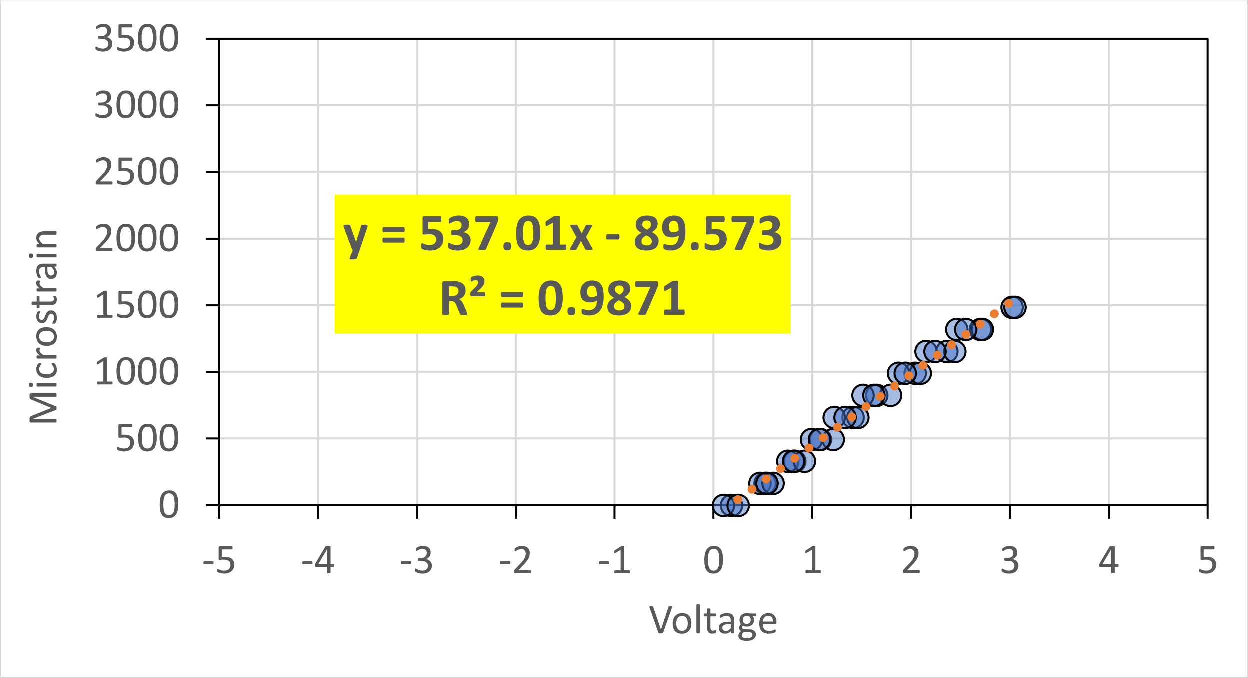

Figure A.62: ASG Channel 6 Calibration Graph

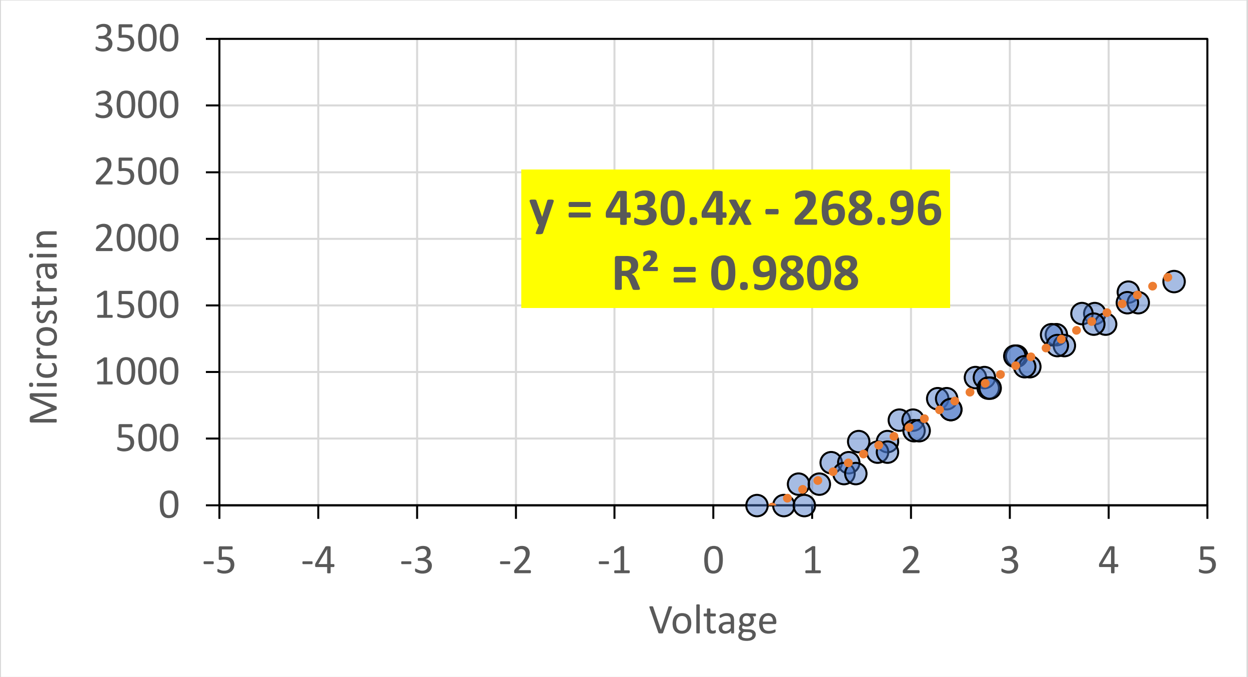

Figure A.63: ASG Channel 7 Calibration Graph

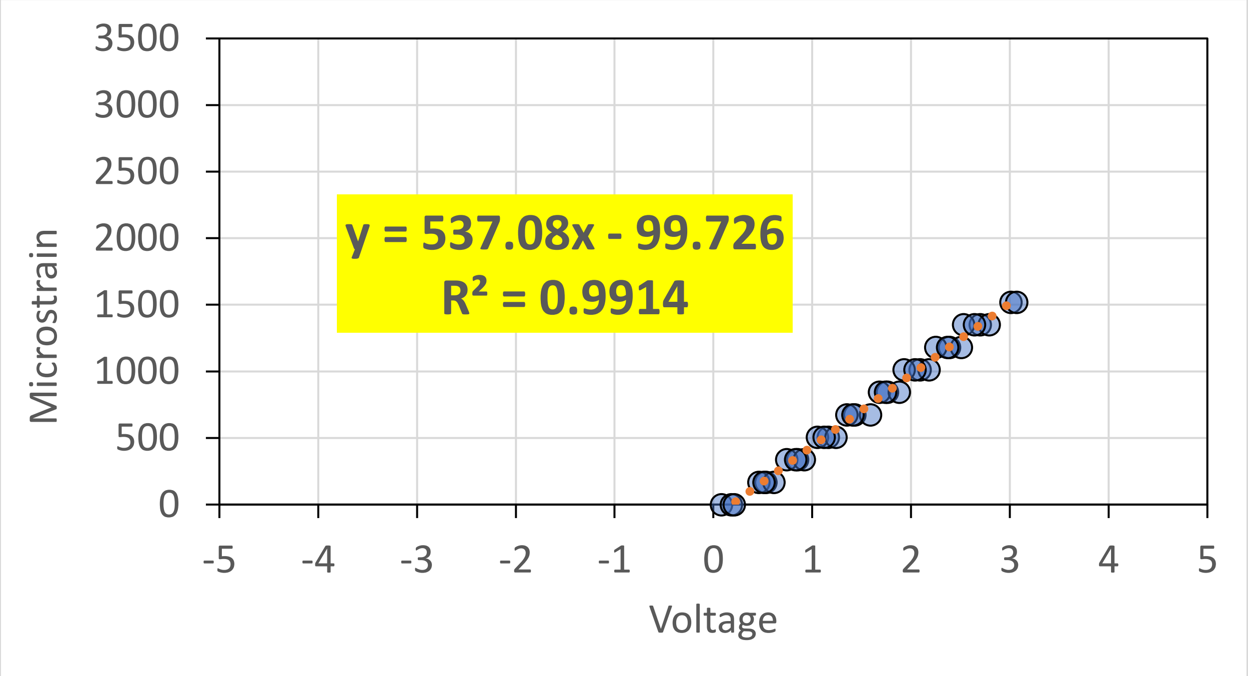

Figure A.64: ASG Channel 8 Calibration Graph

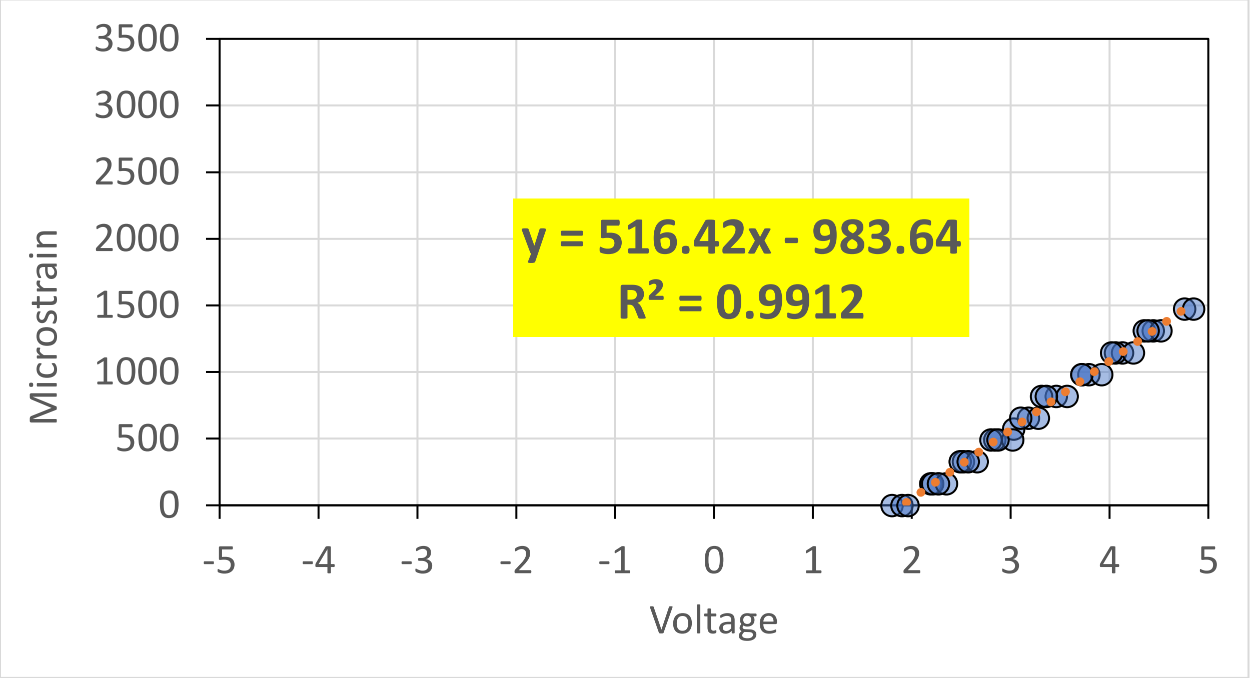

Figure A.65: ASG Channel 9 Calibration Graph

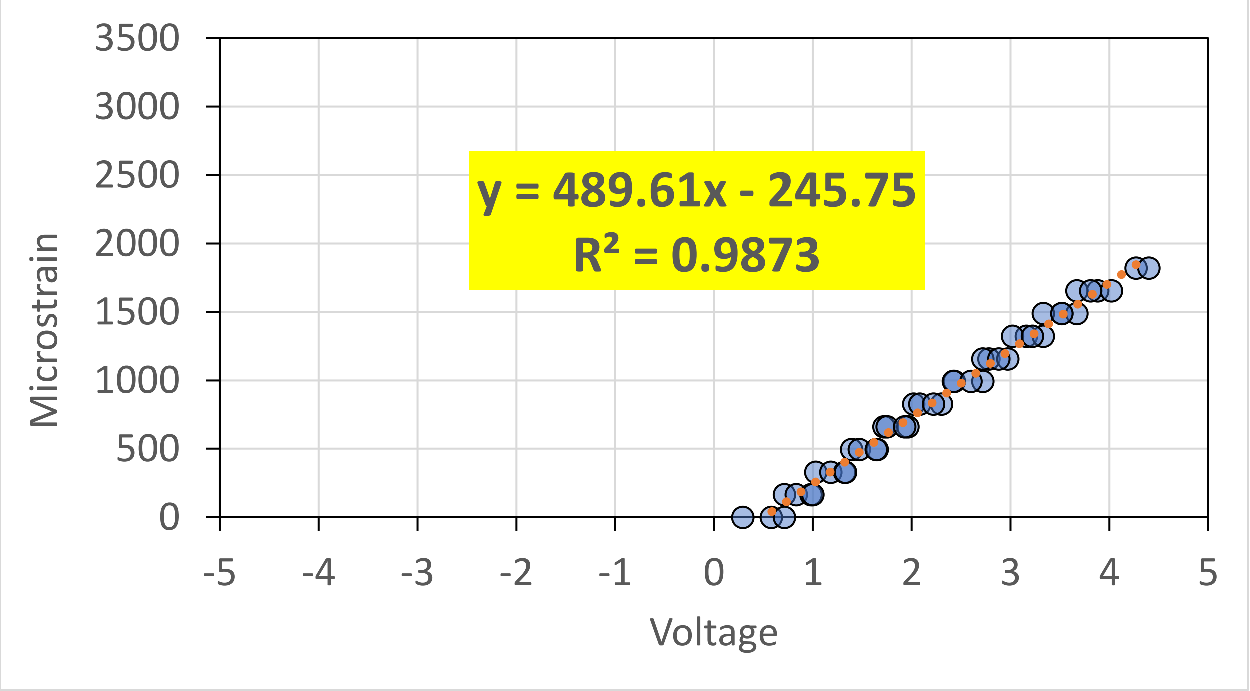

Figure A.66: ASG Channel 10 Calibration Graph

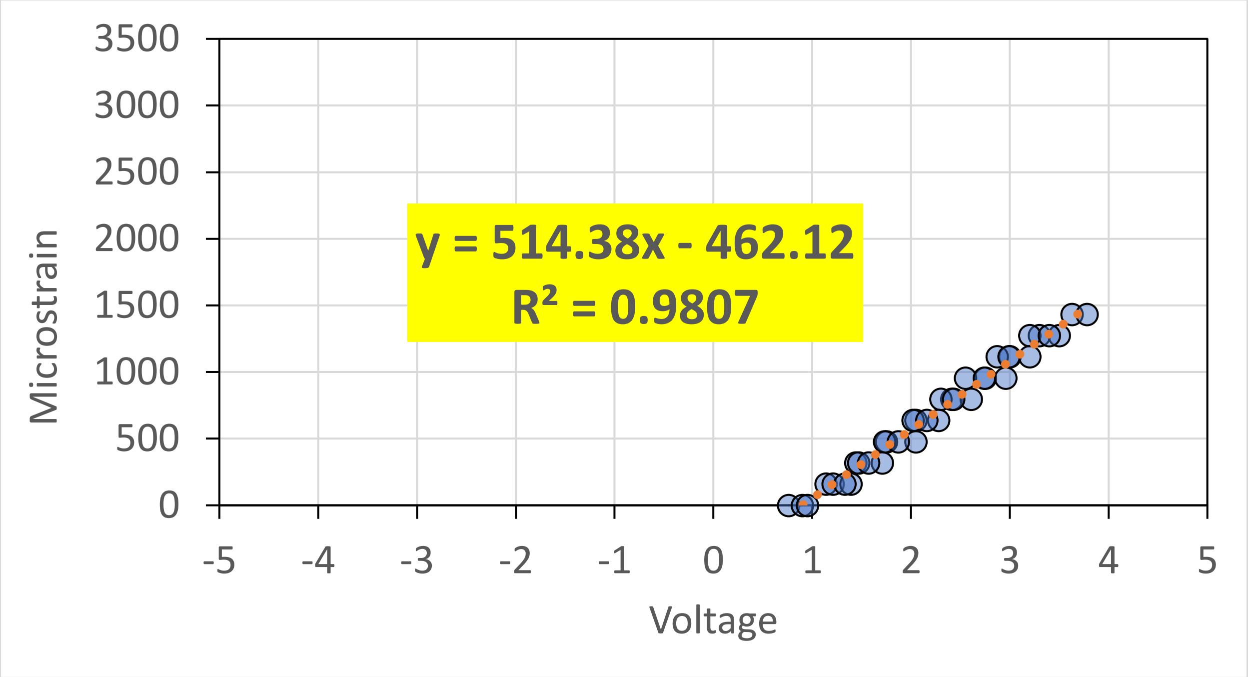

Figure A.67: ASG Channel 11 Calibration Graph

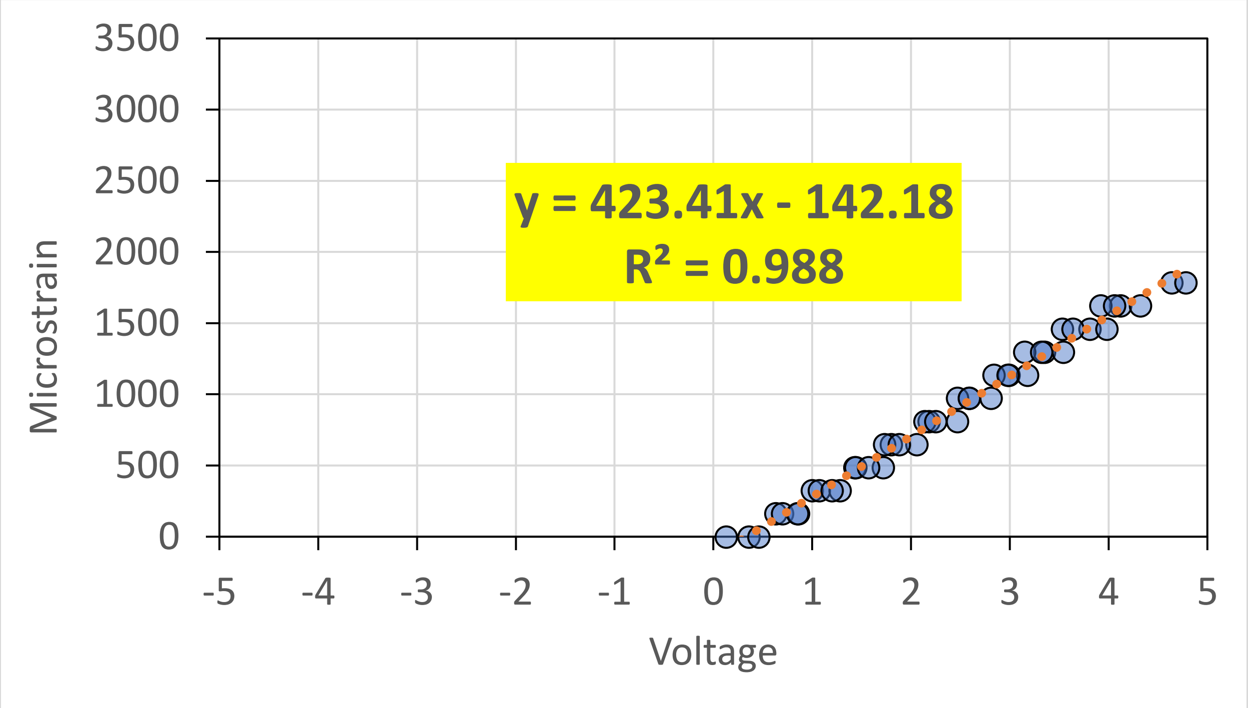

Figure A.68: ASG Channel 12 Calibration Graph

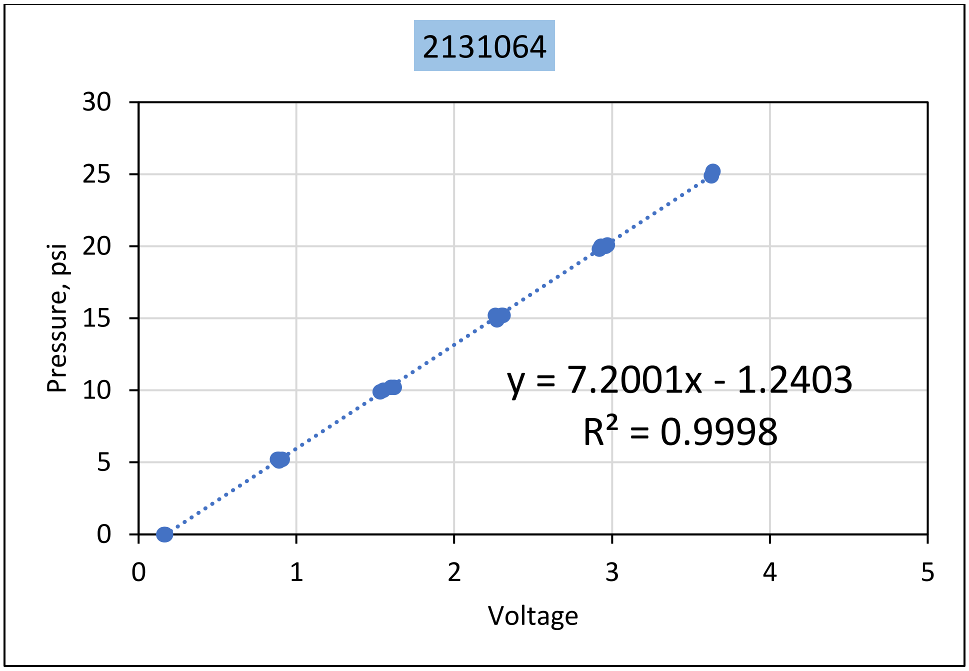

Figure A.69: EPC Channel 13 Calibration Graph

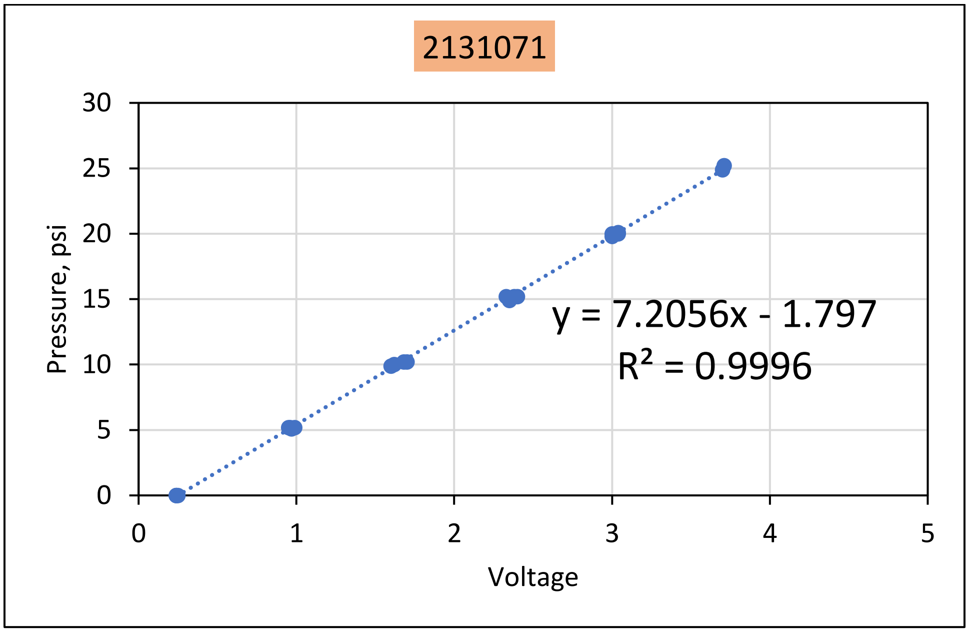

Figure A.70: EPC Channel 14 Calibration Graph

S6-WetPlastic Section

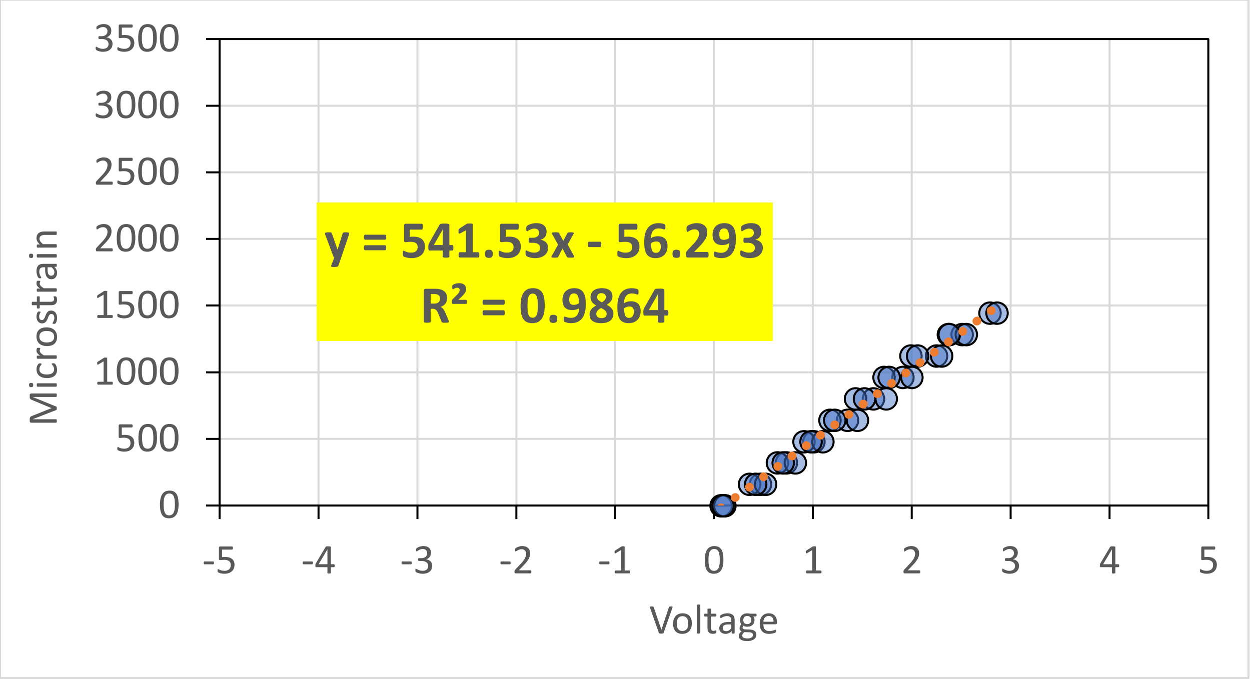

Figure A.71: ASG Channel 1 Calibration Graph

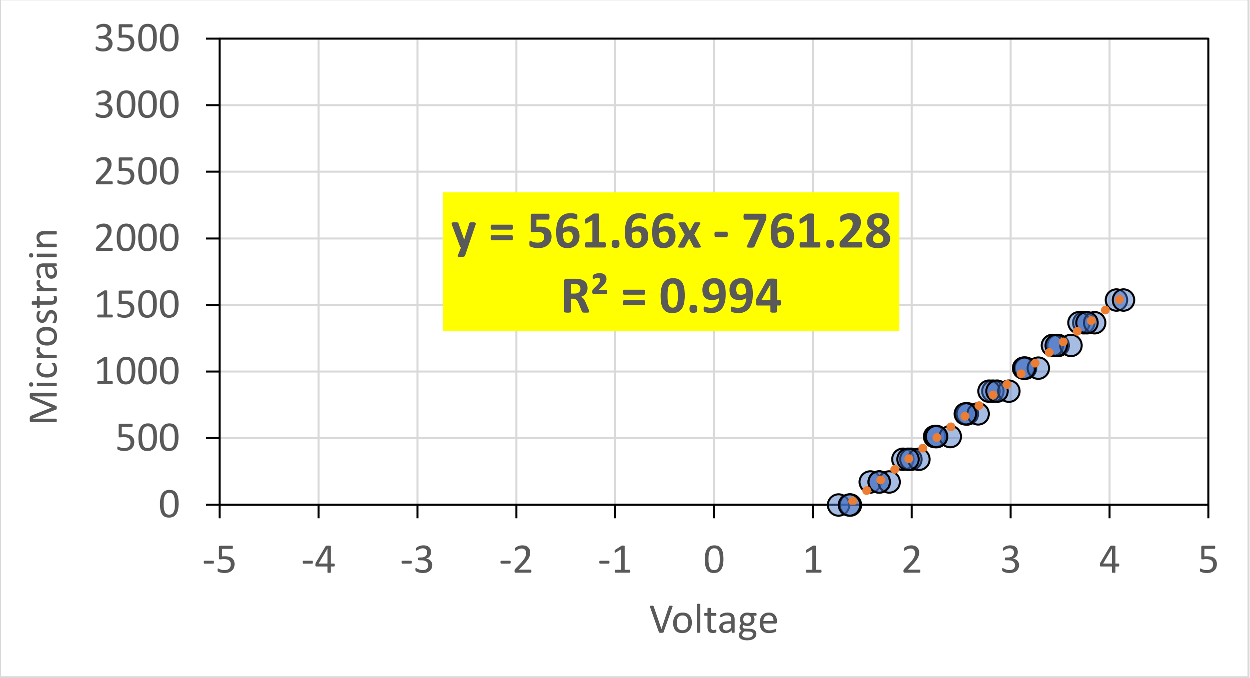

Figure A.72: ASG Channel 2 Calibration Graph

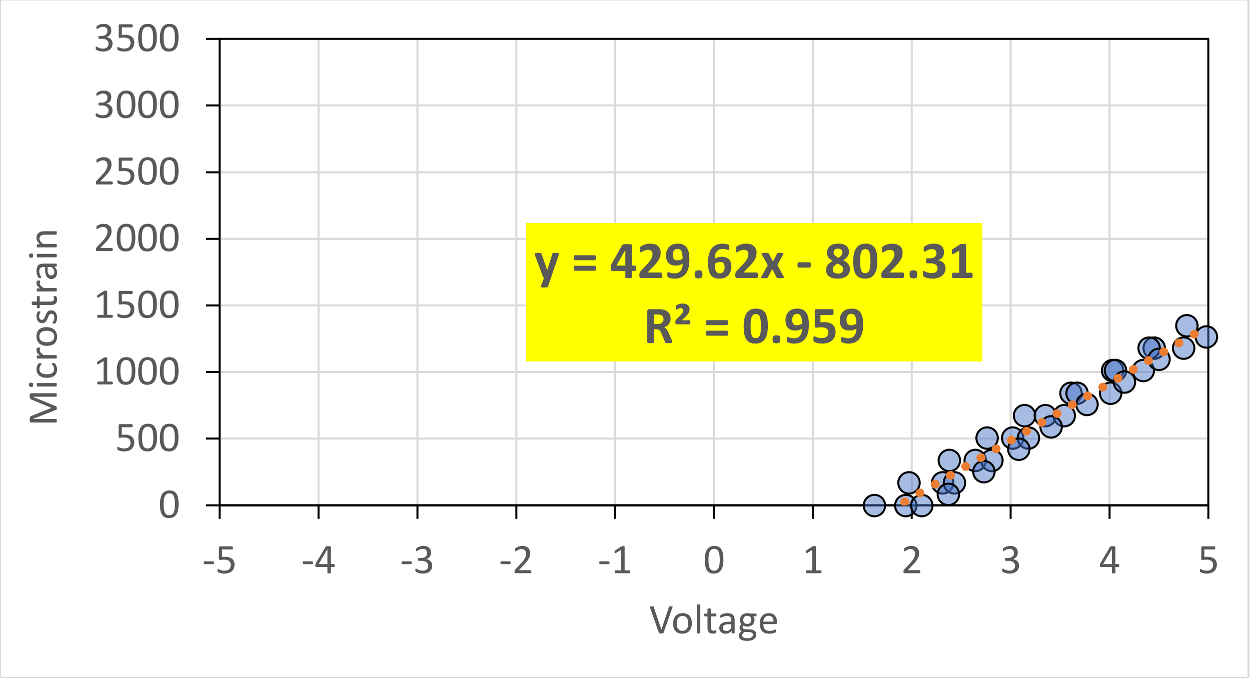

Figure A.73: ASG Channel 3 Calibration Graph

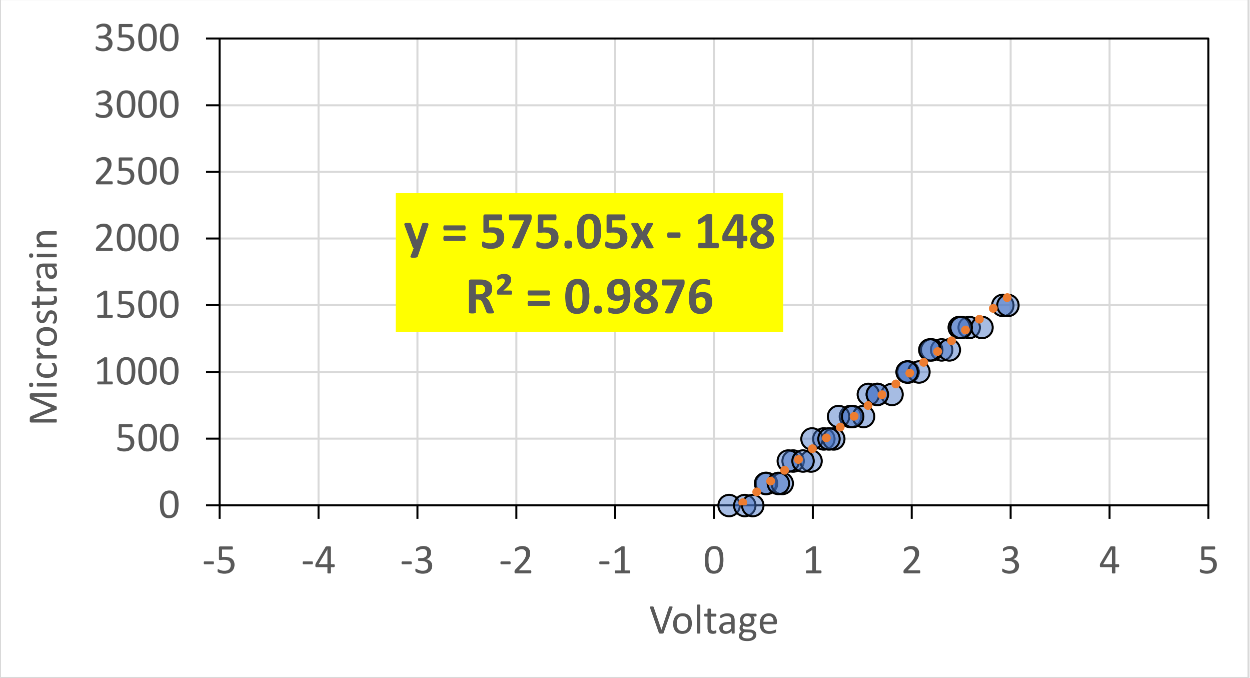

Figure A.74: ASG Channel 4 Calibration Graph

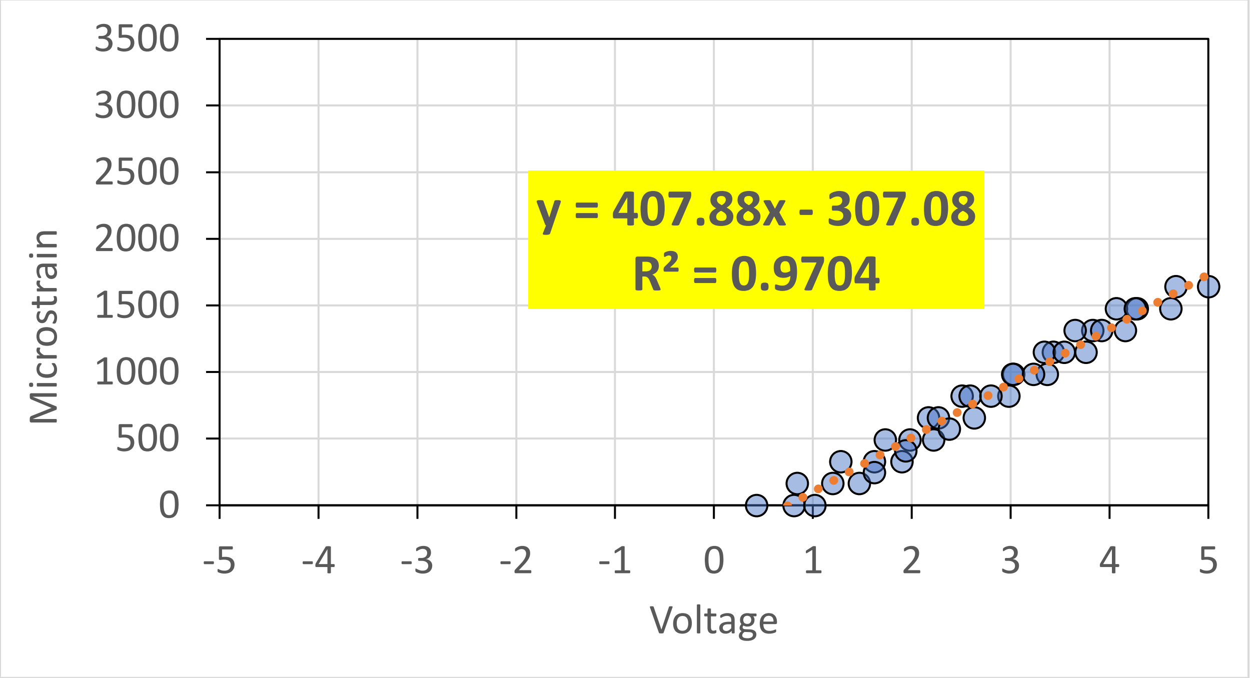

Figure A.75: ASG Channel 5 Calibration Graph

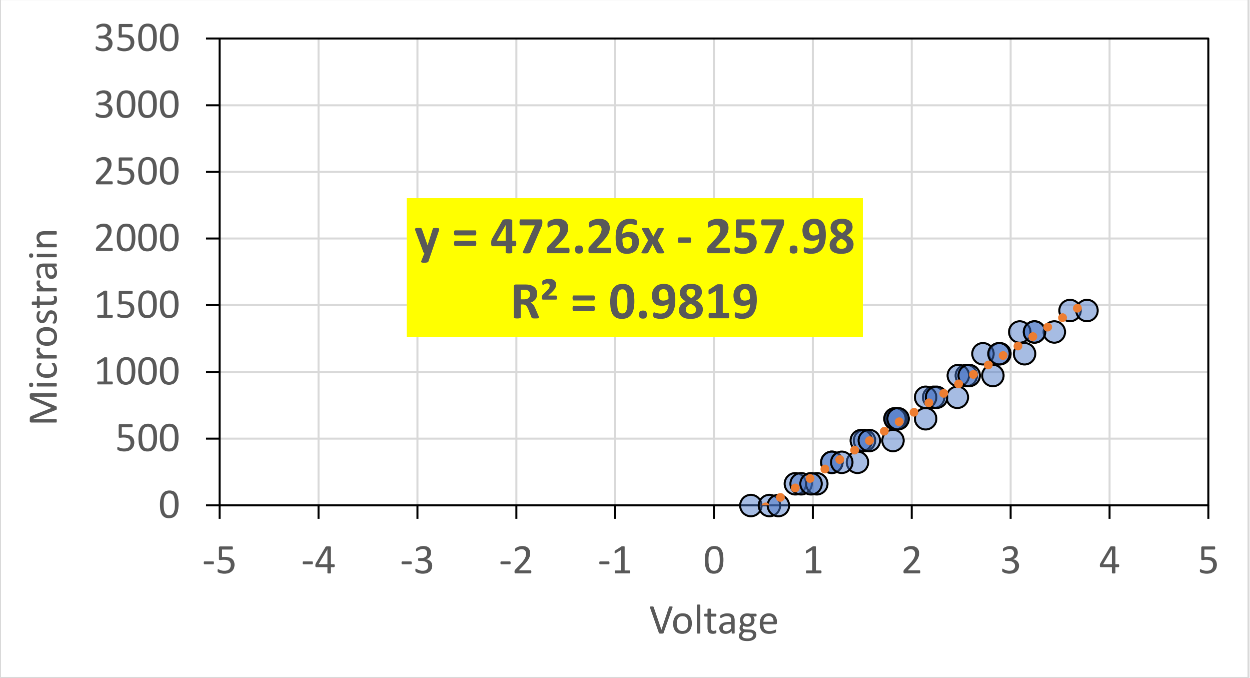

Figure A.76: ASG Channel 6 Calibration Graph

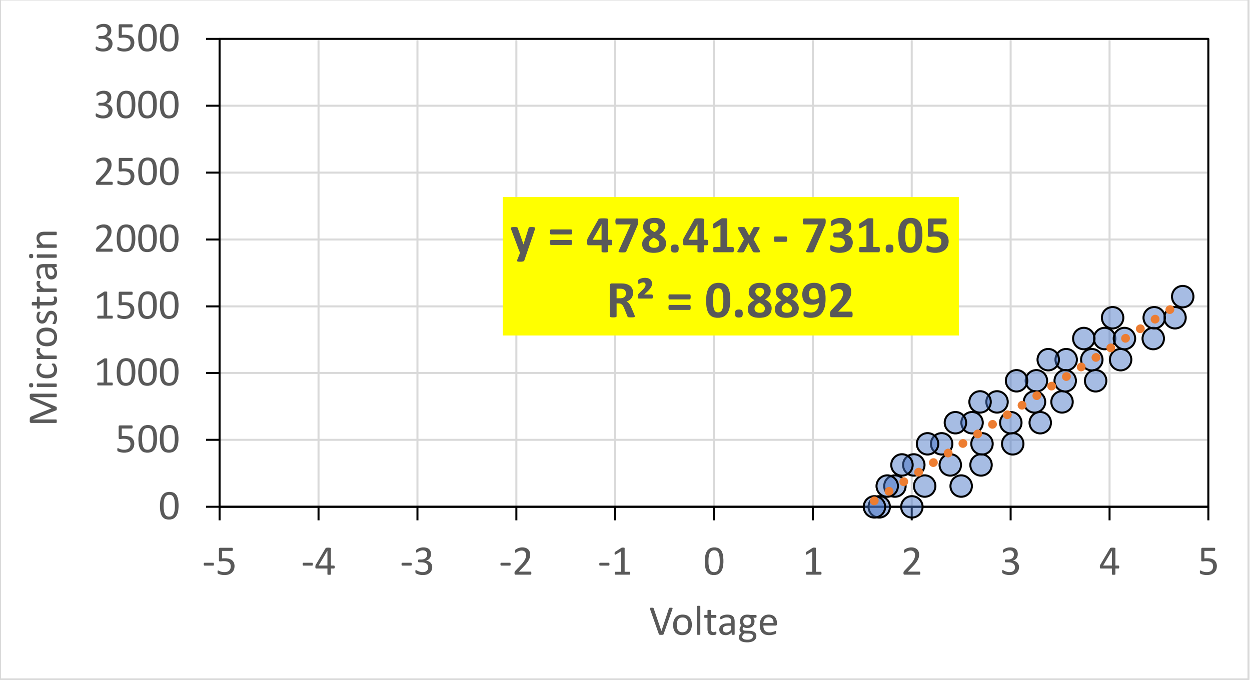

Figure A.77: ASG Channel 7 Calibration Graph

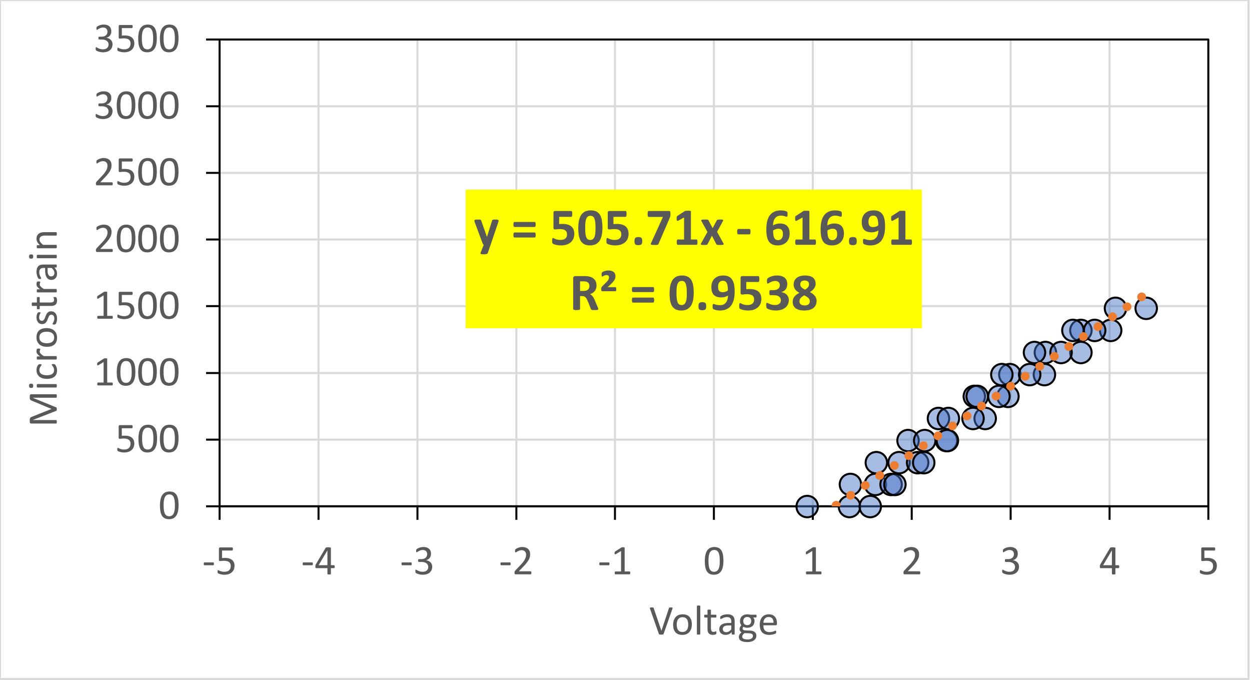

Figure A.78: ASG Channel 8 Calibration Graph

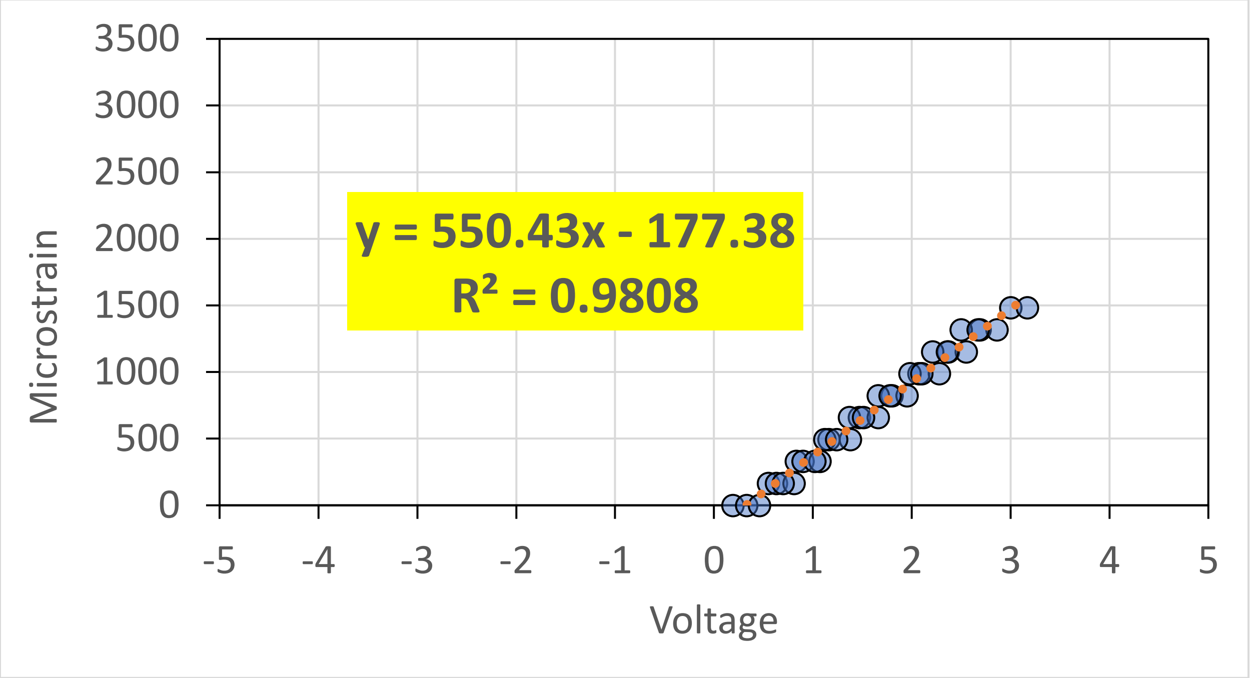

Figure A.79: ASG Channel 9 Calibration Graph

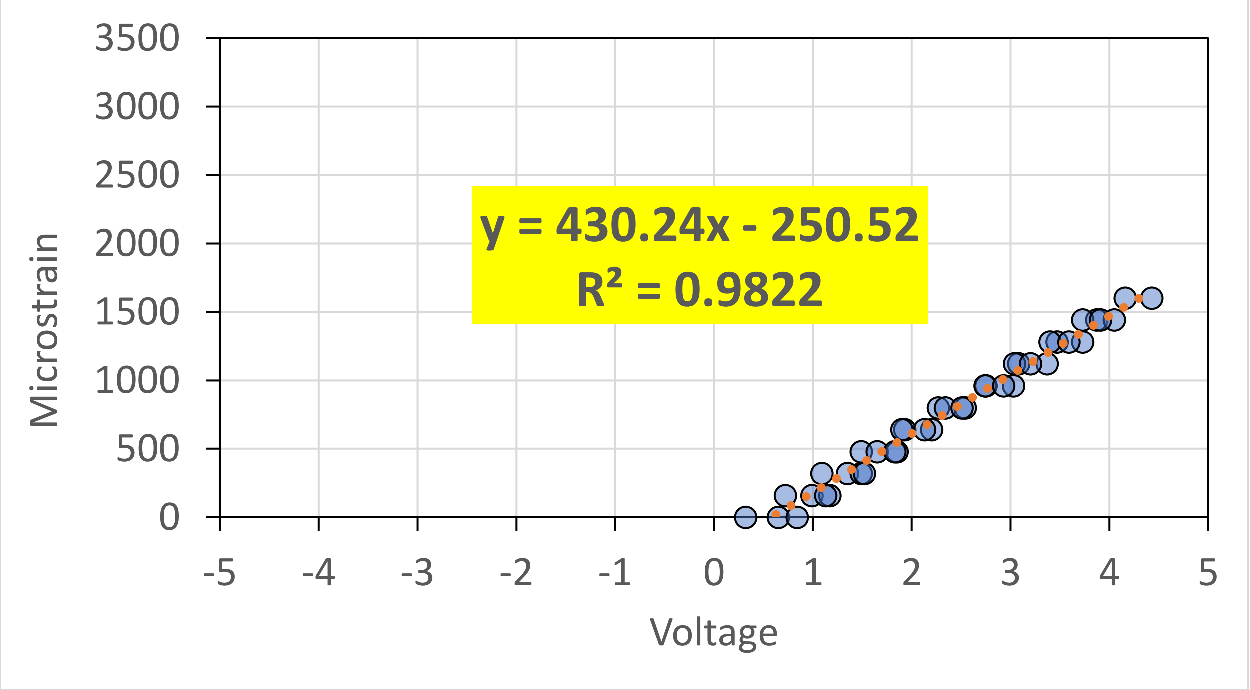

Figure A.80: ASG Channel 10 Calibration Graph

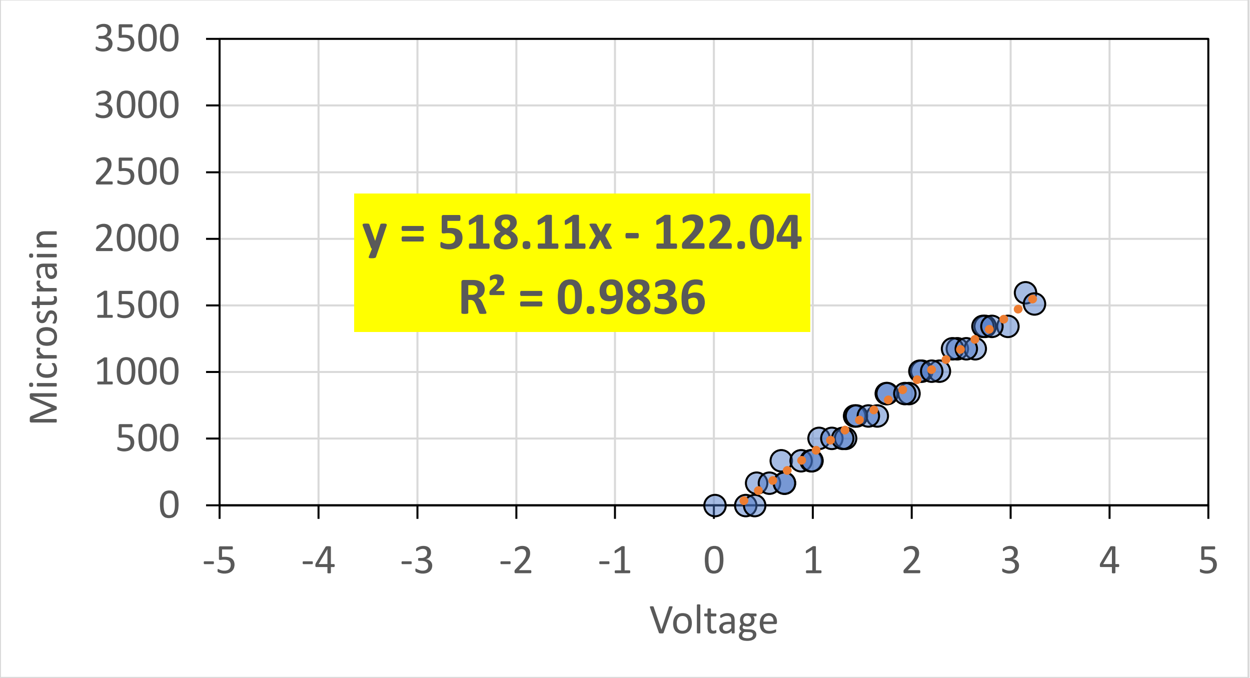

Figure A.81: ASG Channel 11 Calibration Graph

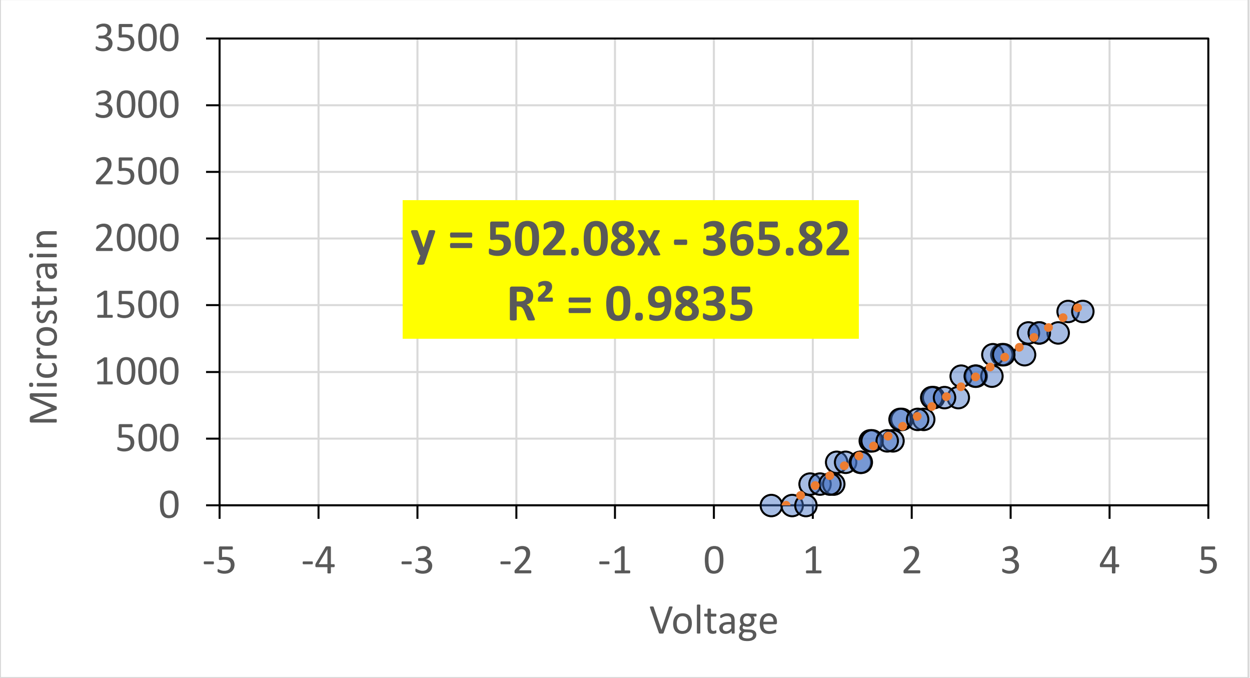

Figure A.82: ASG Channel 12 Calibration Graph

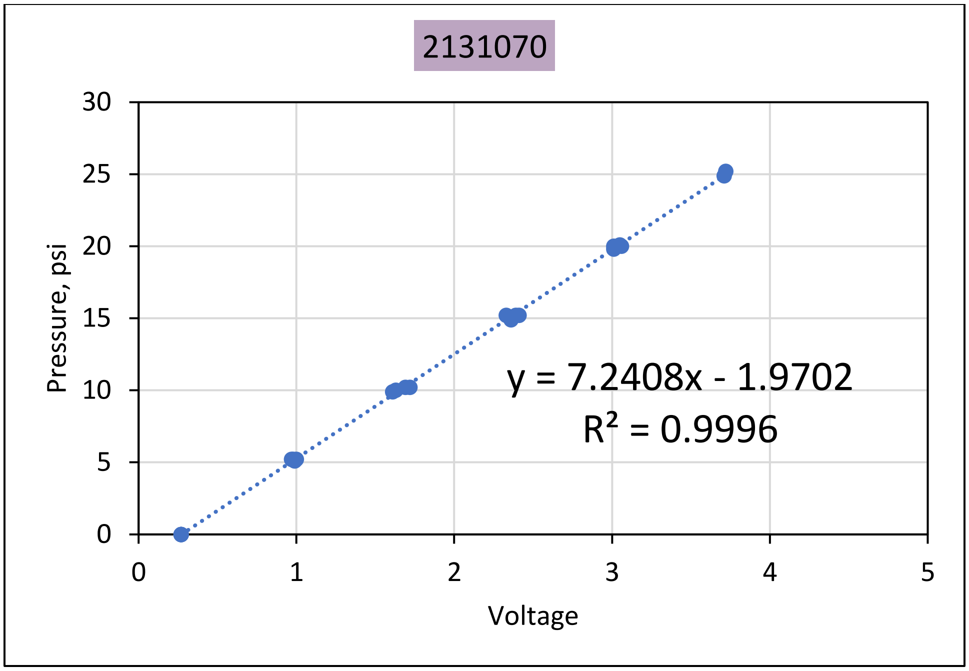

Figure A.83: EPC Channel 13 Calibration Graph

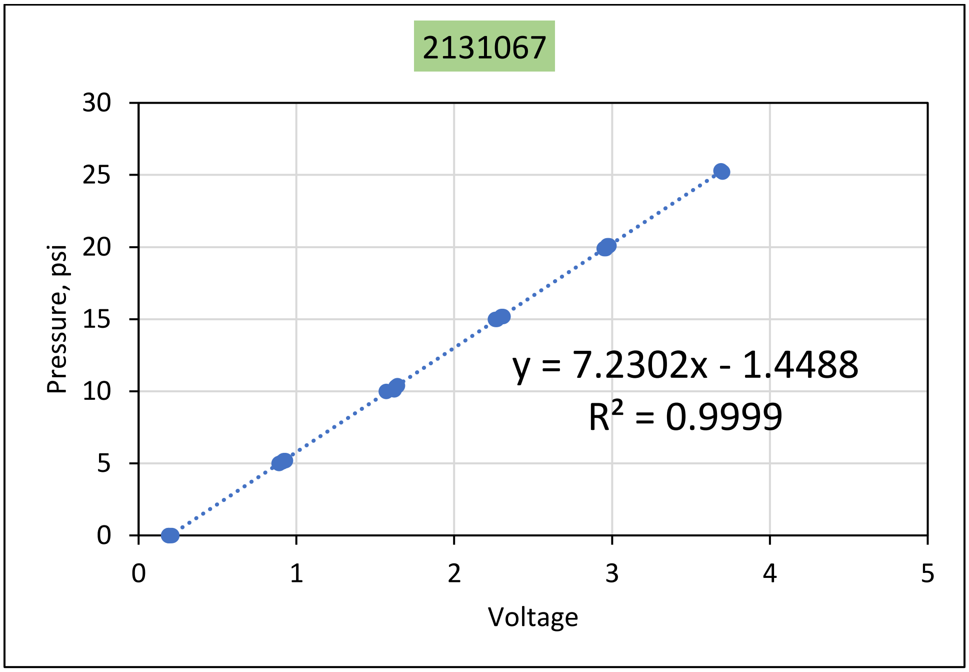

Figure A.84: EPC Channel 14 Calibration Graph

APPENDIX B

Gauge Assignments and Calibration Factors

Table B.1: N1- GTRDry Section Calibration Factors

Channel	Geocomp/Geokon® GaugeID	CalFactor (microstrain/Volt)
1	T43	527.017
2	T28	571.828
3	T4	495.777
4	T21	513.344
5	T13	522.120
6	T6	525.395
7	T17	481.895
8	T34	515.290
9	T16	530.605
10	T7	516.472
11	T42	505.569
12	T37	551.171
13	2131068	7.228
14	2131059	7.213

Table B.2: N2- GTRWet Section Calibration Factors

Channel	Geocomp/Geokon® GaugeID	CalFactor (microstrain/Volt)
1	T11	537.048
2	T55	500.344
3	T59	517.964
4	T65	510.566
5	T48	594.966
6	T63	513.640
7	T35	493.040
8	T54	541.511
9	T52	556.437
10	T60	526.066
11	T58	500.154
12	T57	521.758
13	2131057	7.248
14	2131056	7.266

Table B.3: N5- Aramid Section Calibration Factors

Channel	Geocomp/Geokon® GaugeID	CalFactor (microstrain/Volt)
1	T99	518.155
2	T62	513.785
3	Q10	430.191
4	T77	509.644
5	Q3	477.474
6	T74	488.787
7	Q4	462.787
8	T67	503.860
9	T97	471.026
10	Q2	467.737
11	T69	504.107
12	Q11	461.016
13	2131058	7.251
14	2131069	7.232

Table B.4: N7- Ctrl Section Calibration Factors

Channel	Geocomp/Geokon® GaugeID	CalFactor (microstrain/Volt)
1	T39	494.535
2	T26	472.154
3	T23	484.070
4	T22	542.481
5	T1	509.186
6	T29	545.096
7	T3	505.724
8	T18	509.559
9	T2	509.762
10	T5	455.885
11	T45	507.906
12	T41	559.582
13	2131065	7.219
14	2131066	7.224

Table B.5: S5- DryPlastic Section Calibration Factors

Channel	Geocomp/Geokon® GaugeID	CalFactor (microstrain/Volt)
1	T64	582.055
2	T98	475.647
3	Q21	434.743
4	T56	490.298
5	Q6	479.591
6	T79	537.006
7	Q25	430.401
8	T88	537.080
9	T102	516.419
10	Q24	489.611
11	T66	514.384
12	Q16	423.409
13	2131064	7.200
14	2131071	7.206

Table B.6: S6- WetPlastic Section Calibration Factors

Channel	Geocomp/Geokon® GaugeID	CalFactor (microstrain/Volt)
1	T100	541.527
2	T61	561.664
3	Q29	429.615
4	T84	575.055
5	Q23	407.875
6	T101	472.260
7	Q1	478.407
8	T47	505.707
9	T68	550.434
10	Q9	430.243
11	T81	518.113
12	T51	502.084
13	2131070	7.241
14	2131067	7.230

APPENDIX C

Construction Data Reports

3/3/2022

Quadrant: N
Section: 1
Sublot: 1

Laboratory Diary

General Desccription of Mix and Materials

Design Method:	BMD
Compactive Effort:	60 gyrations
Binder Performance Grade:	67-22
Modifier Type:	NA
Aggregate Type:	Grn/Sand/RAP
Design Gradation Type:	DGA

Avg. Lab Properties of Plant Produced Mix

Sieve Size	Target	QC
25 mm (1"):	100	100
19 mm (3/4"):	100	100
12.5 mm (1/2"):	98	97
9.5 mm (3/8"):	89	87
4.75 mm (#4):	55	59
2.36 mm (#8):	41	44
1.18 mm (#16):	33	34
0.60 mm (#30):	22	20
0.30 mm (#50):	12	10
0.15 mm (#100):	7	7
0.075 mm (#200):	4.5	4.3
Binder Content (Pb):	5.6	5.6
Eff. Binder Content (Pbe):	5.0	5.0
Dust-to-Eff. Binder Ratio:	0.9	0.9
RAP Binder Replacement (%):	21	20
RAS Binder Replacement (%):	0	0
Total Binder Replacement (%):	21	20
Rice Gravity (Gmm):	2.453	2.449
Bulk Gravity (Gmb):	2.344	2.328
Air Voids (Va):	4.4	4.9
Aggregate Gravity (Gsb):	2.627	2.622
VMA (via Gsb):	15.8	16.2
VFA:	72	69

Construction Diary

Relevant Conditions for Construction

Completion Date:	September 14, 2021
24 Hour High Temperature (F):	88
24 Hour Low Temperature (F):	70
24 Hour Rainfall (in):	0.00
Planned Subot Lift Thickness (in):	5.5
Paving Machine:	Vogele

Plant Configuration and Placement Details

Component	% Setting
Binder Content (Plant Setting)	5.7
78 Granite	39.0
Sand	23.0
89 Granite	18.0
Processed RAP	20.0
Evotherm P25	0.5
Smart Mix (% by Total Binder)	12.0

As-Built Sublot Lift Thickness (in):	Pending
Total Thickness of All New Sublots (in):	Pending
Approx. Underlying HMA Thickness (in):	0.0
Type of Tack Coat Utilized:	NA
Undilluted Target Tack Rate (gal/sy):	NA
Approx. Avg. Temperature at Plant (F):	330
Avg. Measured Mat Compaction:	93.7%

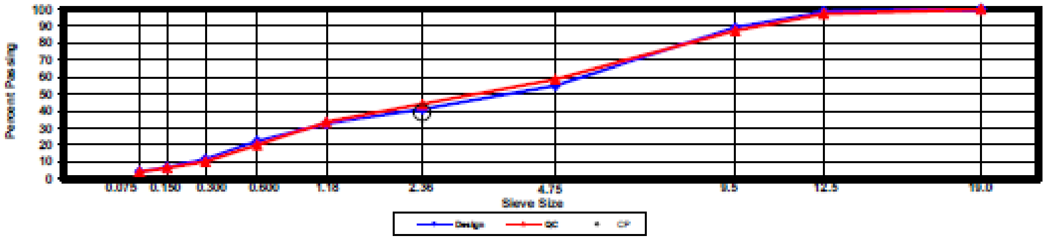

General Notes:

- References are by quadrant (E=East, N=North, W=West, S=South, R=Off-Ramp, L=Lee Rd 159, U=US-280), section #, and sublot (top=1).
- DGA, SMA, & OGFC refer to dense graded asphalt, stone matrix asphalt, & open-graded friction course, respectively.
- Production Gsb estimated using the actual production Gse and the difference between Gse and Gsb in the mix design.

Section and/or Sublot Specific Notes:

This is the Additive Group (AG) section designed with "dry" recycled tire rubber additive.

Figure C.1: Section N1-GTRDry Construction Report

3/3/2022

Quadrant: N
Section: 2
Sublot: 1

Laboratory Diary

General Desccription of Mix and Materials

Design Method:	BMD
Compactive Effort:	60 gyrations
Binder Performance Grade:	Entech
Modifier Type:	Wet RTR
Aggregate Type:	Grn/Sand/RAP
Design Gradation Type:	DGA

Avg. Lab Properties of Plant Produced Mix

Sieve Size	Target	QC
25 mm (1"):	100	100
19 mm (3/4"):	100	100
12.5 mm (1/2"):	98	97
9.5 mm (3/8"):	89	86
4.75 mm (#4):	55	57
2.36 mm (#8):	41	42
1.18 mm (#16):	33	32
0.60 mm (#30):	22	19
0.30 mm (#50):	12	10
0.15 mm (#100):	7	6
0.075 mm (#200):	4.5	4.1
Binder Content (Pb):	5.6	5.8
Eff. Binder Content (Pbe):	4.9	5.2
Dust-to-Eff. Binder Ratio:	0.9	0.8
RAP Binder Replacement (%):	21	19
RAS Binder Replacement (%):	0	0
Total Binder Replacement (%):	21	19
Rice Gravity (Gmm):	2.457	2.453
Bulk Gravity (Gmb):	2.314	2.351
Air Voids (Va):	5.8	4.2
Aggregate Gravity (Gsb):	2.627	2.636
VMA (via Gsb):	16.8	16.0
VFA:	65	74

Construction Diary

Relevant Conditions for Construction

Completion Date:	September 14, 2021
24 Hour High Temperature (F):	88
24 Hour Low Temperature (F):	70
24 Hour Rainfall (in):	0.00
Planned Subot Lift Thickness (in):	5.5
Paving Machine:	Vogele

Plant Configuration and Placement Details

Component	% Setting
Binder Content (Plant Setting)	6.1
78 Granite	39.0
Sand	23.0
89 Granite	18.0
Processed RAP	20.0
Evotherm P25	0.5

As-Built Sublot Lift Thickness (in):	Pending
Total Thickness of All New Sublots (in):	Pending
Approx. Underlying HMA Thickness (in):	0.0
Type of Tack Coat Utilized:	NA
Undilluted Target Tack Rate (gal/sy):	NA
Approx. Avg. Temperature at Plant (F):	330
Avg. Measured Mat Compaction:	94.1%

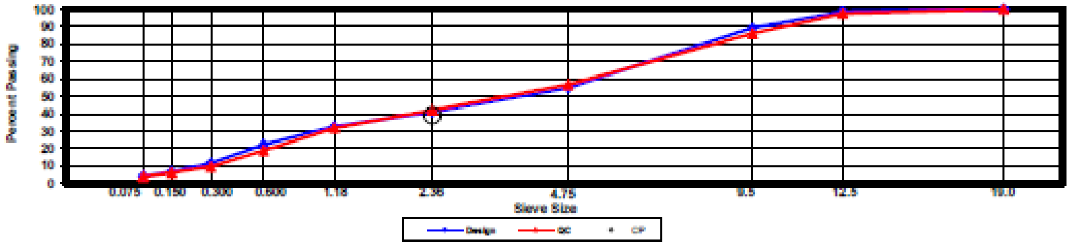

General Notes:
- References are by quadrant (E=East, N=North, W=West, S=South, R=Off-Ramp, L=Lee Rd 159, U=US-280), section #, and sublot (top=1).
- DGA, SMA, & OGFC refer to dense graded asphalt, stone matrix asphalt, & open-graded friction course, respectively.
- Production Gsb estimated using the actual production Gse and the difference between Gse and Gsb in the mix design.

Section and/or Sublot Specific Notes:
This is the Additive Group (AG) section designed with "wet" recycled tire rubber binder.

Figure C.2: Section N2-GTRWet Construction Report

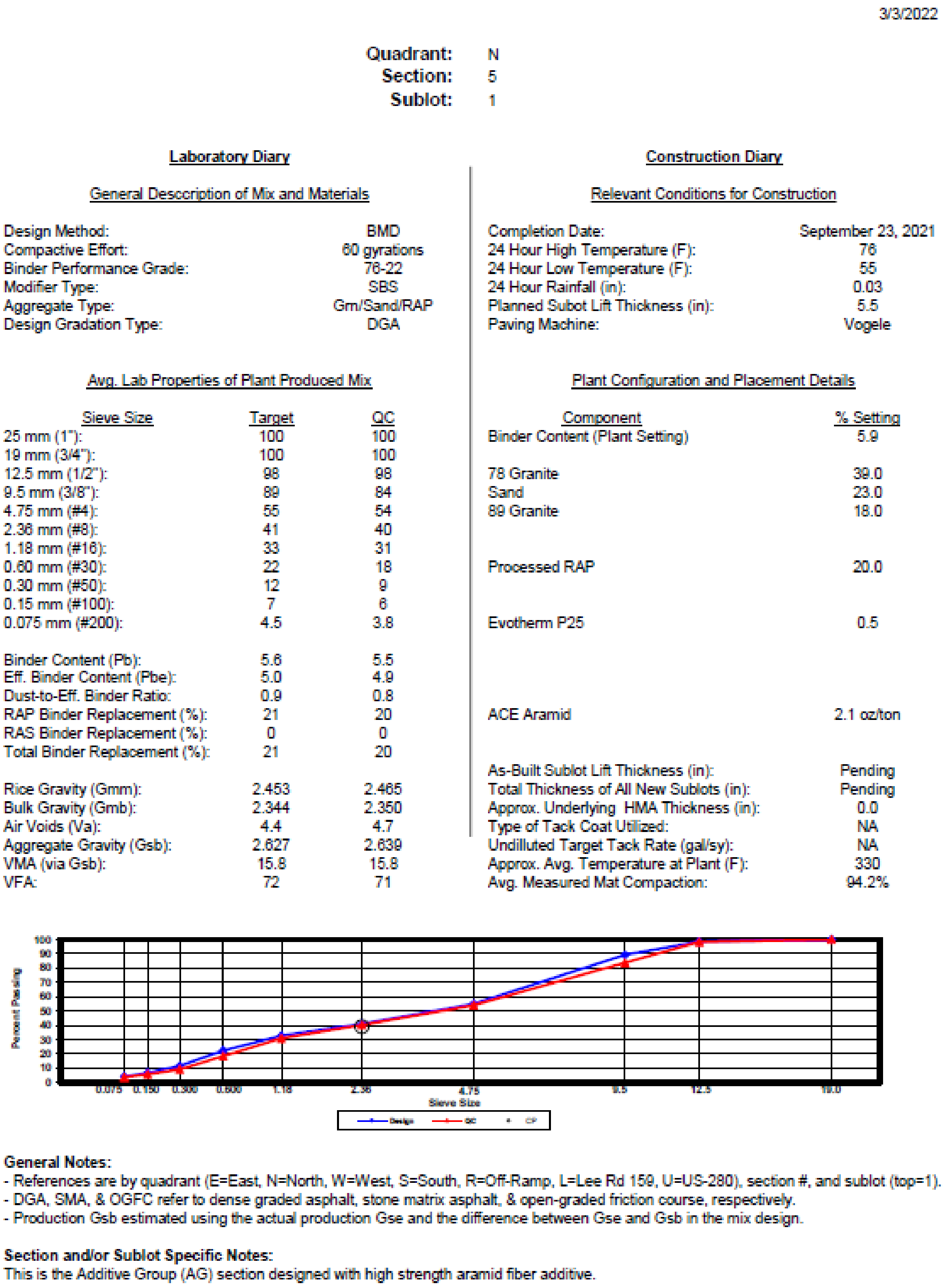

3/3/2022

Quadrant: N
Section: 5
Sublot: 1

Laboratory Diary

General Desccription of Mix and Materials

Design Method:	BMD
Compactive Effort:	60 gyrations
Binder Performance Grade:	76-22
Modifier Type:	SBS
Aggregate Type:	Grn/Sand/RAP
Design Gradation Type:	DGA

Avg. Lab Properties of Plant Produced Mix

Sieve Size	Target	QC
25 mm (1"):	100	100
19 mm (3/4"):	100	100
12.5 mm (1/2"):	98	98
9.5 mm (3/8"):	89	84
4.75 mm (#4):	55	54
2.36 mm (#8):	41	40
1.18 mm (#16):	33	31
0.60 mm (#30):	22	18
0.30 mm (#50):	12	9
0.15 mm (#100):	7	6
0.075 mm (#200):	4.5	3.8
Binder Content (Pb):	5.6	5.5
Eff. Binder Content (Pbe):	5.0	4.9
Dust-to-Eff. Binder Ratio:	0.9	0.8
RAP Binder Replacement (%):	21	20
RAS Binder Replacement (%):	0	0
Total Binder Replacement (%):	21	20
Rice Gravity (Gmm):	2.453	2.465
Bulk Gravity (Gmb):	2.344	2.350
Air Voids (Va):	4.4	4.7
Aggregate Gravity (Gsb):	2.627	2.639
VMA (via Gsb):	15.8	15.8
VFA:	72	71

Construction Diary

Relevant Conditions for Construction

Completion Date:	September 23, 2021
24 Hour High Temperature (F):	76
24 Hour Low Temperature (F):	55
24 Hour Rainfall (in):	0.03
Planned Subot Lift Thickness (in):	5.5
Paving Machine:	Vogele

Plant Configuration and Placement Details

Component	% Setting
Binder Content (Plant Setting)	5.9
78 Granite	39.0
Sand	23.0
89 Granite	18.0
Processed RAP	20.0
Evotherm P25	0.5
ACE Aramid	2.1 oz/ton
As-Built Sublot Lift Thickness (in):	Pending
Total Thickness of All New Sublots (in):	Pending
Approx. Underlying HMA Thickness (in):	0.0
Type of Tack Coat Utilized:	NA
Undilluted Target Tack Rate (gal/sy):	NA
Approx. Avg. Temperature at Plant (F):	330
Avg. Measured Mat Compaction:	94.2%

General Notes:
- References are by quadrant (E=East, N=North, W=West, S=South, R=Off-Ramp, L=Lee Rd 159, U=US-280), section #, and sublot (top=1).
- DGA, SMA, & OGFC refer to dense graded asphalt, stone matrix asphalt, & open-graded friction course, respectively.
- Production Gsb estimated using the actual production Gse and the difference between Gse and Gsb in the mix design.

Section and/or Sublot Specific Notes:
This is the Additive Group (AG) section designed with high strength aramid fiber additive.

Figure C.3: Section N5-Aramid Construction Report

3/3/2022

Quadrant: N
Section: 7
Sublot: 1

Laboratory Diary

General Desccription of Mix and Materials

Design Method:	BMD
Compactive Effort:	60 gyrations
Binder Performance Grade:	76-22
Modifier Type:	SBS
Aggregate Type:	Grn/Sand/RAP
Design Gradation Type:	DGA

Avg. Lab Properties of Plant Produced Mix

Sieve Size	Target	QC
25 mm (1"):	100	100
19 mm (3/4"):	100	100
12.5 mm (1/2"):	98	97
9.5 mm (3/8"):	89	84
4.75 mm (#4):	55	54
2.36 mm (#8):	41	41
1.18 mm (#16):	33	32
0.60 mm (#30):	22	20
0.30 mm (#50):	12	10
0.15 mm (#100):	7	6
0.075 mm (#200):	4.5	4.0
Binder Content (Pb):	5.6	5.7
Eff. Binder Content (Pbe):	5.0	5.0
Dust-to-Eff. Binder Ratio:	0.9	0.8
RAP Binder Replacement (%):	21	20
RAS Binder Replacement (%):	0	0
Total Binder Replacement (%):	21	20
Rice Gravity (Gmm):	2.453	2.455
Bulk Gravity (Gmb):	2.344	2.369
Air Voids (Va):	4.4	3.5
Aggregate Gravity (Gsb):	2.627	2.632
VMA (via Gsb):	15.8	15.1
VFA:	72	77

Construction Diary

Relevant Conditions for Construction

Completion Date:	September 3, 2021
24 Hour High Temperature (F):	86
24 Hour Low Temperature (F):	69
24 Hour Rainfall (in):	0.00
Planned Subot Lift Thickness (in):	5.5
Paving Machine:	Vogele

Plant Configuration and Placement Details

Component	% Setting
Binder Content (Plant Setting)	5.9
78 Granite	39.0
Sand	23.0
89 Granite	18.0
Processed RAP	20.0
Evotherm P25	0.5

As-Built Sublot Lift Thickness (in):	Pending
Total Thickness of All New Sublots (in):	Pending
Approx. Underlying HMA Thickness (in):	0.0
Type of Tack Coat Utilized:	NA
Undilluted Target Tack Rate (gal/sy):	NA
Approx. Avg. Temperature at Plant (F):	330
Avg. Measured Mat Compaction:	95.9%

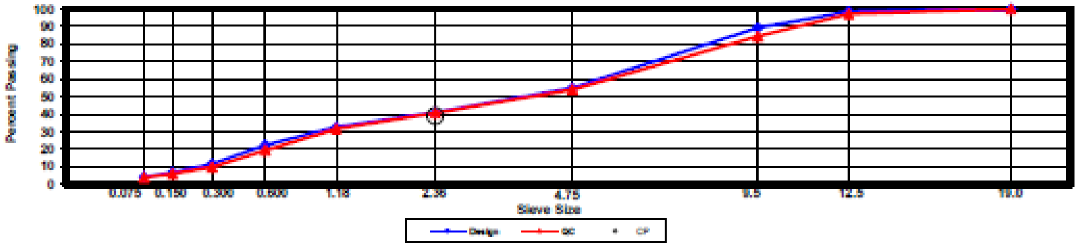

General Notes:
- References are by quadrant (E=East, N=North, W=West, S=South, R=Off-Ramp, L=Lee Rd 159, U=US-280), section #, and sublot (top=1).
- DGA, SMA, & OGFC refer to dense graded asphalt, stone matrix asphalt, & open-graded friction course, respectively.
- Production Gsb estimated using the actual production Gse and the difference between Gse and Gsb in the mix design.

Section and/or Sublot Specific Notes:
This is the Additive Group (AG) section designed as the control section.

Figure C.4: Section N7-Ctrl Construction Report

3/3/2022

Quadrant: S
Section: 5
Sublot: 1

Laboratory Diary

General Desccription of Mix and Materials

Design Method:	BMD
Compactive Effort:	60 gyrations
Binder Performance Grade:	76-22
Modifier Type:	SBS
Aggregate Type:	Grn/Sand/RAP
Design Gradation Type:	DGA

Avg. Lab Properties of Plant Produced Mix

Sieve Size	Target	QC
25 mm (1"):	100	100
19 mm (3/4"):	100	100
12.5 mm (1/2"):	98	97
9.5 mm (3/8"):	89	87
4.75 mm (#4):	55	56
2.36 mm (#8):	41	43
1.18 mm (#16):	33	33
0.60 mm (#30):	22	20
0.30 mm (#50):	12	9
0.15 mm (#100):	7	6
0.075 mm (#200):	4.5	3.8
Binder Content (Pb):	5.6	5.8
Eff. Binder Content (Pbe):	5.0	5.1
Dust-to-Eff. Binder Ratio:	0.9	0.7
RAP Binder Replacement (%):	21	19
RAS Binder Replacement (%):	0	0
Total Binder Replacement (%):	21	19
Rice Gravity (Gmm):	2.453	2.439
Bulk Gravity (Gmb):	2.344	2.359
Air Voids (Va):	4.4	3.3
Aggregate Gravity (Gsb):	2.627	2.616
VMA (via Gsb):	15.8	15.0
VFA:	72	78

Construction Diary

Relevant Conditions for Construction

Completion Date:	September 21, 2021
24 Hour High Temperature (F):	90
24 Hour Low Temperature (F):	73
24 Hour Rainfall (in):	0.06
Planned Subot Lift Thickness (in):	5.5
Paving Machine:	Vogele

Plant Configuration and Placement Details

Component	% Setting
Binder Content (Plant Setting)	5.9
78 Granite	39.0
Sand	23.0
89 Granite	18.0
Processed RAP	20.0
Evotherm P25	0.5
Dry Plastic (% by Aggregate)	0.5

As-Built Sublot Lift Thickness (in):	Pending
Total Thickness of All New Sublots (in):	Pending
Approx. Underlying HMA Thickness (in):	0.0
Type of Tack Coat Utilized:	NA
Undilluted Target Tack Rate (gal/sy):	NA
Approx. Avg. Temperature at Plant (F):	330
Avg. Measured Mat Compaction:	93.5%

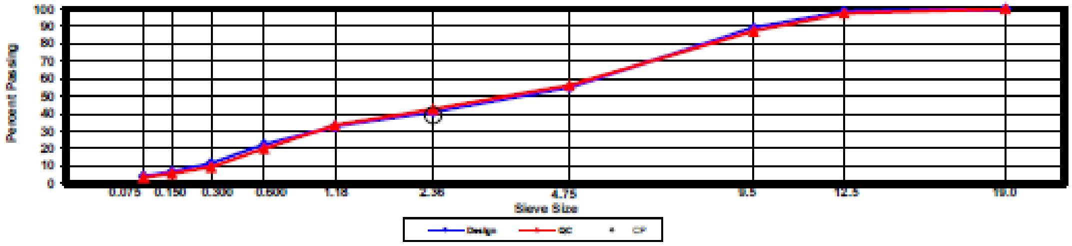

General Notes:
- References are by quadrant (E=East, N=North, W=West, S=South, R=Off-Ramp, L=Lee Rd 159, U=US-280), section #, and sublot (top=1).
- DGA, SMA, & OGFC refer to dense graded asphalt, stone matrix asphalt, & open-graded friction course, respectively.
- Production Gsb estimated using the actual production Gse and the difference between Gse and Gsb in the mix design.

Section and/or Sublot Specific Notes:
This is the Additive Group (AG) section designed with "dry" recycled low density plastic additive.

Figure C.5: Section S5-DryPlastic Construction Report

3/3/2022

Quadrant: S
Section: 6
Sublot: 1

Laboratory Diary

General Desccription of Mix and Materials

Design Method:	BMD
Compactive Effort:	60 gyrations
Binder Performance Grade:	Dow
Modifier Type:	Dow
Aggregate Type:	Grn/Sand/RAP
Design Gradation Type:	DGA

Avg. Lab Properties of Plant Produced Mix

Sieve Size	Target	QC
25 mm (1"):	100	100
19 mm (3/4"):	100	100
12.5 mm (1/2"):	98	97
9.5 mm (3/8"):	89	86
4.75 mm (#4):	55	56
2.36 mm (#8):	41	42
1.18 mm (#16):	33	32
0.60 mm (#30):	22	20
0.30 mm (#50):	12	10
0.15 mm (#100):	7	6
0.075 mm (#200):	4.5	4.0
Binder Content (Pb):	5.6	5.7
Eff. Binder Content (Pbe):	5.0	5.0
Dust-to-Eff. Binder Ratio:	0.9	0.8
RAP Binder Replacement (%):	21	20
RAS Binder Replacement (%):	0	0
Total Binder Replacement (%):	21	20
Rice Gravity (Gmm):	2.453	2.463
Bulk Gravity (Gmb):	2.344	2.333
Air Voids (Va):	4.4	5.3
Aggregate Gravity (Gsb):	2.627	2.641
VMA (via Gsb):	15.8	16.7
VFA:	72	68

Construction Diary

Relevant Conditions for Construction

Completion Date:	September 22, 2021
24 Hour High Temperature (F):	82
24 Hour Low Temperature (F):	64
24 Hour Rainfall (in):	1.15
Planned Subot Lift Thickness (in):	5.5
Paving Machine:	Vogele

Plant Configuration and Placement Details

Component	% Setting
Binder Content (Plant Setting)	5.9
78 Granite	39.0
Sand	23.0
89 Granite	18.0
Processed RAP	20.0
Evotherm P25	0.5

As-Built Sublot Lift Thickness (in):	Pending
Total Thickness of All New Sublots (in):	Pending
Approx. Underlying HMA Thickness (in):	0.0
Type of Tack Coat Utilized:	NA
Undilluted Target Tack Rate (gal/sy):	NA
Approx. Avg. Temperature at Plant (F):	330
Avg. Measured Mat Compaction:	93.9%

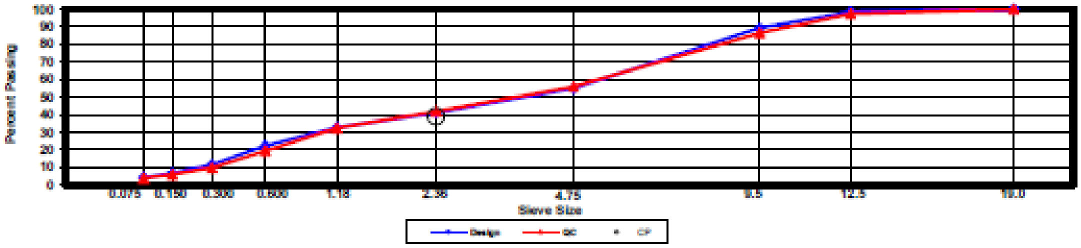

General Notes:
- References are by quadrant (E=East, N=North, W=West, S=South, R=Off-Ramp, L=Lee Rd 159, U=US-280), section #, and sublot (top=1).
- DGA, SMA, & OGFC refer to dense graded asphalt, stone matrix asphalt, & open-graded friction course, respectively.
- Production Gsb estimated using the actual production Gse and the difference between Gse and Gsb in the mix design.

Section and/or Sublot Specific Notes:
This is the Additive Group (AG) section designed with "wet" recycled low density plastic binder.

Figure C.6: Section S6-WetPlastic Construction Report

APPENDIX D

Post-Grind Thicknesses

Table D.1: Section N1-GTRDry Thicknesses

Point Type	ID	GB	AC
RL1	IWP	5.94	5.43
RL1	BWP	6.01	5.59
RL1	OWP	5.96	5.56
RL2	IWP	5.92	5.82
RL2	BWP	5.93	5.84
RL2	OWP	5.95	5.73
RL4	IWP	6.05	5.55
RL4	BWP	5.99	5.84
RL4	OWP	5.96	5.71
RL3	IWP	6.13	5.40
RL3	BWP	5.97	5.37
RL3	OWP	6.09	5.17
Gauge	1		5.97
Gauge	2		5.78
Gauge	3		5.44
Gauge	4		6.02
Gauge	5		5.92
Gauge	6		5.59
Gauge	7		5.82
Gauge	8		5.74
Gauge	9		5.45
Gauge	10		6.03
Gauge	11		5.93
Gauge	12		5.56
Gauge	13		6.27
Gauge	14	6.09	5.77
All, Avg		6.00	5.70
All, St Dev		0.07	0.25
Non-Gauge Avg		5.99	5.58
Non-Gauge St Dev		0.07	0.21
Gauge Avg			5.81
Gauge STD			0.24

Table D.2: Section N2-GTRWet Thicknesses

Point Type	ID	GB	AC
RL1	IWP	5.94	5.58
RL1	BWP	6.12	5.34
RL1	OWP	6.03	5.58
RL2	IWP	6.11	5.58
RL2	BWP	5.90	5.72
RL2	OWP	6.11	5.58
RL4	IWP	6.03	5.63
RL4	BWP	6.11	5.86
RL4	OWP	6.03	5.72
RL3	IWP	5.93	5.23
RL3	BWP	5.88	5.33
RL3	OWP	6.13	5.45
Gauge	1		5.58
Gauge	2		5.97
Gauge	3		5.84
Gauge	4		5.86
Gauge	5		5.94
Gauge	6		5.97
Gauge	7		5.99
Gauge	8		5.99
Gauge	9		5.95
Gauge	10		5.91
Gauge	11		5.81
Gauge	12		5.95
Gauge	13		5.93
Gauge	14	6.16	5.92
All, Avg		6.04	5.74
All, St Dev		0.10	0.23
Non-Gauge Avg		6.03	5.55
Non-Gauge St Dev		0.09	0.18
Gauge Avg			5.90
Gauge STD			0.11

Table D.3: Section N5-Aramid Thicknesses

Point Type	**Number**	**GB**	**AC**
RL1	IWP	6.12	5.22
RL1	BWP	5.95	5.35
RL1	OWP	5.98	5.54
RL2	IWP	5.92	5.37
RL2	BWP	5.90	5.61
RL2	OWP	6.10	5.69
RL4	IWP	5.87	5.73
RL4	BWP	6.08	5.77
RL4	OWP	5.95	5.36
RL3	IWP	6.00	5.31
RL3	BWP	5.94	5.68
RL3	OWP	6.03	6.09
Gauge	1		5.90
Gauge	2		5.77
Gauge	3		5.43
Gauge	4		5.82
Gauge	5		5.42
Gauge	6		5.28
Gauge	7		5.69
Gauge	8		5.56
Gauge	9		5.45
Gauge	10		5.65
Gauge	11		5.57
Gauge	12		5.54
Gauge	13		5.91
Gauge	14	5.93	5.90
All, Avg		5.98	5.60
All, St Dev		0.08	0.23
Non-Gauge Avg		5.99	5.56
Non-Gauge St Dev		0.08	0.25
Gauge Avg			5.63
Gauge STD			0.20

Table D.4: Section N7-Ctrl Thicknesses

Point Type	Number	GB	AC
RL1	IWP	5.92	5.41
RL1	BWP	6.05	5.71
RL1	OWP	6.10	5.78
RL2	IWP	5.96	5.61
RL2	BWP	6.13	5.74
RL2	OWP	6.02	5.65
RL4	IWP	5.98	6.41
RL4	BWP	6.08	6.08
RL4	OWP	5.80	5.71
RL3	IWP	6.04	6.06
RL3	BWP	5.78	6.08
RL3	OWP	5.91	5.61
Gauge	1		5.59
Gauge	2		5.65
Gauge	3		5.33
Gauge	4		5.61
Gauge	5		5.47
Gauge	6		5.40
Gauge	7		5.67
Gauge	8		5.58
Gauge	9		5.43
Gauge	10		5.66
Gauge	11		5.60
Gauge	12		5.34
Gauge	13		5.81
Gauge	14	6.11	5.64
All, Avg		5.99	5.68
All, St Dev		0.11	0.25
Non-Gauge Avg		5.98	5.82
Non-Gauge St Dev		0.11	0.28
Gauge Avg			5.56
Gauge STD			0.14

Table D.5: Section S5-DryPlastic Thicknesses

Point Type	Number	GB	AC
RL1	IWP	6.04	5.67
RL1	BWP	5.91	5.65
RL1	OWP	5.73	5.35
RL2	IWP	5.88	5.35
RL2	BWP	5.88	5.51
RL2	OWP	5.90	5.35
RL4	IWP	6.06	5.39
RL4	BWP	6.15	5.27
RL4	OWP	6.11	4.95
RL3	IWP	6.06	5.57
RL3	BWP	6.13	5.62
RL3	OWP	6.09	5.40
Gauge	1		5.32
Gauge	2		5.11
Gauge	3		4.96
Gauge	4		5.26
Gauge	5		5.02
Gauge	6		5.30
Gauge	7		5.27
Gauge	8		5.09
Gauge	9		5.37
Gauge	10		5.26
Gauge	11		4.79
Gauge	12		4.95
Gauge	13		5.55
Gauge	14	6.28	4.97
All, Avg		6.02	5.28
All, St Dev		0.15	0.24
Non-Gauge Avg		6.00	5.42
Non-Gauge St Dev		0.13	0.20
Gauge Avg			5.16
Gauge STD			0.21

Table D.6: Section S6-WetPlastic Thicknesses

Point Type	Number	GB	AC
RL1	IWP	5.87	5.75
RL1	BWP	6.00	5.69
RL1	OWP	5.88	5.96
RL2	IWP	6.01	5.53
RL2	BWP	6.05	5.60
RL2	OWP	5.93	5.56
RL4	IWP	6.01	5.70
RL4	BWP	5.92	6.03
RL4	OWP	6.10	5.73
RL3	IWP	5.84	5.88
RL3	BWP	6.05	5.99
RL3	OWP	5.95	6.08
Gauge	1		5.62
Gauge	2		5.37
Gauge	3		5.50
Gauge	4		5.62
Gauge	5		5.44
Gauge	6		5.42
Gauge	7		6.08
Gauge	8		5.85
Gauge	9		5.70
Gauge	10		5.95
Gauge	11		5.63
Gauge	12		5.49
Gauge	13		5.73
Gauge	14	6.05	6.18
All, Avg		5.97	5.73
All, St Dev		0.08	0.23
Non-Gauge Avg		5.97	5.79
Non-Gauge St Dev		0.08	0.19
Gauge Avg			5.69
Gauge STD			0.25

APPENDIX E

Early Structural Behavior Plots

N1-GTRDry

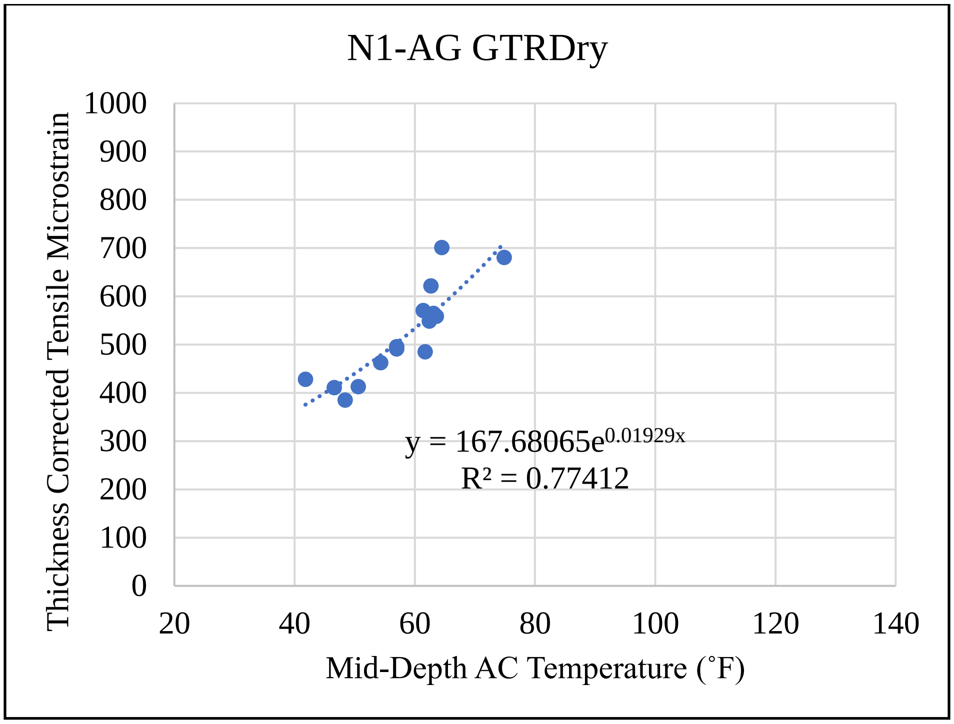

Figure E.1: Thickness Corrected Tensile Microstrain Versus Temperature

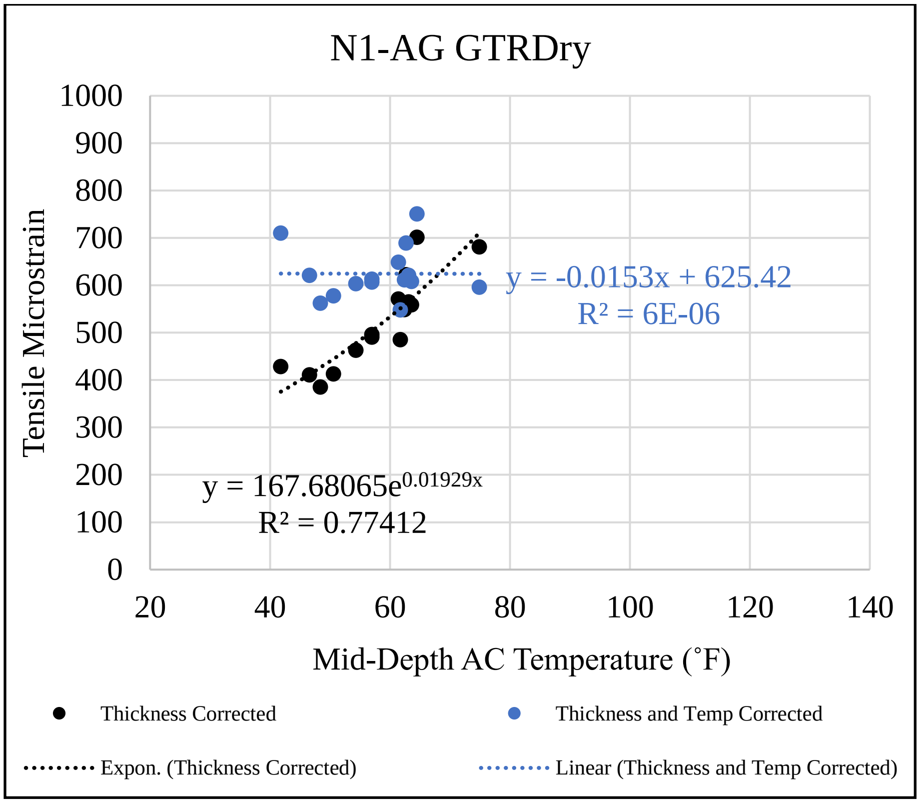

Figure E.2: Thickness, Temperature Corrected Tensile Microstrain Versus Temperature

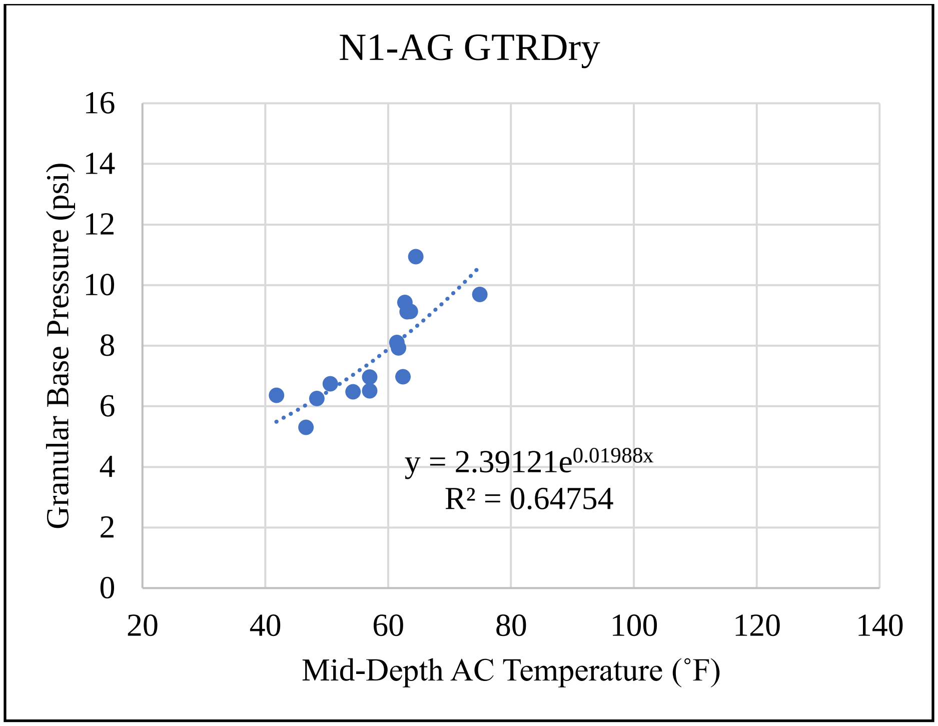

Figure E.3: Measured GB Pressure Versus Temperature

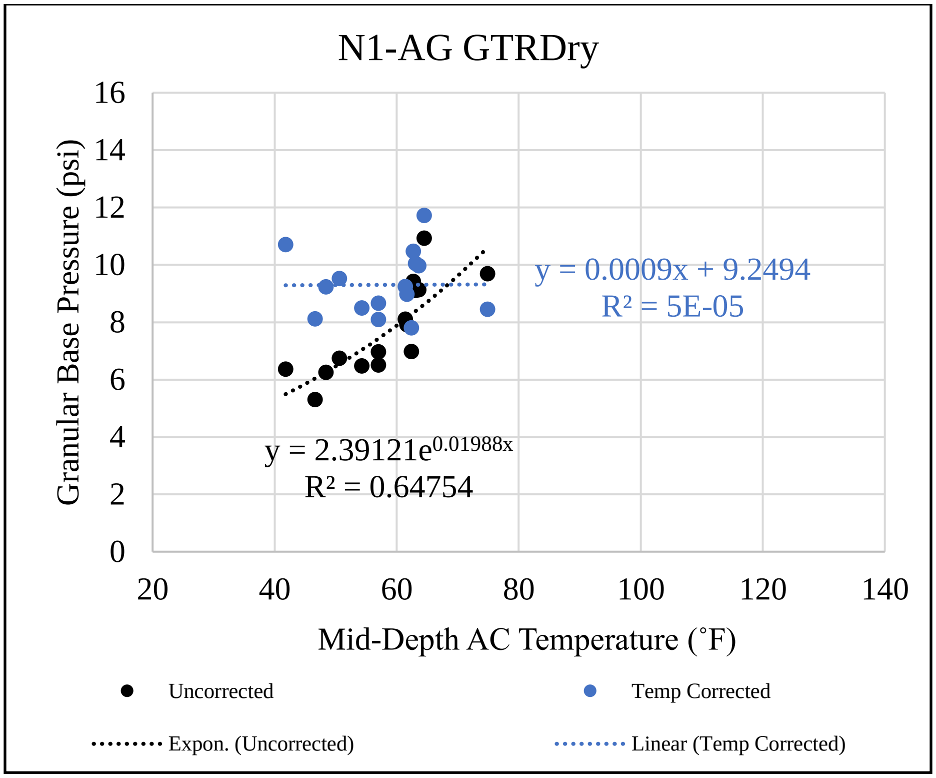

Figure E.4: Measured, Temperature Corrected GB Pressure Versus Temperature

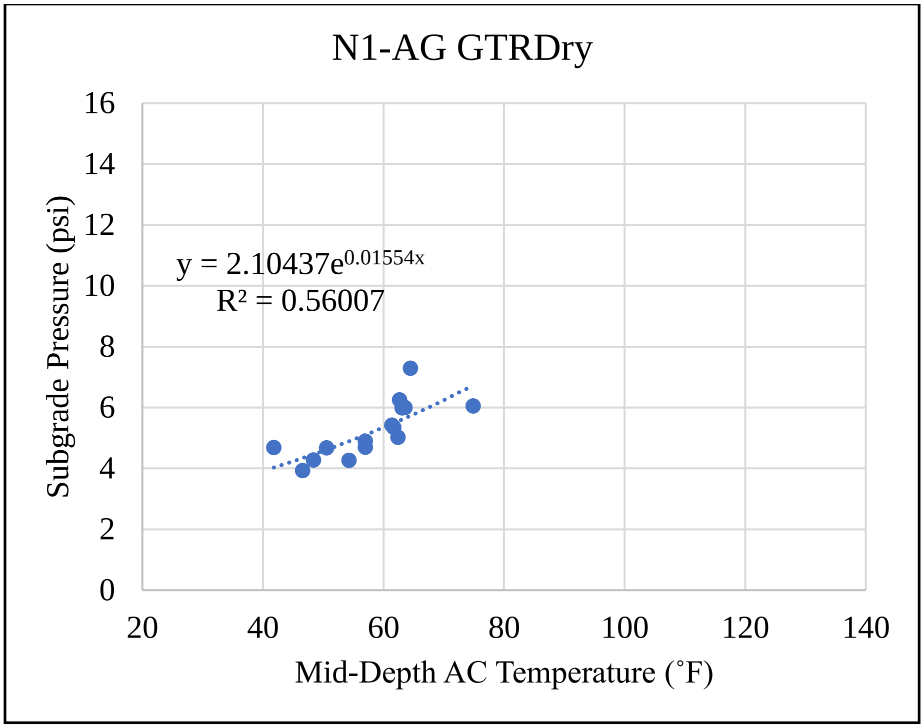

Figure E.5: Measured Subgrade Pressure Versus Temperature

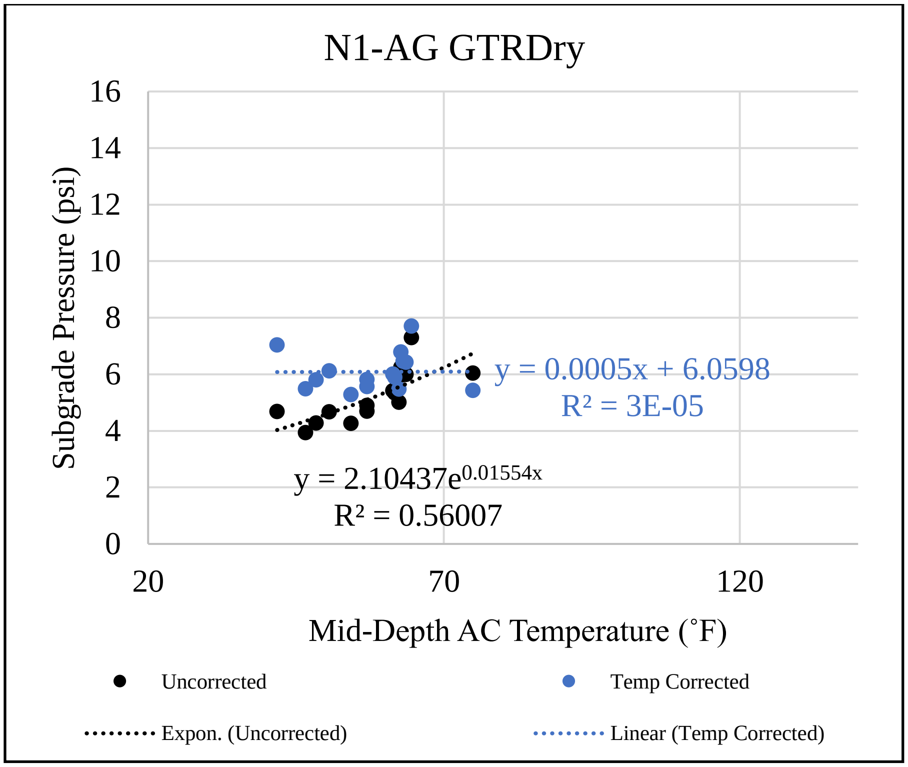

Figure E.6: Measured, Temperature Corrected Subgrade Pressure Versus Temperature

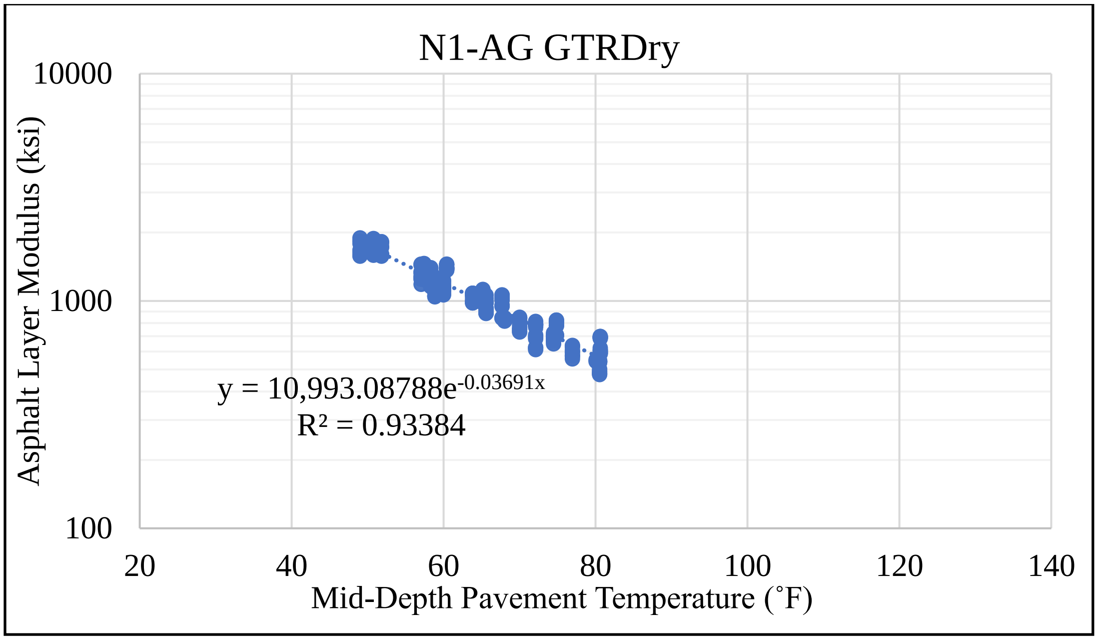

Figure E.7: Uncorrected Asphalt Layer Modulus Versus Temperature

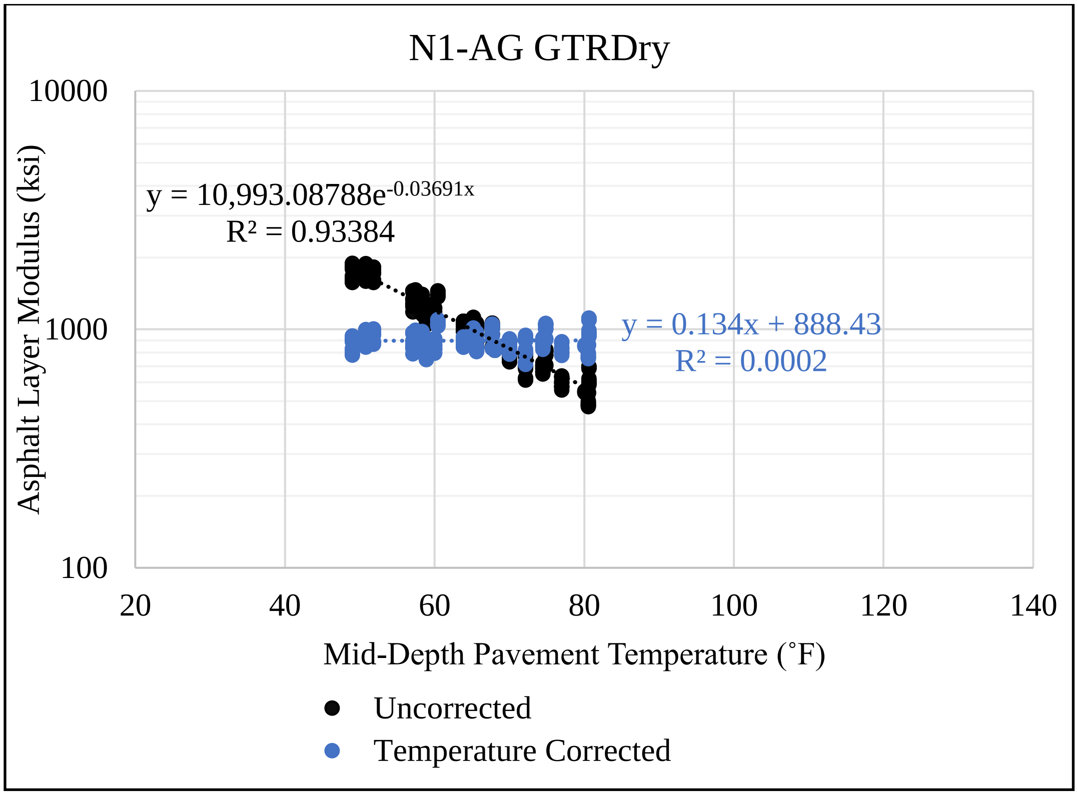

Figure E.8: Uncorrected, Temperature Corrected Asphalt Layer Modulus Versus Temperature

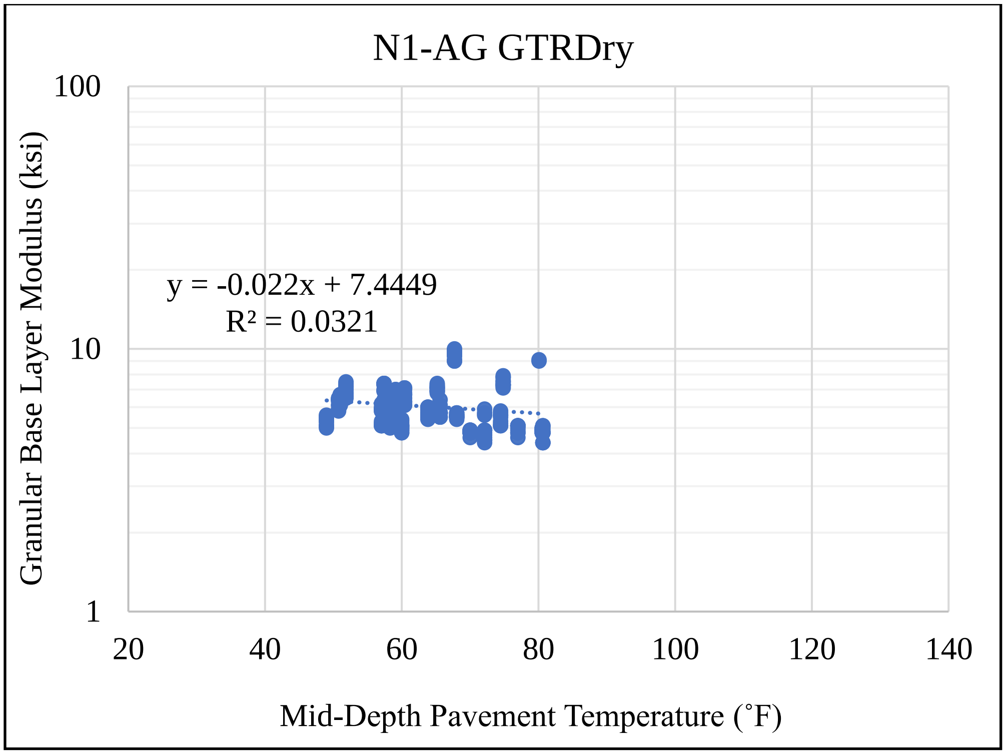

Figure E.9: Uncorrected GB Layer Modulus Versus Temperature

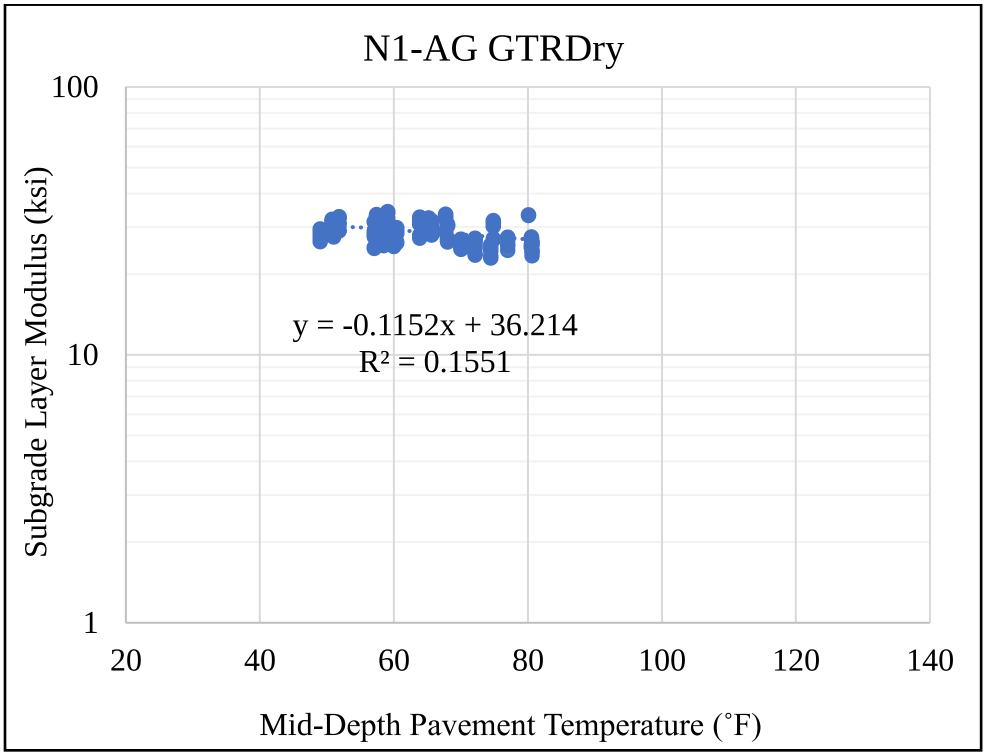

Figure E.10: Uncorrected Subgrade Layer Modulus Versus Temperature

N2-GTRWet

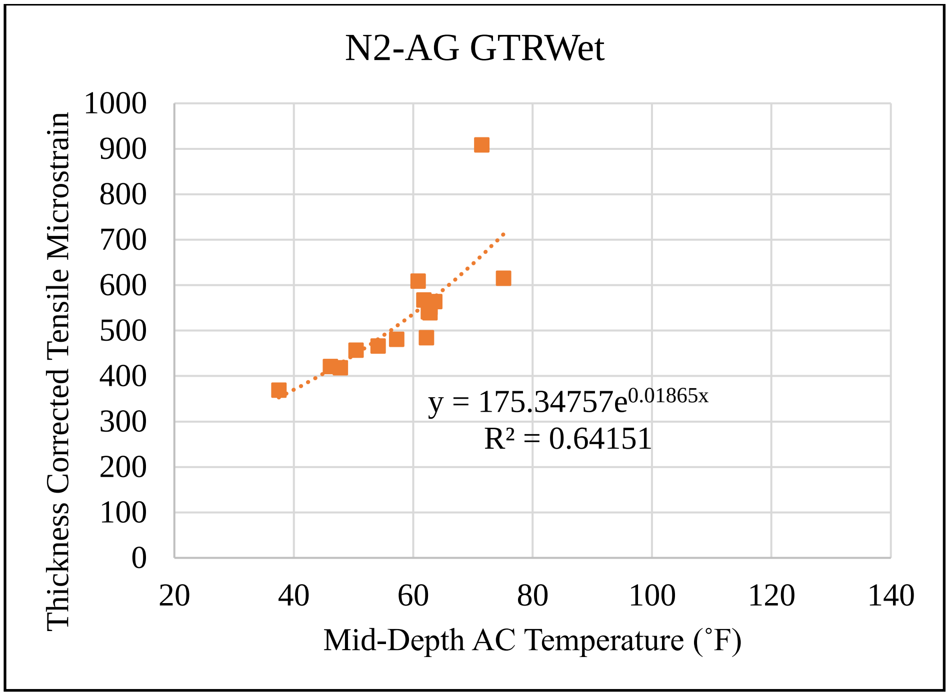

Figure E.11: Thickness Corrected Tensile Microstrain Versus Temperature

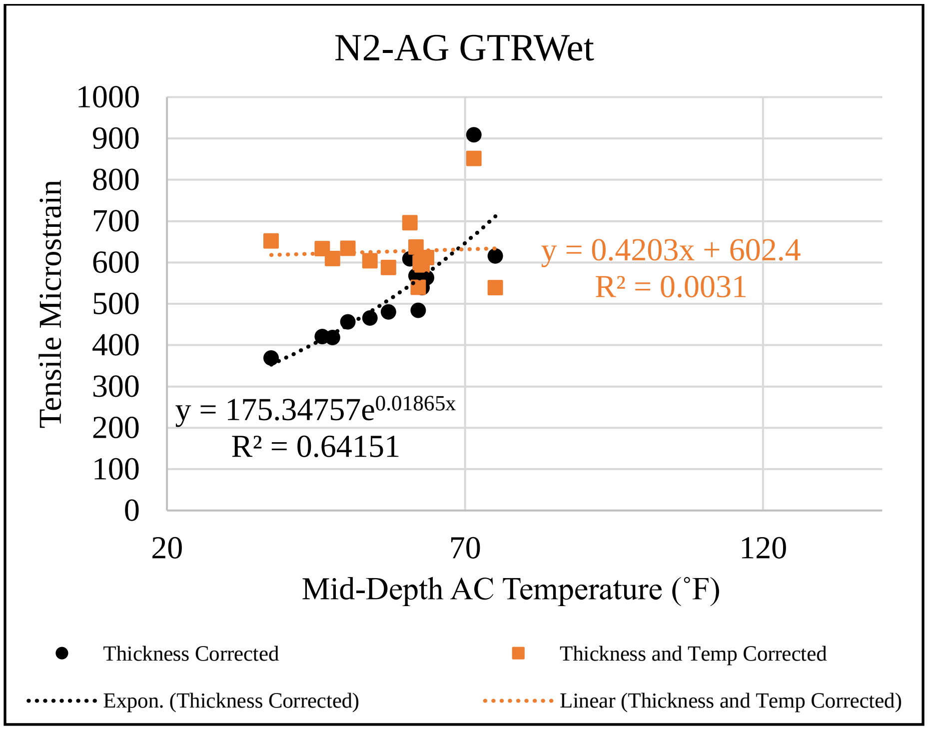

Figure E.12: Thickness, Temperature Corrected Tensile Microstrain Versus Temperature

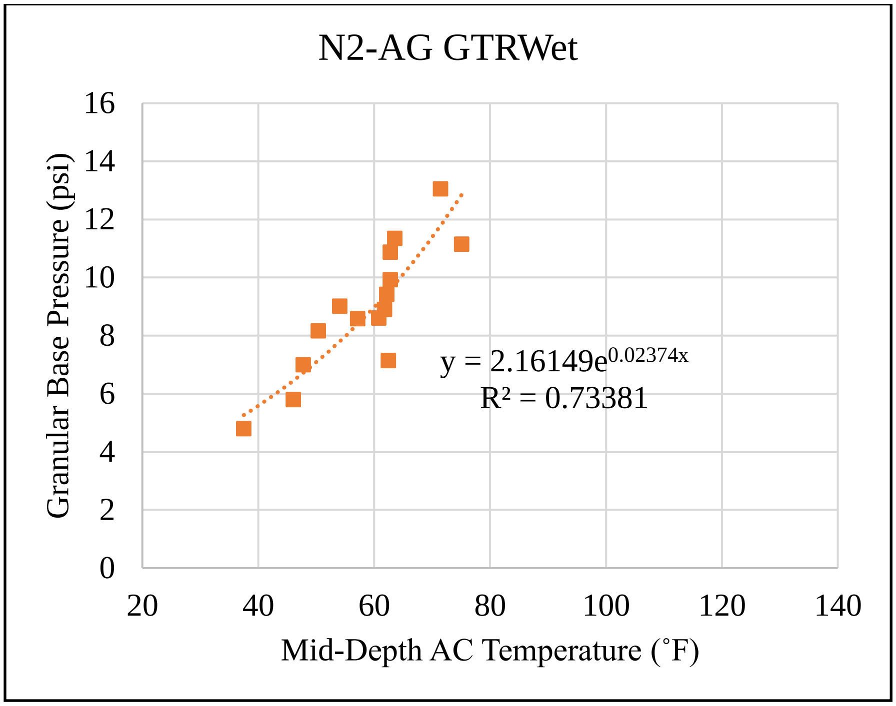

Figure E.13: Measured GB Pressure Versus Temperature

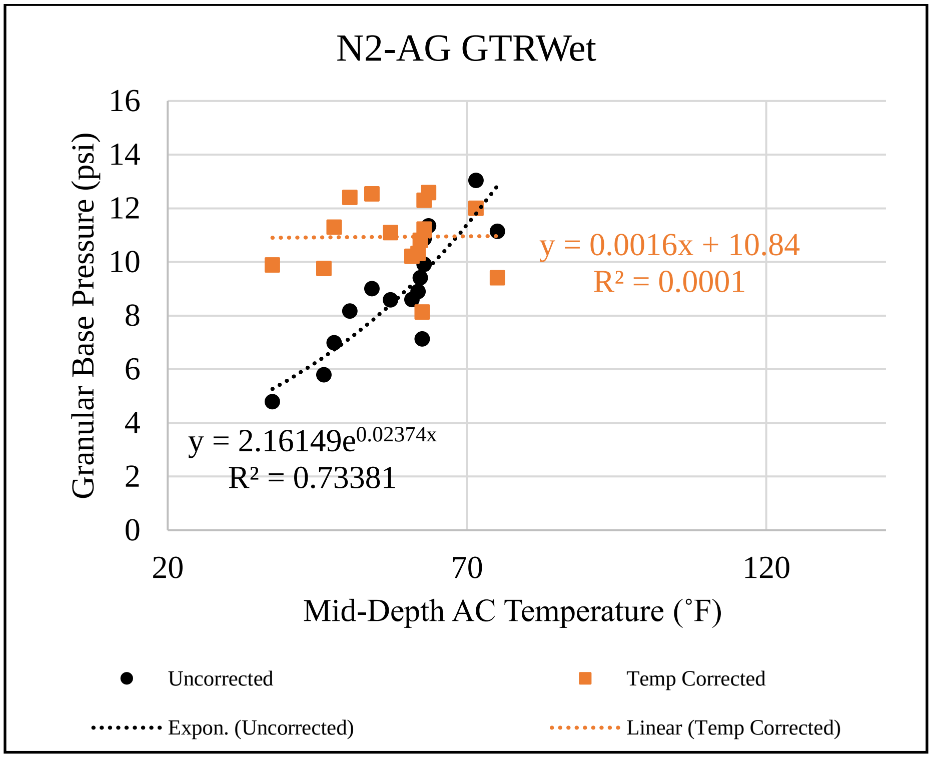

Figure E.14: Measured, Temperature Corrected GB Pressure Versus Temperature

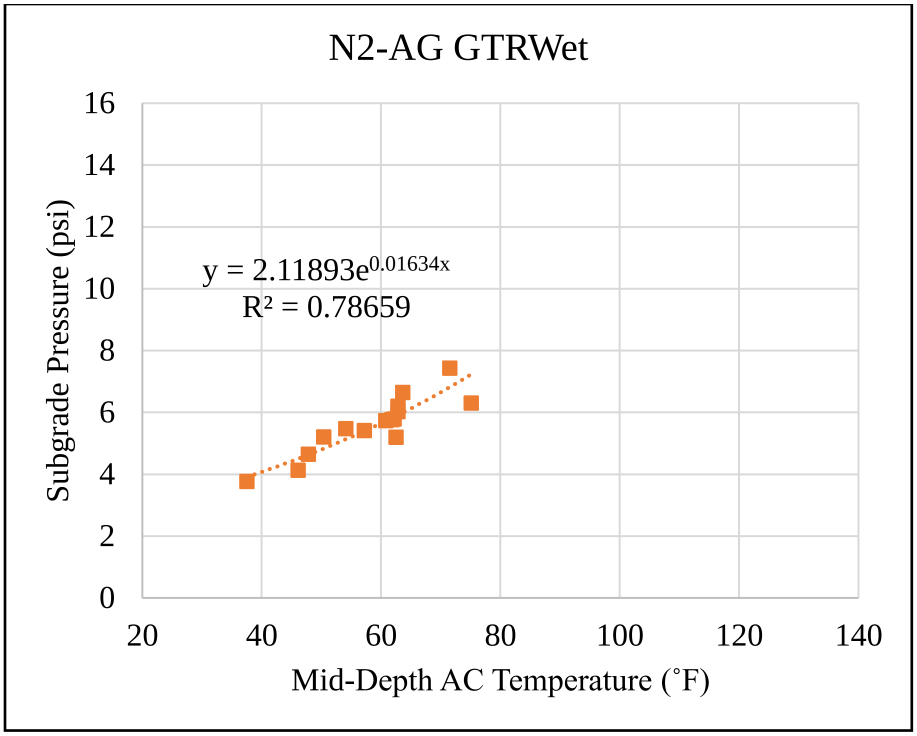

Figure E.15: Measured Subgrade Pressure Versus Temperature

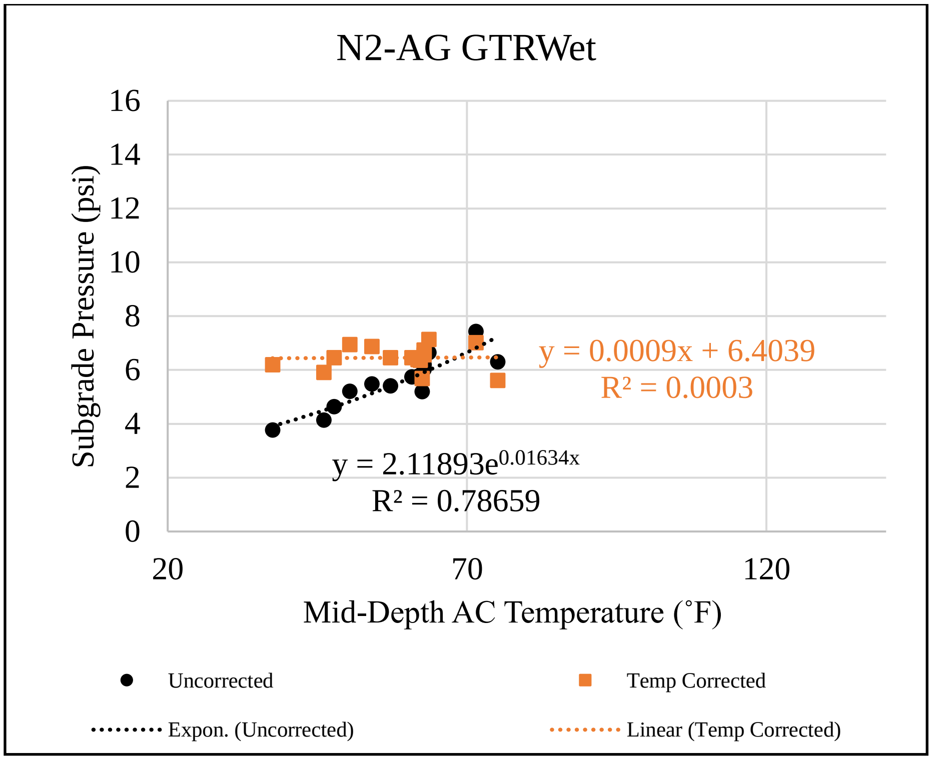

Figure E.16: Measured, Temperature Corrected Subgrade Pressure Versus Temperature

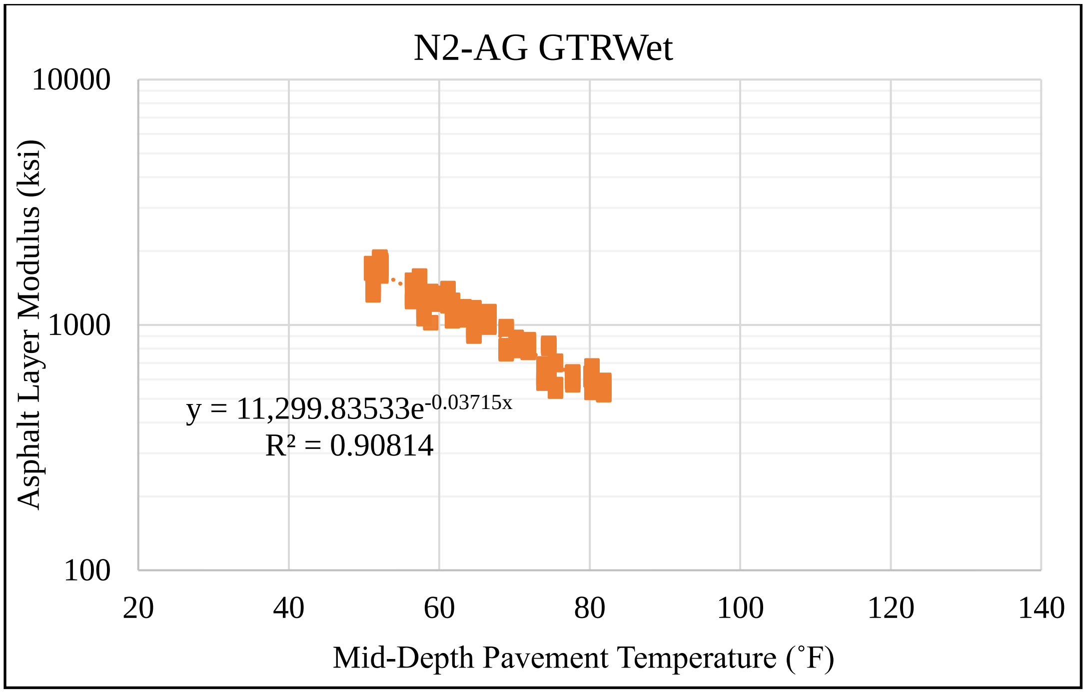

Figure E.17: Uncorrected Asphalt Layer Modulus Versus Temperature

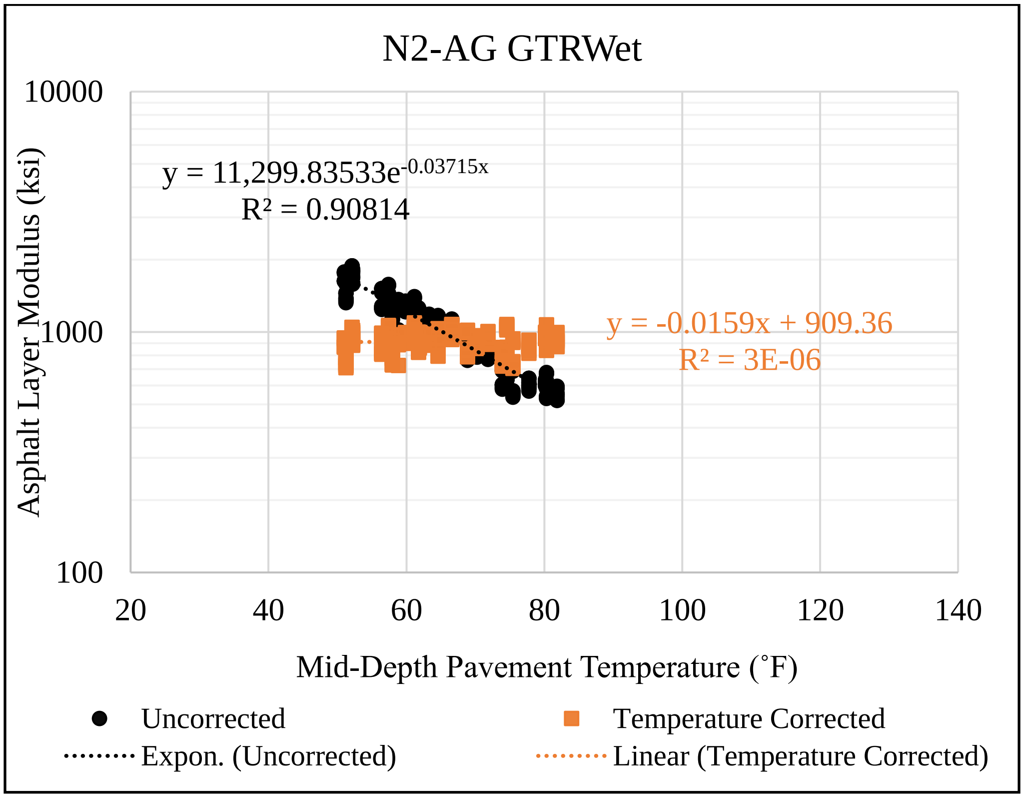

Figure E.18: Uncorrected, Temperature Corrected Asphalt Layer Modulus Versus Temperature

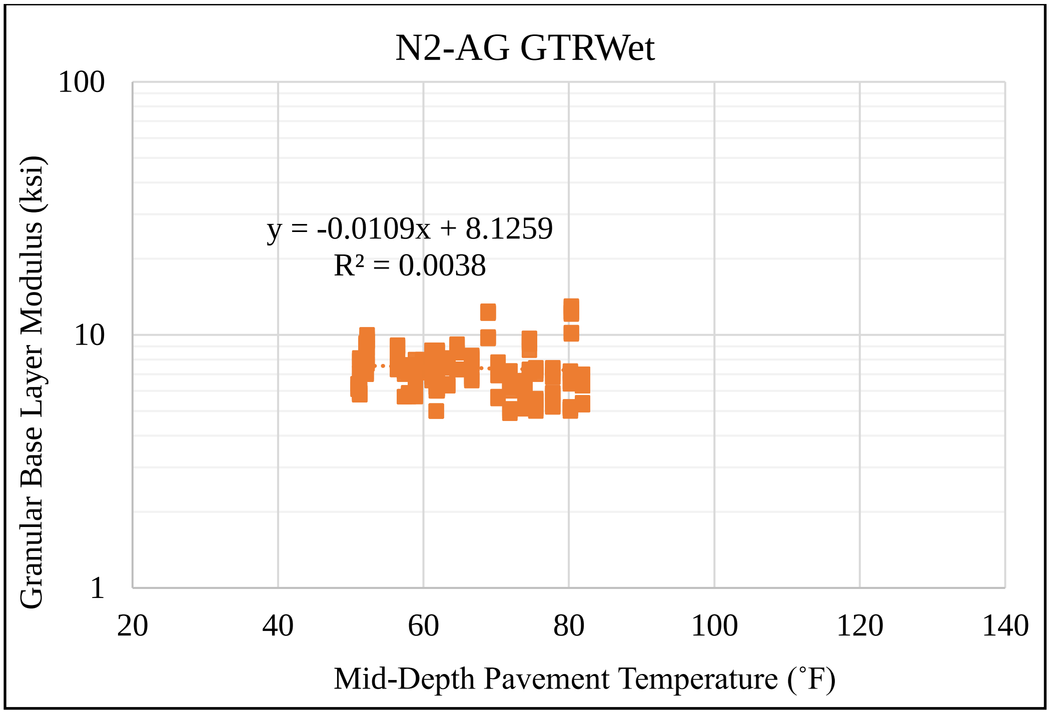

Figure E.19: Uncorrected GB Layer Modulus Versus Temperature

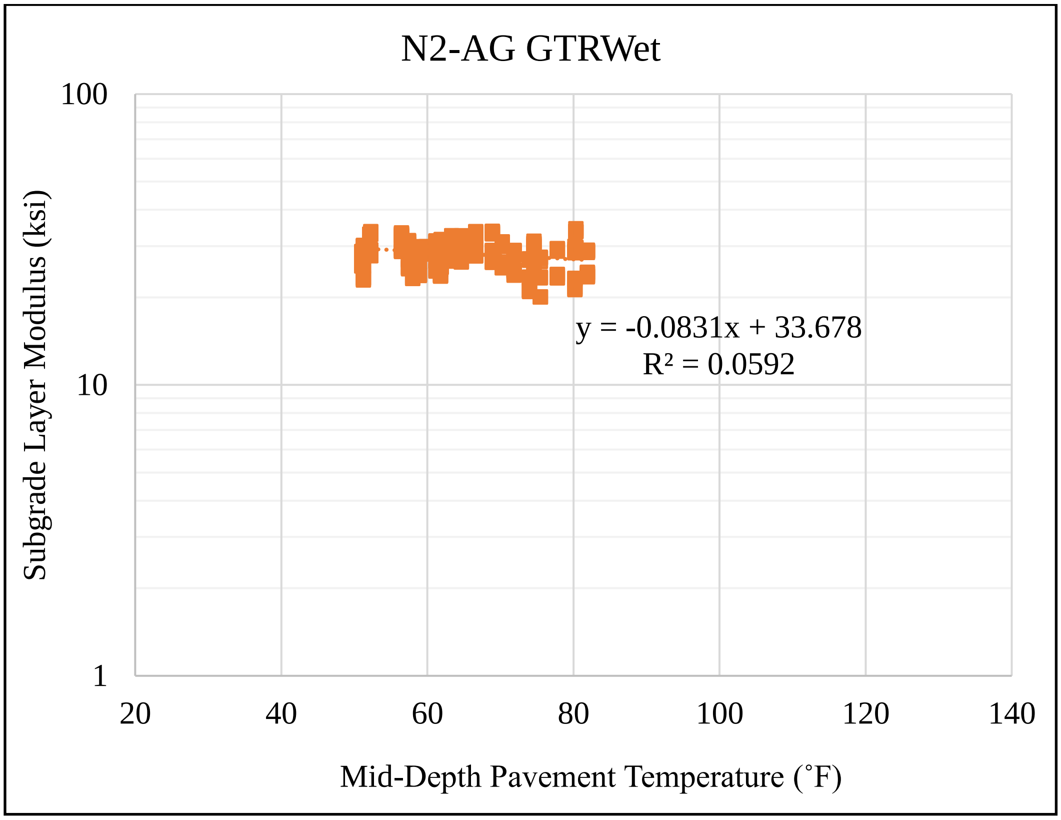

Figure E.20: Uncorrected Subgrade Layer Modulus Versus Temperature

N5-Aramid

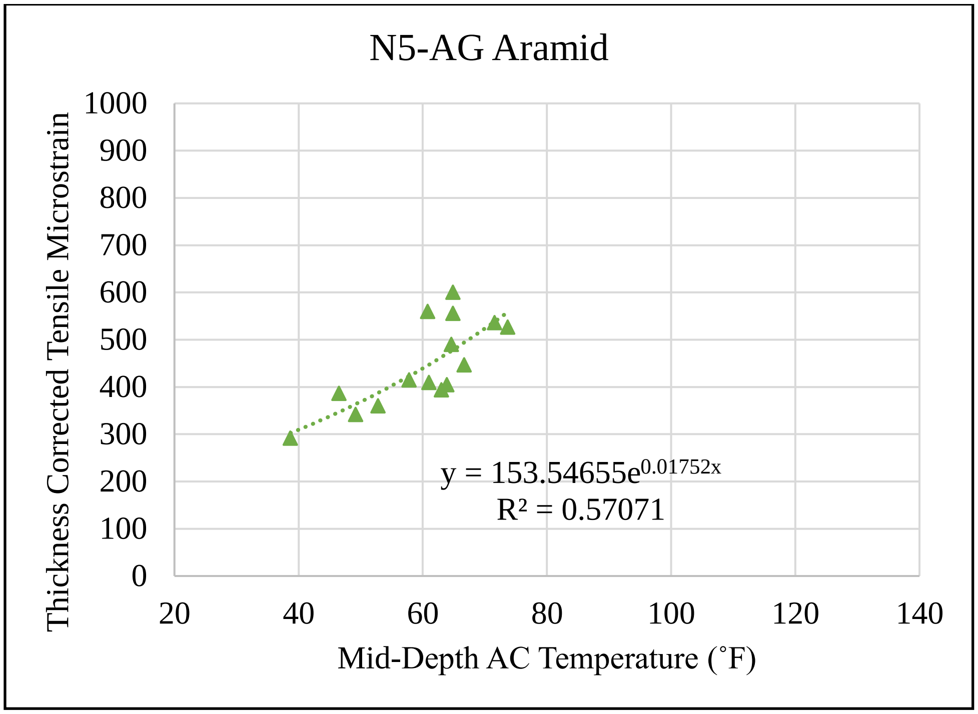

Figure E.21: Thickness Corrected Tensile Microstrain Versus Temperature

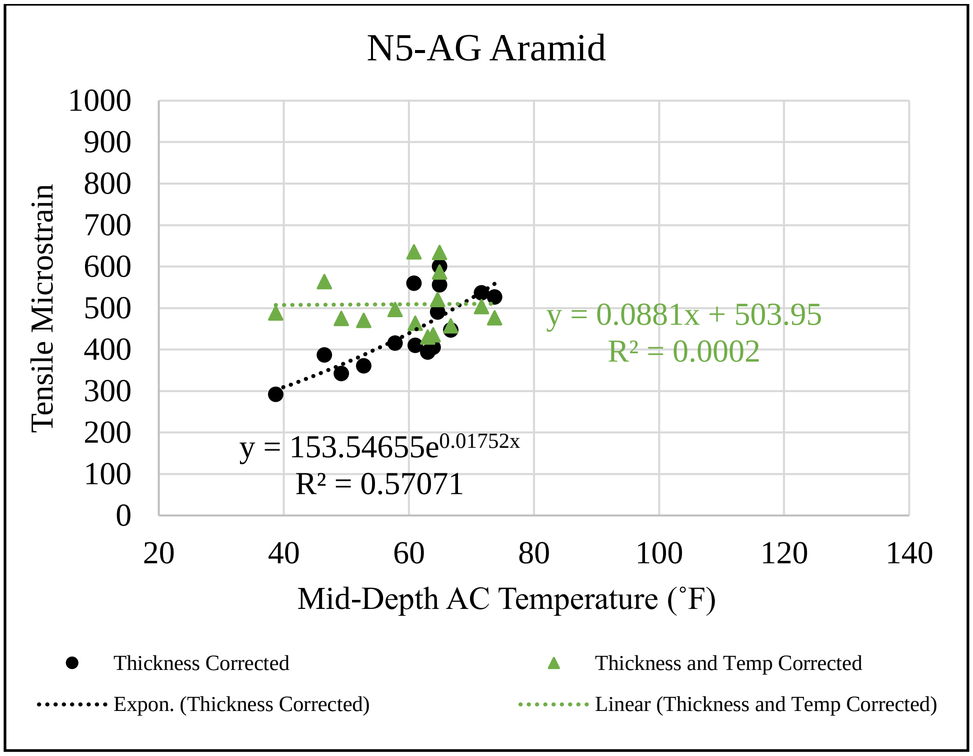

Figure E.22: Thickness, Temperature Corrected Tensile Microstrain Versus Temperature

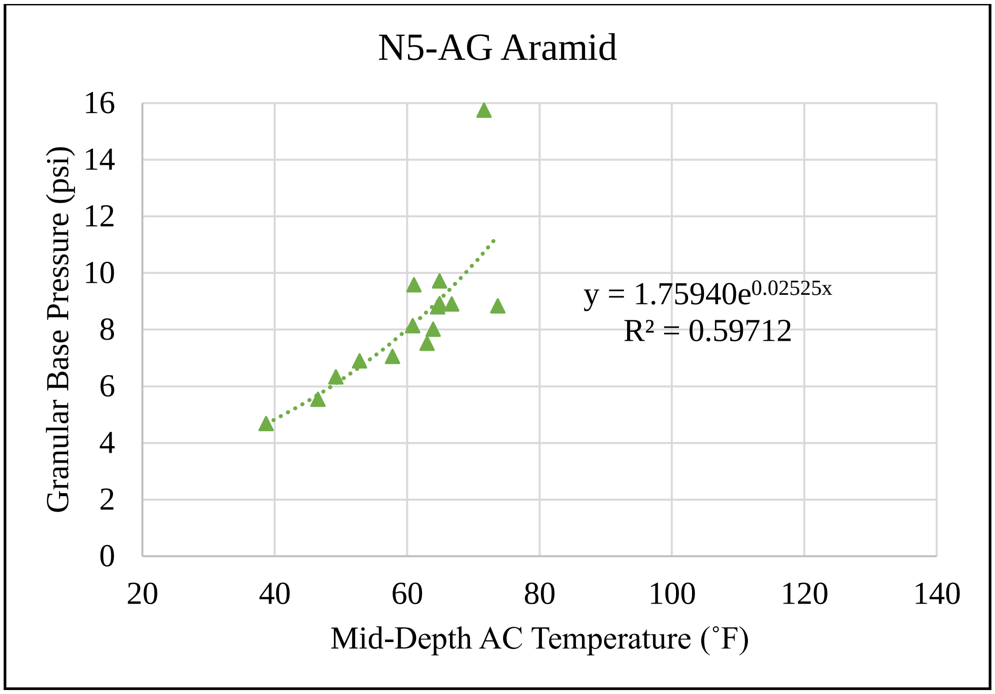

Figure E.23: Measured GB Pressure Versus Temperature

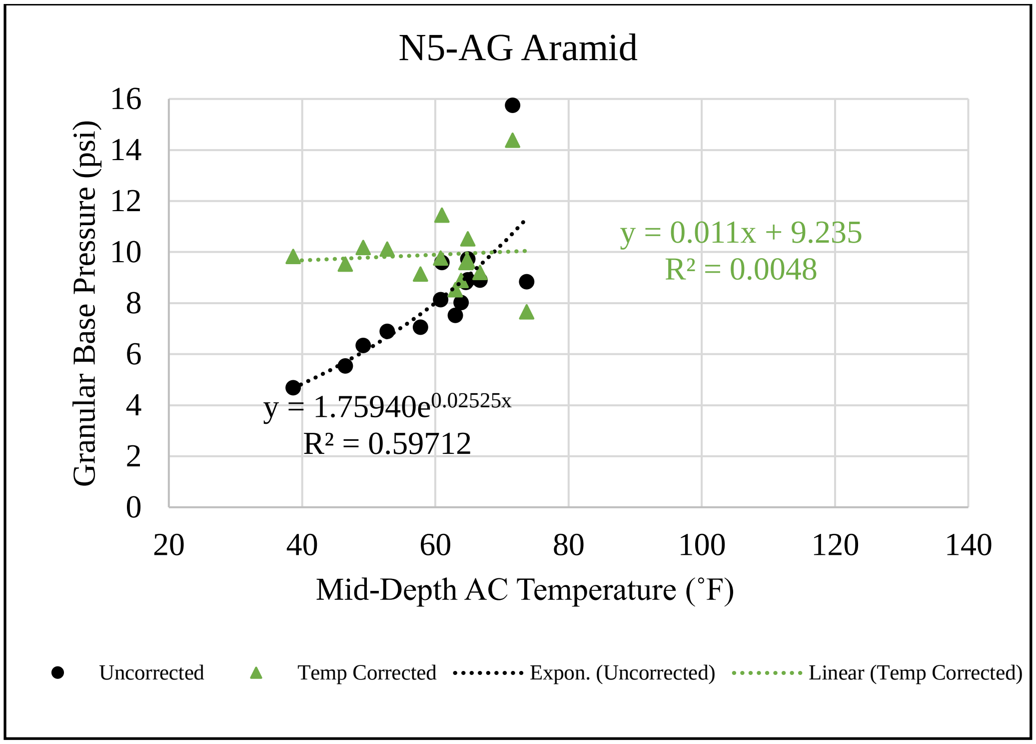

Figure E.24: Measured, Temperature Corrected GB Pressure Versus Temperature

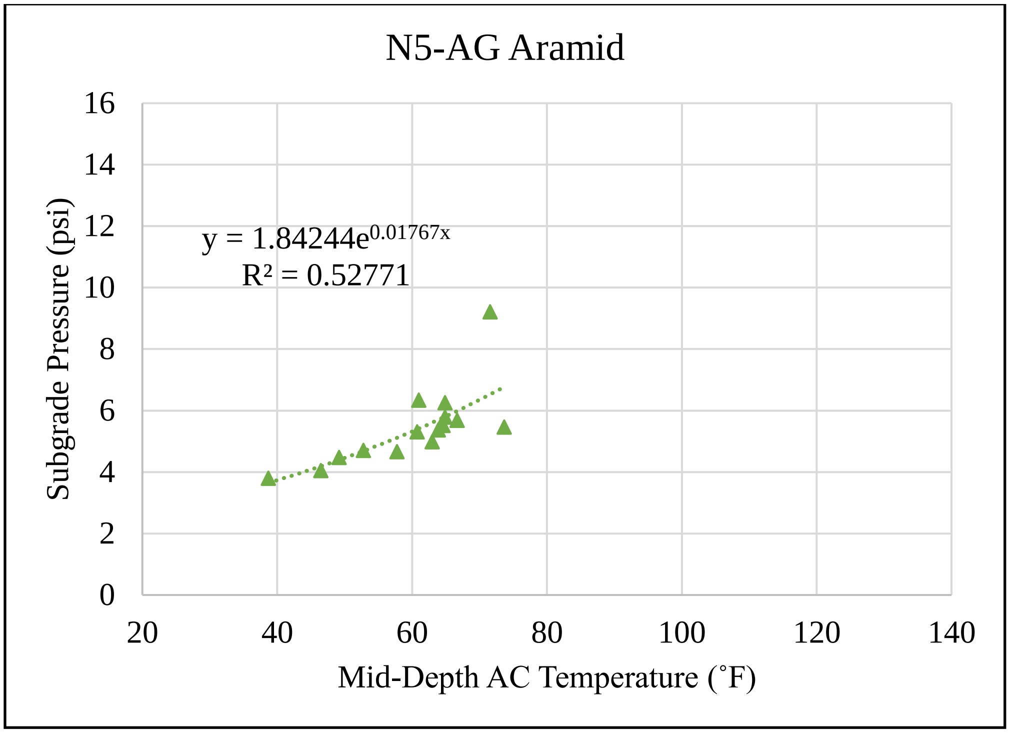

Figure E.25: Measured Subgrade Pressure Versus Temperature

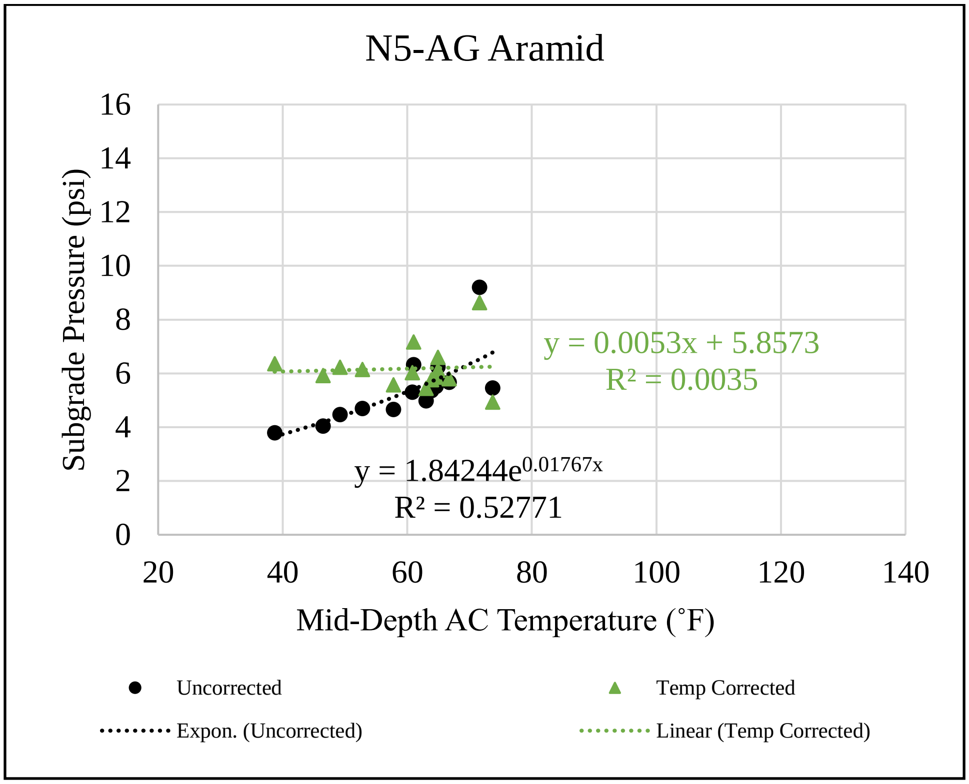

Figure E.26: Measured, Temperature Corrected Subgrade Pressure Versus Temperature

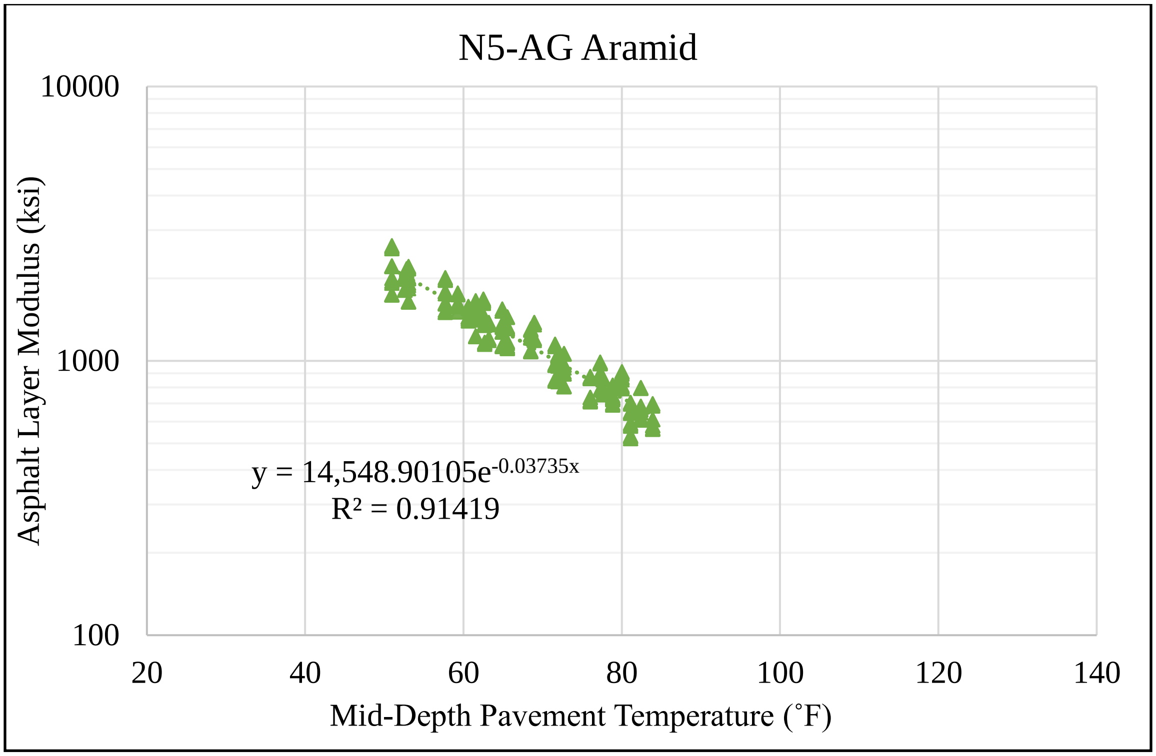

Figure E.27: Uncorrected Asphalt Layer Modulus Versus Temperature

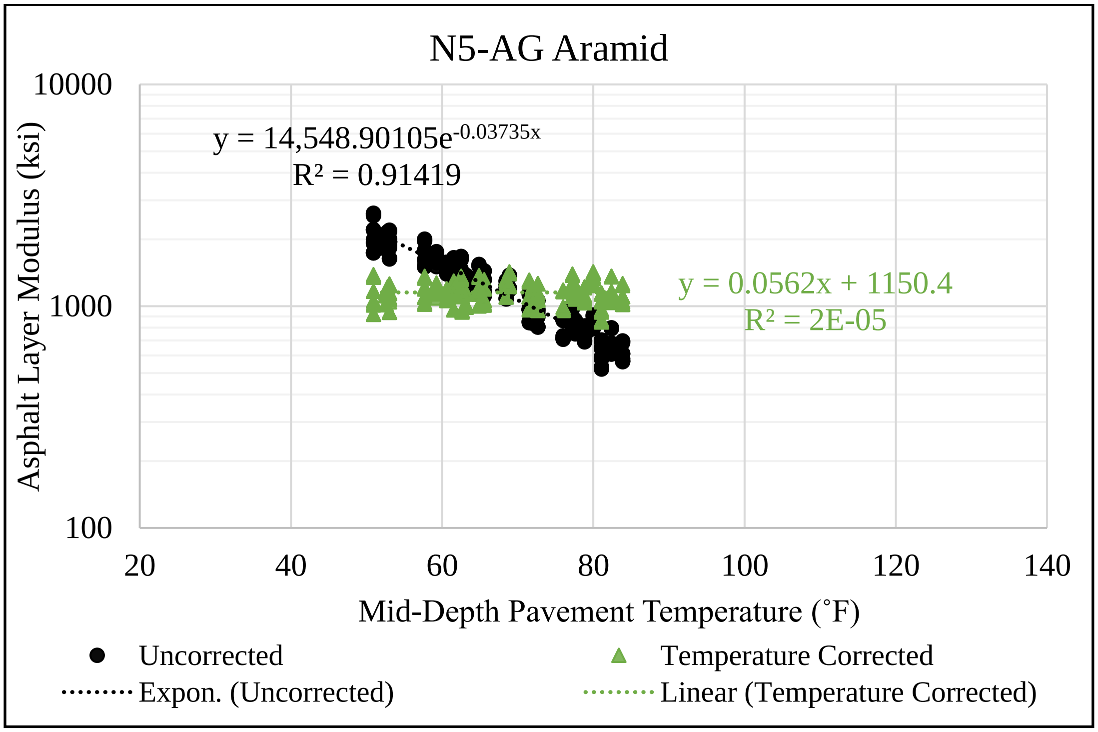

Figure E.28: Uncorrected, Temperature Corrected Asphalt Layer Modulus Versus Temperature

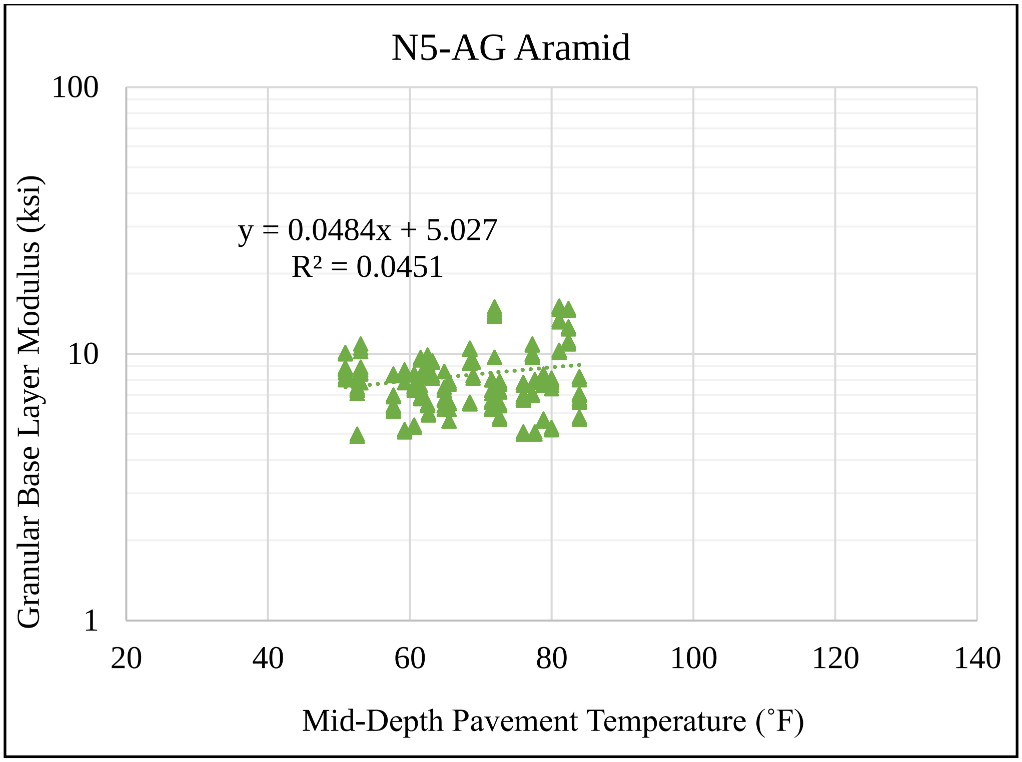

Figure E.29: Uncorrected GB Layer Modulus Versus Temperature

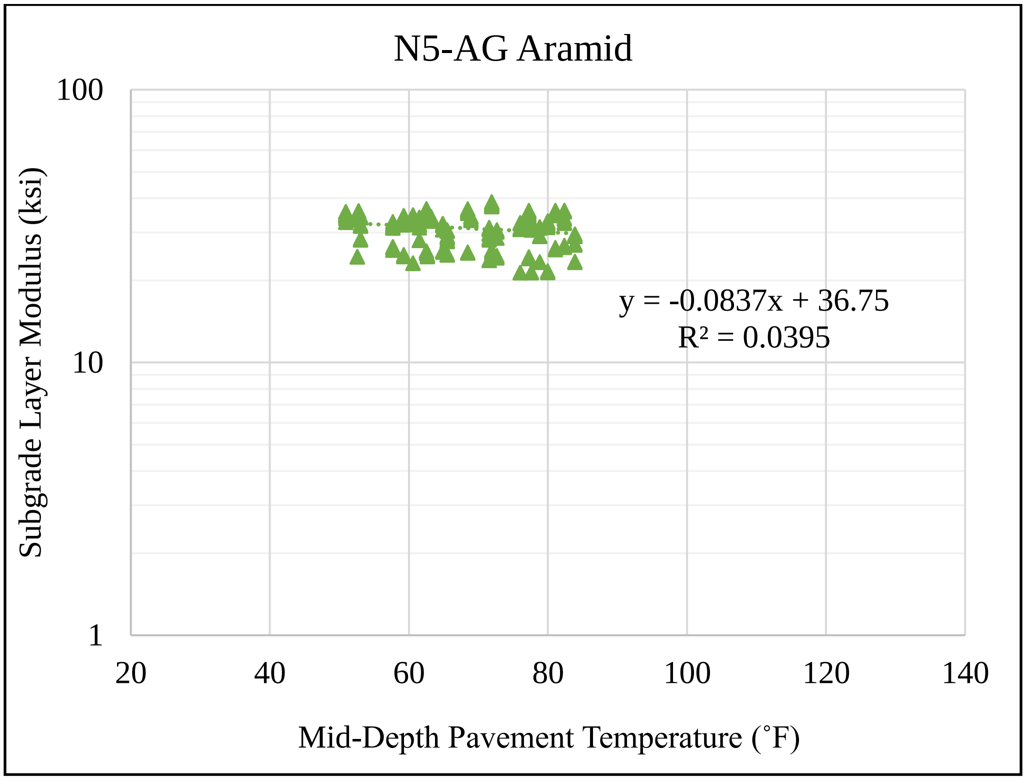

Figure E.30: Uncorrected Subgrade Layer Modulus Versus Temperature

N7-Ctrl

(See Chapter 5)

S5-DryPlastic

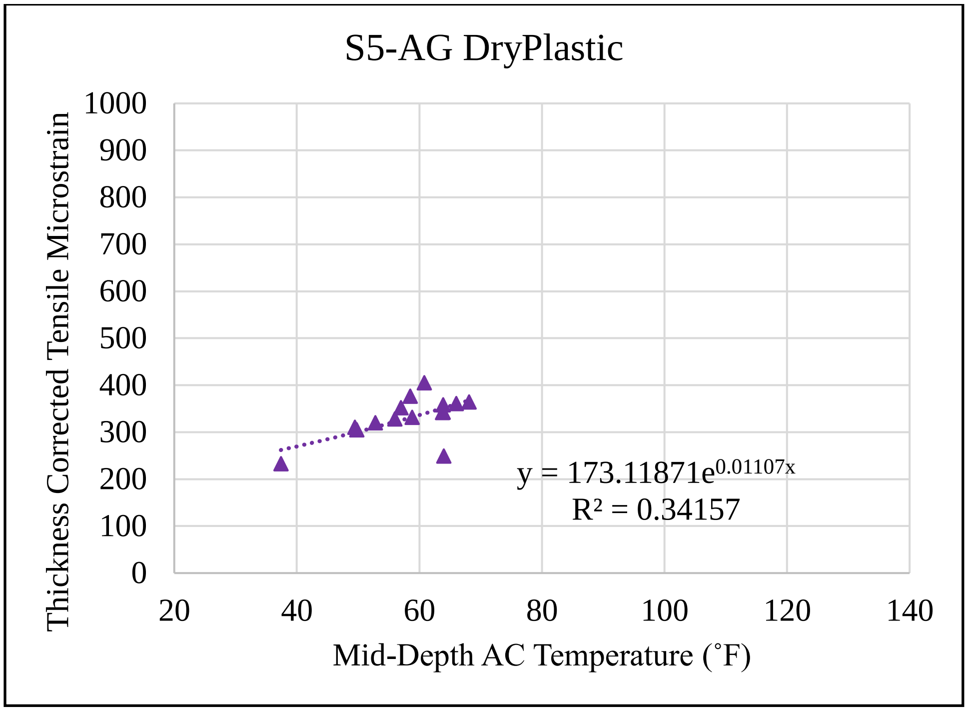

Figure E.31: Thickness Corrected Tensile Microstrain Versus Temperature

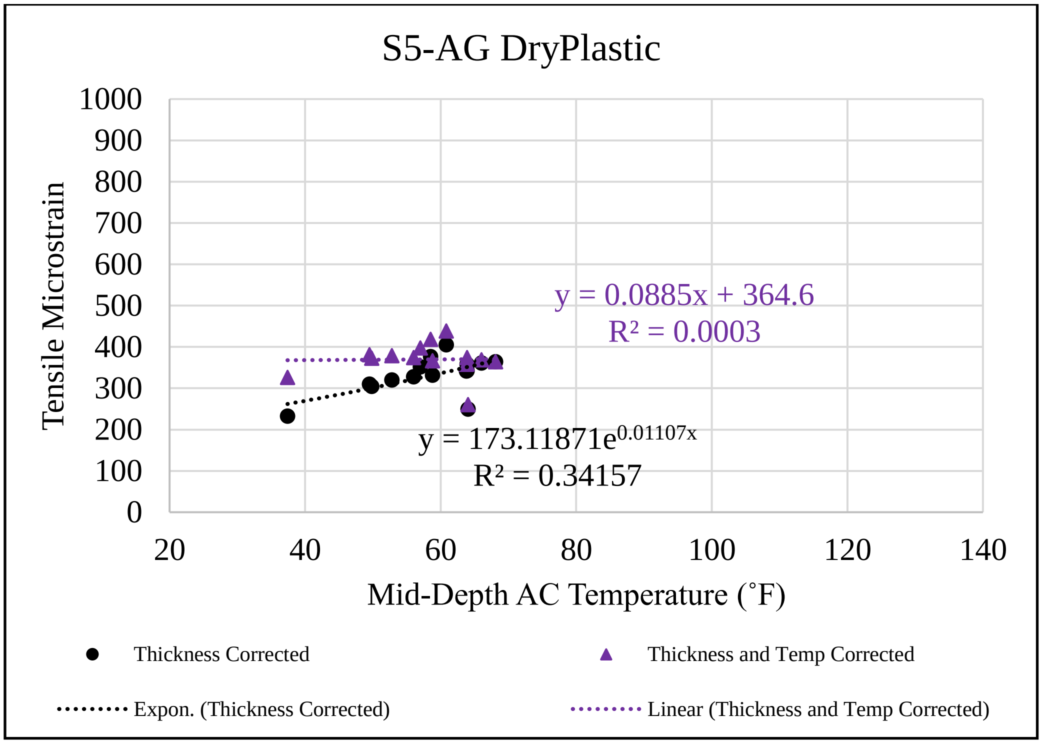

Figure E.32: Thickness, Temperature Corrected Tensile Microstrain Versus Temperature

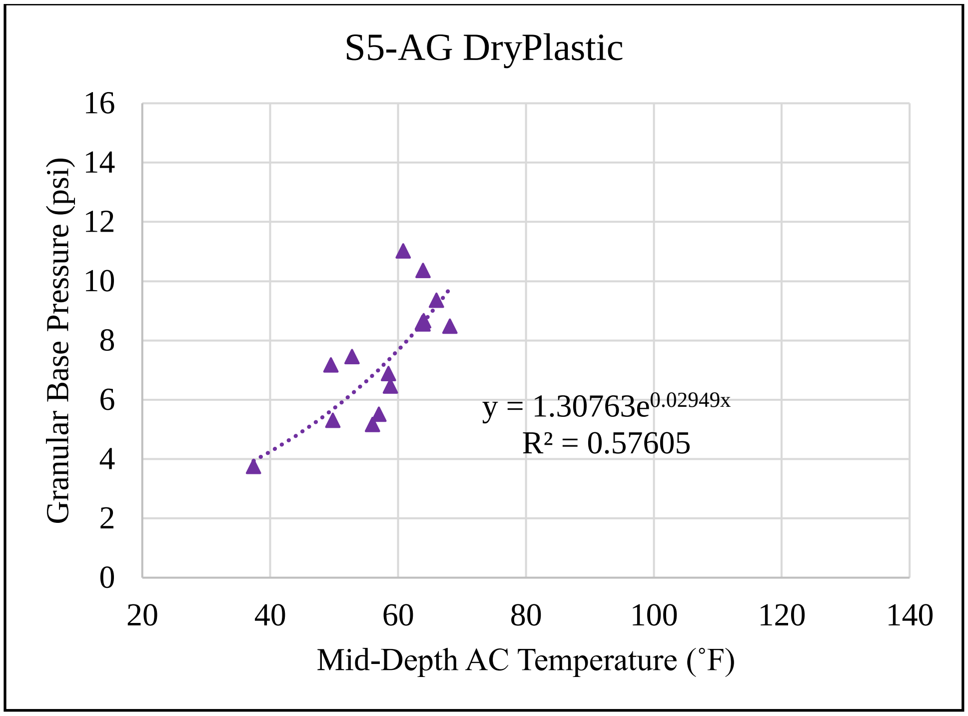

Figure E.33: Measured GB Pressure Versus Temperature

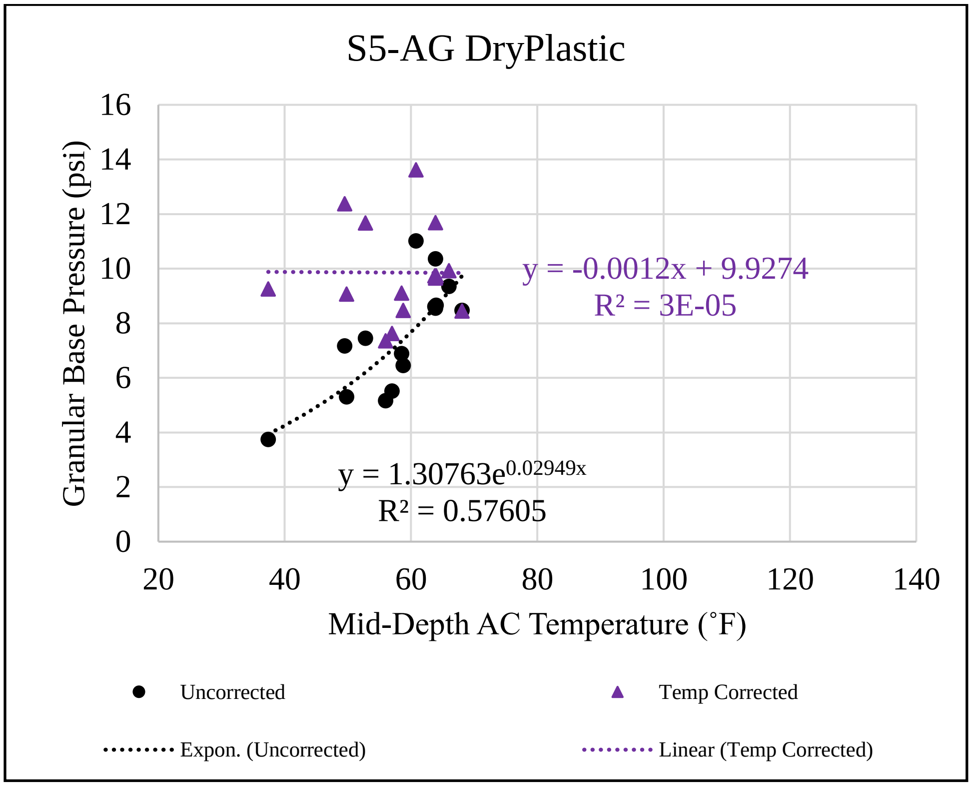

Figure E.34: Measured, Temperature Corrected GB Pressure Versus Temperature

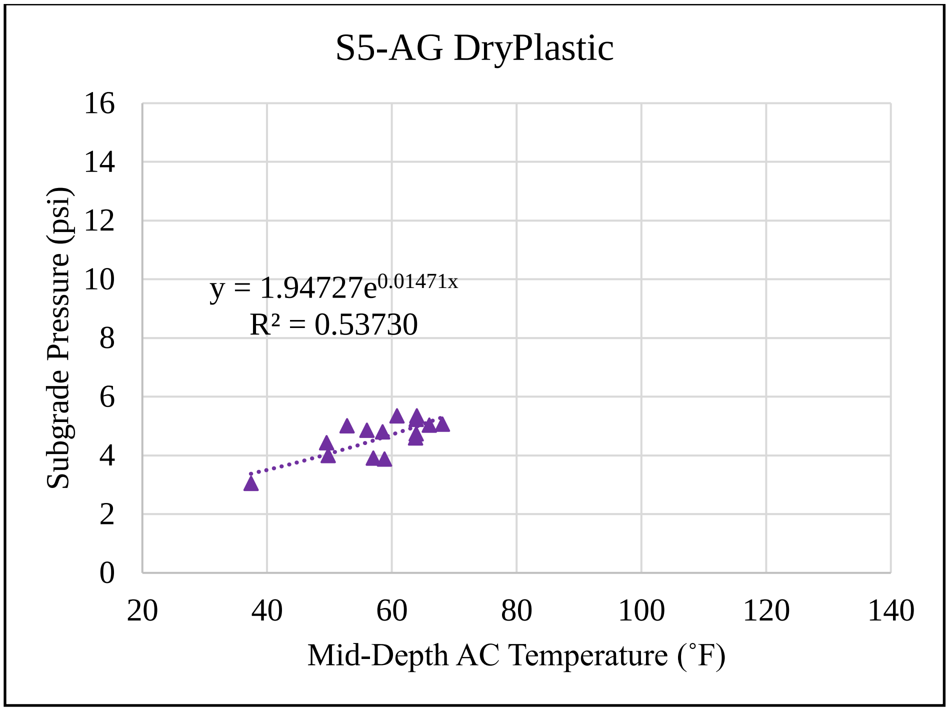

Figure E.35: Measured Subgrade Pressure Versus Temperature

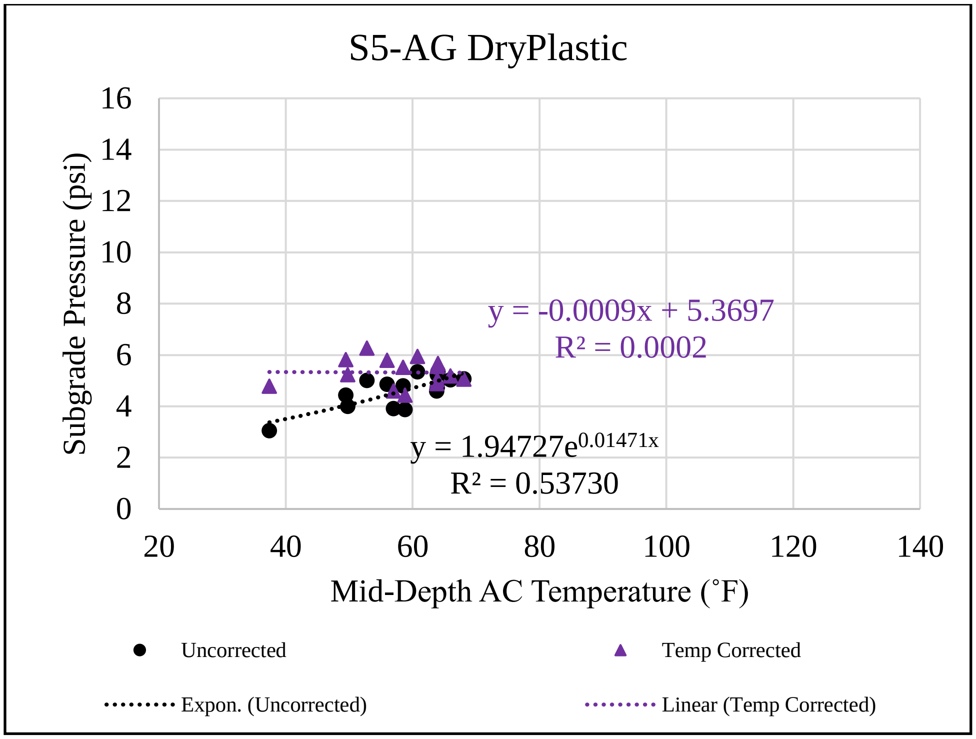

Figure E.36: Measured, Temperature Corrected Subgrade Pressure Versus Temperature

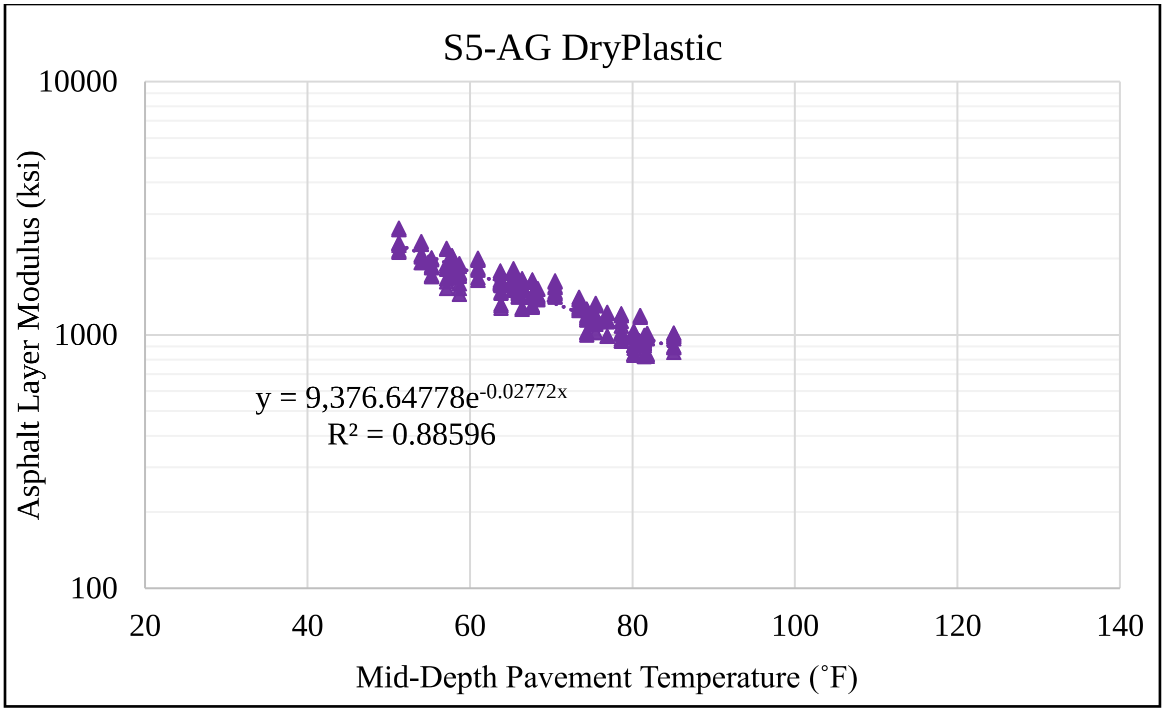

Figure E.37: Uncorrected Asphalt Layer Modulus Versus Temperature

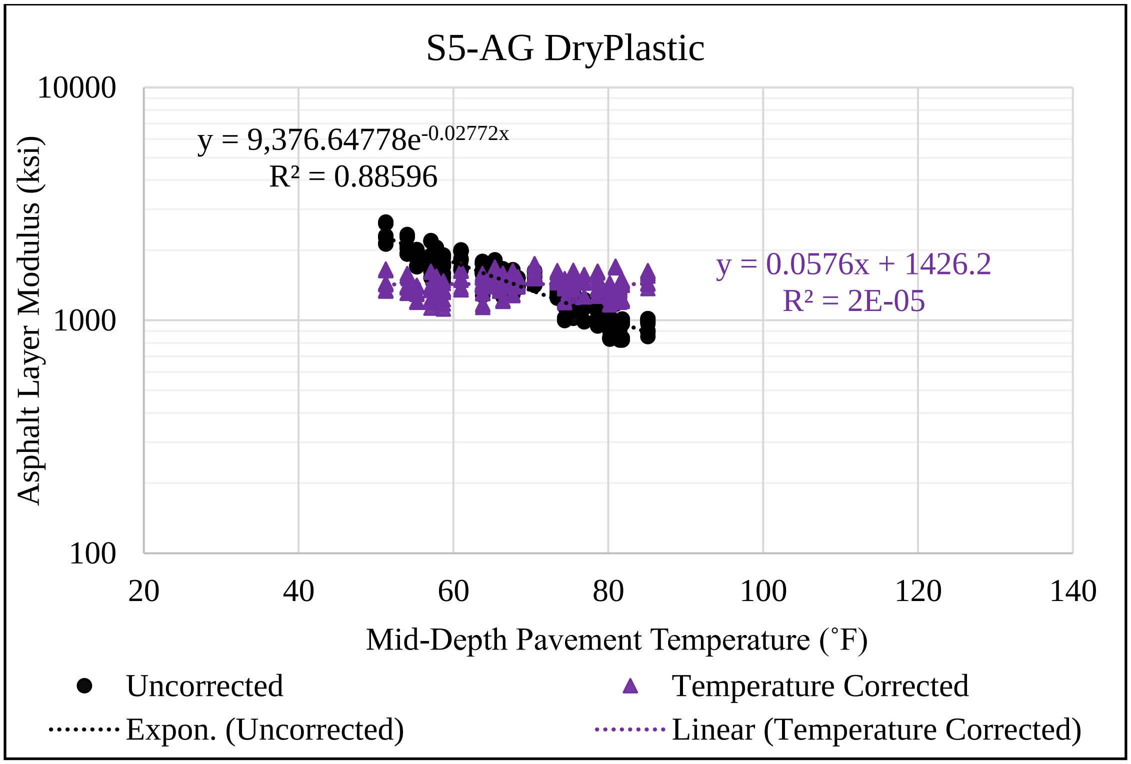

Figure E.38: Uncorrected, Temperature Corrected Asphalt Layer Modulus Versus Temperature

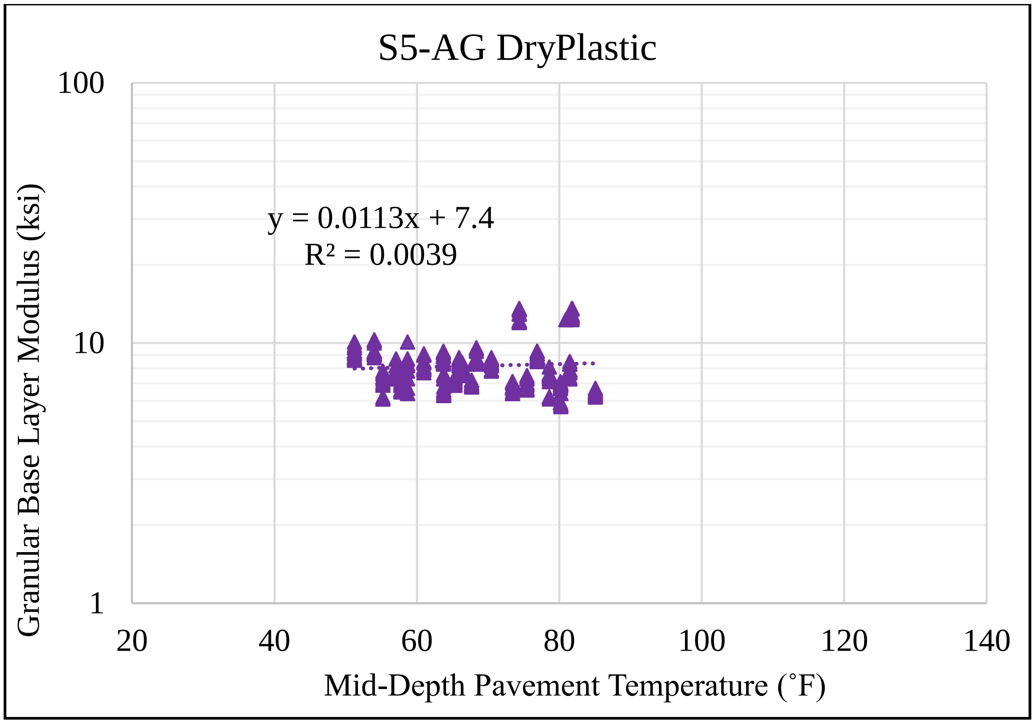

Figure E.39: Uncorrected GB Layer Modulus Versus Temperature

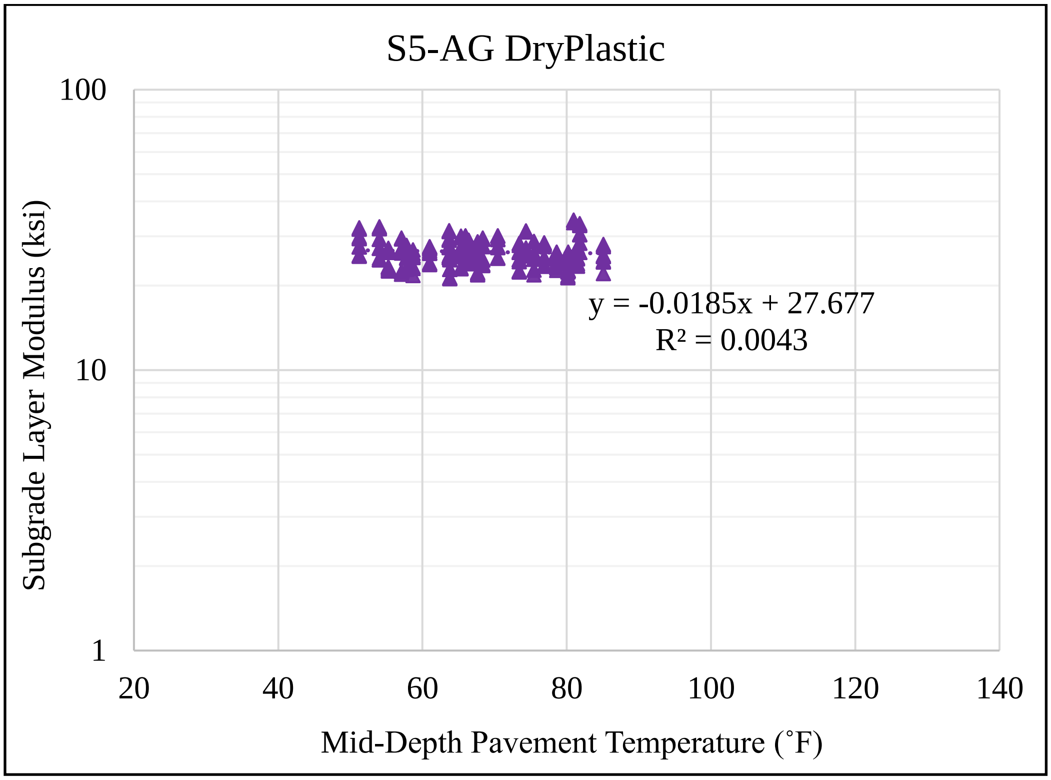

Figure E.40: Uncorrected Subgrade Layer Modulus Versus Temperature

S6-WetPlastic

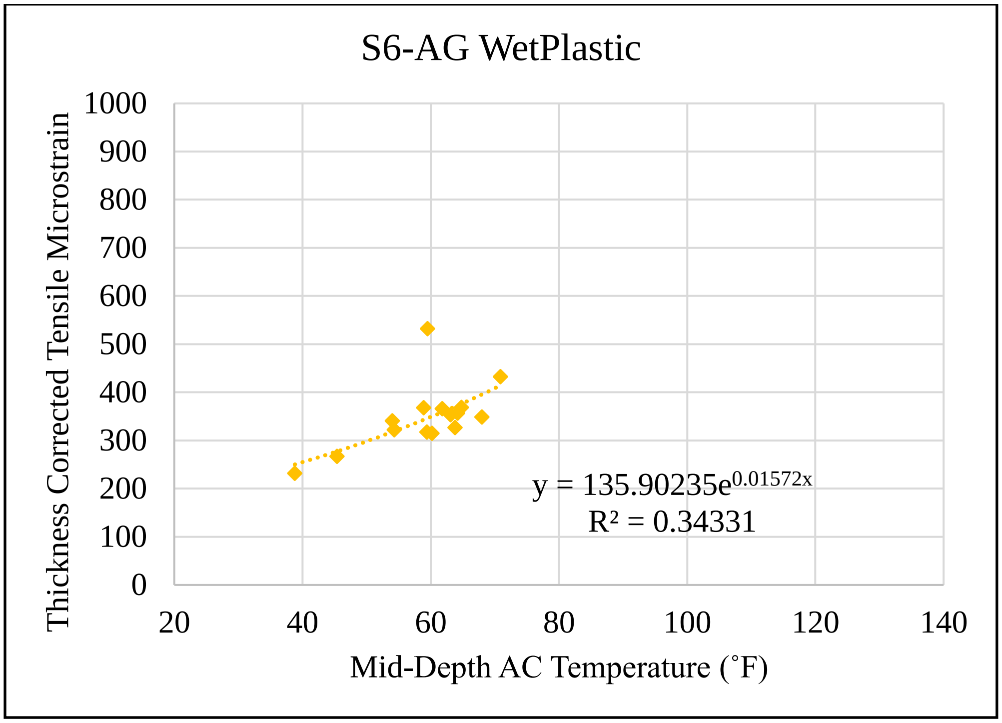

Figure E.41: Thickness Corrected Tensile Microstrain Versus Temperature

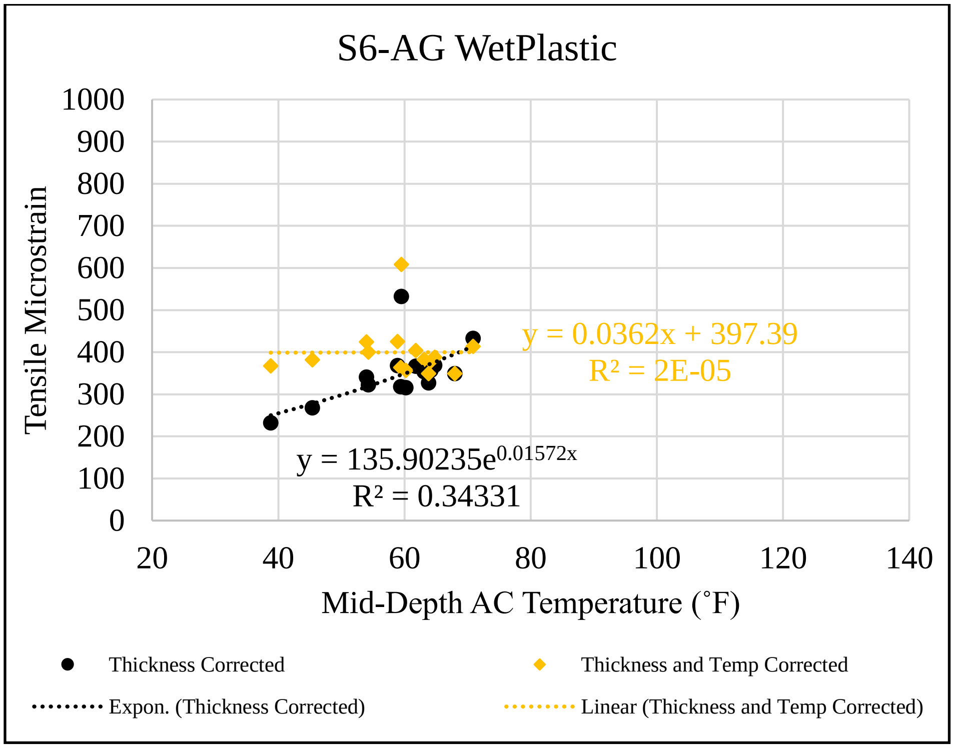

Figure E.42: Thickness, Temperature Corrected Tensile Microstrain Versus Temperature

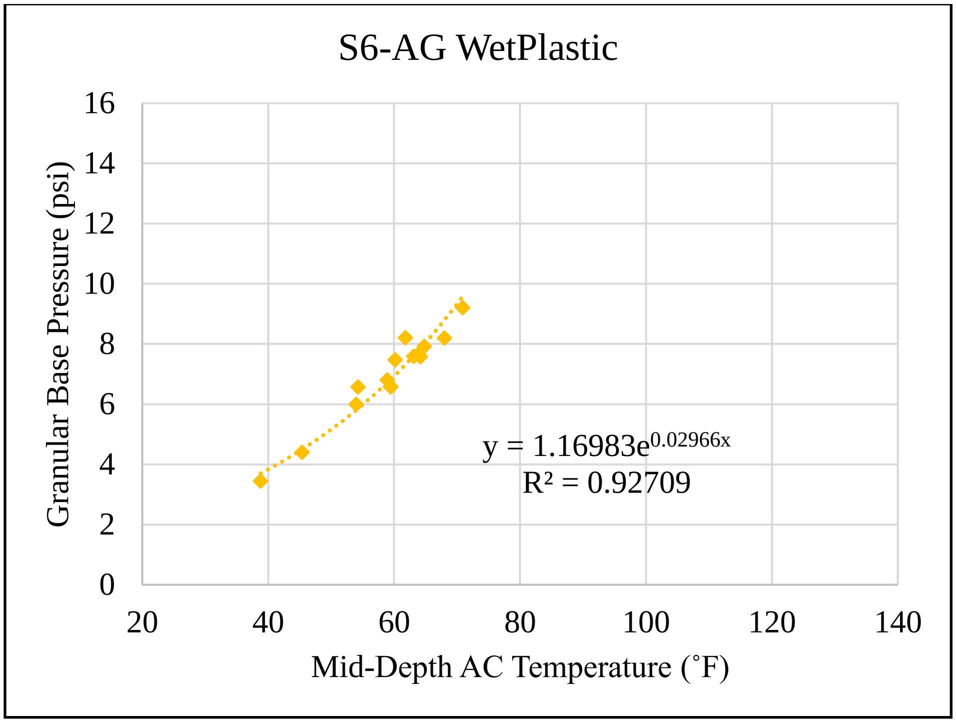

Figure E.43: Measured GB Pressure Versus Temperature

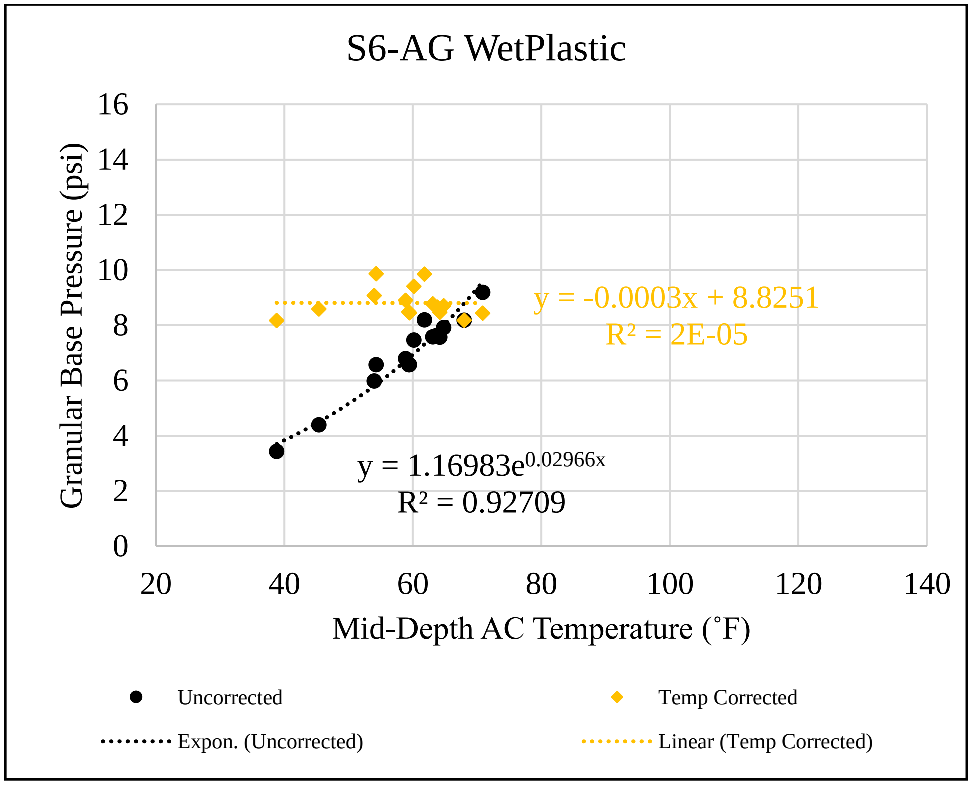

Figure E.44: Measured, Temperature Corrected GB Pressure Versus Temperature

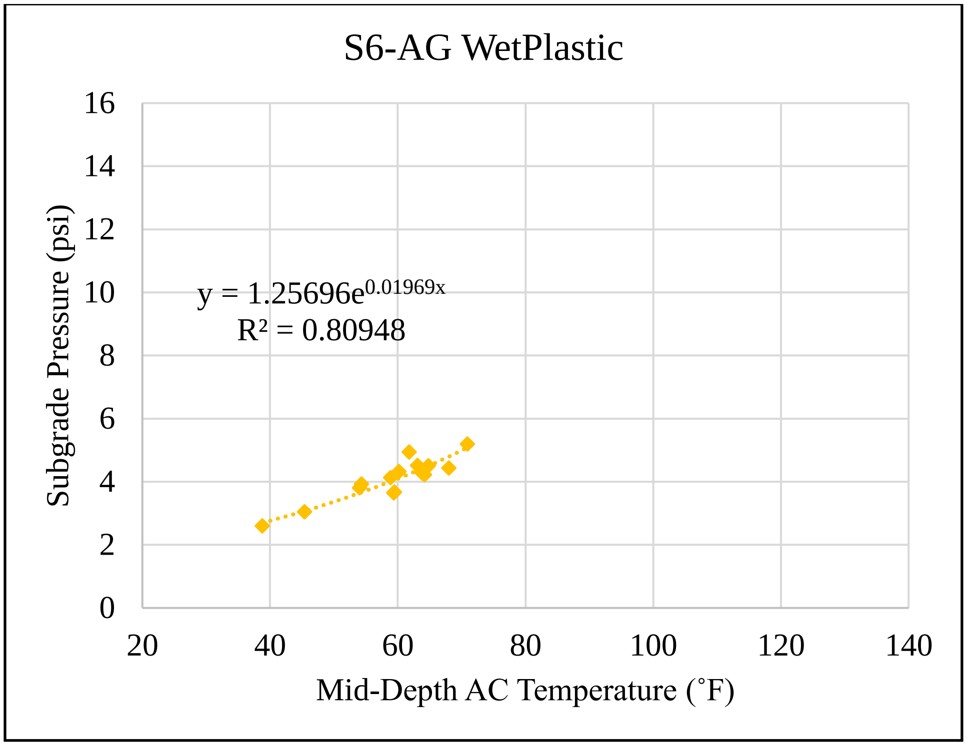

Figure E.45: Measured Subgrade Pressure Versus Temperature

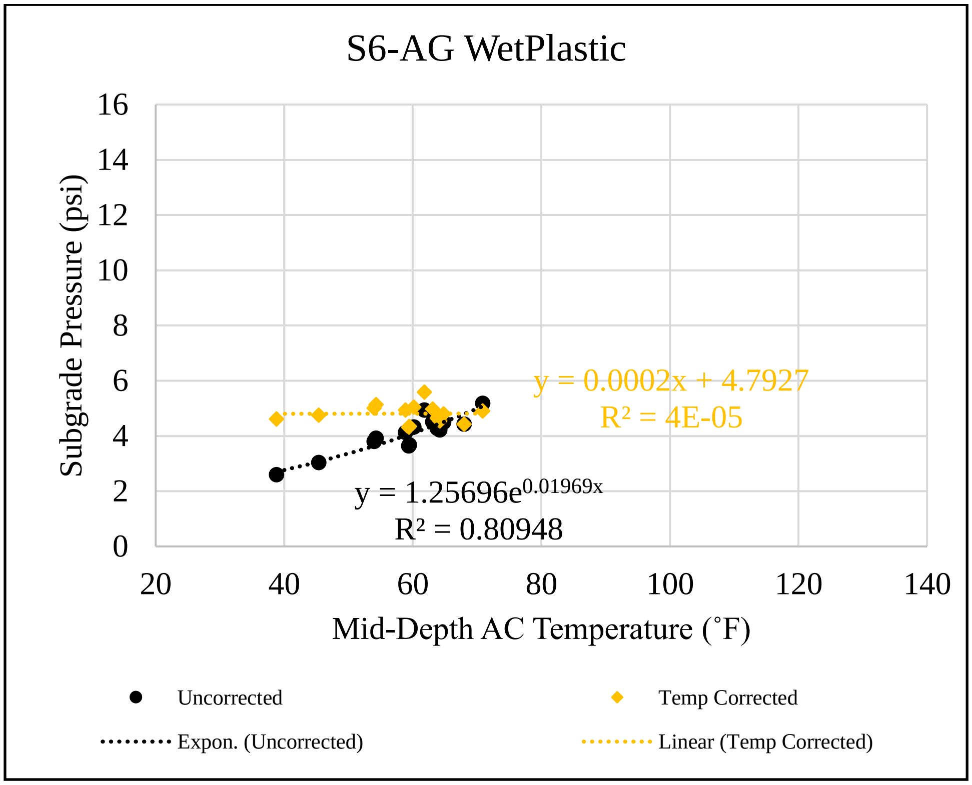

Figure E.46: Measured, Temperature Corrected Subgrade Pressure Versus Temperature

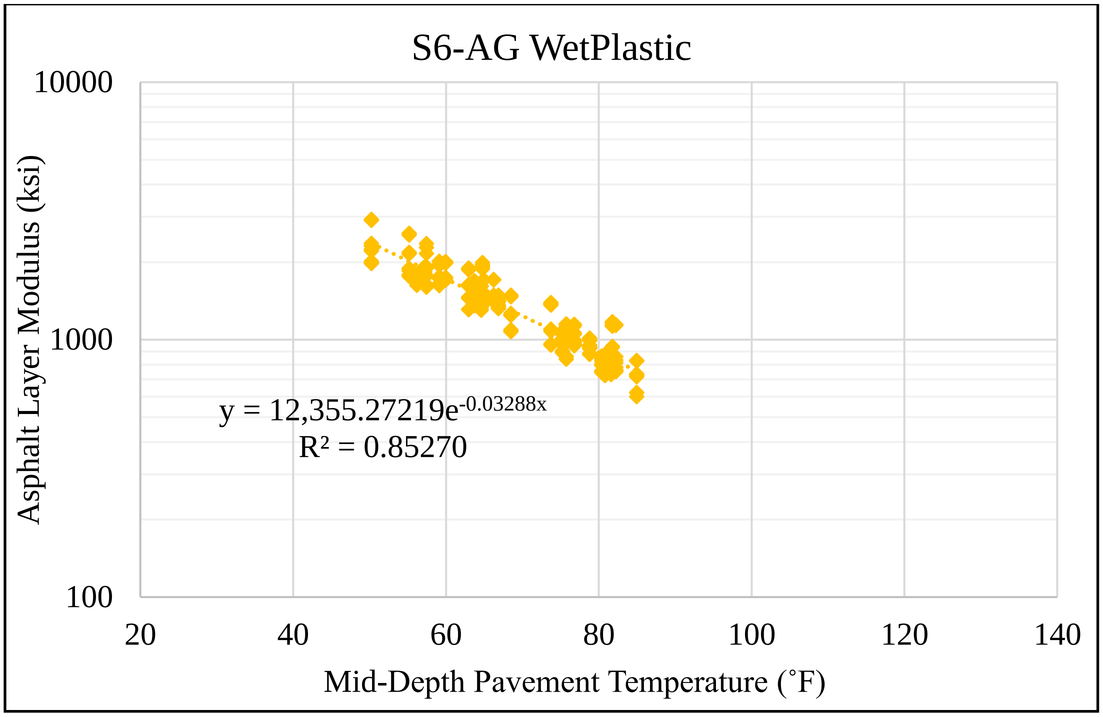

Figure E.47: Uncorrected Asphalt Layer Modulus Versus Temperature

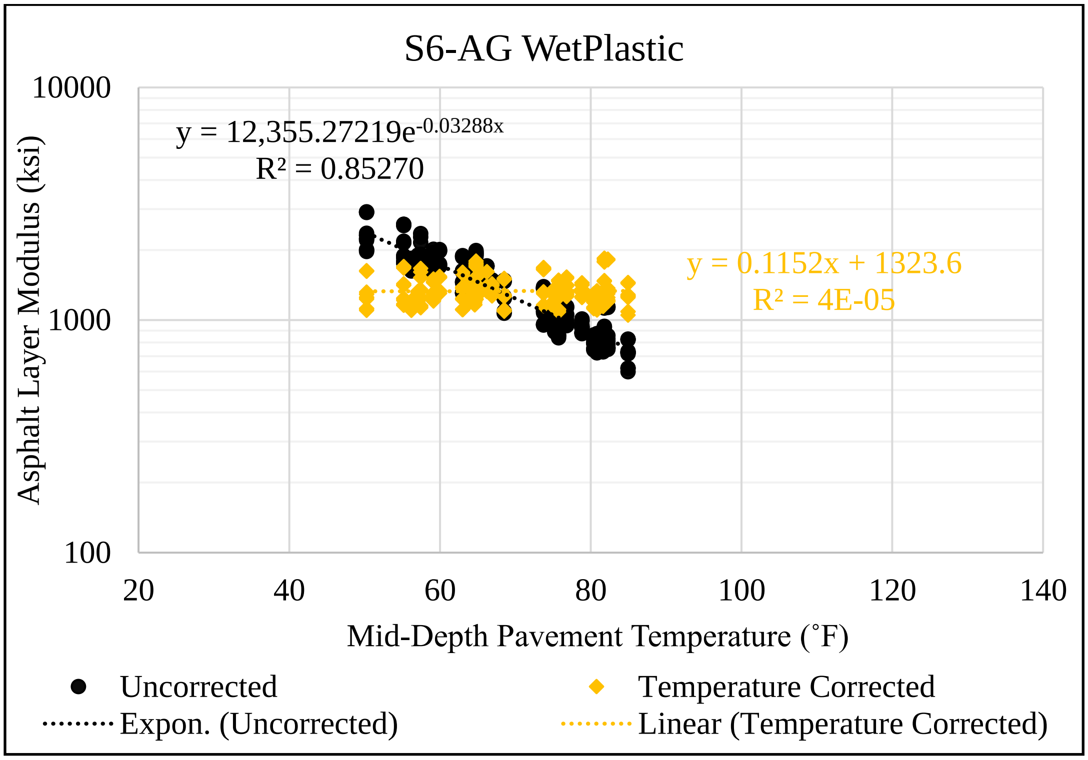

Figure E.48: Uncorrected, Temperature Corrected Asphalt Layer Modulus Versus Temperature

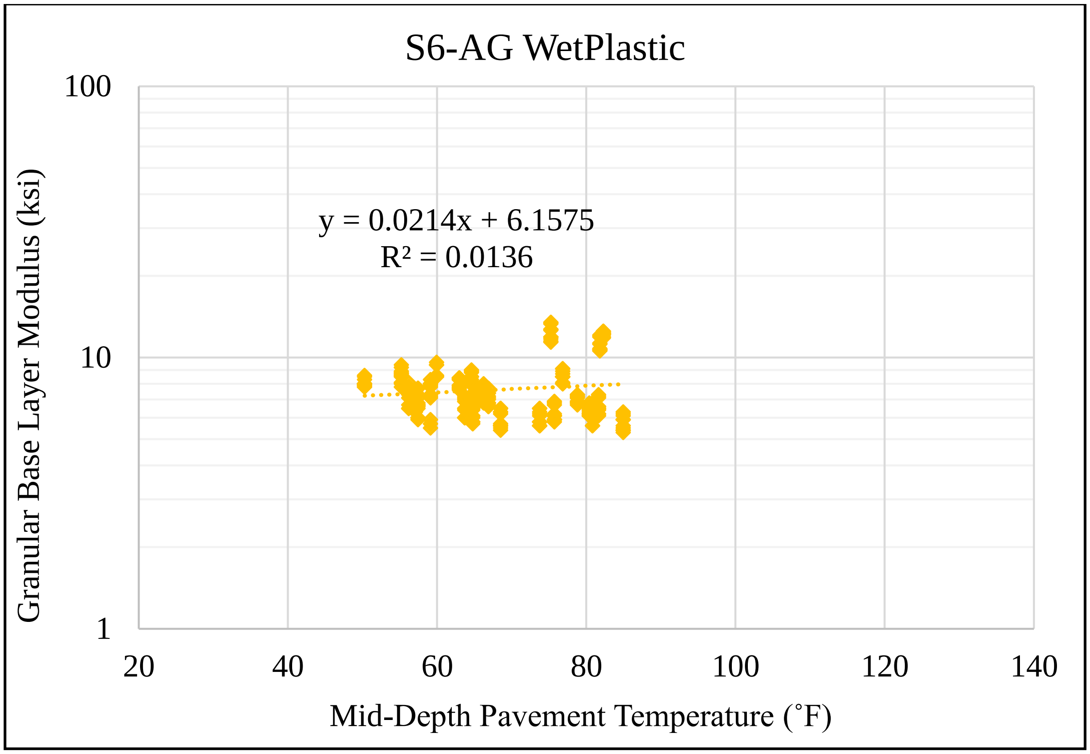

Figure E.49: Uncorrected GB Layer Modulus Versus Temperature

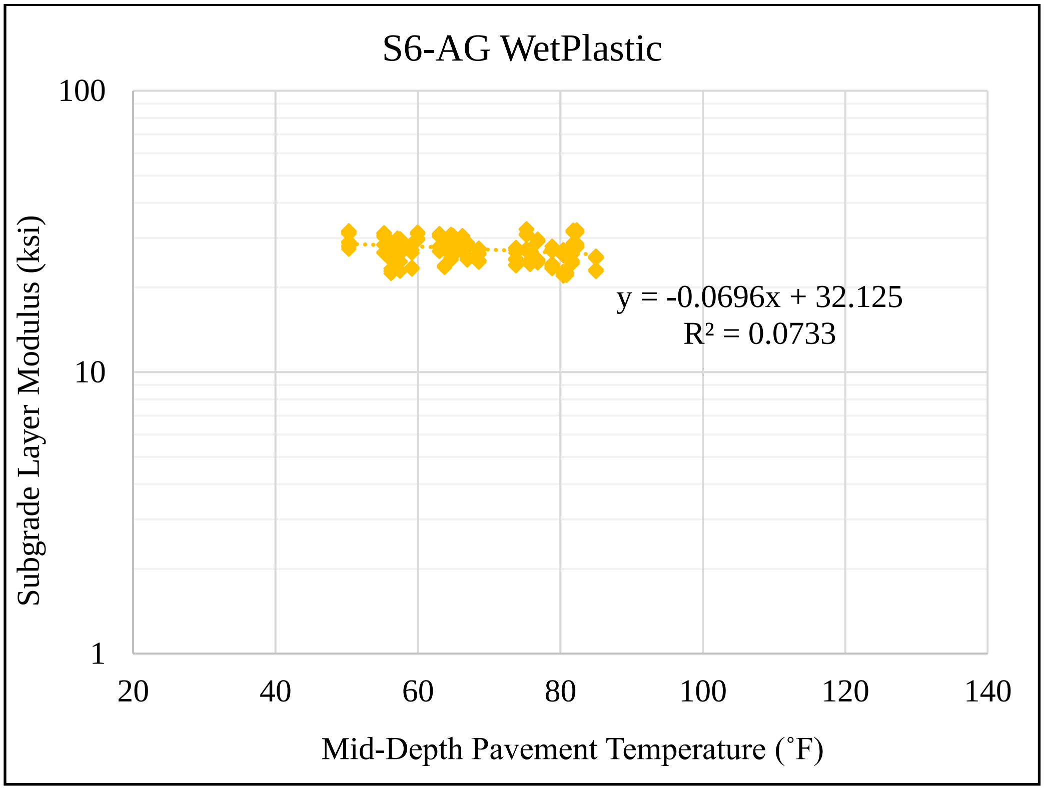

Figure E.50: Uncorrected Subgrade Layer Modulus Versus Temperature

APPENDIX F

Statistical Analysis

Table F.1: Thickness and Temperature Corrected Tensile Microstrain ANOVA

ANOVA: Single Factor

DESCRIPTION					Alpha	0.05		
Group	*Count*	*Sum*	*Mean*	*Variance*	*SS*	*Std Err*	*Lower*	*Upper*
N1-AG GTRDry	15	9368.02	624.5345	2994.64	41925.00617	14.4093	595.88	653.1889622
N2-AG GTRWet	15	9404.25	626.9497	5435.4	76095.6415	14.4093	598.295	655.604191
N5-AG Aramid	15	7638.52	509.2346	4388.73	61442.25983	14.4093	480.58	537.8890732
N7-AG Ctrl	15	5196.07	346.405	304.693	4265.700409	14.4093	317.751	375.0594575
S5-AG DryPlastic	15	5545.97	369.7316	1587.85	22229.86375	14.4093	341.077	398.386075
S6-AG WetPlastic	15	5992.95	399.5303	3975.2	55652.75837	14.4093	370.876	428.1847625

ANOVA								
Sources	*SS*	*df*	*MS*	*F*	*P value*	*Eta-sq*	*RMSSE*	*Omega Sq*
Between Groups	1E+06	5	239457.1	76.8866	7.20154E-30	0.82068	2.26402	0.80827936
Within Groups	261611	84	3114.419					
Total	1E+06	89	16392.1					

Table F.2: Thickness and Temperature Corrected Tensile Microstrain Tukey-Kramer

TUKEY HSD/KRAMER			alpha	0.05	
group	*mean*	*n*	*ss*	*df*	*q-crit*
N1-AG GTRDry	624.5344866	15	41925.01		
N2-AG GTRWet	626.9497154	15	76095.64		
N5-AG Aramid	509.2345976	15	61442.26		
N7-AG Ctrl	346.4049819	15	4265.7		
S5-AG DryPlastic	369.7315994	15	22229.86		
S6-AG WetPlastic	399.5302869	15	55652.76		
		90	261611.2	84	4.12429

Q TEST

group 1	*group 2*	*mean*	*std err*	*q-stat*	*lower*	*upper*	*p-value*	*mean-crit*	*Cohen d*
N1-AG GTRDry	N2-AG GTRWet	2.41523	14.4093	0.16762	-57.013	61.8433	0.999996606	59.4281	0.04328
N1-AG GTRDry	N5-AG Aramid	115.3	14.4093	8.00177	55.8718	174.728	3.04411E-06	59.4281	2.06605
N1-AG GTRDry	N7-AG Ctrl	278.13	14.4093	19.3021	218.701	337.558	-5.59552E-14	59.4281	4.98378
N1-AG GTRDry	S5-AG DryPlastic	254.803	14.4093	17.6832	195.375	314.231	-5.59552E-14	59.4281	4.56579
N1-AG GTRDry	S6-AG WetPlastic	225.004	14.4093	15.6152	165.576	284.432	-5.55112E-14	59.4281	4.03183
N2-AG GTRWet	N5-AG Aramid	117.715	14.4093	8.16938	58.287	177.143	1.8473E-06	59.4281	2.10933
N2-AG GTRWet	N7-AG Ctrl	280.545	14.4093	19.4697	221.117	339.973	-5.59552E-14	59.4281	5.02705
N2-AG GTRWet	S5-AG DryPlastic	257.218	14.4093	17.8508	197.79	316.646	-5.59552E-14	59.4281	4.60907
N2-AG GTRWet	S6-AG WetPlastic	227.419	14.4093	15.7828	167.991	286.848	-5.55112E-14	59.4281	4.07511
N5-AG Aramid	N7-AG Ctrl	162.83	14.4093	11.3003	103.402	222.258	9.47523E-11	59.4281	2.91773
N5-AG Aramid	S5-AG DryPlastic	139.503	14.4093	9.68145	80.0749	198.931	1.73466E-08	59.4281	2.49974
N5-AG Aramid	S6-AG WetPlastic	109.704	14.4093	7.61344	50.2762	169.132	9.5167E-06	59.4281	1.96578
N7-AG Ctrl	S5-AG DryPlastic	23.3266	14.4093	1.61886	-36.101	82.7547	0.861136605	59.4281	0.41799
N7-AG Ctrl	S6-AG WetPlastic	53.1253	14.4093	3.68688	-6.3028	112.553	0.10687946	59.4281	0.95195
S5-AG DryPlastic	S6-AG WetPlastic	29.7987	14.4093	2.06802	-29.629	89.2268	0.688872643	59.4281	0.53396

Table F.3: Temperature Corrected AC Layer Modulus ANOVA

ANOVA: Single Factor

DESCRIPTION Alpha 0.05

Group	*Count*	*Sum*	*Mean*	*Variance*	*SS*	*Std Err*	*Lower*	*Upper*
N1-AG GTRDry	282	252947.8	896.9781169	6800.285	1910880.17	7.59979377	882.0723	911.8839403
N2-AG GTRWet	278	252511.2	908.3136787	8355.041	2314346.429	7.65427328	893.301	923.3263552
N5-AG Aramid	284	327811	1154.264105	15682.41	4438121.37	7.57298666	1139.411	1169.11735
N7-AG Ctrl	281	340353.9	1211.22374	18104.79	5069340.946	7.61330453	1196.291	1226.156063
S5-AG DryPlastic	293	419038.4	1430.165065	17631.55	5148412.161	7.45577085	1415.542	1444.78841
S6-AG WetPlastic	306	407466.7	1331.590397	29838.41	9100714.052	7.29567784	1317.281	1345.899744

ANOVA

Sources	*SS*	*df*	*MS*	*F*	*P value*	*Eta-sq*	*RMSSE*	*Omega Sq*
Between Groups	68261160	5	13652232.02	838.2063	0	0.70925862	1.707699	0.708292595
Within Groups	27981815	1718	16287.43605					
Total	96242975	1723	55857.79176					

Table F.4: Temperature Corrected AC Layer Modulus Tukey-Kramer

TUKEY HSD/KRAMER			alpha	0.05	
group	*mean*	*n*	*ss*	*df*	*q-crit*
N1-AG GTRDry	896.9781169	282	1910880.17		
N2-AG GTRWet	908.3136787	278	2314346.43		
N5-AG Aramid	1154.264105	284	4438121.37		
N7-AG Ctrl	1211.22374	281	5069340.95		
S5-AG DryPlastic	1430.165065	293	5148412.16		
S6-AG WetPlastic	1331.590397	306	9100714.05		
		1724	27981815.1	1718	4.03

Q TEST

group 1	*group 2*	*mean*	*std err*	*q-stat*	*lower*	*upper*	*p-value*	*mean-crit*	*Cohen d*
N1-AG GTRDry	N2-AG GTRWet	11.33556	7.62708217	1.486225	-19.4016	42.0727	0.900436394	30.73714	0.088821
N1-AG GTRDry	N5-AG Aramid	257.286	7.58640206	33.9141	226.7128	287.8592	3.84248E-13	30.5732	2.015996
N1-AG GTRDry	N7-AG Ctrl	314.2456	7.60655215	41.31249	283.5912	344.9	3.84248E-13	30.65441	2.462311
N1-AG GTRDry	S5-AG DryPlastic	533.1869	7.52812674	70.82598	502.8486	563.5253	3.84248E-13	30.33835	4.177853
N1-AG GTRDry	S6-AG WetPlastic	434.6123	7.44928791	58.3428	404.5917	464.6329	3.84248E-13	30.02063	3.405459
N2-AG GTRWet	N5-AG Aramid	245.9504	7.61373845	32.3035	215.2671	276.6338	3.84248E-13	30.68337	1.927175
N2-AG GTRWet	N7-AG Ctrl	302.9101	7.63381639	39.68003	272.1458	333.6743	3.84248E-13	30.76428	2.37349
N2-AG GTRWet	S5-AG DryPlastic	521.8514	7.55567397	69.06748	491.402	552.3008	3.84248E-13	30.44937	4.089032
N2-AG GTRWet	S6-AG WetPlastic	423.2767	7.47712561	56.60955	393.1439	453.4095	3.84248E-13	30.13282	3.316638
N5-AG Aramid	N7-AG Ctrl	56.95964	7.59317235	7.501428	26.35915	87.56012	1.90315E-06	30.60048	0.446314
N5-AG Aramid	S5-AG DryPlastic	275.901	7.5146073	36.71529	245.6171	306.1848	3.84248E-13	30.28387	2.161856
N5-AG Aramid	S6-AG WetPlastic	177.3263	7.43562513	23.8482	147.3607	207.2919	3.84248E-13	29.96557	1.389462
N7-AG Ctrl	S5-AG DryPlastic	218.9413	7.5349494	29.05677	188.5755	249.3072	3.84248E-13	30.36585	1.715542
N7-AG Ctrl	S6-AG WetPlastic	120.3667	7.4561827	16.1432	90.31824	150.4151	3.84359E-13	30.04842	0.943148
S5-AG DryPlastic	S6-AG WetPlastic	98.57467	7.37615869	13.36396	68.84875	128.3006	3.84248E-13	29.72592	0.772394

Table F.5: GB Layer Modulus ANOVA

ANOVA: Single Factor

DESCRIPTION Alpha 0.05

Group	*Count*	*Sum*	*Mean*	*Variance*	*SS*	*Std Err*	*Lower*	*Upper*
N1-AG GTRDry	282	1702.7	6.037943	1.30094	365.564	0.112753	5.816795	6.259091
N2-AG GTRWet	278	2060	7.410072	2.853689	790.4718	0.113561	7.187339	7.632805
N5-AG Aramid	284	2363.6	8.322535	5.237088	1482.096	0.112355	8.102167	8.542903
N7-AG Ctrl	281	3016.2	10.73381	5.749174	1609.769	0.112954	10.51227	10.95535
S5-AG DryPlastic	293	2396.5	8.179181	3.042339	888.363	0.110616	7.962224	8.396138
S6-AG WetPlastic	306	2336.2	7.634641	3.35414	1023.013	0.108241	7.422342	7.846939

ANOVA

Sources	*SS*	*df*	*MS*	*F*	*P value*	*Eta-sq*	*RMSSE*	*Omega Sq*
Between Groups	3358.249	5	671.6497	187.3425	1.8E-159	0.352849	0.815596	0.350833
Within Groups	6159.276	1718	3.585143					
Total	9517.525	1723	5.52381					

Table F.6: GB Layer Modulus Tukey-Kramer

TUKEY HSD/KRAMER			alpha	0.05	
group	*mean*	*n*	*ss*	*df*	*q-crit*
N1-AG GTRDry	6.037943262	282	365.564		
N2-AG GTRWet	7.410071942	278	790.4718		
N5-AG Aramid	8.322535211	284	1482.096		
N7-AG Ctrl	10.73380783	281	1609.769		
S5-AG DryPlastic	8.179180887	293	888.363		
S6-AG WetPlastic	7.634640523	306	1023.013		
		1724	6159.276	1718	4.03

Q TEST

group 1	*group 2*	*mean*	*std err*	*q-stat*	*lower*	*upper*	*p-value*	*mean-crit*	*Cohen d*
N1-AG GTRDry	N2-AG GTRWet	1.372129	0.113158	12.12578	0.916102	1.828155	3.85E-13	0.456027	0.724672
N1-AG GTRDry	N5-AG Aramid	2.284592	0.112554	20.29766	1.830997	2.738186	3.84E-13	0.453595	1.206578
N1-AG GTRDry	N7-AG Ctrl	4.695865	0.112853	41.6103	4.241065	5.150664	3.84E-13	0.454799	2.480061
N1-AG GTRDry	S5-AG DryPlastic	2.141238	0.11169	19.17128	1.691127	2.591348	3.84E-13	0.45011	1.130867
N1-AG GTRDry	S6-AG WetPlastic	1.596697	0.11052	14.44711	1.151301	2.042094	3.84E-13	0.445396	0.843275
N2-AG GTRWet	N5-AG Aramid	0.912463	0.11296	8.077752	0.457234	1.367692	1.97E-07	0.455229	0.481906
N2-AG GTRWet	N7-AG Ctrl	3.323736	0.113258	29.34661	2.867306	3.780165	3.84E-13	0.456429	1.755388
N2-AG GTRWet	S5-AG DryPlastic	0.769109	0.112099	6.861005	0.317352	1.220866	1.97E-05	0.451757	0.406195
N2-AG GTRWet	S6-AG WetPlastic	0.224569	0.110933	2.024358	-0.22249	0.671629	0.707801	0.447061	0.118603
N5-AG Aramid	N7-AG Ctrl	2.411273	0.112655	21.40406	1.957273	2.865272	3.84E-13	0.453999	1.273483
N5-AG Aramid	S5-AG DryPlastic	0.143354	0.111489	1.285812	-0.30595	0.592656	0.944251	0.449302	0.075711
N5-AG Aramid	S6-AG WetPlastic	0.687895	0.110317	6.23559	0.243315	1.132474	0.00016	0.444579	0.363303
N7-AG Ctrl	S5-AG DryPlastic	2.554627	0.111791	22.85179	2.104109	3.005145	3.84E-13	0.450518	1.349193
N7-AG Ctrl	S6-AG WetPlastic	3.099167	0.110622	28.01571	2.653359	3.544976	3.84E-13	0.445809	1.636785
S5-AG DryPlastic	S6-AG WetPlastic	0.54454	0.109435	4.975915	0.103516	0.985564	0.005933	0.441024	0.287592

Table F.7: Subgrade Layer Modulus ANOVA

ANOVA: Single Factor

DESCRIPTION					Alpha	0.05		
Group	*Count*	*Sum*	*Mean*	*Variance*	*SS*	*Std Err*	*Lower*	*Upper*
N1-AG GTRDry	282	8138.7	28.86064	7.352929	2066.173	0.181748	28.50417	29.21711
N2-AG GTRWet	278	7845.2	28.22014	10.55432	2923.547	0.183051	27.86112	28.57917
N5-AG Aramid	284	8819.5	31.05458	17.85033	5051.644	0.181107	30.69936	31.40979
N7-AG Ctrl	281	9158.5	32.59253	6.410623	1794.974	0.182071	32.23542	32.94963
S5-AG DryPlastic	293	7737.1	26.40648	7.373143	2152.958	0.178304	26.05677	26.7562
S6-AG WetPlastic	306	8359.1	27.31732	6.60347	2014.058	0.174475	26.97511	27.65953

ANOVA

Sources	*SS*	*df*	*MS*	*F*	*P value*	*Eta-sq*	*RMSSE*	*Omega Sq*
Between Groups	7835.039	5	1567.008	168.2222	7.8E-146	0.328673	0.765304	0.326592
Within Groups	16003.35	1718	9.315107					
Total	23838.39	1723	13.8354					

Table F.8: Subgrade Layer Modulus Tukey-Kramer

TUKEY HSD/KRAMER			alpha	0.05	
group	*mean*	*n*	*ss*	*df*	*q-crit*
N1-AG GTRDry	28.8606383	282	2066.173		
N2-AG GTRWet	28.22014388	278	2923.547		
N5-AG Aramid	31.05457746	284	5051.644		
N7-AG Ctrl	32.59252669	281	1794.974		
S5-AG DryPlastic	26.40648464	293	2152.958		
S6-AG WetPlastic	27.31732026	306	2014.058		
		1724	16003.35	1718	4.03

Q TEST

group 1	*group 2*	*mean*	*std err*	*q-stat*	*lower*	*upper*	*p-value*	*mean-crit*	*Cohen d*
N1-AG GTRDry	N2-AG GTRWet	0.640494	0.1824	3.511473	-0.09458	1.375568	0.129648	0.735074	0.209856
N1-AG GTRDry	N5-AG Aramid	2.193939	0.181428	12.09264	1.462786	2.925093	3.85E-13	0.731153	0.718837
N1-AG GTRDry	N7-AG Ctrl	3.731888	0.18191	20.51508	2.998793	4.464984	3.84E-13	0.733095	1.222742
N1-AG GTRDry	S5-AG DryPlastic	2.454154	0.180034	13.63161	1.728617	3.179691	3.84E-13	0.725537	0.804096
N1-AG GTRDry	S6-AG WetPlastic	1.543318	0.178149	8.663095	0.825379	2.261257	1.67E-08	0.717939	0.505663
N2-AG GTRWet	N5-AG Aramid	2.834434	0.182081	15.56685	2.100646	3.568222	3.84E-13	0.733788	0.928693
N2-AG GTRWet	N7-AG Ctrl	4.372383	0.182562	23.95019	3.63666	5.108106	3.84E-13	0.735723	1.432598
N2-AG GTRWet	S5-AG DryPlastic	1.813659	0.180693	10.03725	1.085467	2.541851	2.82E-11	0.728192	0.59424
N2-AG GTRWet	S6-AG WetPlastic	0.902824	0.178814	5.048945	0.182202	1.623445	0.004924	0.720622	0.295807
N5-AG Aramid	N7-AG Ctrl	1.537949	0.18159	8.469371	0.806143	2.269755	3.85E-08	0.731806	0.503904
N5-AG Aramid	S5-AG DryPlastic	4.648093	0.179711	25.86431	3.923859	5.372327	3.84E-13	0.724234	1.522933
N5-AG Aramid	S6-AG WetPlastic	3.737257	0.177822	21.01686	3.020635	4.453879	3.84E-13	0.716622	1.224501
N7-AG Ctrl	S5-AG DryPlastic	6.186042	0.180197	34.3293	5.459848	6.912237	3.84E-13	0.726195	2.026838
N7-AG Ctrl	S6-AG WetPlastic	5.275206	0.178313	29.58389	4.556603	5.99381	3.84E-13	0.718603	1.728405
S5-AG DryPlastic	S6-AG WetPlastic	0.910836	0.1764	5.163476	0.199945	1.621726	0.003654	0.710891	0.298432